

University of Alberta

Laboratory Measurements of Static and Dynamic Elastic Properties in
Carbonate

by

Aiman M. Bakhorji

A thesis submitted to the Faculty of Graduate Studies and Research
in partial fulfillment of the requirements for the degree of

Doctor of Philosophy

in

Geophysics

Department of Physics

©Aiman M. Bakhorji

Spring 2010

Edmonton, Alberta

Permission is hereby granted to the University of Alberta Libraries to reproduce single copies of this thesis and to lend or sell such copies for private, scholarly or scientific research purposes only. Where the thesis is converted to, or otherwise made available in digital form, the University of Alberta will advise potential users of the thesis of these terms.

The author reserves all other publication and other rights in association with the copyright in the thesis and, except as herein before provided, neither the thesis nor any substantial portion thereof may be printed or otherwise reproduced in any material form whatsoever without the author's prior written permission.

Examining Committee

Doug Schmitt, Physics

Mauricio Sacchi, Physics

Kim Chow, Physics

John-Paul Zonneveld, Earth and Atmospheric Science

Mike Batzle, Geophysics, Colorado School of Mines

To

My wife

Abstract

The fact that many of the giant hydrocarbon reservoirs, such as the Ghawar field in Saudi Arabia and the Grosmont formation in Alberta, are formed from carbonates make these rocks and the corresponding reservoirs important research topics. Compressional and shear wave velocities (at 1 MHz) and the quasi-static strains of thirty seven carbonate rock samples were measured as functions of saturating fluid and confining pressure. Furthermore, P- and S-wave velocities of the saturated samples were measured at constant differential pressure of 15 MPa. The quasi-static strains of the samples under jacketed and unjacketed conditions were also simultaneously acquired. The lithology, mineralogy, porosity and pore type and size distribution of each sample were obtained using a combination of thinsection and scanning electron microscopy, helium porosimetry and mercury intrusion porosimetry. Due to the lack of closing microcracks and compliant pores in low porosity samples, the travel times show slight changes with the confining pressure. Whereas the high porosity samples show remarkable reduction of travel time with the increase of confining pressure in both P- and S-wave. The samples show high sensitivity to the applied differential pressure specially the high porosity samples. We found that the sample physically deformed at pressure above 25 MPa. An evidence of inelastic deformation were observed in few samples even at 25 MPa differential pressure. The samples show no changes in travel time with increasing confining pressure under constant differential pressure, and this behavior is taken to be representative of full

saturation of the sample and hence used as a measure of quality control. The comparisons of Biot, Gassmann, squirt-Biot and squirt-Gassmann model predictions with the measured water saturated velocities show that the squirt mechanism is not active on all the studied samples. Biot mechanism is likely to be the principle dispersion mechanism in these samples. For S-wave velocities, Gassmann's model consistently over-predict the saturated at low pressure and closely fit the measured velocities at high pressure, whereas, Biot model over-predicts the saturated velocities in most of the studied samples.

The strains measured from the vertical and horizontal strain gages are differing by around 27%. The strains over the horizontal axis are higher than the vertical axis suggesting that the majority of the compliant pores and crack-like pores are oriented almost in direction parallel to the length of the sample. The static bulk modulus is always lower than dynamic one for all measured samples. There is no correlation between porosity and static-dynamic ratio. The measured grain bulk modulus obtained from theunjacketed test is reasonably close to the bulk modulus of the constituent mineral phases.

Acknowledgments

Firstly, all thanks and praise be to my lord the most gracious and most merciful.

A special thanks and gratitude goes to my life-partner, my wife Abrar to her endless support that she showed throughout my life and career. I could never have accomplished anything without her encouragement, companionship and support. Her sacrifices, patience and love can never be repaid but will always be remembered and cherished and I hope someday my Lord will provide me opportunities to make it up to her. During the course of this work my children suffered greatly since I could not give them as much time as I wanted to give them and certainly not nearly as much as they deserved. They have lost a lot due to my research abroad. I thank from the bottom of my heart my daughters, Baraah, Sarah, and Yara and my son Malik, for their patience and their love and for bearing with their father through thick and thin. I am grateful to my mother to her own affectionate way of encouragement and I am what I am today because of her kind wishes and prayers. My special gratitude is due to my brothers, sisters and their families and to my friends for their loving support.

I am deeply grateful to my supervisor, Dr. D. R. Schmitt for his detailed and constructive comments, and for his important support throughout this work. I also would like to thank the members of my defence committee for reviewing my thesis.

A special thank goes to L. Tober and Lucas Duerksen for technical assistance and help in the Rock Physics Laboratory. A special thank goes to Mr. Hassan Hassan for his help and useful discussion in samples description and characterization. During this work I have collaborated with many colleagues for whom I have great regard, and I wish to extend my warmest thanks to all those who have helped me with my work in the experimental geophysics group in the department of physics at University of Alberta for their support.

I would like to express my deep and sincere gratitude to Mr. Craig Phillips and Dr. Aus Tawil from Saudi Aramco for their continued encouragements and support from the beginning to the end of my Ph. D program. I also would like to thank Mr. Ali Al-Qahtani, Mr. Youcef Mousa, Mr. Suhail Humoud for their time and effort they spent to prepare and send the data. I wish to thank Mr. Nazih Najjar and Mr. Mohammed Al-Khalifa for their help in getting my thesis reviewed by Aramco.

I am indebted to Saudi Aramco for sponsoring my Ph.D study as well as providing samples. The fund for the experimental work was partially provided by the National Science and Engineering Research Council (NSERC) of Canada.

Lastly, I offer my regards and blessings to all of those who supported me in any respect during the completion of the project.

Table of contents

Abstract

Acknowledgments

Table of contents

List of tables

List of figures

1 Introduction	1
1.1 Objectives.....	1
1.2 Chapter Descriptions.....	4
2 Background (Literature Review)	7
2.1 Introduction.....	7
2.2 Ultrasonic velocity measurements in carbonate rock.....	9
2.3 Static and dynamic moduli in carbonate.....	14
2.4 Conclusions.....	17
3 Sample Characterization	18
3.1 Introduction.....	18
3.2 Methodology.....	22
3.2.1 Thin Section.....	23

3.2.2	Mercury Intrusion Porosimetry.....	24
3.2.3	Helium Porosimetry.....	27
3.2.4	Scanning Electron Microscope (SEM).....	28
3.3	Results and Discussion.....	29
3.3.1	Porosity and permeability.....	31
3.3.2	Mineralogy and Lithology.....	33
3.3.3	Pore type.....	39
3.3.4	Pore size distribution.....	43
3.4	Conclusions.....	51
4	Theoretical background	52
4.1	Introduction.....	52
4.2	Theory of elasticity.....	53
4.3	Wave equations in isotropic material.....	57
4.4	Gassmann's Equations.....	59
4.5	Bulk Modulus (incompressibility parameters).....	64
4.5.1	Jacketed bulk modulus test.....	65
4.5.2	Unjacketed bulk modulus test.....	67
4.5.3	Effect of cracks on elastic properties.....	68
4.6	Conclusions.....	69
5	Ultrasonic velocity and quasi-static strain experiments	71
5.1	Introduction.....	71
5.2	Ultrasonic velocity measurement.....	73
5.2.1	Ultrasonic transducers.....	73

5.2.2	Velocity calculation and error analysis.....	76
5.3	Strain Measurements.....	81
5.3.1	Strain gage and Wheatstone bridge.....	81
5.3.2	Strain calculation.....	84
5.3.3	Uncertainty analysis.....	85
5.4	Sample preparation.....	87
5.5	Velocity and strain experimental setup.....	89
5.6	Experimental procedure.....	91
5.7	Result and discussion.....	94
5.7.1	Waveforms.....	94
5.7.2	Changes in P- and S-wave velocities with pressure.....	99
5.7.3	Effect of saturation on velocity and dynamic moduli.....	104
5.7.4	Effect of mineralogy on velocity.....	108
5.7.5	Effect of porosity, pore type and texture in velocity.....	112
5.8	Conclusions.....	120
6	Fluid Saturated Ultrasonic Velocities in Carbonate Rocks	122
6.1	Introduction.....	122
6.2	Velocity models in fully saturated rock.....	127
6.3	Modeling results and discussions.....	130
6.3.1	P-wave velocities.....	133
6.3.2	S-wave velocities.....	141
6.4	Conclusions.....	146

7 Static, dynamic and grain bulk moduli in Carbonate	147
7.1 Introduction.....	147
7.2 Dynamic bulk modulus.....	149
7.3 Static bulk modulus.....	153
7.4 Comparison of static and dynamic bulk moduli.....	157
7.5 Grain bulk modulus.....	170
7.6 Conclusions.....	172
8 Conclusion	173
8.1 summary.....	173
8.2 Future work.....	176
References	178
Appendix A	189
Appendix B	257
Appendix C	259

List of tables

3.1	Physical properties of the studied samples.....	30
3.2	Macro, micro and dual porosities samples list.....	45
5.1	Petrological properties for sample 2-368, 3-05, 3-471 and 7-222.....	109
5.2	Moduli and density of common mineral in carbonate.....	109
5.3	Petrological properties for samples 4-151, 3-429, 2-383, 4-09 and 1-304.....	117
B.1	Petrological parameters of the studied samples.....	257
C.1	Dry and saturated velocities of sample 1-11.....	261
C.2	Saturated velocities of sample 1-11 under constant differential pressure	261
C.3	Dry and saturated velocities of sample 1-132.....	263
C.4	Saturated velocity of sample 1-132 under constant differential pressure.....	263
C.5	Dry and saturated velocities of sample 1-288.....	265
C.6	Saturated velocity of sample 1-288 under constant differential pressure.....	265
C.7	Dry and saturated velocities of sample 1-304.....	267
C.8	Saturated velocity of sample 1-304 under constant differential pressure.....	267

C.9	Dry and saturated velocities of sample 2-10.....	269
C.10	Saturated velocity of sample 2-10 under constant differential pressure.....	269
C.11	Dry and saturated velocities of sample 2-33.....	271
C.12	Saturated velocity of sample 2-33 under constant differential pressure.....	271
C.13	Dry and saturated velocities of sample 2-59.....	273
C.14	Dry and saturated velocities of sample 2-131.....	275
C.15	Saturated velocity of sample 2-131 under constant differential pressure.....	275
C.16	Dry and saturated velocities of sample 2-160.....	277
C.17	Saturated velocity of sample 2-160 under constant differential pressure.....	277
C.18	Dry and saturated velocities of sample 2-368.....	279
C.19	Saturated velocity of sample 2-368 under constant differential pressure.....	279
C.20	Dry and saturated velocities of sample 2-383.....	281
C.21	Saturated velocity of sample 2-383 under constant differential pressure.....	281
C.22	Dry and saturated velocities of sample 2-432.....	283
C.23	Saturated velocity of sample 2-432 under constant differential pressure.....	283
C.24	Dry and saturated velocities of sample 3-05.....	285

C.25	Saturated velocity of sample 3-05 under constant differential pressure.....	285
C.26	Dry and saturated velocities of sample 3-90.....	287
C.27	Saturated velocity of sample 3-90 under constant differential pressure.....	287
C.28	Dry and saturated velocities of sample 3-104.....	289
C.29	Dry and saturated velocities of sample 3-146.....	291
C.30	Saturated velocity of sample 3-146 under constant differential pressure.....	291
C.31	Dry and saturated velocities of sample 3-331.....	293
C.32	Saturated velocity of sample 3-331 under constant differential pressure.....	293
C.33	Dry and saturated velocities of sample 3-429.....	295
C.34	Saturated velocity of sample 3-429 under constant differential pressure.....	295
C.35	Dry and saturated velocities of sample 3-471.....	297
C.36	Saturated velocity of sample 3-471 under constant differential pressure.....	297
C.37	Dry and saturated velocities of sample 3-534.....	299
C.38	Saturated velocity of sample 3-534 under constant differential pressure.....	299
C.39	Dry and saturated velocities of sample 4-09.....	301
C.40	Saturated velocity of sample 4-09 under constant differential	

pressure.....	301
C.41 Dry and saturated velocities of sample 4-55.....	303
C.42 Saturated velocity of sample 4-55 under constant differential pressure.....	303
C.43 Dry and saturated velocities of sample 4-97.....	305
C.44 Saturated velocity of sample 4-97 under constant differential pressure.....	305
C.45 Dry and saturated velocities of sample 4-151.....	306
C.46 Dry and saturated velocities of sample 4-180.....	308
C.47 Saturated velocity of sample 4-180 under constant differential pressure.....	308
C.48 Dry and saturated velocities of sample 4-189.....	310
C.49 Saturated velocity of sample 4-189 under constant differential pressure.....	310
C.50 Dry and saturated velocities of sample 4-326.....	312
C.51 Saturated velocity of sample 4-326 under constant differential pressure.....	312
C.52 Dry and saturated velocities of sample 5-02.....	314
C.53 Saturated velocity of sample 5-02 under constant differential pressure.....	314
C.54 Dry and saturated velocities of sample 5-289.....	316
C.55 Saturated velocity of sample 5-289 under constant differential pressure.....	316

C.56	Dry and saturated velocities of sample 5-295.....	318
C.57	Saturated velocity of sample 5-295 under constant differential pressure.....	318
C.58	Dry and saturated velocities of sample 7-222.....	320
C.59	Saturated velocity of sample 7-222 under constant differential pressure.....	320
C.60	Dry and saturated velocities of sample 7-240.....	322
C.61	Saturated velocity of sample 7-240 under constant differential pressure.....	322
C.62	Dry and saturated velocities of sample 7-20.....	324
C.63	Saturated velocity of sample 7-20 under constant differential pressure.....	324
C.64	Dry and saturated velocities of sample 7-16.....	326
C.65	Saturated velocity of sample 7-16 under constant differential pressure.....	326
C.66	Dry and saturated velocities of sample 8-23.....	328
C.67	Saturated velocity of sample 8-23 under constant differential pressure.....	328
C.68	Dry and saturated velocities of sample 8-90.....	330
C.69	Saturated velocity of sample 8-90 under constant differential pressure.....	330
C.70	Dry and saturated velocities of sample 8-115.....	332
C.71	Saturated velocity of sample 8-115 under constant differential	

pressure.....	332
C.72 List of buffer pair sets and the samples measured using each pair.....	333
C.73 P- and S-wave travel time of aluminum buffer set 4.....	334
C.74 P- and S-wave travel time of aluminum buffer set 5.....	335
C.75 P- and S-wave travel time of aluminum buffer set 6.....	336
C.76 P- and S-wave travel time of aluminum buffer set 8.....	337
C.77 P- and S-wave travel time of aluminum buffer set 9.....	338
C.78 P- and S-wave travel time of aluminum buffer set 10.....	339

List of Figures

3.1	Dunham's carbonate rocks classification.....	20
3.2	Choquette and Pray carbonate pore types classification.....	22
3.3	Thin section photomicrograph of sample 8-23.....	24
3.4	Pore throat distribution of sample 2-33.....	26
3.5	Porosity-permeability cross plot for all samples.....	32
3.6	Thin section photomicrograph of sample 2-33 and 3-90.....	36
3.7	Thin section photomicrograph of sample 5-02 and 7-240.....	37
3.8	Thin section photomicrograph of sample 2-432 and 7-20.....	38
3.9	Thin section photomicrograph of sample 7-222.....	39
3.10	Thin sections photomicrograph of different pore types.....	42
3.11	Mercury intrusion plots for samples 1-132 and 2-33.....	46
3.12	Mercury intrusion plots for samples 7-240 and 2-59.....	47
3.13	Mercury intrusion plots for samples 8-23 and 3-05.....	48
3.14	SEM images of different microporostiy types.....	50
4.1	Schematic illustration of pours rock model.....	61
4.2	Jacketed and unjacketed test.....	67
5.1	Schematic of the source/receiver transducer.....	76
5.2	Aluminum buffer with transducers.....	76

5.3	Schematic of the wave propagation through the sample.....	77
5.4	Normalized <i>P</i> - and <i>S</i> - wave waveforms obtained on aluminum buffer.	79
5.5	Two <i>P</i> -wave signals through aluminum buffer with and without sample at 15 MPa confining pressure.....	80
5.6	Schematic of the bounded foil strain gage.....	83
5.7	Schematic of Wheatstone bridge circuit.....	84
5.8	Schematic illustration of pressure effect on strain gage response.....	86
5.9	The sample with the affixed strain gages, pair of transducers and the tygon tubing.	88
5.10	The jacketed assembly of the sample.....	89
5.11	The experimental setup used.....	91
5.12	Normalized <i>P</i> - and <i>S</i> - wave waveforms for sample 7-222 at different confining pressure.....	96
5.13	Normalized <i>P</i> - and <i>S</i> - wave waveforms for sample 3-104 at different confining pressure.....	97
5.14	Normalized <i>P</i> - and <i>S</i> - wave waveforms for sample 8-115 at constant differential pressure.....	98
5.15	<i>P</i> - and <i>S</i> - wave velocities for sample 3-104 at different confining pressure.....	101
5.16	<i>P</i> - and <i>S</i> - wave velocities for sample 3-90 at different confining pressure.....	102
5.17	<i>P</i> - and <i>S</i> - wave velocities for sample 1-11 at different confining pressure.....	103

5.18	Cross plots of dry and saturated P- and S-wave velocities for all measured samples.	106
5.19	Cross plots of dry and saturated bulk and shear moduli for all measured samples.	107
5.20	Dry P- and S-wave velocities for sample 2-368, 3-05, 3471 and 7-222 at different confining pressure.	110
5.21	Dry bulk and shear moduli for sample 2-368, 3-05, 3471 and 7-222 at different confining pressure.	111
5.22	Velocity-porosity cross plot for dry P- and S-wave velocities.	112
5.23	Dry P- and S-wave velocities at different pressure.	115
5.24	Calculated P- and S-wave velocities for non-porous material.....	116
5.25	Dry P- and S-wave velocities for sample 2-33 and 1-132 at different confining pressure.	117
5.26	Mercury intrusion curve, thin section and SEM image for sample 1-132.....	118
5.27	Mercury intrusion curve, thin section and SEM image for sample 2-33	119
6.1	P-wave velocity as a function of confining and differential pressure for water saturated sample 4-55, 8-23 and 4-09.....	126
6.2	The observed velocity and model predictions for P-wave velocities of sample 4-55, 4-97 and 4-326.....	131
6.3	The observed velocity and model predictions for S-wave velocities of sample 4-55, 4-97 and 4-327.....	132

6.4	The observed velocity and model predictions for P-wave velocities of sample 4-55, 4-97 and 1-288.....	135
6.5	The observed velocity and model predictions for P-wave velocities of sample 2-160, 2-33 and 2-131.....	136
6.6	Thin section photomicrography and mercury intrusion curve of sample 4-55.....	137
6.7	SEM images of sample 4-55.....	138
6.8	Thin section photomicrography and mercury intrusion curve of sample 2-33.....	139
6.9	SEM images of sample 2-33.....	140
6.10	The observed velocities and model predictions for S-wave velocities of three different samples 4-55, 4-97 and 1-288.....	142
6.11	The observed velocities and model predictions for S-wave velocities of samples 1-11 and 7-222.....	143
6.12	Saturated velocity models and Mercury intrusion curve for sample 2-160	144
6.13	Saturated velocity models and Mercury intrusion curve for sample 3-331.....	145
7.1	Normalized P- and S-wave waveforms for sample 2-33 at different confining pressure.....	151
7.2	P- and S-wave velocities of sample 2-33 at different confining pressure.	152
7.3	Bulk and shear moduli of sample 2-33 at different confining pressure...	153

7.4	Stress-strain relations for sample 4-55.....	156
7.5	Static bulk moduli of sample 4-55 at different confining pressure.....	156
7.6	Stress-strain relations for sample 7-222.....	157
7.7	Comparison of dynamic and static bulk moduli of sample 4-55.....	160
7.8	Comparison of dynamic and static bulk moduli of sample 4-326.....	161
7.9	Comparison of dynamic and static bulk moduli of sample 1-288.....	162
7.10	Comparison of dynamic and static bulk moduli of sample 2-383.....	163
7.11	Comparison of dynamic and static bulk moduli of sample 4-09.....	164
7.12	Comparison of dynamic and static bulk moduli of sample 3-429.....	165
7.13	Comparison of dynamic and static bulk moduli of sample 7-222.....	166
7.14	Cross plots of dry static against dry dynamic bulk moduli at 5, 10, 15, 20, and 25 MPa pressure.....	168
7.15	Cross plots of dry against saturated static bulk moduli at 5, 10, 15, 20, and 25 MPa pressure.....	169
7.16	Grain bulk modulus for sample 4-55 and sample 2-383.....	171
A.1	Thin section photomicrograph of sample 2-10.....	191
A.2	Pore throat size distribution of sample 2-10.....	191
A.3	Thin section photomicrograph of sample 2-33.....	192
A.4	Pore throat size distribution of sample 2-33.....	193
A.5	SEM images of sample 2-33.....	193
A.6	Thin section photomicrograph of sample 2-59.....	195
A.7	Pore throat size distribution of sample 2-59.....	196
A.8	Thin section photomicrograph of sample 2-131.....	197

A.9	SEM images of sample 2-131.....	198
A.10	Thin section photomicrograph of sample 2-160.....	199
A.11	Pore throat size distribution of sample 2-160.....	200
A.12	SEM images of sample 2-160.....	201
A.13	Thin section photomicrograph of sample 2-368.....	202
A.14	Pore throat size distribution of sample 2-368.....	203
A.15	Thin section photomicrograph of sample 2-383.....	204
A.16	Thin section photomicrograph of sample 2-432.....	205
A.17	Pore throat size distribution of sample 3-05.....	206
A.18	Thin section photomicrograph of sample 3-90.....	207
A.19	Pore throat size distribution of sample 3-90.....	208
A.20	SEM images of sample 3-90.....	208
A.21	Thin section photomicrograph of sample 3-104.....	209
A.22	Pore throat size distribution of sample 3-104.....	210
A.23	Thin section photomicrograph of sample 3-146.....	211
A.24	Pore throat size distribution of sample 3-146.....	212
A.25	Thin section photomicrograph of sample 3-331.....	213
A.26	Pore throat size distribution of sample 3-331.....	214
A.27	SEM images of sample 3-331.....	214
A.28	Thin section photomicrograph of sample 3-429.....	215
A.29	Thin section photomicrograph of sample 3-471.....	216
A.30	Thin section photomicrograph of sample 3-534.....	217
A.31	Pore throat size distribution of sample 3-534.....	218

A.32	SEM images of sample 3-534.....	218
A.33	Thin section photomicrograph of sample 4-09.....	219
A.34	Thin section photomicrograph of sample 4-55.....	220
A.35	SEM images of sample 4-55.....	221
A.36	Pore throat size distribution of sample 4-55.....	222
A.37	Thin section photomicrograph of sample 4-97.....	223
A.38	Pore throat size distribution of sample 4-97.....	224
A.39	Thin section photomicrograph of sample 4-151.....	225
A.40	Thin section photomicrograph of sample 4-180.....	226
A.41	Thin section photomicrograph of sample 4-189.....	227
A.42	Pore throat size distribution of sample 4-189.....	228
A.43	SEM images of sample 4-189.....	229
A.44	Thin section photomicrograph of sample 4-326.....	230
A.45	Pore throat size distribution of sample 4-326.....	231
A.46	Thin section photomicrograph of sample 7-240.....	232
A.47	Pore throat size distribution of sample 7-240.....	233
A.48	Thin section photomicrograph of sample 7-20.....	234
A.49	SEM images of sample 7-20.....	235
A.50	Thin section photomicrograph of sample 7-222.....	236
A.51	Thin section photomicrograph of sample 7-16.....	237
A.52	Pore throat size distribution of sample 7-16.....	238
A.53	Thin section photomicrograph of sample 5-289.....	239
A.54	Thin section photomicrograph of sample 5-295.....	240

A.55	Thin section photomicrograph of sample 5-02.....	241
A.56	Pore throat size distribution of sample 5-02.....	242
A.57	Thin section photomicrograph of sample 1-132.....	244
A.58	Pore throat size distribution of sample 1-132.....	245
A.59	Thin section photomicrograph of sample 1-11.....	246
A.60	Thin section photomicrograph of sample 1-288.....	247
A.61	Thin section photomicrograph of sample 1-304.....	248
A.62	Thin section photomicrograph of sample 8-91.....	249
A.63	Pore throat size distribution of sample 8-91.....	250
A.64	SEM images of sample 8-91.....	251
A.65	Thin section photomicrograph of sample 8-23.....	252
A.66	Pore throat size distribution of sample 8-23.....	253
A.67	SEM images of sample 8-23.....	254
A.68	Thin section photomicrograph of sample 8-115.....	255
A.69	Pore throat size distribution of sample 8-115.....	256
C.1	Normalized waveforms of sample 1-11.....	260
C.2	Normalized waveforms of sample 1-132.....	262
C.3	Normalized waveforms of sample 1-288.....	264
C.4	Normalized waveforms of sample 1-304.....	266
C.5	Normalized waveforms of sample 2-10.....	268
C.6	Normalized waveforms of sample 2-33.....	270
C.7	Normalized waveforms of sample 2-59.....	272
C.8	Normalized waveforms of sample 2-131.....	274

C.9	Normalized waveforms of sample 2-160.....	276
C.10	Normalized waveforms of sample 2-368.....	278
C.11	Normalized waveforms of sample 2-383.....	280
C.12	Normalized waveforms of sample 2-432.....	282
C.13	Normalized waveforms of sample 3-05.....	284
C.14	Normalized waveforms of sample 3-90.....	286
C.15	Normalized waveforms of sample 3-104.....	288
C.16	Normalized waveforms of sample 3-146.....	290
C.17	Normalized waveforms of sample 3-331.....	292
C.18	Normalized waveforms of sample 3-429.....	294
C.19	Normalized waveforms of sample 3-471.....	296
C.20	Normalized waveforms of sample 3-534.....	298
C.21	Normalized waveforms of sample 4-09.....	300
C.22	Normalized waveforms of sample 4-55.....	302
C.23	Normalized waveforms of sample 4-97.....	304
C.24	Normalized waveforms of sample 4-151.....	306
C.25	Normalized waveforms of sample 4-180.....	307
C.26	Normalized waveforms of sample 4-189.....	309
C.27	Normalized waveforms of sample 4-326.....	311
C.28	Normalized waveforms of sample 5-02.....	313
C.29	Normalized waveforms of sample 5-289.....	315
C.30	Normalized waveforms of sample 5-295.....	317
C.31	Normalized waveforms of sample 7-222.....	319

C.32	Normalized waveforms of sample 7-240.....	321
C.33	Normalized waveforms of sample 7-20.....	323
C.34	Normalized waveforms of sample 7-16.....	325
C.35	Normalized waveforms of sample 8-23.....	327
C.36	Normalized waveforms of sample 8-91.....	329
C.37	Normalized waveforms of sample 8-115.....	331

Chapter 1

Introduction

1.1 Objectives

Carbonate reservoirs contain more than half of the world's oil and gas reserves (Baechle et al., 2009). The Ghawar Oil Field in Saudi Arabia is by far the largest conventional oil field in the world. It is globally important as it alone accounts for more than half of the cumulative oil production of Saudi Arabia. The Arab-D carbonate reservoir of this field covers about 693000 acres (2804 km²) (Alsharhan and Kendall, 1986). A second, but nearly untouched, example reservoir lies within the Grosmont carbonate formation of Alberta, Canada. It is thought to contain upwards 318 billion bbl (50 billion m³) of bitumen. It houses about 96% of world's original carbonate-hosted bitumen in place (Potter, 2007). The Khuff carbonate in the Arabian/Persian Gulf region represents the largest gas accumulation in the world (Ehrenberg et al., 2007). This huge oil and gas reserve make carbonates one of the most important targets for research in recent years.

Despite this fact carbonate rock has not received enough attention (Verwer et al. 2008). Most research on the effect of porosity, pore type, saturation, mineralogy and pressure on rock elastic properties has been performed on siliciclastic rocks (i.e. sedimentary rocks such as sandstones and shales formed from silica rich minerals that had been transported and deposited). The textures and pore structures of such rocks differs substantially from most carbonates, which were laid down by chemical or biological processes. As such, the predictive models used to describe the behavior of siliclastic material are generally not applicable to carbonates (Anselmetti and Eberli, 1993; Assefa et al. 2003; Baechle et al., 2005; Adam et al., 2006; Verwer et al., 2008).

Carbonate rock composition derives from a combination of biological and chemical components. This adds complexity and heterogeneity to its structure and petrophysical properties. These complexities and heterogeneities make the studies to understand the effects of porosity, pore type, saturation, mineralogy and pressure on the elastic properties a challenge. However, this challenge must be overcome if seismic observations over such reservoirs are to reach their full potential.

In recent years, the compressional and shear velocities of carbonate rocks have been measured attempts to develop relationships between the carbonate's petrophysical and elastic properties (e.g., Anselmetti and Eberli, 1993 and 1997; Best, 1997; Assefa et al. 2003; Baechle et al., 2005; Rafavich et al., 1984; Wang, 1997; Adam et al., 2006; Rogen et al., 2005; Kenter et al. 2007; Verwer et al., 2008; Adam et al. 2009). However, the heterogeneity of carbonate rocks has made

it difficult for researchers to build consensus in their findings. Despite the number of studies conducted, the science community still lacks a solid understanding of these relationships (Adam et al., 2006; Assefa et al., 2003; Scotellaro et al., 2007). Nevertheless, the situation is far from hopeless.

With respect to petroleum geosciences, a general goal of applied geophysicists is to be able to improve the predictive capability of surface seismic observations of the conditions and characteristics of carbonate reservoirs. This large problem will not be solved in its entirety here, but the general objective of this study is to add to the data base of laboratory observations of physical properties on carbonates. In particular, we analyzed the data resulting from the measurements and observations of the P- and S-wave velocities (at 1 MHz) and the quasi-static strains in the carbonate rock samples as functions of saturating fluid and confining pressure. The observed water saturated velocities were compared to the fluid models (e.g. Gassmann (1951) and Biot(1956b)). Uniquely, this study further looked at detail a variety of factors such as the effects of saturation, mineralogy, and pore microstructure on the elastic properties on carbonate rocks. Two main aspects of this research are innovative. First with our work, we hope to increase the understanding of the factors that influence elastic properties in carbonate rocks. The rock physics community is desperate for new laboratory measurements data sets to prove the validity of their predictive techniques! Second, to our knowledge, these are among the first simultaneous measurements of P- and S-wave velocities and quasi-static strain obtained on Arab-D carbonates (or any carbonates for that matter) under in situ conditions.

1.2 Chapter Descriptions

In this research study, nearly sixty five core plug samples were received from Saudi Aramco Oil Company. The samples are from seven different wells in Arab formation of the Ghawar oil field. Thirty seven representative samples were used in this project. P- and S-wave velocities were measured in all samples on dry and saturated conditions at different confining pressure. Furthermore, P- and S-wave velocities of the saturated samples were measured at constant differential pressure of 15 MPa. The quasi-static strains of the samples under jacketed and unjacketed conditions were measured simultaneously with the ultrasonic measurements on twenty three of the samples. Each of the thirty seven samples was photographed and weighted before it underwent testing. Thin sections of selected samples were made in the Earth and Atmospheric Science department at University of Alberta. A complete petrographic analysis from thin section for most of these samples was obtained from Aramco and the rest were made in the Earth and Atmospheric Science Department at University of Alberta. The bulk and grain density and porosity on each sample were measured using helium pycnometer. Pore size distributions on selected samples were measured using mercury porosimeter (Micromeritics Autopore IV). Furthermore SEM images for 15 samples were made.

Chapter 2 contains a literature review of previous works attempted to measure and study factors, such as pressure, saturation and pore structure, that influence the elastic properties in carbonate rocks. A short review of quasi-static

strain measurements on different material such as glass, steel, sandstone, granite, and carbonate. This includes the studies that compare dynamic and static moduli.

In chapter 3 the Arab formation carbonate samples were characterized using thin section photomicrograph and SEM images. Including mineralogy, lithology, grain type and pore types. The pore size distributions were obtained using Mercury intrusion data.

In chapter 4 a brief review of the theory of elasticity and wave equations in isotropic material are shown. Gassmann's equations and its assumptions and applicability were reviewed. Physical and mathematical definition of bulk modulus of material as well as the difference between static and dynamic bulk moduli also included.

A detail description of the methodologies that used to measure, ultrasonic velocities, quasi-static strains, petrophysical properties, and petrological description of the samples were shown in chapter 5. This includes experimental configuration, transducer and sample preparation. Velocity and strain determination from the recorded ultrasonic wave signals and changes in voltage data respectively are also shown. This chapter also provides examples and discussion of the changes in velocity and elastic properties with pressure, saturation, porosity and texture.

Chapter 6 compares the measured velocities in water saturated samples to predicted velocities obtained based on the dry measurements using Gassmann (1951), Biot (1956b) and Mavko-Jizba (1991) models.

The analysis of the relationship of statically and dynamically measured bulk moduli on selected carbonate samples is discussed in chapter7. This chapter is also show a preliminary result of measured grain bulk modulus in carbonate.

The final chapter, Chapter 8 summarized conclusions and results of all chapters and give directions of future work.

Chapter 2

Background (Literature Review)

2.1 Introduction

Geophysical methods were used for decades to study and explore the subsurface for hydrocarbon discoveries. Seismic exploration in particular used to image the subsurface geological structures in 2D and 3D images which led to a great success on discovering potential oil and gas fields around the world. Now seismic is not limited to only the discovery stage of the hydrocarbon reservoirs but it is focusing in monitoring production and potential changes on reservoir rocks. Petrophysical (porosity, permeability and saturation) and environmental properties (pressure and temperature) of reservoirs undergo changes caused by the extraction of hydrocarbon and the injection of different fluid during production. These changes in particular pore fluid and pore pressure might lead to many problems in reservoirs. Therefore, Understanding the effects of these changes on the elastic properties of reservoir rock is essential for the adequate interpretation

of seismic reflection amplitudes and amplitude versus offset responses which in turn helps to overcome the problems and enhanced hydrocarbon recovery.

The fact that many of the giant hydrocarbon reservoirs, such as the Ghawar field in Saudi Arabia and the Grosmont formation in Alberta, are formed from carbonates make these rocks and the reservoirs they form important research topics. In recent years, the compressional and shear velocities of carbonate rocks have been measured attempts to develop relationships between the carbonate's petrophysical and elastic properties (e.g., Anselmetti and Eberli, 1993 and 1997; Best, 1997; Assefa et al. 2003; Baechle et al., 2005; Rafavich et al., 1984; Wang, 1997; Adam et al., 2006; Rogen et al., 2005; Kenter et al. 2007; Verwer et al., 2008; Adam et al. 2009). However, the heterogeneity of carbonate rocks has made it difficult for researchers to build consensus in their findings. Despite the number of studies conducted, the science community still lacks a solid understanding of these relationships (Adam et al., 2006; Assefa et al., 2003; Scotellaro et al., 2007). Nevertheless, the situation is far from hopeless.

A general goal of exploration geophysicists is to be able to improve the predictive capability of surface seismic observations of the conditions and characteristics of carbonate reservoirs. This large problem will not be solved in its entirety here, but the general objective of this study is to add to the data base of laboratory observations of physical properties on carbonates. Two main aspects of this research are innovative. First with our work, we hope to increase the understanding of the factors that influence elastic properties in carbonate rocks. The rock physics community is desperate for new laboratory measurements data

sets to prove the validity of their predictive techniques! Second, to our knowledge, these are the first simultaneous measurements of P- and S-wave velocities and pseudo-static strain obtained on Arab-D carbonates (or any carbonates for that matter) under in situ conditions.

In this chapter we listed and briefly reviewed some of the published studies which were attempted to measure and discuss the measured ultrasonic velocities in carbonate rocks and its relation to petrophysical and environmental properties. Studies that compare static and dynamic moduli in different rocks and material are shown as well.

2.2 Ultrasonic velocity measurements in carbonate rock

Carbonate reservoirs contain more than half of the world's oil and gas reserves make carbonates one of the most important targets for research in recent years. As such, there are a number of precursory studies on carbonates that essentially employ the pulse-transmission method. In this conceptually simple measurement an ultrasonic P or S wave pulse is propagated from one end to the other of a sample of known length. The transmit time of this pulse is measured and the velocity is simply the ratio of the length to this time. Of course, the measurement is usually not so easily technically accomplished but the technique remains highly popular in the rock physics community. Consequently, many studies were conducted to measure compressional and shear velocities in carbonate rocks (Anselmetti and Eberli, 1993; Anselmetti et al., 1997; Best, 1997; Assefa et al., 2003; Baechle et al., 2005; Rafavich et al., 1984; Wang, 1997;

Adam et al., 2006; Rogen et al., 2005; Kenter et al. 2007; Verwer et al., 2008, Baechle et al., 2009). These studies showed that velocity in general decrease with increasing porosity and in addition they reported large variability in velocities. Most of these studies have shown large deviation with respect to the conventional velocity-porosity relation and huge variability in velocity at a given porosity (Anselmetti and Eberli, 1993; Assefa et al. 2003; Baechle et al., 2005; Rafavich et al., 1984; Wang, 1997, Rogen et al., 2005; Kenter et al., 2007; Verwer et al., 2008). Stressing that porosity and pore type are the main controlling factors of velocities in carbonates.

A brief review of the literature on laboratory experiments in carbonates follows. These earlier workers have mostly employed Gassmann's (1951) relation as a point of reference. This relation and its underlying assumptions will be discussed in more detail later, but it is important to note at this point that given some knowledge of the rock frame, the saturating fluid, and the mineral constituents, Gassmann's formula allows for a 'low-frequency' prediction of the bulk and shear moduli of the fluid saturated rock relative to its 'dry' (i.e. usually compressible gas filled) reference.

Rafavich et al. (1984) presented ultrasonic compressional and shear velocities in carbonate samples with different porosity (0–20%) and mineralogy. Their results showed that compressional velocity varies between 4200 m/s and 6300 m/s and shear wave velocity varies between 2600 m/s and 3500 m/s. They concluded that porosity and density are the major factors that influence the velocity. They showed that velocity decreases with increasing quartz content

though its influence is less than that of porosity and density. Their results showed that the influence of calcite and dolomite are negligible also pore fluid has no influence in the velocity.

Anselmetti and Eberli (1993) have measured compressional and shear velocities in different carbonate samples from different depositional environments. Their study showed that the compressional velocity varies greatly between 1700 m/s and 6500 m/s and shear velocity varies between 700 m/s and 3400 m/s. They indicated that the influence of mineral compositions in carbonates is minimal, and it cannot be a reason for large changes in velocities. Also they showed that rocks with interparticle or intercrystalline porosity (between grains) have lower velocity values than the ones with intraparticle or moldic (within grains) for a given porosity value.

Best (1997) studied the effect of pressure on ultrasonic velocity in low porosity (0.2-2.2%) carbonate samples. His measurements showed slight increase in velocity with increasing pressure and that is due to the lack of microcrack in the samples.

Assefa et al. (2003) measured ultrasonic compressional and shear velocities in limestone samples. Their result showed that the compressional wave velocity changes by 60% and the shear wave velocity changes by around 37%. They concluded that the velocities of rocks with high aspect ratio pores are greater than those with low aspect ratio. Their study showed deviation from Gassmann's assumption (see chapter 4), in which dry shear modulus is lower than the water

saturated shear modulus. They related this change in shear modulus to the matrix softening at grain contact areas after saturation.

Baechle et al. (2005) reported changes of 50% in compressional velocity and 40% in shear wave velocity with porosity. Upon saturation of their samples with water, the shear wave velocities of the samples could increase or decrease relative to that predicted by Gassmann's relation suggesting that the water caused the shear modulus to 'strengthen' or to 'weaken', respectively. They suggested that rock frame alteration during saturation (caused by rock-fluid interactions) is the reason for the shear modulus change.

Adam et al. (2006) measured carbonate samples over a wide range of frequency (seismic and ultrasonic frequency). They observed shear modulus changes with brine saturation especially at seismic frequency which they also attributed to the weakening of the solid matrix due to the growth of subcritical cracks.

Scotellaro et al. (2007) have measured compressional and shear wave velocities in carbonate samples with wide range of porosity (1-52%) and different mineral contents under both dry and water saturated condition. They observed a general decrease in compressional and shear velocities with increasing porosity which is in agreement with the results reported in the literature. Their observation showed that the velocities of samples with anhydrite contents are less than those with pure calcite which is in contrast with the observations reported by Anselmetti and Eberli (1993) and Rafavich et al. (1984) that changes in mineralogy cannot be a reason for large changes in velocity.

Rogen et al. (2005) studied the effects of porosity, pore fluid and texture in North Sea Chalk. Their data follow the general velocity-porosity relation. Over a porosity range of 14-45%, the compressional wave velocity varies between 1900 m/s to 4300 m/s and shear wave velocity between 1300 m/s and 2600 m/s. In accordance with Assefa et al. (2003) Baechle et al. (2005) and Adam et al. (2006), they observed a slight weakening of saturated shear modulus which they related to the result of fluid-solid interaction weakening grain contacts. In contrast to most of the carbonate studies, they found that the observed compressional and shear velocities are well correlated with the velocities estimated from Gassmann's relationships.

Kenter et al. (2007) showed that Poisson's ratio-compressional velocity relation can be used as a discriminator between granular and crystalline fabric rocks. Their data showed that at high (>25%) and low (<10%) porosities acoustic velocities are slightly influenced by mineralogy. However between 25% and 10% porosity values the mineralogy effects on the acoustic velocity is significant.

Verwer et al. (2008) measured the compressional and shear wave velocities in carbonate samples from Mallorca. Their results show that around 4000 m/s variation in compressional velocity and 2400 m/s variation in shear wave velocity. In agreement with Anselmetti and Eberli (1993) they emphasize that the changes in velocity at a given porosity shows no correlation with mineralogy. However their observation showed no influence of pore type in velocity and the changes in velocity must be influenced by the texture of the sample. They observed that Wyllie time-average (Wyllie et al., 1958) and

empirical Raymer equations (Raymer et al., 1980) underestimated the velocity by 50% and 25% respectively. In the same vein as Kenter et al. (2007) they have used the changes in rock texture (granular and crystalline) to rationalize the scatter in the velocity-porosity relation and Poisson's ratio-compressional wave velocity to describe the texture of the sample. They observed lower velocity values in samples with granular texture than samples with crystalline texture.

Baechle et al. (2009) also recently observed shear wave velocities increase and decrease in the saturated samples relative to the predictions of Gassmann's relation. Correspondingly, they found that shear modulus changes upon water saturation on average to vary from 0.75-1.23 GPa; this observation contradicts a primary inherent to Gassmann's relation concluding that this assumption most likely not applicable in most of carbonate rocks. They related the weakening of shear modulus to the fluid-rock interaction at grain contacts. They assumed that weakening of shear modulus at low frequency is higher than high frequency as velocity dispersion mechanism which is active only at high frequency tends to strengthen the rock frame.

Agersborg, et al. (2008) measured saturated velocity on six carbonate rock samples. The shear wave velocities changes with the direction of measurements which they related to the anisotropy of the samples.

2.3 Static and dynamic moduli in carbonate

Many studies attempted to study the relationship between static (i.e. that measured at zero frequency) and the dynamic moduli (i.e. those measured using

propagating wave pulses). Early in the last century, Zisman (1933) found that the static bulk modulus is always smaller than the dynamic modulus based on measurements made on two limestone samples from Pennsylvania and southwest Persia. He attributed this difference to the presence of cracks and cavities between the crystals that form the rock based on the fact that the static and dynamic moduli are in good agreement in theunjacketed test (the rock opened to confining fluid). He also observed that the difference is high at low pressure and decreases with increasing pressure, suggesting that most of cracks are closed at high pressure. He observed a little difference on jacketed and unjacketed compressibility (inverse of bulk modulus) in limestone sample which he relates to the stiffness of the rock. This interpretation has not significantly changed since Zisman made his conclusions, and has been repeated by many authors since (e.g., Birch, 1961; Ide, 1963; Simmons and Brace, 1965; King, 1969; Cheng and Johnston, 1981; Fjaer, 2009).

Ide (1935) measured dynamic young's modulus in different rocks and compared his result with previously measured static modulus. He observed 5-80% higher dynamic modulus than the static modulus. He concluded that the observed differences between static and dynamic measurements were caused mainly by the existence of cracks in the rock and by the inelastic response of the sample to the applied static stress.

Cheng and Johnston (1981) measured static and dynamic moduli on series of sandstone, limestone and granite samples. They observed that in sandstone and granite the static to dynamic ratio increases with confining pressure and becomes

equal at high pressure. They ascribed this behaviour to the existences of cracks which completely closed at high pressure. Whereas, for their limestone sample the ratio decreases pressure, which they attributed to pore collapse with pressure. Another source of differences between static and dynamic moduli is the differences of the strain amplitude between the two measurements. The peak strain in dynamic measurement is of the order of 10^{-6} , while the static measurement is greater than 10^{-2} .

Fjaer (2009) found that the static and dynamic moduli continuously differ in sandstone samples except immediately after beginning the unloading cycle. As Cheng and Johnston (1981) he supported the idea that the differences between the static and the dynamic moduli results from differences of the strain amplitude. He hypothesized that the fictional sliding inside cracks is a possible reason for the differences between the two moduli. This mechanism must be activated by large strain amplitude which not valid in the strain produced by elastic wave.

King (1969) concluded from the result of his measurements of dynamic and static moduli on Berea sandstone sample. His result shows that the dynamic moduli always exceed the static moduli. Same as most of the studies he related his findings to the presence of the cracks in the sample. He noticed that the differences between the two moduli depend on the direction of the strain measurements. He found that the difference is greater in direction perpendicular to the bedding plane within which he suggested that the cracks were aligned parallel.

2.4 Conclusions

Carbonate reservoirs contain more than 50% of the world remaining hydrocarbon, but can be tremendously difficult to extract. Unlike clastic rocks which form by erosion and transportation of particles from existing rocks, carbonate rock composition derives from a combination of biological and chemical components. This adds complexity and heterogeneity to its structure and petrophysical properties, which make the studies to understand the effects of porosity, pore type, saturation, mineralogy and pressure on the elastic properties a challenge.

In recent years, the compressional and shear velocities of carbonate rocks have been measured in attempts to develop relationships between the carbonate's petrophysical and elastic properties. Despite the number of studies conducted, the science community still lacks a solid understanding of these relationships. Generally all studies showed that the velocity-porosity relation in carbonate follow the conventional inverse relation where that velocity increase when porosity decrease. However, large deviation with respect to the conventional velocity-porosity relation and huge variability in velocity at a given porosity are observed.

Studies attempt to compare static and dynamic moduli in different rocks and material almost reach a consensus that dynamically measured moduli are higher than the statically measured moduli. These differences depend on the presence of cracks and on the difference in strain amplitude associated to each measurement.

Chapter 3

Sample Characterization

3.1 Introduction

The laboratory measurements described in later chapters cannot be fully appreciated and interpreted in the absence of detailed knowledge of the material characteristics. This is particularly true in carbonate rocks that often have taken a complex path from initial deposition to what we see today. This leads to a variety of minerals forming the grains and the rock cements as well as an array of different pore styles and sizes. In this chapter, we describe the carbonate materials as fully as possible to assist our later understanding of the measurements.

In this research study, nearly sixty five core plug samples were received from Saudi Aramco Oil Company. The samples are from seven different wells on Arab-D reservoir in Saudi Arabia. Only thirty seven representative samples were used in this project. This study is not intended to lead to a specific geological

conclusion, but focuses instead in a more generic way the factors that influence the laboratory observations. As such, the full context and specific locations from where the samples were taken is not directly relevant to the current study; and such information is not included.

A complete petrographic analysis using microscopic thin sections for most of these samples were obtained from Aramco, but for a subset additional thin sections were made in the Department of Earth and Atmospheric Sciences at the University of Alberta. In the petrographic description the factors that are considered useful for the current study were emphasized (i.e. mineralogy, lithology, texture and pore nature). The bulk and grain density and porosity on each sample were measured using Helium pycnometer. Pore size distributions using mercury porosimetry (Micromeritics Autopore IV) as well as SEM (Scanning Electron Microscope) on selected samples were measured.

As already noted, the porosity within carbonate rocks can be particularly complex and a variety of workers have in the past attempted to provide overall guidelines for a geological characterization of such materials. This is doubly complicated in carbonates as one must first have some understanding of the rock's origins and then second an evaluation of the types of pores it contains.

With regards to formation, two carbonate classification systems are in common use today. The first one is by R.J. Dunham (1962) and it is based on depositional texture (the amount of matrix surrounding the grains at the time of deposition). The other one is by R.L. Folk (1959) is based on the relative amounts of allochems, calcite cement (spar) and microcrystalline to cryptocrystalline

calcite matrix (micrite). Although each of the two classifications has its strength, in this research the Dunham classification is used. The following nomenclatures with their respective definitions are used in Dunham classifications (figure 3.1):

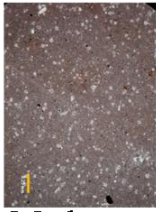

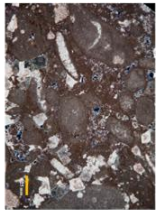
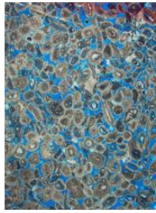
Original components not bound together at deposition				Original components bound together at deposition.
Contains mud (particles of clay and fine silt size)		Lacks mud		
Mud-supported		Grain-supported		
Less than 10% Grains 	More than 10% Grains 			
Mudstone	Wackestone	Packstone	Grainstone	Boundstone

Figure 3.1: Dunham's carbonate rocks classification (modified after Dunham (1962), AAPG©1962, reprinted by permission of the AAPG whose permission is required for further use).

Mudstone: the rock is mostly made of carbonate mud or cryptocrystalline carbonate matrix. Grains (fossils, ooids, etc.) will be less than 10 % of the rock.

Wackestone: grains make up more than 10% of the rock but the grains are "matrix supported" they float in the matrix.

Packstone: grains with matrix between them but the grains are grain supported.

Grainstone: grains with spar (cement) between them, little or no mud.

Floatstone: 10% or more of the grains are greater than 2mm in diameter and matrix is like a packstone.

Rudstone: 10% or more of the grains are greater than 2 mm in diameter and spar (cement) is between the grains like grainstone.

Boundstone: Original components organically bound during deposition such as stromatolites.

These genetic classifications are insufficient to describe other petrophysical aspects of carbonates, and in particular carbonate porosity takes many different forms and must be considered here. In the literature, there are different porosity classifications (Archie, 1952; Choquette and Pray, 1970; Lucia, 1983, 1995 and 1999). These classifications are suited for different purposes. While the classifications of Archie (1952) and Lucia (1983, 1995 and 1999) are more preferred by petrophysicists and reservoir engineers; the classification of Choquette and Pray (1970) is preferred by petrographers and petroleum geologists. Choquette and Pray classification (1970) reflects more of the sedimentological fabric and it is the one used by Saudi Aramco scientists (figure 3.2). The pore type nomenclatures such as interparticle, intercrystalline, intraparticle and moldic are adapted from their report. One modification that Saudi Aramco scientists adapted in their scheme is the separation of intraparticle pores into intraparticle (i.e. proper) and intraskeletal (i.e. this when the pores are related with fossil skeletons).

porosemetry is used to measure grain density and porosity. This section describes briefly the methods that used to characterize the samples.

3.2.1 Thin Section

Geological thin sections, usually between 30 to 40 μm in thickness, are prepared from rocks for microscopic studies. At this thickness light easily gets transmitted through the slides. Using either polarized or cross polarized light different optical properties yield information on mineralogy, paleontology and fabric. Their preparation involves the following steps:

- Sorting, labeling and arranging.
- Slabbing and trimming.
- Preparation of slides to uniform thickness.
- Cleaning and drying.
- Impregnating with dye epoxy (generally blue colored for pore space identification).
- Face lapping of cut material.
- Bonding samples to glass slides.
- Grinding slides to 30 – 40 μm .

More than half of the thin-sections of Arab-D samples were provided by Saudi Aramco Oil Company and the rest were made in the Earth and Atmospheric Science Department at University of Alberta. Figure 3.3 shows an example thin section photomicrograph of Sample 8-23 from Arab-D formation, showing ooids and skeletal grains with associated interparticle and intraparticle pore types.

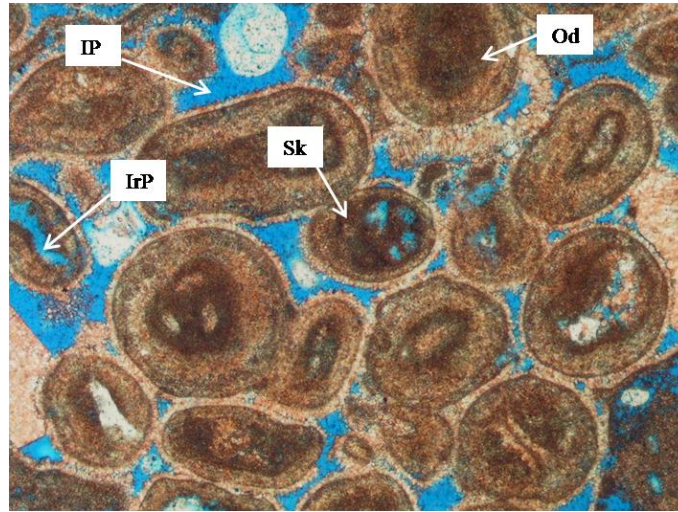


Figure 3.3: Thin section photomicrograph of Sample 8-23, showing ooids (Od) and skeletal (Sk) grains. The blue color is the associated interparticle (IP) and intraparticle (IrP) pore types.

3.2.2 Mercury Intrusion Porosimetry

Mercury Intrusion Porosimetry (MIP) is used for measuring the pore throat size distribution of different magnitudes. This measurement relies on the fact that liquid mercury metal is nonwetting relative to other fluids. Because of this, mercury will not automatically intrude a porous medium as might, for example, water that will be pulled into the pore space by capillary effects. The mercury can only be forced into the medium by pressure. Significantly, the greater the pressure the smaller the pore throat that the mercury can penetrate; and hence if the volume of mercury injected versus the confining pressure is carefully monitored then one can make inferences about the distribution of pore throat

sizes. The technique has been used for many decades, particularly in petroleum engineering, and the reader may find additional information in the contributions of Katz and Thompson (1987), Thompson et al., (1987) and Vanbrakel et al., (1981) for example.

The measurement starts with placing the sample into sealed 'penetrometers' which are weighed both before and after being loaded with the sample. Samples prepared for testing are dried to remove all moisture from the pore structure. The penetrometers are then placed into the machine where they are evacuated and then filled with mercury in the low pressure cycle. The pressurized testing then commences in the high pressure cycle and the machine calculates and records how much mercury is being forced into the pore structure. The precise recording of the decrease of free mercury in the penetrometer stem, which is equal to the volume injected into the rock's pore structure, is based on a capacitance system. As the applied pressure is increased the radius of the pore throats that can be filled with mercury decreases and consequently the total amount (i.e. cumulative amount) of mercury intruded increases. The data obtained give the pore volume distribution directly and with the aid of a pore physical model, permit a simple calculation of the dimensional distribution of the pore throat size. The pressure required to inject additional mercury to the pore space of the sample is a function of the pore throat size, the higher the pressure the smaller the pore throat intruded by mercury. Since mercury is a non-wetting fluid with a contact angle θ of about 141.3° , the penetration of the mercury can be expressed by:

$$D = -\frac{1}{P} 4\gamma \cos \theta, \quad (3.1)$$

where D is the pore throat diameter, γ is the surface tension of mercury (480 mN/m²), θ is the contact angle (wetting angle), and P is the pressure exerted. The relationship is commonly known as the Washburn equation (Washburn, 1921) based on the assumption that the pore is considered to be cylindrical. Although in almost any porous substance there are no cylindrical pores, this equation is generally used to calculate a pore throat size distribution from mercury porosimetry data. The MIP measurements and analysis were made in the Experimental Geophysics Group at University of Alberta. Figure 3.4 shows an example of the pore throat distribution for sample 2-33.

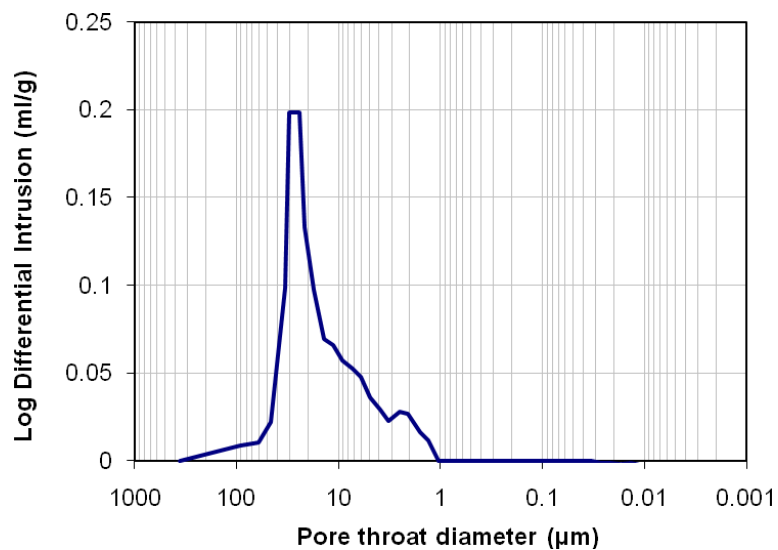


Figure 3.4: Pore throat distribution of sample 2-33, shows that the dominated pore size is around 30 μm .

3.2.3 Helium Porosimetry

A helium pycnometer (Micromeritics model MVP-6DC) is used to measure the mineral grain volume, and hence grain density, of the sample. The grain volume is the volume of the solid portion of the sample (rock matrix). Using the measured dry mass and grain volume, the grain density of the sample (the density of the solid portion of the sample excluding any void spaces) basically is the ratio of the sample dry mass to the grain volume. The pycnometer measured the sample grain volume based on Boyle's law. Boyle's law states that at a constant temperature, the volume of a given quantity of an ideal gas varies inversely with the pressure to which the gas is subjected. If temperature is held constant and a volume of gas is allowed to flow from one cell into another, then the following relationship holds for a perfect gas:

$$P_1V_1 = P_2V_2 \quad (3.2)$$

The procedure based on filling a reference cell with helium (a nearly perfect gas) and measuring the pressure P_1 . The volume of the reference cell V_1 is known. The gas is allowed to flow into a second cell containing the sample where the pressure P_2 is measured. Solving the above equation for V_2 gives the total volume of the reference cell plus the cell which host the sample minus the grain volume of the sample. Since the volumes of the reference cell and the sample cell are known, the grain volume can be easily calculated using the following equation:

$$V_g = V_c - [(P_1 - P_2) / P_2] V_r, \quad (3.3)$$

where, V_r , V_c and V_g are the volumes of the reference cell, the sample cell and the sample grain respectively. Then the porosity ϕ can be calculated using the following relation:

$$\phi = \frac{V_b - V_g}{V_b}, \quad (3.4)$$

where V_b is the sample bulk volume (the volume of the rock solid matrix plus the pore space volume), and can be calculated using the length and the diameter of the sample. The largest uncertainty in this measurement comes from trying to estimate the bulk (or envelope) volume.

3.2.4 Scanning Electron Microscope (SEM)

The Scanning Electron Microscope (SEM) is an instrument which produces highly resolved microscopic images of samples using either secondary or back scattered electrons rather than light that used by optical microscope. SEM produces images magnified up to 300,000 times. During SEM observation a beam of electrons (Primary electrons) is focused on a small area of the sample. As a result some electrons will be ejected from the sample's focused area itself which so-called Secondary electrons. These secondary electrons are attracted and recorded by a detector and an image is produced. SEM assists to examine the micro-structure of the samples in a qualitative sense.

3.3 Results and Discussion

Thirty seven Arab formation samples were selected from seven different wells (Table 3.1). The majority of the samples are similar in mineralogy. They are either nearly pure limestone or dolomite with traces (<1%) of quartz and anhydrite. This purity of composition allows for useful comparisons later (see appendix A). One sample consisted of 50% anhydrite, 48% dolomite and traces of calcite. Two samples consist of a mix between calcite and dolomite. Porosity ranged between less than 1% - 38% and permeability values varied between 0.1 - 3300 mD. All samples are free of clay. The pore types of the samples are varies from macroporosity to microporosity in size (described in detail later in this chapter). The Macropore types include interparticle pores (inter-grain and inter-crystalline), intraparticle, interskeletal, moldic and leached dolomite. The samples are free of vuggy pores and fractures visible to naked eyes.

Table 3.1 Physical properties of the thirty seven selected samples.

Number	Sample	Depth (m)	Length (mm)	Diameter (mm)	Dry Mass (g)	Grain Density (g/cm ³)
1	1-11	2124.212	36.97	25.35	51.04	2.85
2	1-132	2155.058	34.48	25.45	28.72	2.72
3	1-288	2184.258	36.53	25.43	40.53	2.69
4	1-304	2188.982	36.81	25.46	46.3	2.69
5	2-10	2037.07	35.53	25.2	34.93	2.86
6	2-33	2041.246	25.13	25.13	22.5	2.71
7	2-59	2045.391	18.95	25.05	16.45	2.72
8	2-131	2057.278	22.91	25.2	22.95	2.72
9	2-160	2062.307	34.12	25.2	33.35	2.72
10	2-368	2096.475	36.33	25.32	47.57	2.83
11	2-383	2098.883	25.84	25.38	31.87	2.75
12	2-432	2108.302	35.62	25.34	44.55	2.72
13	3-05	2175.419	23.34	25.26	32.49	2.87
14	3-90	2188.373	34.08	24.9	30.63	2.72
15	3-104	2190.506	34.54	24.96	32.17	2.73
16	3-146	2196.755	35.15	25.35	33.73	2.73
17	3-331	2224.796	29.01	37.89	70.1	2.72
18	3-429	2240.036	42.14	38.055	123.41	2.84
19	3-471	2246.437	26.01	25.31	35.01	2.74
20	3-534	2256.038	33.43	25.26	38.486	2.69
21	4-09	2036.155	49.83	37.94	139.7	2.74
22	4-55	2043.135	49	38.03	107	2.71

Cont'd Table 3.1

Number	Sample	Depth (m)	Length (mm)	Diameter (mm)	Dry Mass (g)	Grain Density (g/cm ³)
23	4-97	2049.536	49.31	38.01	109.7	2.72
24	4-151	2057.766	49.9	38.02	140.32	2.78
25	4-180	2062.185	49.43	38	149.8	2.79
26	4-189	2063.557	49.3	38.04	113.46	2.70
27	4-326	2084.436	49.65	38.04	132.43	2.71
28	5-02	2206.661	34.925	25.61	41.59	2.71
29	5-289	2264.42	35.37	25.62	48.65	2.71
30	5-295	2265.335	35.22	25.625	46.01	2.71
31	7-222	2042.465	37.75	24.995	51.34	2.82
32	7-240	2045.178	37.56	24.98	38.56	2.71
33	7-20	2088.916	37.8	24.95	48.62	2.81
34	7-16	2100.163	36.47	24.92	43.07	2.73
35	8-23	2219.188	25.96	25.26	25.81	2.74
36	8-91	2239.579	16.51	25.22	16.68	2.75
37	8-115	2243.45	35.82	25.36	40.92	2.73

3.3.1 Porosity and permeability

The porosity was calculated from the measured grain volume obtained from helium porosimetry. Porosities of the samples ranged between less than 1% - 38% and as already noted permeability normally range from less than 0.1 mD to 3300 mD. Figure 3.5 shows the porosity-permeability cross plot for the samples, it is

clearly shows that the samples can be classified into five distribution patterns. The groups are:

- Low porosity ($\leq 10\%$) and low permeability (≤ 1 mD),
- Medium porosity ($10\% < \phi < 20\%$) and medium permeability (1 mD $< K < 10$ mD),
- Medium porosity ($10\% < \phi < 20\%$) and high permeability (10 mD $< K \leq 100$ mD),
- High porosity ($20\% < \phi < 40\%$) and high permeability (10 mD $< K \leq 100$ mD) and
- High porosity ($20\% < \phi < 40\%$) and very high permeability (> 100 mD).

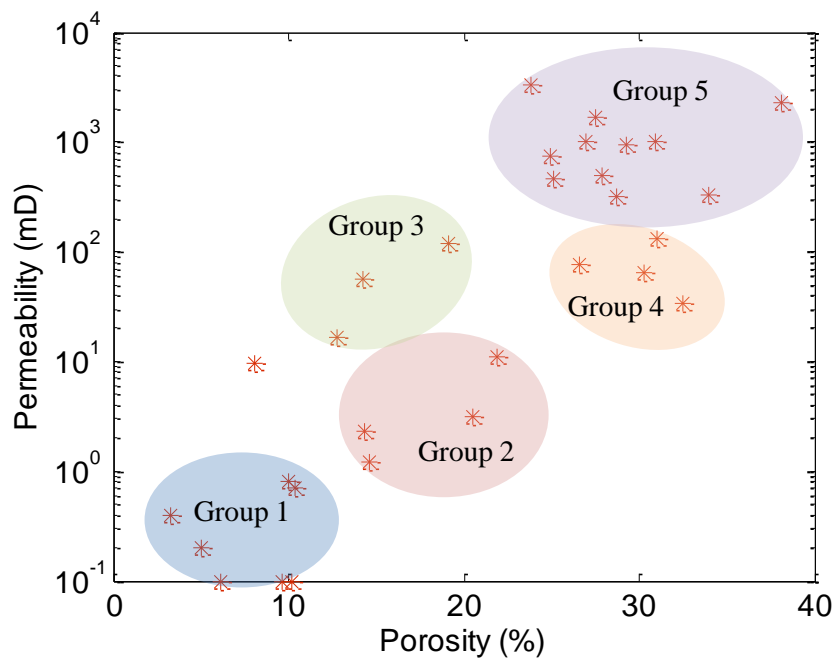


Figure 3.5: Porosity and permeability distributions of all the studied samples. The groups are highlighted.

3.3.2 Mineralogy and Lithology

Based on overall volumes, carbonate rocks can for the most part be generally subdivided into two major groups, limestone and dolomite. Although there are more carbonate minerals as well as rocks, limestone (composed of calcite mineral, CaCO_3) and dolomite (composed of dolomite mineral, $\text{CaMg}(\text{CO}_3)_2$) make up the bulk of global carbonates. Limestone, which is common in Arab-D formation, consists of grains, micrite and cement that are described in more detail shortly. As mentioned earlier, Dunham's (1962) classification is used in this study. Dunham (1962) classified carbonate rocks based on the amount of matrix surrounding the grains at the time of deposition with his main rock types being called Grainstone, Packstone, Wackestone, Mudstone and Boundstone as defined above.

Grains in limestone in the literature (Bathurst, 1975) are subdivided into 1) bioclasts, 2) precipitates, 3) peloids, and 4) intraclasts.

- Bioclasts are carbonate grains that are of fossil skeletal origin which are remains of shells, corals, and sponges and can be classified by dominant fossil type.
- Precipitate grains form of carbonate spherical or nearly spherical precipitates small in size. A good example of such grains is oolites. They are composed of spherical grains precipitated from warm ocean water on carbonate platforms. They form ovoid or spherical crystalline deposits (envelopes) around preexisting grains with a concentric or radial structure.

- Peloids are non-skeletal grains that are internally structureless, and ovoid to irregular in shape. When the peloids exhibit a certain shape and distribution they are assumed as faecal remains of other organisms and they are referred as pellets.
- Intraclasts formed by reworking of preexisting and lithified materials formed within the depositional environment.

In the Arab-D formation the dominant skeletal grains are forams, cladocropsis, stromatoporoids, bivalve, gastropods, echinoderms and dasyclads. The precipitates are mainly ooids, coated grains (i.e. non-skeletal carbonate grains that show one or more series of coatings around a central core), and oncoids (i.e. grains coated by blue-green algae). Meanwhile peloids are classified into different sizes that are very fine, fine to medium and coarse. The last grain type intraclasts are less common in Arab-D formation. In this section examples from each type of lithology will be given.

Grainstone

Sample 2-33 (figure 3.6a) is an example of ooid grainstone. In this sample the dominant mineral is calcite (99 %) with traces of Anhydrite. Seventy percent of the constituent grains are oolites and about one third of the grains are skeletal. The bulk of the skeletal grains are forams and dasyclads. These grains are cemented by blocky and rim cements. Another example of grainstone is sample 3-90, peloidal skeletal grainstone (figure 3.6b). Its mineralogy is 100% calcite. More than half of the grains peloids and the rest are skeletal. The cement is rim and blocky calcite.

Packstone

Sample 5-02 (Fig. 3.7a) is skeletal peloidal grain dominated packstone. Calcite is the dominant mineral (100 %). Seventy percent of the constituent skeletal, 25% peloids and 5% lime mud. The skeletal grains are forams. Sample 7-240 (Fig. 3.7b) is dolomitic peloidal packstone. The dominant mineral in this sample is calcite 97% and 3% dolomite. The grains are overwhelmingly peloids with few coated grains. Dolomite rhombs are about 0.1-0.2 mm. The dolomitization that produced the dolomites appear to have reduced in part the interparticle pores.

Wackstone

Sample 2-432 (Fig. 3.8a) is sponge spicule wackestone. Calcite is (95.5 %) and dolomite is (4%) also there is a trace amount of quartz (0.5%). More than Eighty percent of the sample is lime mud and the remaining is skeletal.

Mudstone

Sample 7-20 (Fig. 3.8b) is dolomitic lime mudstone. It is 90% calcite and 10% dolomite. Calcite is present as micrite while dolomite is present as minute scattered rhombs.

Crystalline carbonate

Sample 7-222 Non fabric preserving leached dolomite (figure 3.9). It is 100% dolomite with the poorly interconnected leached dolomite pores. The crystals vary between 1 -3 mm.

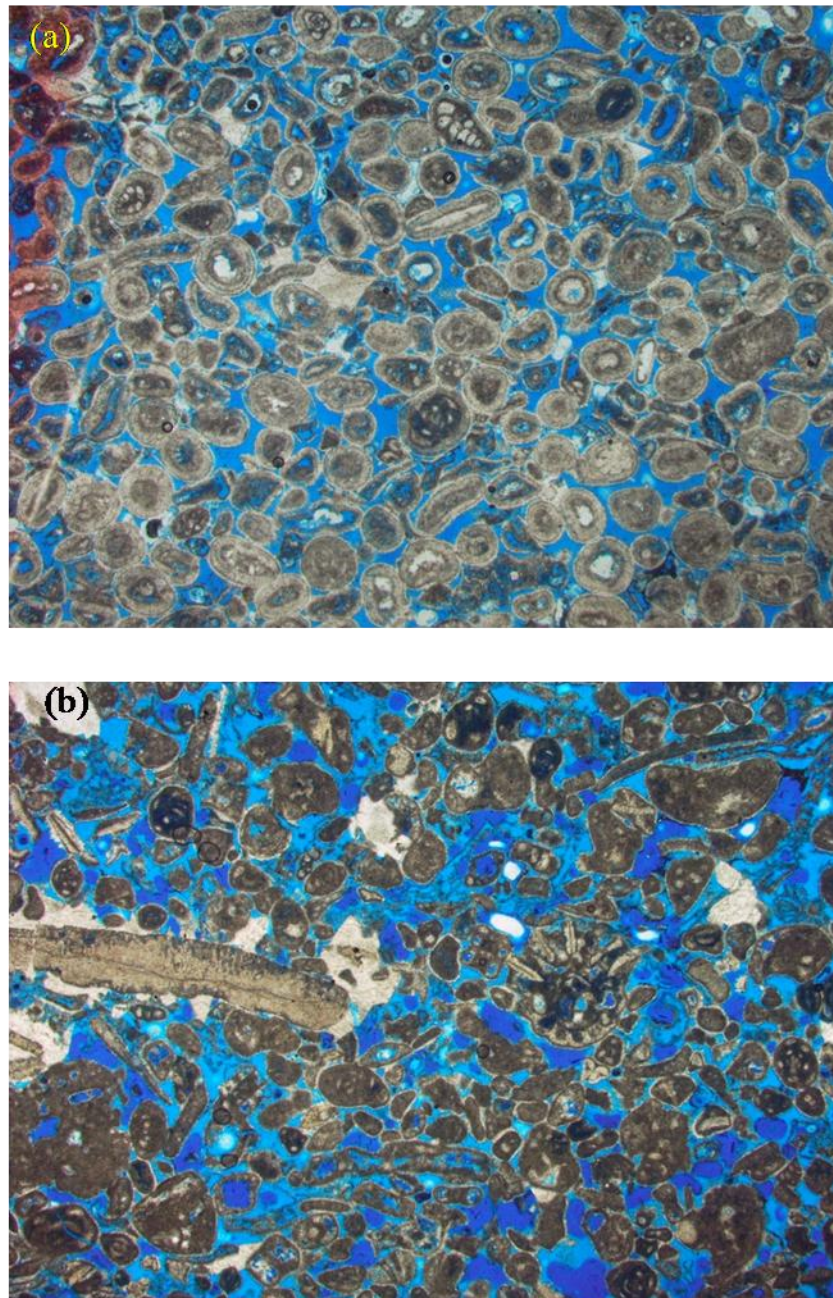


Figure 3.6: (a) Thin section photomicrograph of Sample 2-33 showing ooids and skeletal grains with associated interparticle and intraparticle pore types. (b) Thin section photomicrograph of Sample 3-90 showing peloids and skeletal grains with associated interparticle and intraparticle pore types.

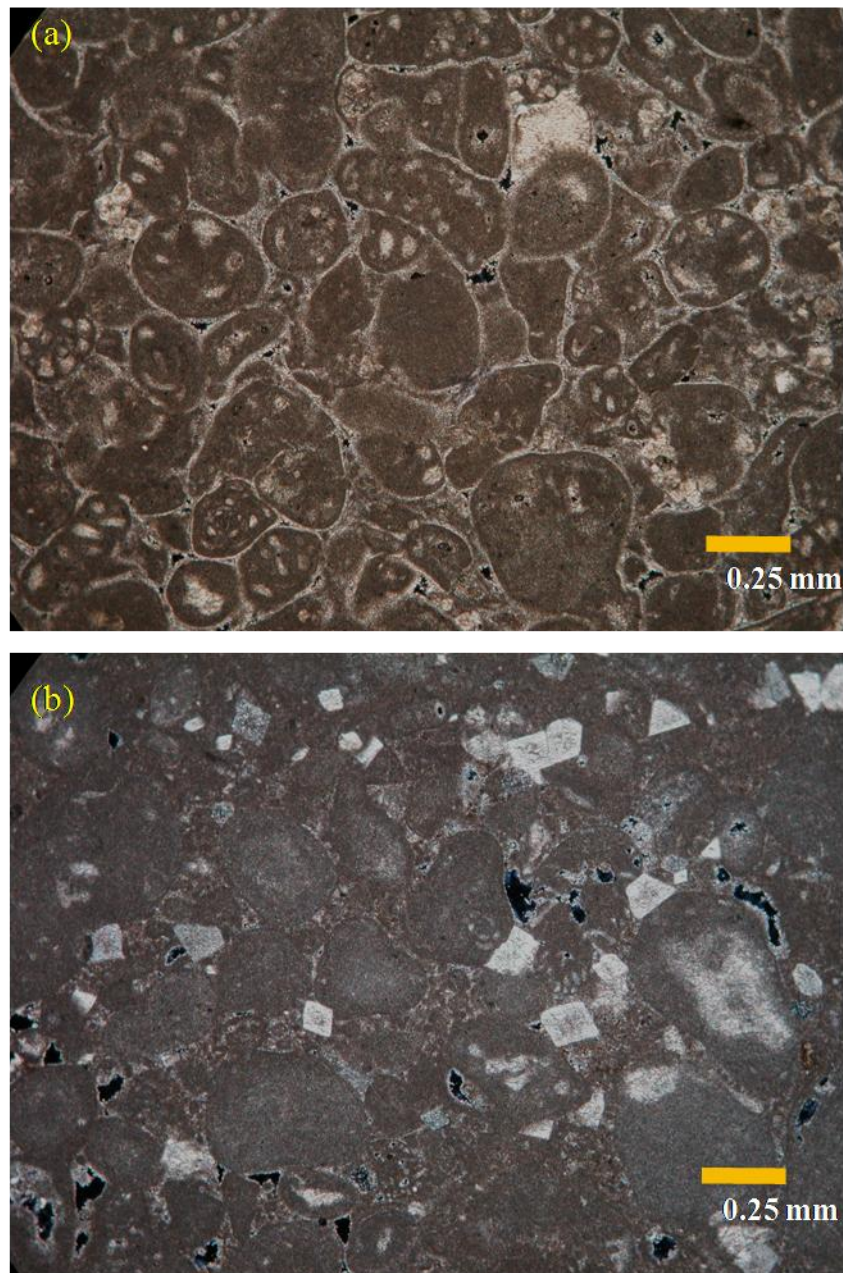


Figure 3.7: (a) Thin section photomicrograph of sample 5-02 showing skeletal peloidal grain dominated packstone. (b) Thin section photomicrograph of sample 7-240 dolomitic peloidal packstone showing peloids, lime mud and dolomite crystals.

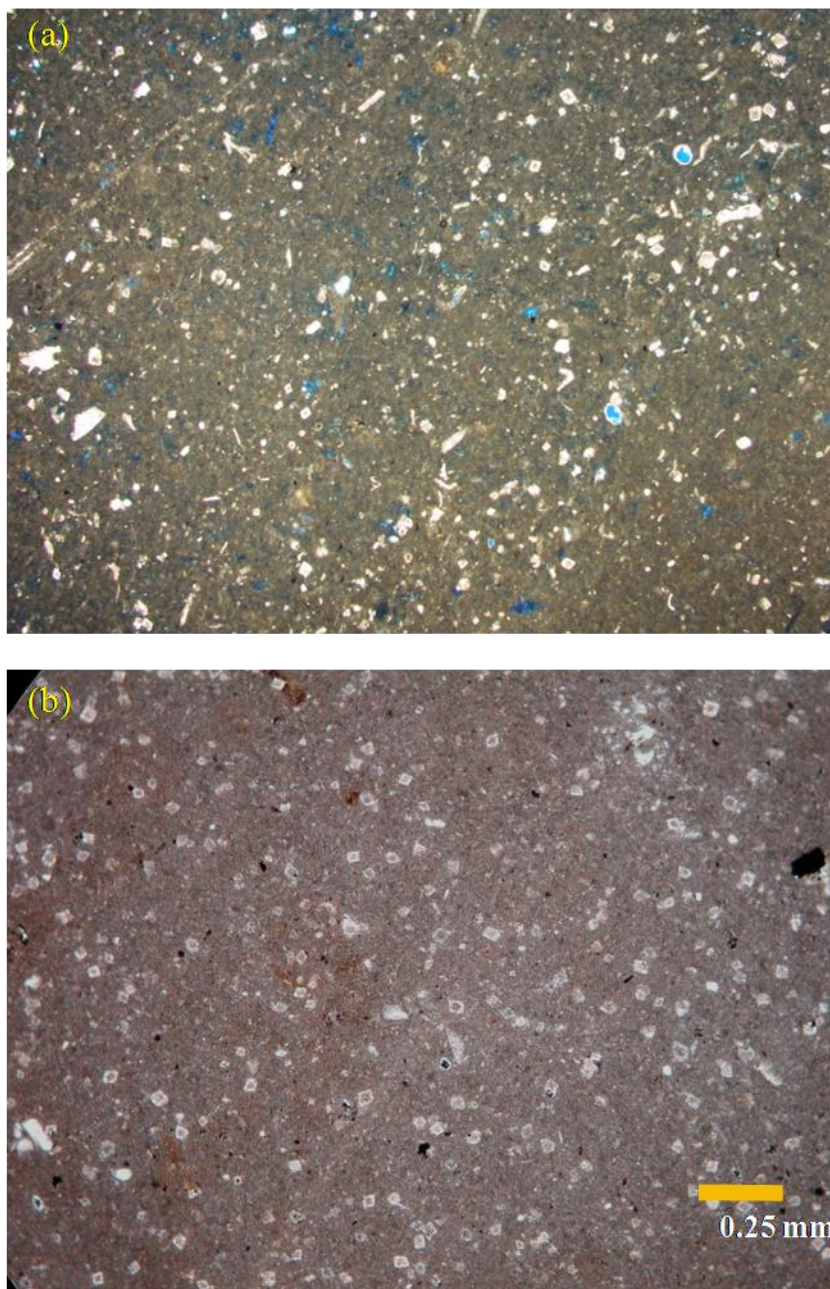


Figure 3.8: (a) Thin section photomicrograph of sample 2-432 sponge spicule wackestone, showing grains and lime mud. (b) Thin section photomicrograph of sample 7-20 olomitic lime mudstone sample showing lime mud and dolomite rhombs.



Figure 3.9: Thin section photomicrograph of sample 7-222, Non-fabric preserving leached dolomite showing dolomite with the poorly interconnected leached dolomite pores.

3.3.3 Pore type

Carbonate rocks exhibit different pore types result of very complex physical and chemical processes that play different roles during depositional and diagenetic history of the rocks. Not only the pore types are different but they also show a very complex pore network. Sedimentary rock porosities, in general, are constituted of primary pores that have formed during deposition and subsequent secondary pores that are due to diagenetic modifications. While clastic rocks are mainly dominated by primary pores such as intergranular (Choquette and Pray, 1970) and micropores, carbonate rocks show both primary pore types and very heterogeneous and complex secondary pore systems. The secondary pores are pores modified by post-deposition diagenetic processes. The post-deposition

diagenetic processes that modify the rock fabric are compaction, dissolution, precipitation and organic activities. Each of these processes could produce a certain pore type. Also the combination of one or more of the processes could complicate the end result and produce complex pore structure.

As already noted above, in the literature, there are different porosity classifications (Archie, 1952; Choquette and Pray, 1970; Lucia, 1983, 1995 and 1999). The Choquette and Pray classification (1970) reflects more of the sedimentological fabric. This classification includes pore type nomenclatures such as interparticle, intercrystalline, intraparticle and moldic but modified the subdivision of intraparticle pores into intraparticle (i.e. proper) and intraskeletal (i.e. when the pores are related to fossil skeletons).

The secondary pore types that develop due to post-depositional processes could either form matrix porosity, fracture porosity or porosity due to biological activities. The main matrix porosities are intraparticle, intercrystalline and vugs; whereas the fractures porosities could be open fractures with different sizes such as relatively big ones and hairlines. The biological (organic) activities could also result in burrows and borings. These two features could be filled with different materials than the original rock. In the studied samples burrows and borings aren't that common. Also fractures are not that frequent.

The major pore types that are found in the studied samples are porous fabrics such as interparticle, intraparticle, intraskeletal, moldic, intercrystal, micropores and non porous fabrics, nearly impermeable (i.e. tight) samples. These pore types include

- Interparticle pores are pores that form between adjacent particles. They are primary pore and they are syngeneetic. However, they are seldom preserved because later diagenetic processes either obliterate or alter them. In the studied samples, interparticle pores play an important role and they are frequent (figure 3.10a).
- Intraparticle pores are pores that are present within non-skeletal particles for pores within peloids, oolites, etc.
- Intraskelatal pores are the intrapores that have formed within fossils (skeletal, figure 3.10b).
- Moldic pores are pores that are formed due to selective removal of preexisting rock material (figure 3.10c).
- Intercrystalline pores are unique to dolomite samples and they are pores between dolomite crystals. Figure 3.10d shows a dolomite sample with intercrystalline pores.

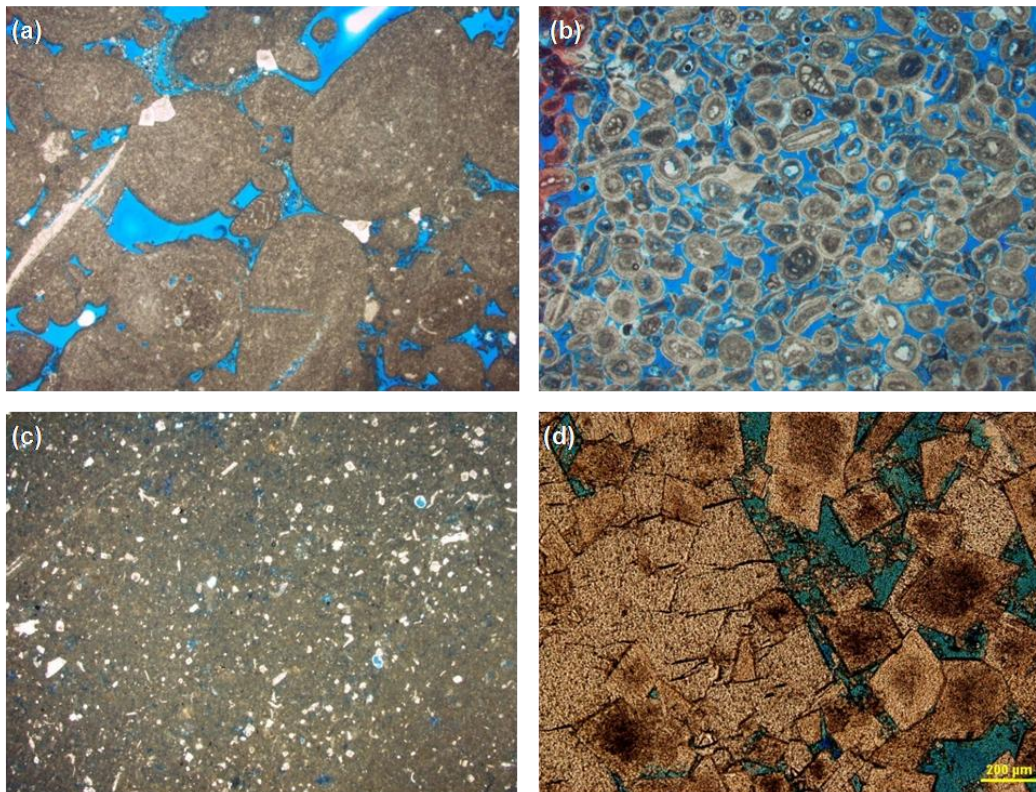


Figure 3.10: (a) Thin section photomicrograph of sample 3-331 shows interparticle pores that form between adjacent particles. (b) Thin section photomicrograph of sample 2-33 shows intraparticle pores that are presented within non-skeletal particles such as peloids and oolites and intraskeletal pores that have formed within foraminifera. (c) Thin section photomicrograph of sample 2-432 shows moldic pores that are formed due to selective removal of preexisting rock material. (d) Thin section photomicrograph of sample 4-151 shows a dolomite sample with intercrystalline pores. Porosity is filled with blue-dyed epoxy.

3.3.4 Pore size distribution

Different diameter limits have been proposed in the literature for macro- and micro- size pores. Choquette and Pray (1970) defined pores with less than 62.5 microns average diameter as micropores. On the other hand Pittman (1971) considers pores with less than one micron in diameter (in at least one direction) as micropores. Considering the fact that many petrographically visible pores are less than 62.5 microns and that no pores in the one-micron range are optically resolvable with a standard petrographic microscope, Cantrell and Hagerty (1999) felt that none of the above two definitions are appropriate. Then they developed a microporosity definition that could be suitable for petrographic characterization. Cantrell and Hagerty (1999) defined microporosity as all pores that are approximately 10 microns in diameter or smaller. They admitted that their definition is empirical and is based on the idea that microporosity is the difference between the porosity that is observed from the thin section and total measured helium porosity (Cantrell and Hagerty 1999).

For this study the microporosity definition of Cantrell and Hagerty (1999) is adopted. Under this scheme, the studied samples include macroporosity dominated, microporosity dominated and dual (bimodal) porosity samples (Table 3.2). Sample 1-132 is a typical sample where the dominant pore throats are macropores. As it is clearly shown on the pore throat size distribution plot (figure 3.11a), the dominant size is above the 10 microns. Sample 2-33 (Figure 3.11b) also shares similar characteristics the dominant pore throat size is above 10 microns. At the other spectrum of the throat sizes are samples with micropore

sizes. These samples are dominant by pores that are less than 10 microns in diameter or less. Samples 7-240 (figure 3.12a) and sample 2-59 (figure 3.12b) are typical of this nature. As shown in the figures the dominant pore throat size distribution is at the right side of the 10 micron limit. Sample 2-59 is also a micropore size pore throats.

Though macro- and micro- size pore throats make up the majority of the studied samples, there are also some with both macro and micro sizes. The proportions of the two sizes might differ in different samples but their common denominator is the presence of dual size distribution all the samples of this group. This very bimodal nature might affect some sample characteristics and influence test results. Sample 8-23 and 3-05 are typical of this group as pore throat size distribution plot shows (figure 3.13). There are two peaks that fall on both sides of the 10 micron benchmark. The difference between samples lies in the nature of their distributions. Sample 8-23 (3.13a) shows some intermediate throat sizes whereas Sample 3-05 (figure 3.13b) shows two distinct and separated peaks.

Table 3.2: Macro, micro and dual porosities samples.

Pore size	Macro	Micro	Dual
Samples	1-11	2-10	1-304
	1-132	2-59	2-160
	1-288	2-368	2-131
	2-33	2-383	3-05
	3-146	2-432	3-90
	3-331	3-534	3-104
	3-429	4-151	4-189
	4-09	3-471	5-295
	4-55	5-02	8-23
	4-97	5-289	8-115
	4-180	7-20	-
	4-326	7-16	-
	8-91	7-222	-
	-	7-240	-

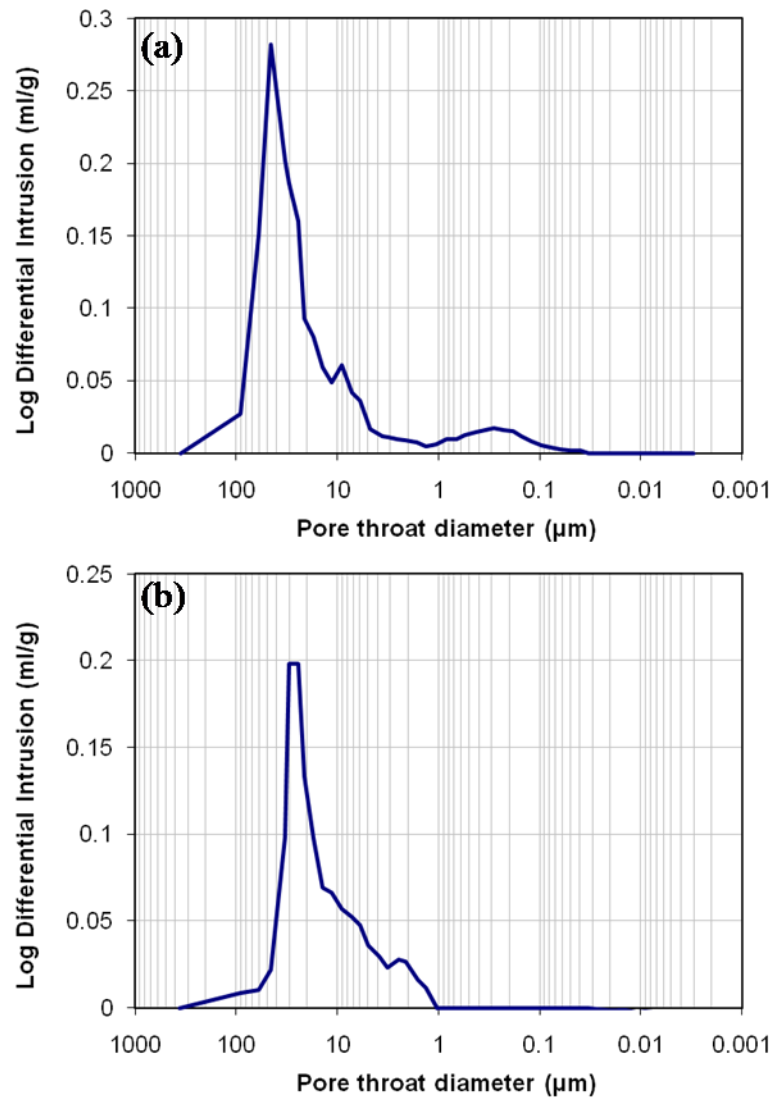


Figure 3.11: Mercury intrusion plots for sample 1-132 (a) and sample 2-33 (b) show that macropores is the dominant pore size with size above 10 microns.

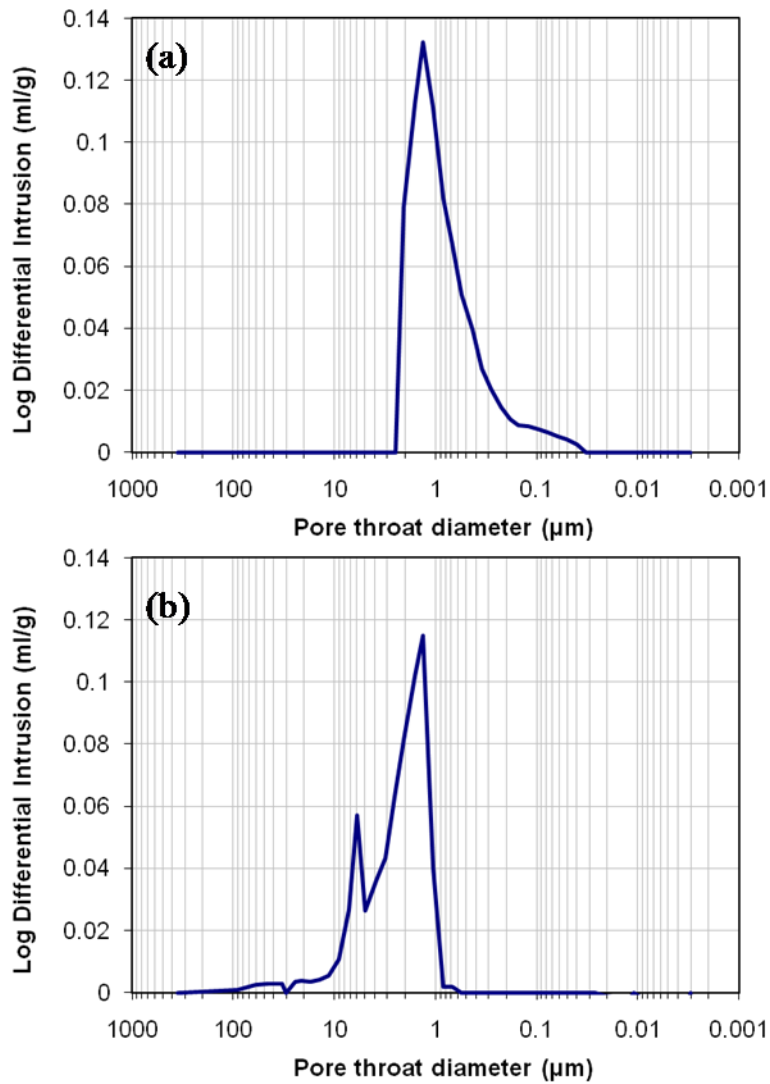


Figure 3.12: Mercury intrusion plots for sample 7-240 (a) and sample 2-59 (b) show that micropores is the dominant pore size with size below 10 microns.

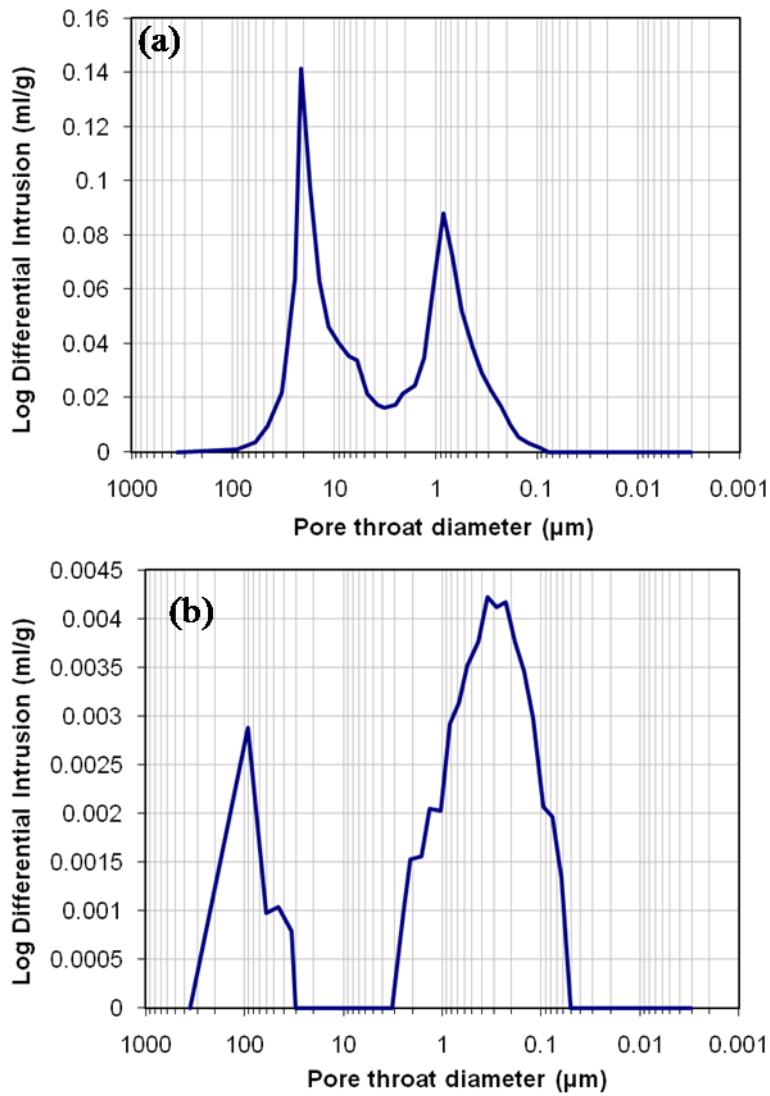


Figure 3.13: Mercury intrusion plots for sample 8-23 (a) and sample 3-05 (b) show two peaks that fall on both sides of the 10 micron benchmark (Dual porosity). Sample 8-23 shows some intermediate throat sizes whereas Sample 3-05 shows two distinct and separate peaks.

Cantrell and Hagerty (1999) recognized four types of microporosity in carbonate; microporous grains, microporous matrix, microporous bladed cements and microporous equant cements. In our samples microporous grains found on skeletal (forams) and non-skeletal grains (peloids, oolites). Figure 3.14 shows different type of microporous grains and cements observed in our samples. Figure 3.14a shows microporous foraminifera consisting of subhedral calcite crystals with size varies from 1-10 microns surrounded by microporous cements. Higher magnification view of the foraminifera shows 1-5 microns subhedral crystals (figure 3.14b). Non-skeletal microporous grains consisted of subhedral calcite crystals surrounded by bladed calcite cements (figure 3.14c). High magnification view of the microporous grain shown in 3.14c shows the micritized grains in microporous matrix. The size of micropores in skeletal and non-skeletal grains is 0.1-4 microns and the size of microporous matrix and cements is less than 1.0.

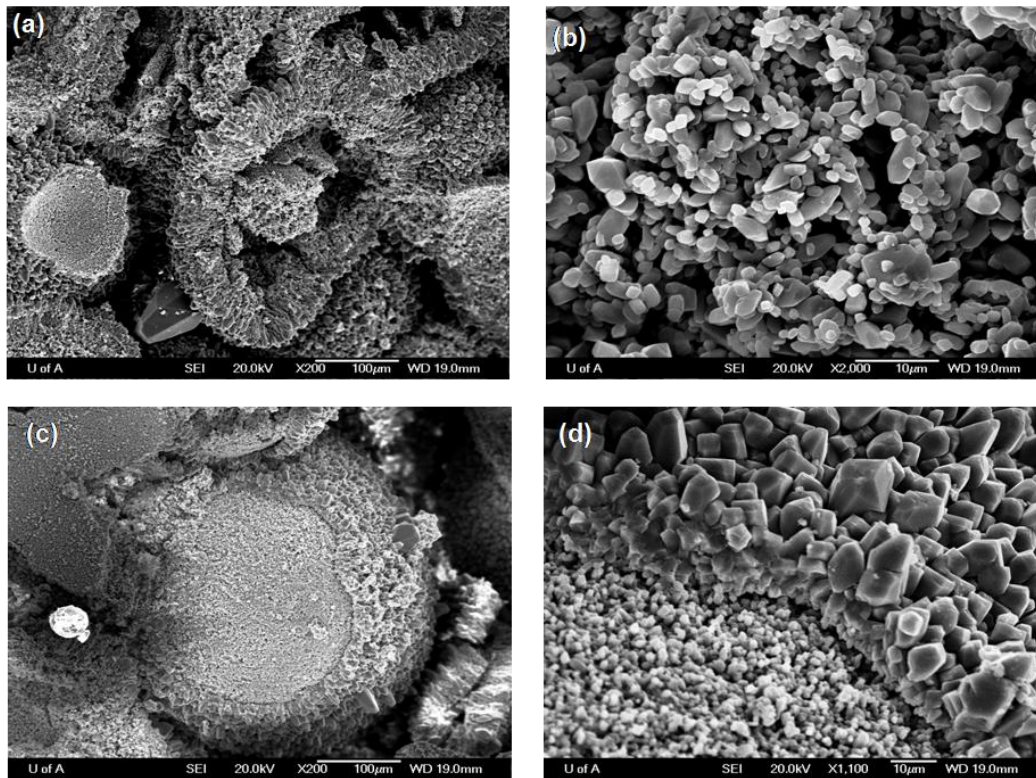


Figure 3.14: (a) Microporous foraminifera consisting of subherdal calcite crystals with size vary from 1-10 microns surrounded by microporous cements (sample 2-33). (b) Higher magnification view of (a) shows 1-5 microns subherdal crystals. (c) Non-skeletal microporous grains consisted of subhedral calcite crystals surrounded by bladed calcite cements (sample 2-33). (d) High magnification view of (c) shows the micritized grains in microporous matrix.

3.4 Conclusions

Thirty seven carbonate samples from seven different wells on Arab-D reservoir in Saudi Arabia were used in this study. A complete petrographic analysis using microscopic thin sections and SEM images were conducted and shown. The bulk and grain density and porosity on each sample were measured using Helium pycnometer. Pore size distributions using mercury porosimetry (Micromeritics Autopore IV). All Methods used to characterize the samples were briefly discussed.

The majority of Arab formation samples are similar in mineralogy. They are fairly either pure limestone or dolomite with traces (<1%) of quartz and anhydrite. One sample consisted of 50% anhydrite, 48% dolomite and traces of calcite. Two samples consist of a mix between calcite and dolomite. Porosity ranged between less than 1% - 38% and permeability values varied between 0.1 – 3300 mD. All samples are free of clay. The pore types of the samples are varies from macroporosity to microporosity. The Macropore types include interparticle pores (intergrain and intercrystalline), intraparticle, interskeletal, moldic and leached dolomite. The samples are free of vuggy pores and fractures. Mercury intrusion analysis showed that the sample can be divided into three groups to the respect to pore size distribution. The studied samples include macroporosity dominated, microporsity dominated and dual (bimodal) porosity samples (Table 3.2). For this study the microporsity definition of Cantrell and Hagerty (1999) is adopted. They defined microporosity as all pores that are approximately 10 microns in diameter or smaller.

Chapter 4

Theoretical background

4.1 Introduction

It is well known that seismic wave velocity of a fluid-saturated porous material is influenced by the physical properties of the constituents but also as the environmental parameters such as pressure and temperature. With respect to petroleum geosciences, a general goal of applied geophysicists is to be able to improve the predictive capability of surface seismic observations of the conditions and characteristics of carbonate reservoirs. Seismic observations utilize the propagation of waves through the rock to describe and characterize the rock. The propagation information depends on the elastic properties of the rock as well as the influence of the environmental properties. In recent years, the compressional and shear velocities of carbonate rocks have been measured on dry and saturated conditions attempt to develop relationships between the carbonate's petrophysical and elastic properties (e.g., Anselmetti and Eberli, 1993; Assefa et al. 2003;

Rafavich et al., 1984; Adam et al., 2006; Kenter et al. 2007; Verwer et al., 2008). However, particularly relative to siliclastic rocks, the elastic properties of carbonates have to some degree stubbornly resisted classification. This is usually attributed to the complex heterogeneous and multiscaled pore and matrix structure of carbonates.

In this chapter we will first briefly discuss the basic concepts of elasticity and its relation to wave velocity followed by a review of the various wave equations in isotropic material. Fluid substitution is an important factor in seismic and rock physics analysis, which provides a perfect tool for fluid identification in reservoir rocks. Therefore, Gassmann's fluid substitution relations and its assumptions are provided as it one of the most commonly relations used in fluid substitution analysis. Finally, two quasi-static types of tests that are commonly used to measure elastic properties in rock samples (jacketed and unjacketed tests) are shown.

4.2 Theory of elasticity

The theory of elasticity essentially relates forces (stresses) to deformation (changes in volume and shape). The details of this topic are rich and are already covered in detail in many texts in a variety of fields. Some important reference works employed by Geophysicists include Lay and Wallace (1995). Hence, there is little need to provide an extensive review of the topic; and this section will deal more with those aspects that relate directly to the measurements within this thesis.

When forces are applied to the external surface of a solid body changes to the size and shape (deformation) of the body will occur. As a result internal forces will be generated which resist the deformation. Thus the body tends to return to its original state when the external forces are removed. This resistance to the change of size and shape and the tendency of returning to the original state is called elasticity. A material said to be perfectly elastic if it completely returns to its original volume and shape when the external forces are removed. The theory of elasticity relates the external forces, which can be expressed in term of stress, applied to the surface of a body to the resulting deformation or so-called strain.

In an elastic solid material, the relation between stress and strain can be described using Hooke's law which states that amount of strain is linearly proportional to the amount of stress:

$$\sigma_{ij} = C_{ijkl}\varepsilon_{kl} \quad (4.1)$$

where σ_{ij} and ε_{kl} are the second-order symmetric stress and strain tensors respectively with 6 components each and $i, j, k, l=1, 2, 3$ represent the three orthogonal axes. The Einstein repeated indices summation rule applies here, and as such Eqn 4.1 is shorthand for 9 separate equations the right hand side of each will include 9 products. The constants C_{ijkl} are the fourth-order elastic stiffness tensor comprising eighty-one components. The constants C_{ijkl} define the material properties and known as elastic stiffnesses. The symmetry properties of the stress and strain tensors imply:

$$C_{ijkl} = C_{jikl} = C_{ijlk} = C_{jilk}, \quad (4.2)$$

reducing the number of independent component to thirty-six. Furthermore the existence of a strain energy function requires that:

$$C_{ijkl} = C_{klij}, \quad (4.3)$$

reducing the number of independent components to twenty-one.

With this realization, Eqn. 4.1 may be simplified by the use of the Voigt notation with

$$\sigma_i = C_{ij} \varepsilon_j, \quad (4.4)$$

In which the indices are substituted according to the recipe 1 = 11, 2 = 22, 3 = 33, 4 = 23, 5 = 31, and 6 = 12 such that the stress and strain tensors may be vectorized and the 3X3X3X3 81 component stiffness tensor reduced to a 6X6 symmetric matrix with

$$\begin{aligned} \sigma_1 &\leftrightarrow \sigma_{11} & \varepsilon_1 &\leftrightarrow \varepsilon_{11} \\ \sigma_2 &\leftrightarrow \sigma_{22} & \varepsilon_2 &\leftrightarrow \varepsilon_{22} \\ \sigma_3 &\leftrightarrow \sigma_{33} & \varepsilon_3 &\leftrightarrow \varepsilon_{33} \\ \sigma_4 &\leftrightarrow \sigma_{12} = \sigma_{21} & \varepsilon_4 &\leftrightarrow 2\varepsilon_{12} = 2\varepsilon_{21} \\ \sigma_5 &\leftrightarrow \sigma_{13} = \sigma_{31} & \varepsilon_5 &\leftrightarrow 2\varepsilon_{13} = 2\varepsilon_{31} \\ \sigma_6 &\leftrightarrow \sigma_{23} = \sigma_{32} & \varepsilon_6 &\leftrightarrow 2\varepsilon_{23} = 2\varepsilon_{32} \end{aligned}, \quad (4.5)$$

to allow explicitly

$$\begin{bmatrix} \sigma_1 \\ \sigma_2 \\ \sigma_3 \\ \sigma_4 \\ \sigma_5 \\ \sigma_6 \end{bmatrix} = \begin{bmatrix} C_{11} & C_{12} & C_{13} & C_{14} & C_{15} & C_{16} \\ C_{21} & C_{22} & C_{23} & C_{24} & C_{25} & C_{26} \\ C_{31} & C_{32} & C_{33} & C_{34} & C_{35} & C_{36} \\ C_{41} & C_{42} & C_{43} & C_{44} & C_{45} & C_{46} \\ C_{51} & C_{52} & C_{53} & C_{54} & C_{55} & C_{56} \\ C_{61} & C_{62} & C_{63} & C_{64} & C_{65} & C_{66} \end{bmatrix} \begin{bmatrix} \varepsilon_1 \\ \varepsilon_2 \\ \varepsilon_3 \\ \varepsilon_4 \\ \varepsilon_5 \\ \varepsilon_6 \end{bmatrix} \quad (4.6)$$

Or conversely, with compliances S_{ij} :

$$\begin{bmatrix} \varepsilon_1 \\ \varepsilon_2 \\ \varepsilon_3 \\ \varepsilon_4 \\ \varepsilon_5 \\ \varepsilon_6 \end{bmatrix} = \begin{bmatrix} S_{11} & S_{12} & S_{13} & S_{14} & S_{15} & S_{16} \\ S_{21} & S_{22} & S_{23} & S_{24} & S_{25} & S_{26} \\ S_{31} & S_{32} & S_{33} & S_{34} & S_{35} & S_{36} \\ S_{41} & S_{42} & S_{43} & S_{44} & S_{45} & S_{46} \\ S_{51} & S_{52} & S_{53} & S_{54} & S_{55} & S_{56} \\ S_{61} & S_{62} & S_{63} & S_{64} & S_{65} & S_{66} \end{bmatrix} \begin{bmatrix} \sigma_1 \\ \sigma_2 \\ \sigma_3 \\ \sigma_4 \\ \sigma_5 \\ \sigma_6 \end{bmatrix} \quad (4.7)$$

Anisotropic materials, that is, when the elastic constants depend on direction, are described by up to the full twenty-one elastic constants. In contrast isotropic materials are only requiring two independent elastic constants using the following simple form:

$$C_{ij} = \begin{bmatrix} \lambda + 2\mu & \lambda & \lambda & 0 & 0 & 0 \\ \lambda & \lambda + 2\mu & \lambda & 0 & 0 & 0 \\ \lambda & \lambda & \lambda + 2\mu & 0 & 0 & 0 \\ 0 & 0 & 0 & \mu & 0 & 0 \\ 0 & 0 & 0 & 0 & \mu & 0 \\ 0 & 0 & 0 & 0 & 0 & \mu \end{bmatrix} \quad (4.8)$$

The quantities λ and μ are known as Lamé's parameters. Alternatively, the matrix can be defined by the bulk modulus K and shear modulus μ using the

$$\text{identity } K = \lambda + \frac{2\mu}{3}.$$

Again, conversely for this isotropic case but in terms of stiffness.

$$S_{ij} = \begin{bmatrix} \frac{1}{E} & \frac{-\nu}{E} & \frac{-\nu}{E} & 0 & 0 & 0 \\ \frac{-\nu}{E} & \frac{1}{E} & \frac{-\nu}{E} & 0 & 0 & 0 \\ \frac{-\nu}{E} & \frac{1}{E} & \frac{1}{E} & 0 & 0 & 0 \\ 0 & 0 & 0 & \frac{1}{\mu} & 0 & 0 \\ 0 & 0 & 0 & 0 & \frac{1}{\mu} & 0 \\ 0 & 0 & 0 & 0 & 0 & \frac{1}{\mu} \end{bmatrix} \quad (4.9)$$

4.3 Wave equations in isotropic material

With the knowledge of Hooke's law above, it is now possible to show that a transient disturbance will propagate within the medium. The derivation of the wave equation from first principles for a fully elastic medium is quite involved, as this is done in numerous textbooks (e.g. Lay and Wallace (1995) it need not be repeated here. However, for purposes of this study we reduce the wave equation to its simplest scalar form that describes the displacement $u = u(x,t)$

$$\frac{\partial^2 u}{\partial t^2} = c^2 \nabla^2 u, \quad (4.10)$$

In the case of an isotropic elastic material the elastic properties and the density of the material define the wave velocity and can be given by the general relation:

$$c = \sqrt{\frac{M}{\rho}} \quad (4.11)$$

where c is the wave velocity, M is the appropriate ‘elastic modulus’ for the wave discussed and ρ is the material bulk density. This equation may take a number of different forms depends on the type of wave and the elastic constants that are used. For an elastic isotropic medium two distinct body waves exist.

Body waves can propagate by a series of compression and dilatation of the material or by shearing the material back and forth. The first wave type called compressional wave or primary wave (P -wave) the latter name being due to the fact that it usually observed first on earthquake records. P -waves involved compressional motions and volumetric changes as the wave propagate through the material. The particles of the material are squeezed and pulled back and forth parallel to the direction of the wave propagation. The second wave type is shear wave or secondary wave (S -wave) since it arrives after P -wave on earthquake records. S -wave involves shearing motions without volume change. Particle motions for S -wave are perpendicular to the propagation direction of the wave.

In solid isotropic elastic material velocity of compressional wave is given by:

$$V_p = \sqrt{\frac{\lambda + 2\mu}{\rho_b}} = \sqrt{\frac{K + \frac{4}{3}\mu}{\rho_b}}, \quad (4.12)$$

and the shear wave velocity is given by:

$$V_s = \sqrt{\frac{\mu}{\rho_b}} \quad (4.13)$$

In fluid medium only compressional waves will propagate with velocity:

$$V_p = \sqrt{\frac{K}{\rho_b}} \quad (4.14)$$

where K is the bulk modulus (incompressibility), μ is the shear modulus, λ is the second Lamé's parameter and ρ_b is the material bulk density. Considering equation (4.12) and (4.13) when the P - and S -wave velocity and bulk density of a material are known the elastic parameters of the material can be easily calculated by rewriting these equations as:

$$K = \rho_b \left(V_p^2 - \frac{4}{3} V_s^2 \right) \quad (4.15)$$

$$\mu = \rho_b V_s^2 \quad (4.16)$$

4.4 Gassmann's Equations

In this section, the results of the last are examined for the case of a porous medium consisting of a solid frame and with the void space filled with either vacuum, gas, or liquid. The equations describing wave propagation above do not change, but the complications arise now in attempting to determine the values of the appropriate modulus and density for compressional and shear wave propagation. This problem is critical in applied geophysics as the wave speeds through the rock, and hence their final signature in a given seismic trace, can be highly dependent upon the fluid within the pore space. This is particularly true for high porosity, compliant rock frames. Here, the simplest expressions for the moduli of a fluid-saturated rock are given, and because of their simplicity they are employed widely in applied geophysics. These equations were developed by F.

Gassmann (1951) using quasi-static arguments, but the low-frequency limit of Biot's (1956a, 1956b) dynamic developments provide the same result. Berryman (1999) also provides an alternative derivations of what has come to be referred to as Gassmann's equation.

One of the important factors that affect elastic properties in reservoir rocks is fluid substitution. It refers to the prediction of velocities in rocks saturated with one fluid from dry velocities or from saturated with another fluid. Gassmann's equations (1951) are one of the widely used relations to predict the effect of fluid substitution on seismic properties. It calculates the bulk modulus of fluid-saturated rock K_{sat} using the rock frame (dry) bulk modulus K_d , the bulk modulus of the rock forming minerals (matrix) or so-called grain bulk modulus K_m , the bulk modulus of the pore fluid K_f and the rock porosity ϕ (figure 4.1):

$$K_{sat} = K_d + \frac{(1 - K_d/K_m)^2}{\frac{\phi}{K_f} + \frac{1-\phi}{K_m} + \frac{K_d}{K_m^2}} \quad (4.17)$$

The shear modulus of the rock is assumed to be constant and independent of the fluid saturation and remain constant during the fluid saturations, so that

$$\mu_{sat} = \mu_d, \quad (4.18)$$

where μ_{sat} and μ_d are the fluid-saturated shear modulus and the rock frame (dry) shear modulus respectively. It is these two moduli, K_{sat} and μ_{sat} as well as the saturated bulk density ρ_b , that are employed in Eqns 4.12 and 4.13 above to estimate the saturated wave speeds.

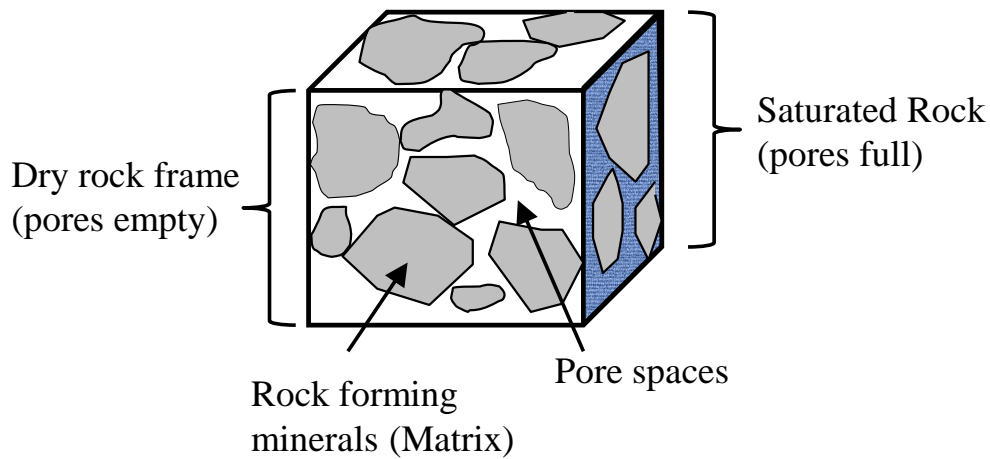


Figure 4.1: Schematic illustration of porous rock model.

As shown in equations (4.17) and (4.18) several parameters are required to calculate the bulk and shear moduli of the fluid-saturated rock (e.g. frame bulk, frame shear, mineral bulk and fluid bulk moduli and porosity). The rock frame bulk K_d and shear μ_d moduli can be calculated from the dry measurements of the ultrasonic P - and S -wave velocities and dry bulk density using Eqns (4.15) and (4.16) respectively.

To calculate the bulk modulus of the rock forming minerals (matrix) K_m (grain bulk modulus), we need to estimate the volume fractions of the mineral constituents using either point count of thin-sections or X-ray diffraction methods. Once the mineral composition is known K_m can be estimated from Voigt-Reuss-Hill average (Hill, 1952):

$$K_m = \frac{1}{2}(K_V + K_R) \quad (4.19)$$

where K_V is the Voigt (1928) average,

$$K_V = \sum_{i=1}^n C_i K_i \quad (4.20)$$

and K_R is the Reuss (1929) average,

$$\frac{1}{K_R} = \sum_{i=1}^n \frac{C_i}{K_i} \quad (4.21)$$

where C_i and K_i are the volume fraction and the bulk modulus of the i th component respectively. The bulk modulus of the rock forming minerals K_m can also be estimated from the direct laboratory measurement from the unjacketed quasi-static strain test as described in chapter (5).

The bulk modulus of the pore fluid K_f is calculated by averaging the values of individual fluid type in case of a fluid mixture using Wood's equation (Wood, 1941) that is essentially the Reuss average for fluids:

$$\frac{1}{K_f} = \frac{S_w}{K_w} + \frac{S_o}{K_o} + \frac{S_g}{K_g} \quad (4.22)$$

where K_w , K_o and K_g are the bulk moduli of water, oil and gas respectively and can be predicted from an empirical relation (e.g. Batzle and Wang, 1992); S_w , S_o and S_g are the water, oil and gas saturation respectively. In case of single fluid K_f is equal to the bulk modulus of that fluid.

The fluid-saturated rock bulk density is given by:

$$\rho_{sat} = \rho_d + \phi \rho_f \quad (4.23)$$

where ρ_{sat} and ρ_d are the fluid-saturated and dry rock densities respectively and ρ_f is the pore fluid density.

$$\rho_d = \rho_m(1 - \phi) \quad (4.24)$$

where ρ_m the rock matrix (grain) density.

The fluid density is calculated by

$$\rho_f = S_w \rho_w + S_o \rho_o + S_g \rho_g \quad (4.25)$$

where ρ_w , ρ_o and ρ_g are the densities of water, oil and gas respectively.

After calculating the saturated bulk modulus and density one can calculate the saturated compressional and shear wave velocities using equation (4.12) and (4.13) respectively with the appropriately substituted moduli and rock density.

The derivation and application of Gassmann's equations for porous rock is based on several assumptions. Firstly, the rock is macroscopically isotropic, homogeneous and monomineralic. This assumption to assure that the grain and pore size is smaller than the wavelength which can be satisfied for most rock types. This assumption can be violated if the rock composed of mixed minerals with large contrasts in elastic properties. In this case the average bulk modulus is estimated as mentioned earlier using Voigt- Reuss-Hill average. The second assumption is that the pore spaces are interconnected means no isolated and/or poorly connected pores. It assumes that the pore fluid can freely flow and relax from the flow induced by the passing wave during time of half of the wave period. This assumption can problematic in carbonate rock due to the diverse pore types and size that normally observed in thin-sections. Thirdly, the pore fluid does not alter the rock frame. When the rock saturated with a fluid, the fluid will interact with the solid frame and it may soften or harden the matrix which in turn will

change the stiffness of the rock. The fourth assumption is that the rock-fluid system is under undrained conditions, meaning that the system is sealed so that the fluid cannot flow in or out the rock. Lastly, Gassmann's equations are valid only at low frequency. If the wave frequency is zero or very low fluid would have enough time to reach the equilibrium stage. At high frequency one can use other theory's that developed for high frequency such as Biot (1956b, 1962) which can be reduced to Gassmann's equations at very low frequency.

4.5 Bulk Modulus (incompressibility parameters)

The bulk modulus (incompressibility), K , is defined as the volumetric dilatation of porous rock to the change of total pressure and pore pressure. In other words, is the ratio of the change in pressure ΔP to the resulting volume change $\Delta V/V$:

$$K = -\frac{\Delta P}{\Delta V/V} \quad (4.26)$$

The bulk modulus generally describes the resistance of the material compression and can be obtained in two ways. One involves measuring the P - and S -wave velocities and density, and then the bulk modulus of the porous rock can be calculated using equation (4.15) which so-called the dynamic bulk modulus. In this case the volumetric deformation is caused by the passage of the seismic wave.

The other method, the static bulk modulus, obtained from measuring the volumetric strain for a given stress which can be measured using strain gauges (chapter 5). The principle of the static bulk modulus determination is based on the

fact that when the sample is subjected to a confining pressure (P_c) all shear stress will be zero and the normal stress will be identical ($\sigma_{xx} = \sigma_{yy} = \sigma_{zz} = P_c$). The measured strain of the sample is:

$$\varepsilon = \frac{\Delta L}{L} \quad (4.27)$$

where $\Delta L/L$ is the relative change of the sample length. Since bulk modulus is related to the volume change the bulk modulus is given by:

$$K = -\frac{\Delta P}{\Delta V/V} = -\frac{\Delta P}{3(\Delta L/L)} = -\frac{\Delta P}{\theta} \quad (4.28)$$

where θ is the volumetric strain.

The two methods are differing in the loading frequency and the strain magnitude. The dynamic measurements involve high loading frequency and low strain magnitudes whereas the static measurements involve low loading frequency and high strain magnitude. The peak strain in dynamic measurement is of the order of 10^{-6} , while the static measurement is greater than 10^{-2} . In either method the measurement of bulk modulus may be made in two different ways, jacketed and unjacketed test. A review of the two techniques based on Biot and Willis (1957) and Kumpel (1991) will be given here.

4.5.1 Jacketed bulk modulus test

A rock sample is sealed by thin impermeable material which isolates the sample from the surrounding confining pressure fluid. The rock sample then is subjected to confining pressure (P_c) and the pore pressure (p_p) kept constant by

enable the pore fluid, in the case of fluid saturated sample, to escape through an opening inlet to the atmosphere, which is so called drained condition test (figure 4.2a). The dry sample measurements can also considered as drain condition as the pore pressure does not change. In the drained test the relative change in volume will be measured and the rock frame bulk modulus is then given by:

$$K = -V \left(\frac{\Delta P_c}{\Delta V} \right)_{dp_p=0} \quad (4.29)$$

The subscript dp_p stands for constant pore pressure.

The undrained condition test performed if the saturated rock is subjected to confining pressure and the sample is totally isolated from the surrounding confining fluid and the atmosphere, means there is no change to the pore fluid volume and the pore pressure shows an incremental increase with the increase of the confining pressure (figure 4.2b). The undrained bulk modulus (K_u) is defined by:

$$K_u = -V \left(\frac{\Delta P_c}{\Delta V} \right)_{dm_f=0} \quad (4.30)$$

where m_f is the fluid mass per unit bulk volume. The drained and undrained conditions terminology are based on the boundary condition, in which the drained condition assumes no change in the pore pressure, whereas the undrained condition assumes no change in pore fluid mass which causes changes in pore pressure (Green and Wang, 1986).

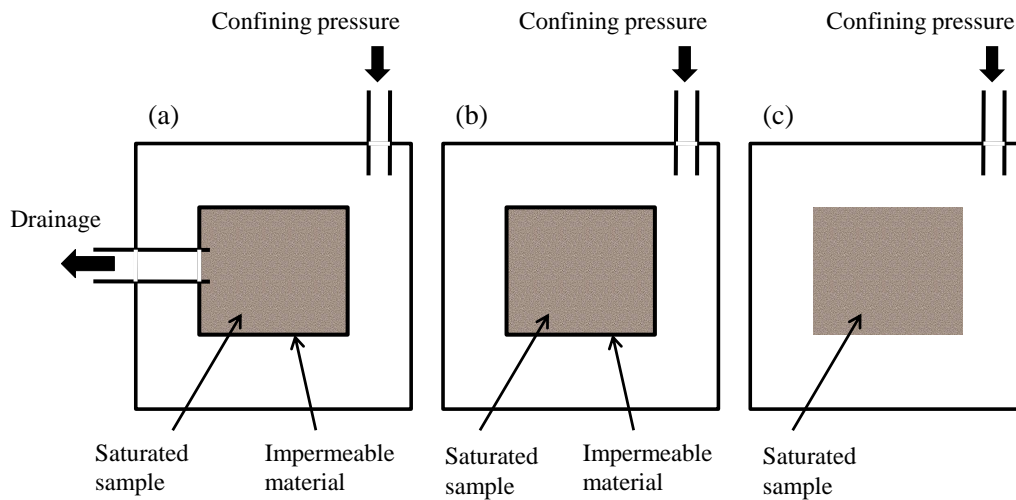


Figure 4.2: Jacketed drained (a) and undrained (b) bulk modulus test. (c) Is theunjacketed bulk modulus test.

4.5.2 Unjacketed bulk modulus test

Biot and Willis (1957) introduced a test to measure grain or mineral modulus, named the unjacketed test. In this test, a sample without the impermeable material is introduced in a pressure vessel and then the confining pressure is applied (open pressure test, figure 4.2c). The confining pressure fluid enters the pore spaces and after a period of time the confining pressure fluid will completely penetrate the pore spaces. In this case, the changes in the pressure are the same inside the sample and equal to the changes in the confining pressure. The relative change in volume will be measured $\Delta V/V$ (volumetric strain) and the unjacketed bulk modulus is given by:

$$K_m = -V \left(\frac{\Delta P_c}{\Delta V} \right)_{dP_c=dp_p} \quad (4.31)$$

If no isolated pores presented in the rock (all pores are connected) theunjacketed bulk modulus is identical to the rock forming minerals bulk modulus or so-called grain bulk modulus.

4.5.3 Effect of cracks on elastic properties

Most of rocks in earth crust contain void spaces with shape varies from spherical pores to thin micro cracks. The effect of the pore spaces and micro cracks on elastic properties of rocks were recognized and studied by many authors (i.e., Adams and Williamson, 1923; Simmons and Brace, 1965; Walsh 1965; Brace, et al. 1972). Adam and Williamson (1923) observed that the elastic properties of the rock increased with increasing the confining pressure which he interpreted as due to the closing of cracks with pressure. Toksöz et al. (1976) showed that small aspect ratio pores (thin cracks) have a great effect on elastic properties of the rock than the high aspect ratio pores (spherical). Birch (1965) showed from his measurements that this effect is due to the closing of thin cracks and the spherical pores have no very little influence. Batzle et al., (1980) studied the behaviour of cracks with pressure increase using scanning electron microscopy (SEM). They observed microcracks closure with increasing pressure and the closure depend on the shape and the orientation of the cracks. The thin microcracks closed at low pressures and the cracks that aligned perpendicular to the maximum stress are closed whereas the cracks aligned parallel are opened. The closure of cracks will decrease the compressibility of the rock and the rock becomes stiffer which in turn increase the elastic properties of the rock sample.

4.6 Conclusions

When a material is subjected to compression or shearing stress it undergoes deformation in volume and/or shape (strain). The material that tends to return to original volume and shape is described as perfectly elastic material. Hooke's law describes the elastic behaviour of a material where the amount of strain is linearly proportional to the amount of stress. The constants of this proportionality are the elastic moduli of the material. We showed that in general twenty-one elements are needed to describe an anisotropic material, whereas isotropic material can be described using only two constants. These elastic constant can be easily calculated using the measured P- and S-wave velocities and bulk density of the material.

Gassmann's equations (1951) are commonly used to calculate the fluid saturation effects on velocity. It calculates the bulk modulus of fluid-saturated rock from the known frame (dry), grain and fluid bulk moduli and porosity. The application of Gassmann's relations is based on several assumptions:

1. The rock is isotropic and homogeneous (monomineralic).
2. Pore spaces are interconnected (no isolated pores).
3. Pore fluid has enough time to reach equilibrium (low frequency).
4. The pore fluid does not alter the rock frame.
5. The rock-fluid system is under undrained conditions.

These assumptions were discussed here in detail.

Two types of static bulk modulus tests were shown, jacketed and unjacketed tests. In the jacketed test, the sample is sealed by thin impermeable

skin and is normally used to measure the frame bulk modulus of the rock under dry and saturated conditions. Theunjacketed test conducted on unsealed sample where the sample exposed to the confining pressure fluid (open pressure test). This type of test is used to measure the grain bulk modulus of the sample.

Chapter 5

Ultrasonic velocity and quasi-static strain experiments

5.1 Introduction

This project involved determining both the dynamic (~ 1 MHz) and static elastic properties of carbonate samples. The dynamic properties are obtained from measuring the P - and S -wave velocities and density of the rock sample, and the static properties; obtained from directly measuring the volumetric strain for a given stress using strain gauges.

There are several different techniques to measure the ultrasonic elastic properties in rock samples and these include pulse transmission, pulse echo, and the resonant ultrasound spectroscopy methods. In this project we used the pulse transmission method, commonly method used to measure the dynamic elastic

properties in rocks (e.g. Birch, 1961) and has been extensively used in carbonate studies (e.g., Verwer et al. 2008; Anselmetti and Eberli, 1993; Adam et al., 2006).

At 'zero' frequency (static), two different techniques are commonly used to measure the strain on rock samples; one employs Linear Variable Differential Transformers (LVDTs). These sensors are typically used to infer changes in the total length of a sample during deformation; they usually do not measure the length change directly but that of the experimental sample holder for which corrections must be made. This is most often used in 'triaxial' stressing machines where the movement of the pistons applying force to the sample is measured. These methods have the advantage that the sensor need not necessarily be subject to the conditions that the sample is experiencing, but on the other hand the measurements usually must be carefully corrected to account for the stressing machine deformations which may or may not be repeatable. This technique was not employed in this study, but a specialized instrument has recently been developed by graduate student Xun Qi (2008) who needed to measure the rather large deformation of unconsolidated oil sands and for which strain gauges could not readily be attached.

The other technique uses strain gauges that are directly applied to the sample. In this project we used the strain gauges technique to measure the strain in our samples which involves measuring the changes of the electrical resistance of a wire with strain using electrical resistance strain gauges. The advantage of this is that the deformation of the sample is directly measured but usually only a along portion of the sample length.

Details of the pulse transmission method used to measure ultrasonic velocities and the strain gauges technique used to measure the strain are given in this chapter. The experimental setup used here will first be described including the technique used to build source/receiver transducers, the method used to prepare and measure samples and the theoretical relations used to determine the velocity and the strain. The experimental procedure followed to measure both velocity and strain will also be shown. Examples of ultrasonic velocities and moduli results and discussions will also be given.

5.2 Ultrasonic velocity measurement

The pulse transmission method conceptually only involves measuring the travel time of the ultrasonic wave traveling through the sample. A typical ultrasonic measurement system consists of several functional units (e.g. source/receiver transducers and recording and displaying device). Driven by the pulser, which produces high voltage electrical pulse, the piezoelectric ceramic transducer setting on one end of the sample generates high frequency ultrasonic waves. The generated wave propagates through the sample and is transformed into an electrical signal by the transducer on the opposite end of the sample then is recorded by a digital oscilloscope.

5.2.1 Ultrasonic transducers

The transducers used as source and receiver of the ultrasonic wave are the main unit in the ultrasonic measurements. The active element of the transducer is

the piezoelectric ceramics made from lead zirconate titanate from Omega Piezo Technologies Inc. The piezoelectric (PZT) ceramic is a polarized material that converts the electrical pulse into mechanical vibration (source mode) and converts the mechanical vibration into electrical signal (receiver mode). The vibration mode of the material is determined by the polarization of the PZT ceramic. The axial polarization causes compression/tension vibration mode and generates compressional wave (P-wave). The lateral polarization causes shear vibration mode and generates shear wave (S-wave). The thickness of the ceramic is determined by the desired frequency. The thinner the ceramic, the higher the frequency generated. Both of the P- and S-wave PZT ceramics here are made with resonant frequencies centered around 1 MHz.

A piezoelectric ceramic staking method is used to allow simultaneous measurements of P- and S-wave (Hemsing, 2007). The P-wave piezoelectric ceramic is glued on top of the S-wave piezoelectric ceramic and separated by an electrode of copper foil using silver conductive epoxy. This electrode is a common electrode between the P- and S-wave PZT ceramics. It acts as the negative side of the P-wave PZT ceramic and as the positive side of the S-wave ceramic. The positive side electrode is glued on top of the P-wave ceramic and the negative S-wave electrode is glued below the S-wave ceramic. The stacked set is allowed to cure for 24 hours then glued onto aluminum buffer using silver epoxy. A small film of nonconductive epoxy is applied to the set to prevent any conduction between the positive and the negative side of the transducer. Then a damping material made of a mix of urethane rubber (Flexane®80 Liquid) and iron

powder is poured on the top of the staking set and allowed to set for 24 hours. Finally, the top of the transducer is covered by the urethane rubber (Flexane®80 Liquid) and the side of the transducer is painted with the same material to prevent the confining oil from leaking inside the transducer and break the bound between the staked piezoelectric ceramics (figure 5.1). The last step is very important as it helps to increase the life time of the transducers.

Our carbonate samples were cut into two different diameters of 2.5 cm and 3.8 cm; therefore two different aluminum buffers are used (2.54 cm and 3.81 cm). As mentioned earlier a pair of transducers is needed in the measurement, one acts as the source (transmitter) and the other as the receiver. For the purpose of controlling the pore pressure and saturating the sample, one transducer end cap was fabricated with a pore pressure inlet for the pore fluid to go through. In the large diameter transducers (3.81 cm) we used the method that developed by He (2006), where the pore pressure inlet goes from the top of the aluminum buffer (figure 5.2a). However, the small diameter transducer (2.54 cm) lacks enough end surface area to allow room for a pore pressure port on the top of the buffer. A new method is developed, where the pore pressure inlet goes from the side of the buffer as shown in figure 2b.

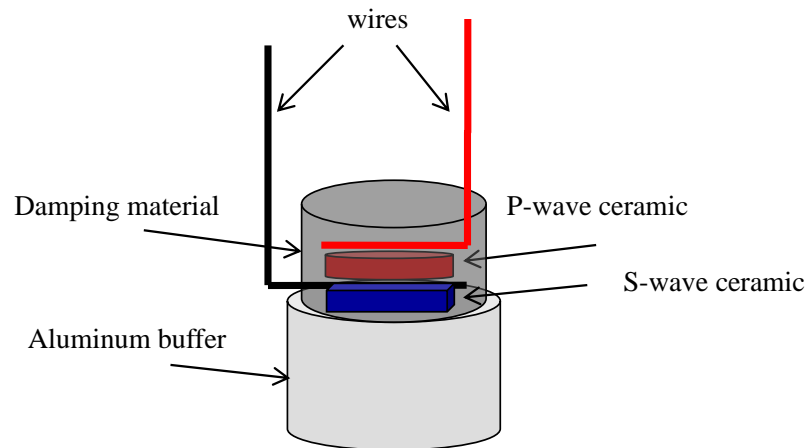


Figure 5.1: Schematic of the source/receiver transducer.

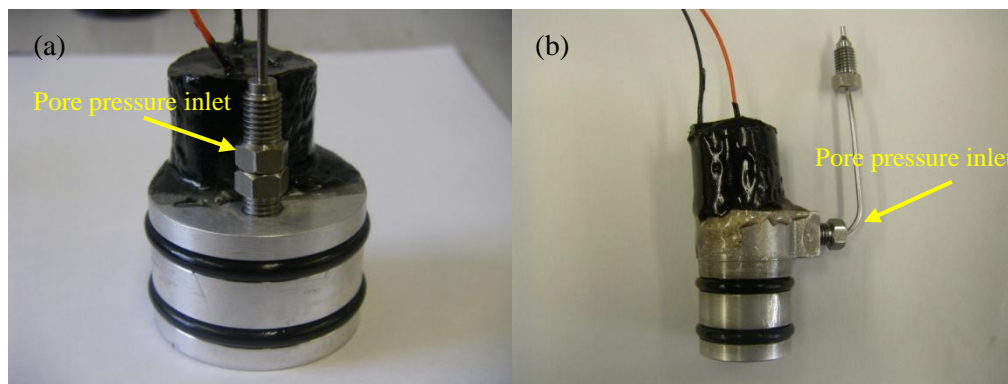


Figure 5.2: (a) The 3.8 cm transducer, the pore pressure inlet goes from the top of the aluminum buffer. (b) The 2.54 cm transducer, due to the lack of the surface area the pore pressure inlet goes from the side of the buffer.

5.2.2 Velocity calculation and error analysis

The pulse-transmission technique used here involves generating compressional or shear wave from one end cap (source). The generated wave propagates through the sample and is received on the opposite end (receiver). In

order to estimate the velocity we measure the time that the wave takes to travel from the top of the sample to the bottom (figure 5.3). Then the wave velocity V of the sample can be calculated using the simple scalar definition of wave speed:

$$V = L/t \quad (5.1)$$

where L is the length and t is the measured travel time through the sample. The latter is estimated in two steps. First, we measured the travel time (t_0) through the aluminum buffer in the absence of any sample (figure 5.4) by picking the first extremum of the recorded signal (figure 5.5a). This buffer transit time t_0 depends on the confining pressure; and this pressure dependence was determined by cap-to-cap direct measurements under pressure.

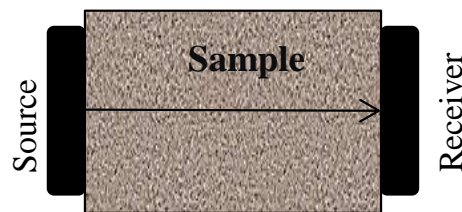


Figure 5.3: Schematic of the wave propagation through the sample from the source to the receiver.

Similarly, then the travel time (t_m) through the aluminum buffer and the sample is measured and picked (figure 5.5b). The travel time through the sample (t_s) is simply the difference $t_m - t_0$.

There are two main errors associated with the determination of the velocity, the travel time picking and the sample length. The travel time error depends on the quality of the signal and it varies between $0.02 \mu\text{s}$ for high quality

signal (high pressure measurements) and 0.05 μs for low quality (low pressure measurements). The samples were prepared with their end faces parallel to within 0.02 mm. The error associated with the velocity can be estimated as:

$$\frac{\Delta V}{V} = \sqrt{\left(\frac{\Delta L}{L}\right)^2 + \left(\frac{\Delta t}{t}\right)^2} \quad (5.2)$$

where $\Delta V/V$ is the error in velocity, ΔL is the measurement error of the length and Δt is the error of the time picking. The shortest sample measured in this project is 1.651 cm with 27% porosity. The maximum error in length is 0.02 mm and 0.07 μs is the maximum error in time. In this case the maximum error in the velocity calculation is about 0.4%. As both L and t increase for most of the other samples and are in the denominator in Eqn. 5.2 this result is the expected maximum uncertainty in the velocity measurements, under the assumption that the waveform is not significantly altered by attenuation as it passes through the sample.

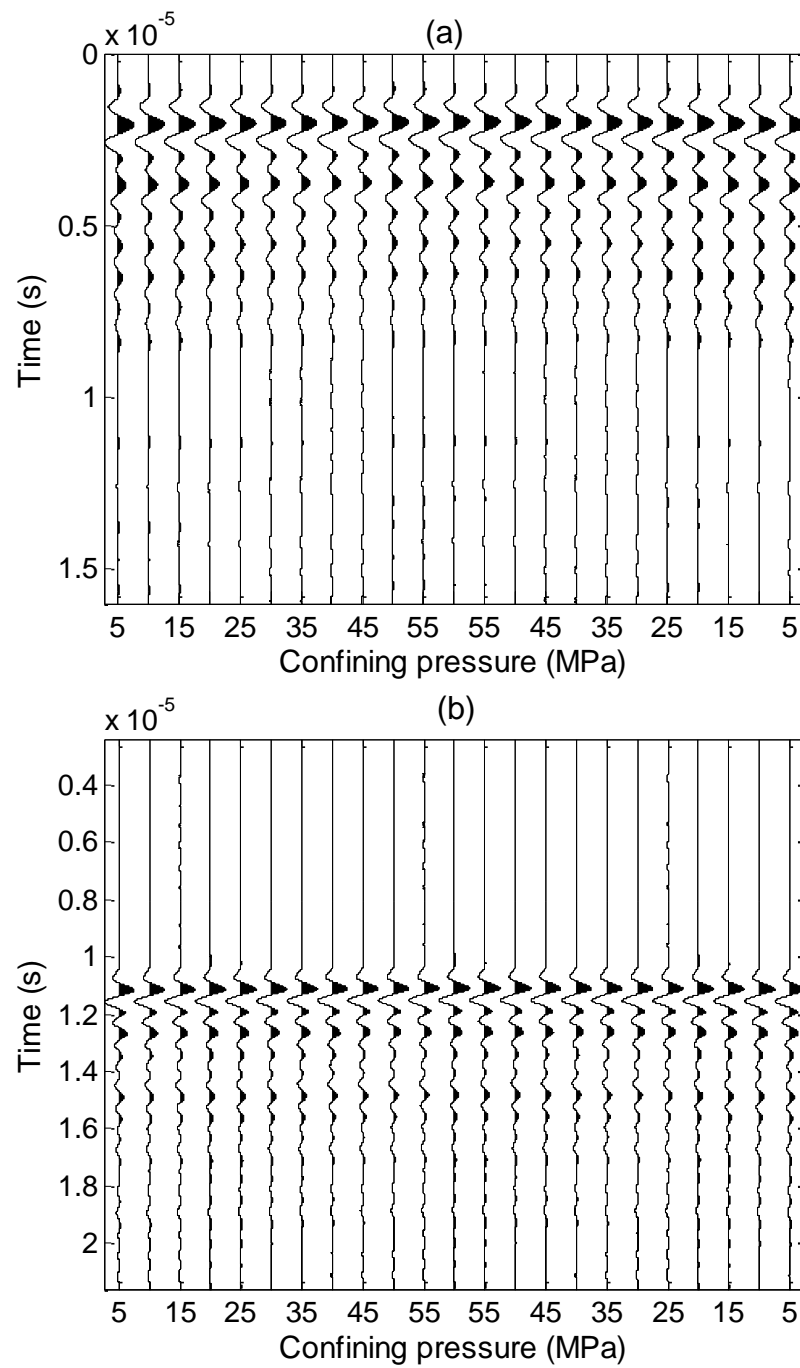


Figure 5.4: Normalized *P*-wave (a) and *S*- wave (b) calibration waveforms obtained on aluminum buffer at different confining pressures.

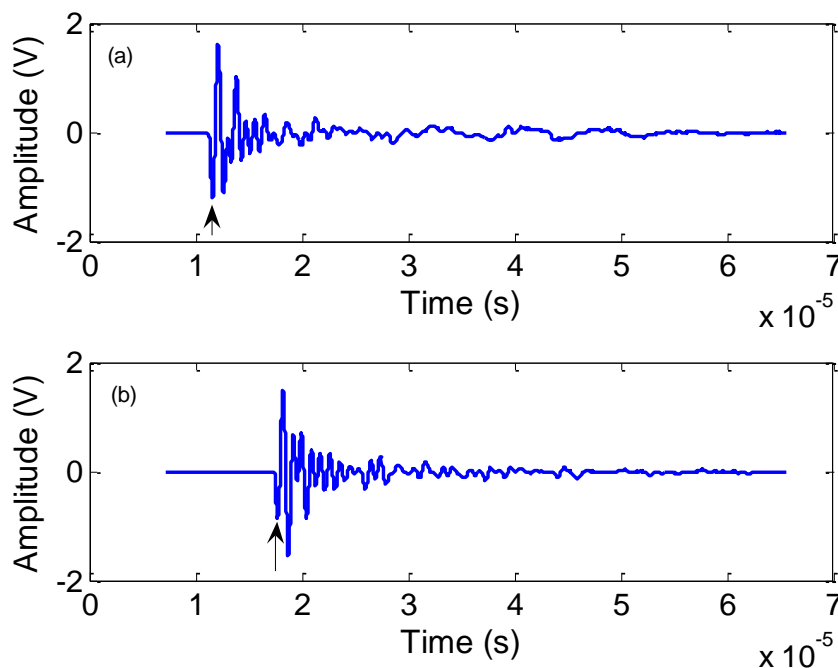


Figure 5.5: Two P-wave signals at 15 MPa confining pressure. (a) The signal through the aluminum buffer in the absence of any sample. (b) The signal through the aluminum buffer and the sample. The travel time is picked at the first extremum, marked by arrows.

The dynamic bulk K and shear μ moduli can be calculated from the measured P - and S -wave velocities (V_p and V_s respectively) and bulk density ρ_b from well known elastic relations:

$$K = \rho_b \left(V_p^2 - \frac{4}{3} V_s^2 \right) \quad (5.3)$$

$$\mu = \rho_b V_s^2 \quad (5.4)$$

5.3 Strain Measurements

Two different techniques are commonly used to measure the strain on rock samples; one is called Linear Variable Differential Transformer (LVDTs), which is basically a series of inductors in a hollow cylindrical shaft and a solid cylindrical magnetic core that is able to produce an electrical output proportional to the position of the core. The measured output voltages can be calibrated and used to measure the displacements of the core sample as a result of applied stress. The other technique involves measuring the changes of the electrical resistance of a wire with strain using electrical resistance strain gauges. In this project we used the foil strain gauge technique to measure the strain in our samples. This technique has been long employed by many workers (e.g., Adam et al., 2009; Schmitt and Li, 1995; Schmitt and Zoback, 1989; Batzle and Simmons, 1976; Schock and Heard, 1974; Walsh and Brace, 1972).

5.3.1 Strain gauge and Wheatstone bridge

When a material is loaded with an external force, stress and strain are the result. Stress σ can be defined as the applied force F per unit area A :

$$\sigma = \frac{F}{A} \quad (5.5)$$

and the strain ϵ can be defined as the ratio of the change in length ΔL to the original length L :

$$\varepsilon = \frac{\Delta L}{L} \quad (5.6)$$

Strain gauge is one of the most widely used techniques to measure strain. A foil strain gauge consists of a flexible plastic backing which supports a thin metallic foil resistor etched onto its surface (figure 5.6). The back-and-forth pattern on the gauge is used to increase the foil's effective length. The plastic backing is glued directly to the sample surface and hence it and its attached foil are assumed to follow the deformation of the sample. Its principal of operation is based on the fact that once the sample is strained, the length of the foil and consequently its DC resistance changes. This relationship between strain and resistivity was initially reported by Lord Kelvin in 1855. When the strain gauge is attached and bonded well to the surface of the sample, the two are considered to deform together. As the sample is deformed, the foil also deforms causing its electrical resistance to change. This change in resistance ΔR is proportional to the strain sensitivity of the wire and mathematically can be given by:

$$\frac{\Delta R}{R} = G_f \cdot \varepsilon \quad (5.7)$$

where R is the resistance of undeformed gauge and G_f is the strain sensitivity factor (gauge factor). Basically when the gauge factor is given by the manufacturer, (usually provided by strain gauge vendors) the strain at the point of attachment of the strain gauge can be obtained by measuring the changes in electric resistance of the strain gauge. Equation 5.7 shows that the quantity that we need to measure is the fractional change in gauge resistance from the unstrained to the strained condition.

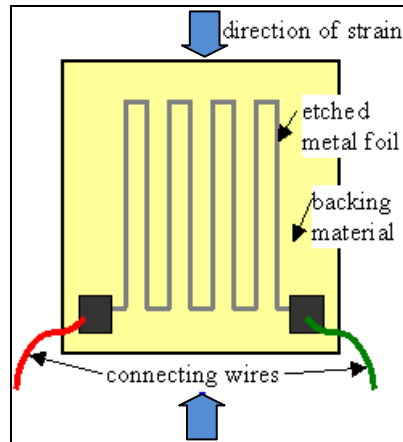


Figure 5.6: Schematic of the bounded foil strain gauge.

The main problem when working with strain gauges is that the changes in resistance are three to six orders magnitude smaller than the resistance itself. Most ohm meters do not have sufficient resolution to measure such a small value. Electrical noise, too, could overwhelm such a small change in the absolute gauge resistance. A more sensitive way to measure the small changes in resistance is with the use of the well known Wheatstone bridge circuit. The Wheatstone bridge is an electrical bridge circuit used to measure resistance. A basic Wheatstone bridge circuit contains of four resistances, a constant voltage input, and a voltage gauge (figure 5.7). The output voltage is measured across the legs in the middle of the bridge.

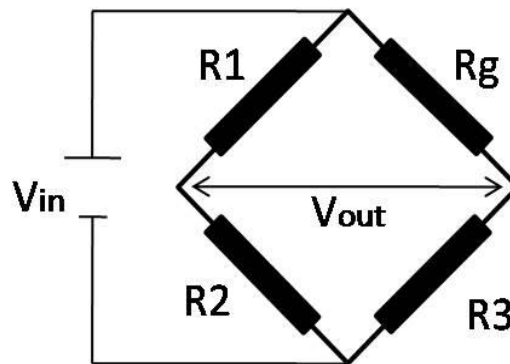


Figure 5.7: Schematic of Wheatstone bridge circuit.

5.3.2 Strain calculation

To measure the strain, one of the resistors is replaced by the strain gauge and in this case the circuit is called Quarter Bridge. In figure 5.7, V_{in} is the constant input voltage and it is equal to 2.5 volt, R_1 , R_2 and R_3 are the resistance of the bridge completion resistors, R_g is the resistance of the strain gauge ($R_1 = R_2 = R_3 = R_g = 350$ ohms) and V_{out} is the bridge output voltage. When the sample undergoes strain, the only resistor in the bridge circuit that varies is the strain gauge R_g . The output voltage V_{out} can be defined as a function of V_{in} , R_1 , R_2 , R_3 and can be written as

$$V_{out} = V_{in} \left[\frac{R_3}{R_3 + R_g} - \frac{R_2}{R_1 + R_2} \right] \quad (5.8)$$

This relation holds for the unstrained and the strained condition. In unstrained condition the value of the strain gauge resistor is R_g and the value of the strain gauge resistor in strained condition is defined as $R_g + \Delta R_g$. If we define V_r as the

difference of the ratio of V_{out} to V_{in} from unstrained to strained condition and by substituting the resistors value, we can drive an equation for $\Delta R_g/R_g$ as:

$$\frac{\Delta R_g}{R_g} = \frac{-4V_r}{1+2V_r} \quad (5.9)$$

From equation (5.7) and (5.9), the strain can be calculated as follow:

$$\varepsilon = \frac{-4V_r}{G_f(1+2V_r)} \quad (5.10)$$

The strain measurement setup consist of constant voltage power supply furnishes V_{in} , digital voltmeter to measure the output voltage V_{out} and computer facilitated with Labview program. The program coded to initiate the experiment and record the voltmeter readings in both unstrained and strained conditions. Since the value of the input voltage ($V_{in}=2.5$ volt) and the gauge factor are known (usually provided by strain gauge vendors) the strain of the sample can be easily calculated using equation (5.10).

5.3.3 Uncertainty analysis

In this experiment, there are two sources of error inherent in the observed strain value indicated by the strain gauge should be accounted for. The first is that due to the applied pressure and the second is temperature on the gauge elements (Jansen, 1997).

Temperature effect can be easily corrected by subtracting the thermal output value obtained from the graph of thermal output (supplied by the vendor) from the strain measurements at the test temperature.

Brace (1964); Kular (1972) and Milligan (1967) have shown that due to the pressure effects the strain that measured using the strain gauge is different from the theoretical strain. Brace (1964) found that the pressure effects is independent of the elastic properties of the sample, however it depend on the strain gauge material. The pressure effects that observed by Brace (1964) and Milligan (1967) on the early strain gauges ranged between 0.36 and 0.74×10^{-06} MPa^{-1} (Jansen, 1997). In order to correct the pressure effects, we used calibration measurements on fused quartz the pressure dependent properties of which are well known. During a measurement, the fused quartz and sample strains were measured simultaneously within the pressure vessel. Then the observed strain values for the standard (fused quartz) were corrected by using the calculated strain values obtained from its known compressibility (figure 5.8). In the meantime, these correction values, which are pressure effects, are used to correct the sample strain values.

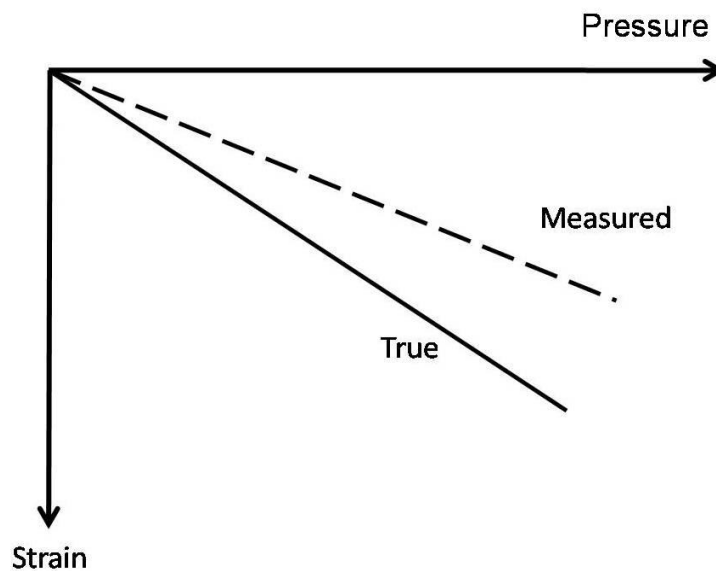


Figure 5.8: Schematic illustration of pressure effect on strain gauge response.

5.4 Sample preparation

This project involved determining dynamic and static elastic properties of carbonate samples. This requires measuring P- and S-wave velocities as well as strains. P- and S-wave velocities were measured for forty samples and strain were measured for the latter twenty three of these. Thirty seven of the samples are obtained from the Saudi Aramco Oil Company from Arab-D reservoir in Saudi Arabia. The samples are cylindrically shaped plugs of 2.54 to 3.8 cm in diameter and 2 to 6 cm in length. As noted earlier, the plugs end faces were ground to parallel (within ± 0.02 mm) in order to enhance the signal transmission and to avoid errors in the velocity measurements as much as possible. Then the samples were dried under vacuum at 70°C temperature for 48 hours and afterward kept in a desiccator jar.

After drying, methods described on chapter 3 were used for petrology characterizations then the sample prepared for strain and velocity measurements.

First, for the strain measurements the gauge area in the sample is smoothed using sand paper, then is cleaned and degreased with alcohol. Two strain gauges are carefully glued directly to the sample, one parallel to its length (vertical) and the other perpendicular (horizontal), using M-bond 200TM catalyst and M-Bond 200TM adhesive. The sample with the affixed strain gauges is inserted into the TygonTM and a small window is cut into the TygonTM tubing to allow access to the soldering area of the strain gauges (figure 5.9). After soldering the wires, thin film of FL-10 Primer (primes the flexane to metal) is applied to the wire and left for an hour to dry. Then a Flexane 80 LiquidTM is poured into the

window to seal the sample from the surrounding hydraulic oil and kept overnight for drying. Next day, an ultrasonic transducer was placed on each end of the sample and the two transducers were aligned so S-wave transducer are properly polarized. To enhance the sealing mechanism and prevent the leakage of the hydraulic oil from reaching the sample, common steel hose iron clamps were tightened around the Tygon just above the aluminum part of the transducers. The same preparation procedure was used to prepare the fused quartz standard. Then the jacketed assembly of the sample (figure 5.10) as well as the fused quartz were placed inside the confining pressure vessel. This method of preparation allows for simultaneous measurements of velocity and strain.

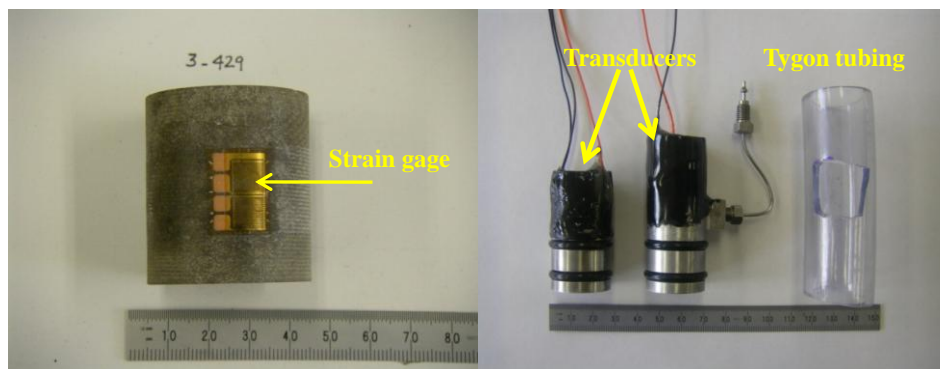


Figure 5.9: The sample with the affixed strain gauges (*left*) and the transducers and the tygon tubing (*right*).

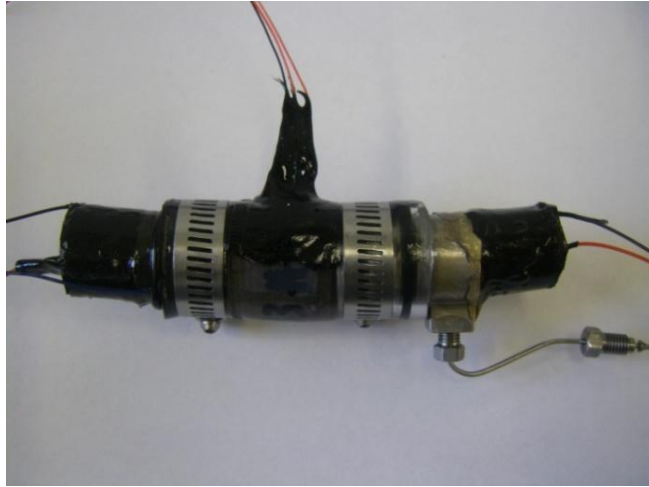


Figure 5.10: The jacketed assembly of the sample.

5.5 Velocity and strain experimental setup

For velocity measurements, the experimental setup consists of a pulse generator, a digital oscilloscope (Gaugescope™), a switch box and a pressure vessel. The transducer is excited by a fast-rising, 200 V square wave, sent by the pulse generator (Panametrics, model 5800 PR). The generated wave propagated through the sample and was recorded by a digital oscilloscope at an 8 nanoseconds time sampling interval. The final wave form is the stack of 256 traces to reduce random noise. The switch box was used to switch between the P- and S-wave.

For strain measurements, the setup consists of a Wheatstone bridge circuit, a constant voltage power supply, a digital voltmeter, and a digital data logger. We used strain gauges (CEA-06-250UT-350) from Vishay Micro-Measurements with gauge factor equal to 2.09 or 2.11 and nominal resistances of 350 ohms, connected in a quarter bridge with three high-quality fixed resistors each also

equal to 350 ohms. The bridge is excited at $V_{in}=2.500$ V using constant voltage power supply the output of which was also continuously measured. Four separate strain gauges are used for each measurement, two of them are connected to the sample and the other two strain gauges are connected the fused quartz. Therefore, a multichannel Wheatstone bridge is employed that allows switching between the strain gauges. It was felt that any switching done inside the bridge arms can cause a change in resistance and affect the output reading. For that reason, all the resistors and strain gauges are permanently connected to the power supply and switch the digital voltmeter from bridge to bridge. A digital data logger (USB-5133) was used to digitally read the voltage across the bridge and the output of the pressure transducer and record them in the computer using LabView® software.

The experimental setup also consists of cylindrical pressure vessel to apply confining pressure up to 200 MPa and pore pressure system to simulate reservoir pressure and used to saturate the sample. A vacuum and a water reservoir are connected to the pore pressure system; the vacuum is used to pump out the air from the sample while it is setting inside the pressure vessel and before acquiring the data for overnight. The water reservoir used to saturate the sample. Figure 5.11 shows the experimental setup used for velocity and strain measurements.

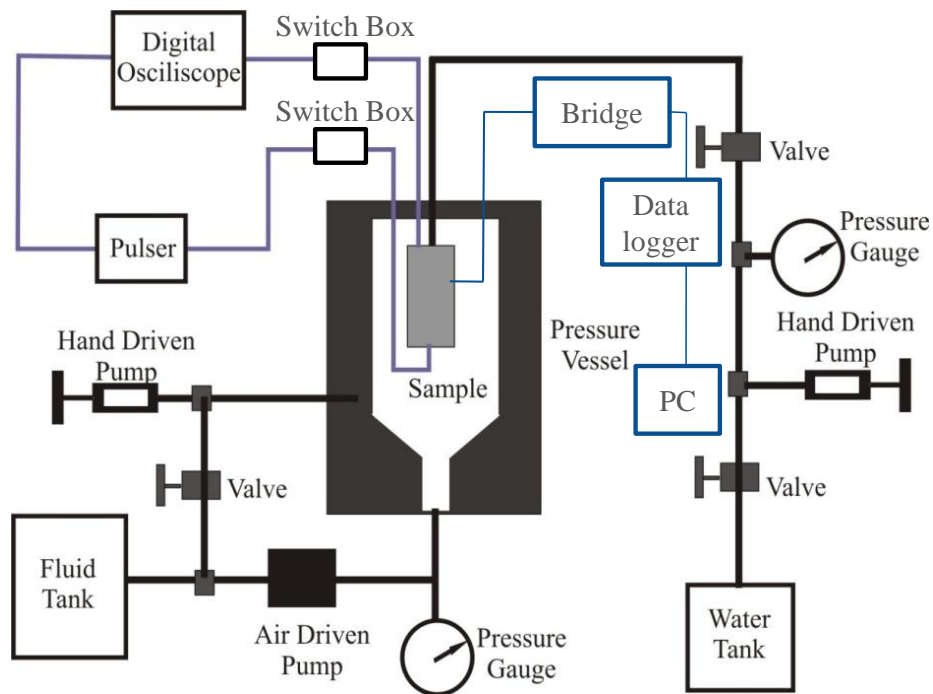


Figure 5.11: The experimental setup used. The purple line represents the velocity recording system and the blue line represents the strain recording system.

5.6 Experimental procedure

P- and S-wave velocities were measured in all 37 samples under dry and water saturated conditions. The strains were measured on fifteen of them. The prepared sample and fused quartz were placed inside the confining pressure vessel. The vacuum was connected to the pore pressure system to pump out the air from the sample, this vacuum was maintained for at least 12 hours (usually, overnight). Velocity and strain measurements conducted for each sample in four distinct cycles. The first three are under ‘jacketed’ (pore fluids pressure is independent of the confining pressure vessel fluid pressure) conditions with pore

fluid saturations of dry (i.e. vacuum), distilled water at room pressure, and distilled water under differential pressure. These three conditions were conducted on jacketed test setup where the sample is enclosed in an impermeable jacket which is the Tygon tubing in our case. The fourth cycle is commonly referred to as the unjacketed test where the impermeable Tygon jacket is broken to allow the pore pressure to be identical to the confining pressure. In this case the confining and pore pressure are essentially the same.

Firstly, the measurements were taken on vacuum dry condition with confining pressure varies from 5 MPa to 25 MPa with 2.5 MPa incremental pressures in both during pressurization and depressurization cycles. The samples were allowed to equilibrate at constant pressure for 15 minutes prior to acquisition of the waveforms.

In the second step and after completion of the velocity measurements of the dry sample, the sample was saturated with water by connecting the water reservoir with the pore pressure system of the vacuum dry sample. The pore pressure was increased to 2.5 MPa to push the water inside the sample and left overnight for the sample to be fully saturated. Then the measurements were taken on saturation condition using same scenario as for vacuum dry condition with pore pressure equal to the ambient room pressure.

In the third step the velocity measurements were taken at constant differential pressure equal to 15 MPa for effective pressure test. The first measurement was taken at 15 MPa confining pressure and pore pressure equal to room pressure. Then the confining pressure and pore pressure were increased for

the same values. Lastly and for the unjacketed test the sample and the fused quartz were pulled outside the pressure vessel and few holes were made in the Tygon tubing, which was initially used to isolate the sample from the surrounding hydraulic oil, to allow the confining oil to intrude the sample pore space. Then the unjacketed sample and the fused quartz were placed back into the pressure vessel and the strain measurements were taken at pressure varies from 5 MPa to 65 MPa. The corrected strain values were used to calculate the grain or rock forming minerals bulk modulus as described in chapter 4.

The principal experimental procedures used in this research are listed below.

1. Measure length, diameter and dry mass for each sample.
2. Measure the grain volume using helium porosimetry.
3. Thin section obtained for selected samples.
4. Measure pore size distribution using Hg-porosimetry on selected sample.
5. Measure P- and S-wave velocities and strain under dry (vacuum) conditions.
6. Measure P- and S-wave velocities and strain under distilled water saturation with the pore pressure equal to the room pressure.
7. Measure P- and S-wave velocities at constant differential pressure (quality control test for saturation).
8. Measure the grain bulk modulus (unjacketed test).

5.7 Result and discussion

The P- and S-wave velocities and quasi-static strain for the Arab formation carbonate samples are measured as a function of differential pressure under both dry and water saturated conditions over both jacketed andunjacketed test. In addition, the velocities are measured under constant differential pressure. The dynamic and static bulk moduli were calculated using the jacketed test and grain bulk modulus was calculated using the unjacketed quasi-static strain test. The dynamic bulk and shear moduli are calculated from the measured ultrasonic velocities and the static bulk modulus calculated from the stress-strain curve. Examples of the measured dry and water saturated P- and S-wave velocities and bulk and shear moduli are shown in this section. Preliminary result of static and grain bulk moduli obtained from jacketed and unjacketed quasi-static strain measurements are discussed in detail in chapter 7.

5.7.1 Waveforms

The full set of normalized P- and S-wave waveforms of samples 7-222 and 3-104 under dry condition are shown in figure 5.12 and figure 5.13 respectively. The samples are pressurized to the peak pressure of 25 MPa and 40 MPa respectively. Obviously, due to the lack of closing microcracks and pores in the sample 7-222 ($\phi=3\%$); the travel times show no remarkable changes with the confining pressure. Whereas, Sample 3-104 ($\phi=31\%$) shows remarkable reduction of travel time with the increase of confining pressure in both P- and S-wave during the pressurization cycle. The reduction in travel time with pressure

continues until the travel time starts to increase at a pressure of 30 MPa. Thus, the travel time on the depressurization cycle is higher than the pressurization one. This increase in travel time is the result of crushing damage to the sample. As mentioned earlier the measurements were carried out at constant differential pressure. Figure 5.14 shows P- and S-wave waveforms under constant differential pressure (15 MPa) for sample 8-115, no remarkable travel time reduction with increasing confining pressure is noticed. This is due to the fact that the equal amount of pore pressure increase cancels the equal amount of confining pressure increase. This observation was used as a QC tool for full water saturation of the sample assuming that samples that show no remarkable increase in travel time over different confining pressure to imply that the sample successfully fully saturated.

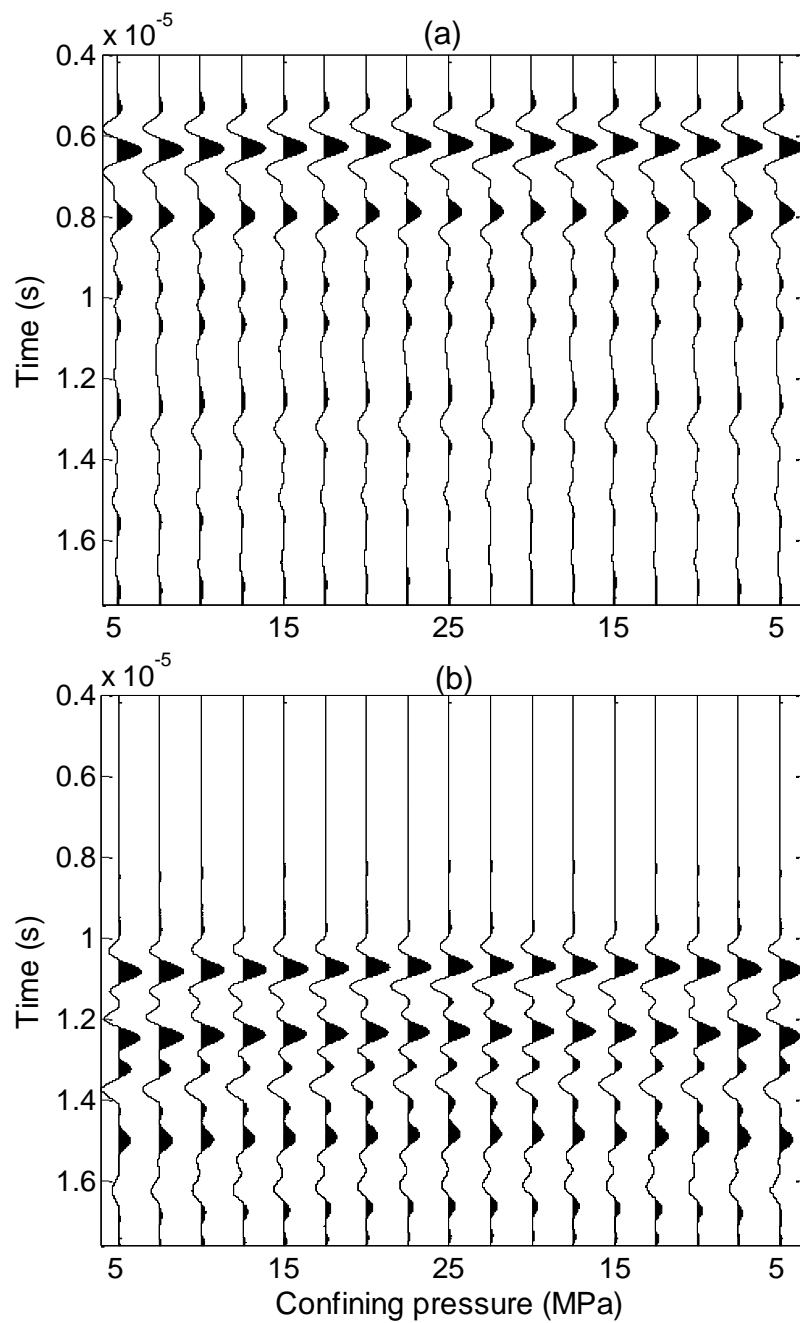


Figure 5.12: Normalized *P*-wave (a) and *S*- wave (b) waveforms for sample 7-222 from Arab formation at different confining pressure.

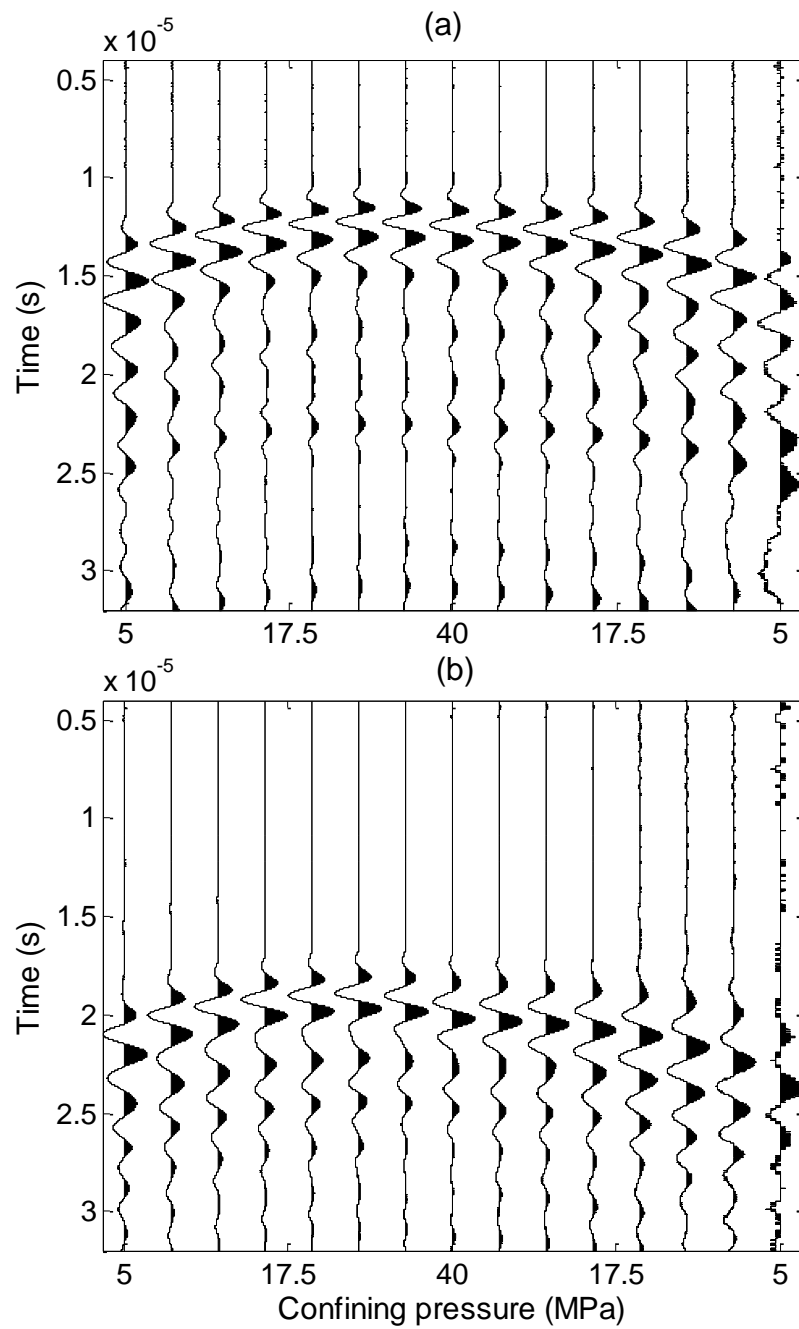


Figure 5.13: Normalized *P*-wave (a) and *S*- wave (b) waveforms for sample 3-104 from Arab formation at different confining pressure.

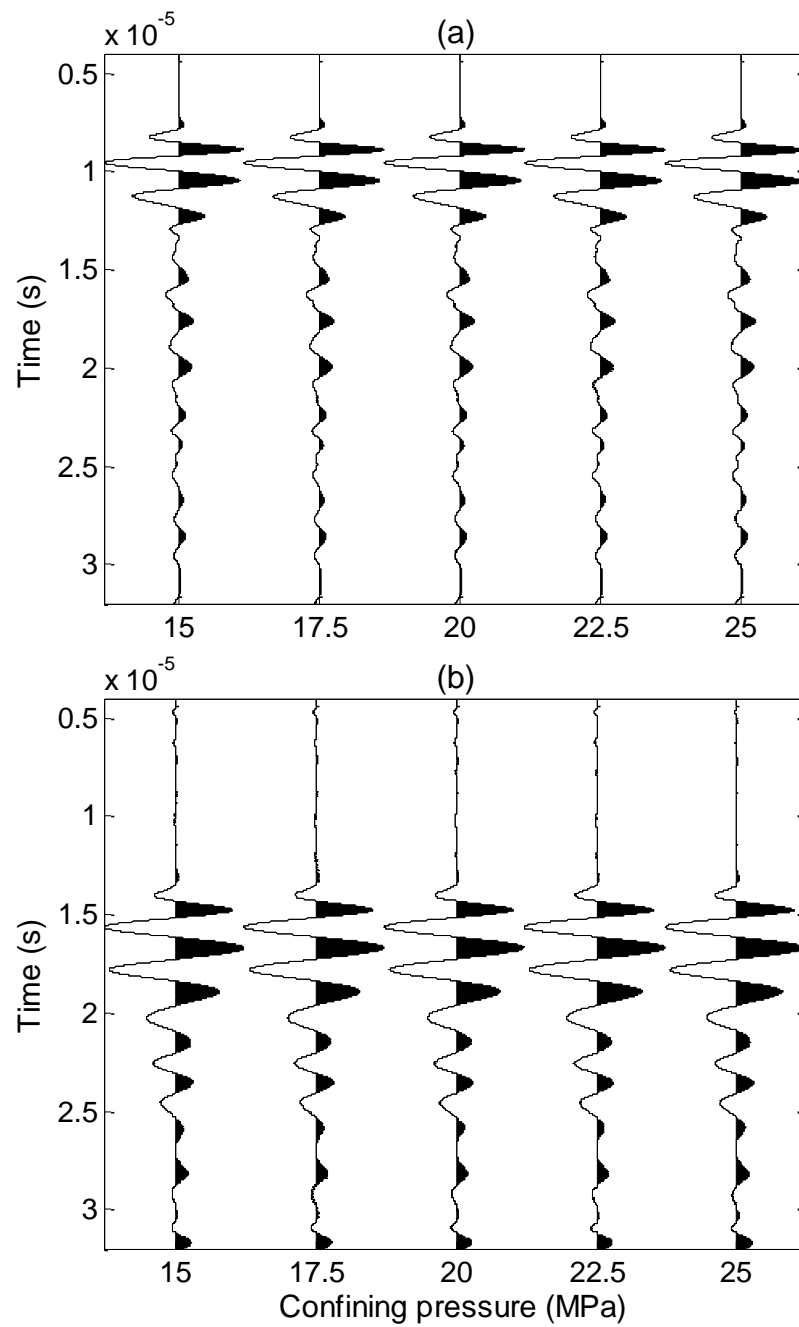


Figure 5.14: The waveform of *P*-wave (a) and *S*-wave (b) traces of the water saturated sample 8-115 at constant differential pressure (15 MPa).

5.7.2 Changes in P- and S-wave velocities with pressure

Figure 5.15 shows the effect of pressure on P- and S-wave velocities with pressure for sample 3-104. The sample has 31% porosity and permeability around 134 mD. This sample was the first sample that we measured from the group, thus the velocities were measured at two different cycles with increasing of peak pressure of 20 MPa (indicated by blue curve) and 40 MPa (indicated by red curve) under dry condition to test the level of consolidation during both pressurization and depressurization. During the first cycle a non-linear increase in both *P*- and *S*-wave velocities upon pressurization and a normal hysteresis upon depressurization. Remarkably, the velocity versus pressure curves does not show any repeatability on the second cycle and the velocities upon depressurization were lower than the velocities acquired during pressurization; suggesting that the rock have been damaged by pressurization. The figure clearly shows that the velocities start decreasing with pressure beyond 30 MPa. After removing the sample from the pressure vessel it was noticed that the sample is broken into three pieces; this behaviour discouraged carrying out the measurements beyond 25 MPa. Obviously, the results from this sample must be eliminated.

Figures 5.16 and 5.17 show the effect of pressure on *P*- and *S*-wave velocities for samples 3-90 ($\phi=34\%$) and 1-11 ($\phi=3\%$) respectively. Both samples show general increase in velocity with pressure increase. The ‘tight’ (i.e. low permeability) sample (1-11) shows less velocity variability with pressure (3% average increase in velocity) than the porous sample which shows around 20%

increase in velocity with pressure; this is due to the lack of microcracks and closing pores in the tight sample. Both samples show that the velocities readings taken during pressurization cycle are slightly lower than the velocities taken during the depressurization cycle. This velocity difference arises during depressurization, the closed microcracks and pores start to reopen, once the pressure drops beyond the critical pressure that caused their initial closure.

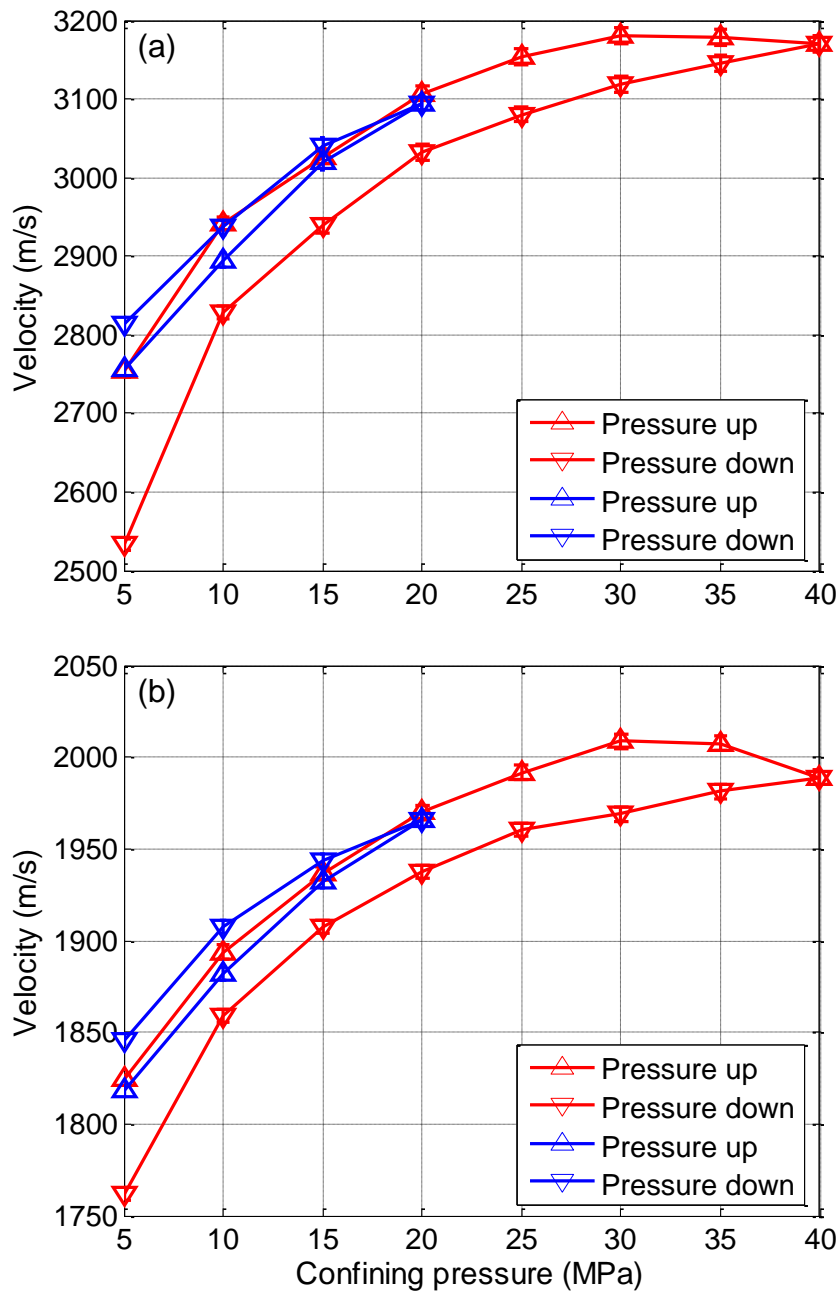


Figure 5.15: P - (a) and S -wave (b) velocities of sample 3-104 at different confining pressure showing measured on two cycles. First cycle the peak pressure equal to 20 MPa (*blue*) and the second cycle equal to 40 MPa (*red*).

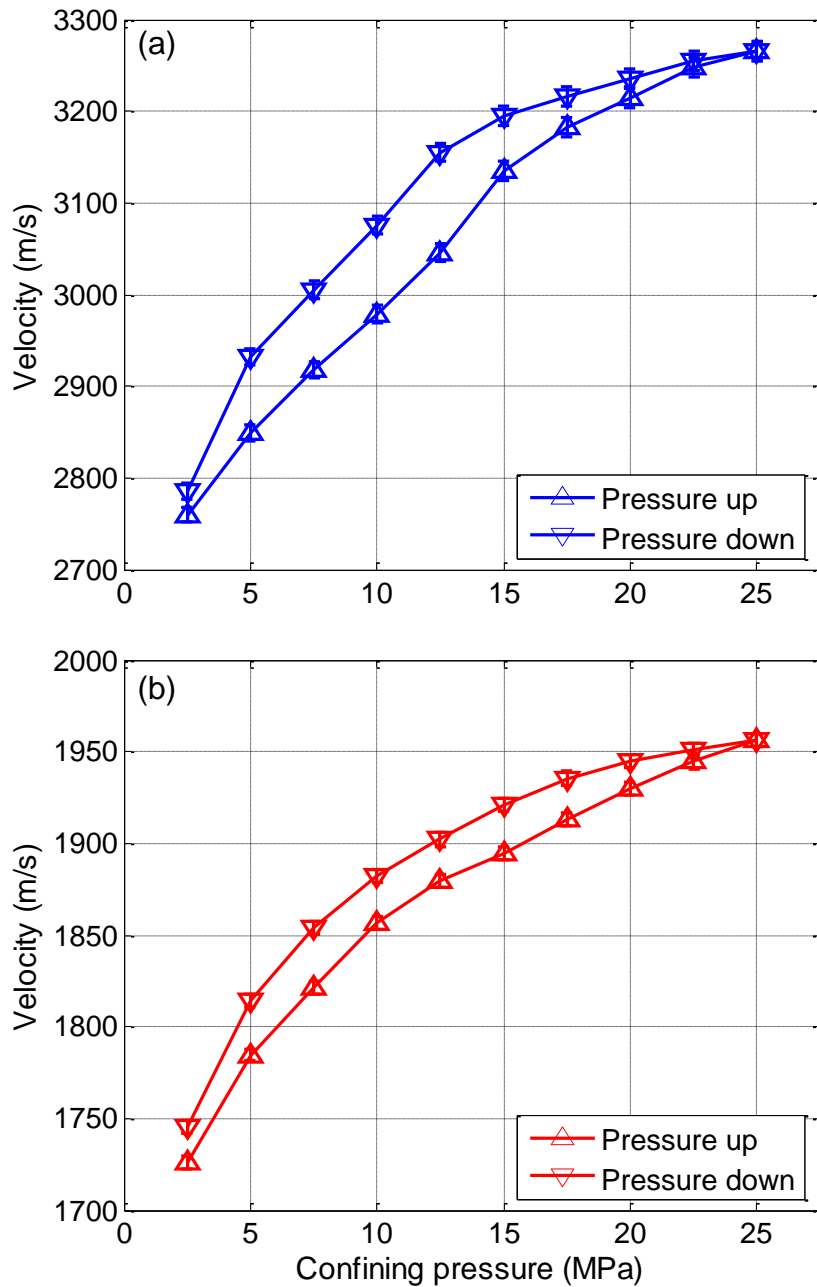


Figure 5.16: *P*- (a) and *S*-wave (b) velocities of sample 3-90 at different confining pressure showing nonlinear increase on velocities upon pressurization.

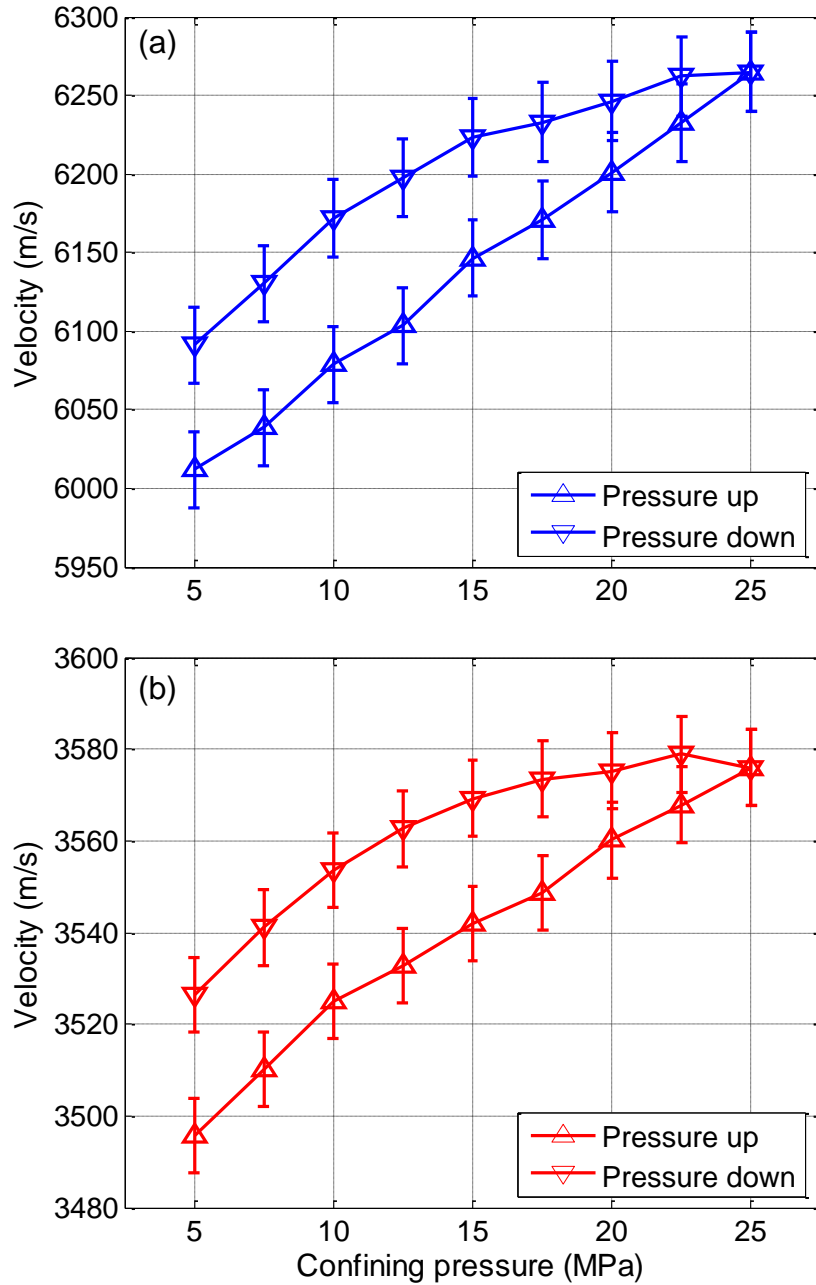


Figure 5.17: *P*- (a) and *S*-wave (b) velocities of sample 1-11 at different confining pressure showing nonlinear increase on velocities upon pressurization.

5.7.3 Effect of saturation on velocity and dynamic moduli

The bulk modulus of the sample usually increases after the sample is fully saturated with water as the pore spaces are filled with less compressible fluid (water). Although the density of the sample increases too after saturation but the bulk modulus increase is more significant and causes an increase in P-wave velocity. In contrast, S-wave velocity decreases with saturation as the fluid has no rigidity and in the absence of any fluid-solid interaction (no changes on rock shear modulus after saturation) the only factor that affects the shear velocity is the changes of density with saturation.

The effects of water saturation on P- and S-wave velocities at different pressures are shown in figures 5.18. As expected the figure shows that most of the studied samples show an increase in P-wave velocities (Figures 5.18a, c, and e) after the sample is fully saturated with water. Some samples show no changes with saturation and others even decrease with saturation which might be due to the fact that some samples have physically deformed or undergo microstructure changes (pore collapse) as a result of pressure during the dry measurements. The relative increase in velocity after saturation decreases with increasing pressure. The increase is up to 30% at 5 MPa and decrease to maximum of 9% at 25 MPa pressure. Most of the samples show S-wave velocities (Figures 5.18b, d and f) decrease after water saturation, these are mostly the samples with high to medium porosity (>14%); the relative decrease is up to 32% at 5 MPa pressure and around 16% at both 15 and 25 MPa. Some samples showed an increase up to 2% of S-wave velocity after saturation and these are the low porosity (<10%) samples. The

increase of the velocity decrease with pressure until the saturated and the dry velocities are almost equal.

As expected, all of the measured samples show an increase of rock bulk modulus after saturation, the maximum increase is up to 60% and the minimum around 2%, one sample shows less than 1% increase (Figure 5.19a, c and e). There is no strong correlation between porosity and the magnitude of the increase; however the increase of bulk modulus in high porosity samples is mostly around the average (23%). The amounts of increase in bulk modulus decrease with increasing pressure. As mentioned earlier the shear modulus of water is zero and when the sample saturated with water theoretically the rock shear modulus will not change. What is interesting, however, is that most of the low porosity samples show an increase in the rock shear modulus after water saturation (Figure 5.19b, d and f). The maximum relative increase in shear modulus after saturation is around 15%. Whereas, high porosity samples show decrease, increase and a few no changes in shear modulus. The magnitudes of increase and decrease are decreasing with increasing pressure.

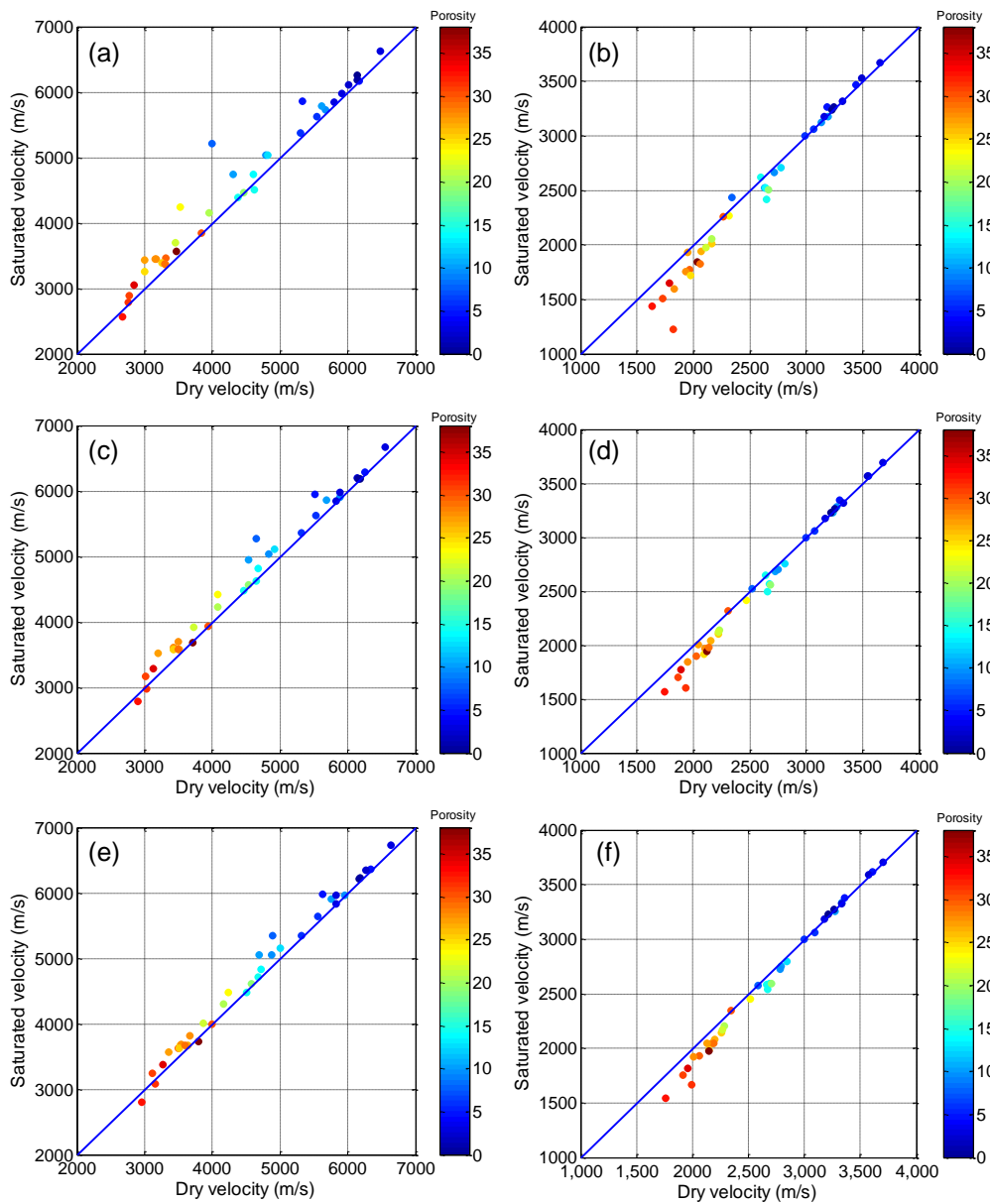


Figure 5.18: (a, c and e) Cross plots of saturated and dry P-wave velocities at 5, 15 and 25 MPa pressure respectively. (b, d and f) Cross plots of saturated and dry S-wave velocities at 5, 15 and 25 MPa pressure respectively. Velocities are color coded with porosity. The blue line represent where the two velocities are equal. Error bars are within the size of the marker.

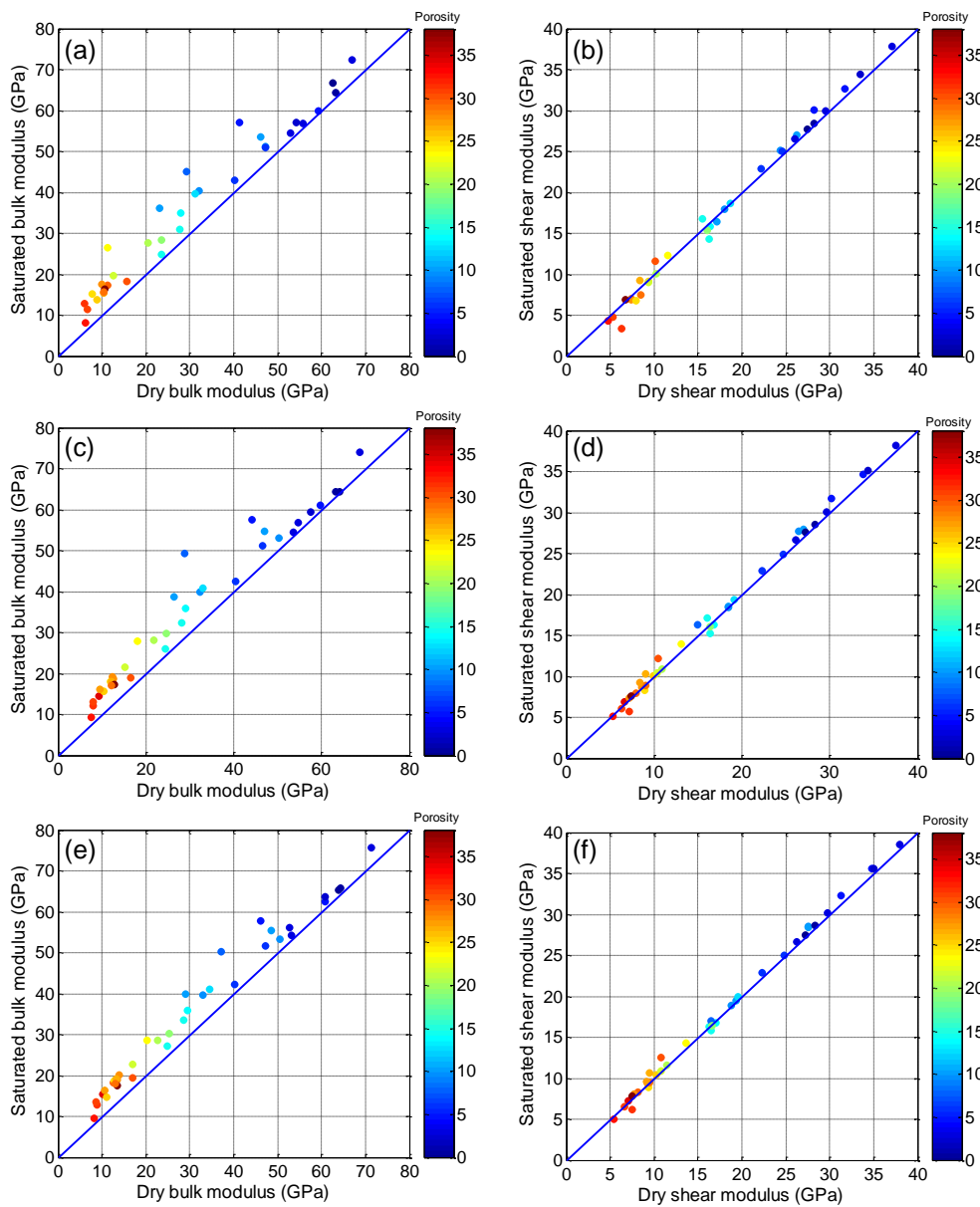


Figure 5.19: (a, c and e) Cross plots of saturated and dry bulk moduli at 5, 15 and 25 MPa pressure respectively. (b, d and f) Cross plots of saturated and dry shear moduli at 5, 15 and 25 MPa pressure respectively. Moduli are color coded with porosity. The blue line represent where the two velocities are equal. Error bars are within the size of the marker.

5.7.4 Effect of mineralogy on velocity

The mineralogy of carbonates is to a degree simple as they are formed from a relatively small number of minerals. Three minerals dominate carbonate rocks (calcite, dolomite and aragonite). Although aragonite is very common during deposition, it transforms into calcite because of its instability (i.e. meta-stable nature). The other two minerals, calcite and dolomite, make up the bulk of the carbonate deposits. Rafavich et al. (1984) and Anselmetti and Eberli (1993) showed that the influence of calcite and dolomite in the velocity are negligible and cannot be a reason for large changes in velocities at a given porosity. However, in reservoir rocks the presence of other minerals such as anhydrite is very common.

Figure 5.20 compares dry P- and S-wave velocities for four different samples. The samples differ in mineralogy and have low porosity (3-5%), the properties of these samples shown in table 5.1. Despite the similarity in porosity the velocity changes up to 1200 m/s. Sample 7-222 dolomite dominated (99%) showed the highest velocity and sample 3-05 consist of 50% anhydrite and 48% dolomite showed the lowest velocity in P- wave only. Samples 2-368 and 3-471 have mix mineralogy between calcite and dolomite showed very little difference in P-wave velocities but a remarkable difference in S-wave velocities up to 160 m/s. Sample 3-05 showed 5% changes in velocity with pressure whereas other samples showed very little change with pressure (<1%). Figure 5.21 compares dry bulk and shear moduli for the samples. Same as the velocity, the bulk and shear moduli on sample 7-222 showed the highest value and sample 3-05 has the lowest

value of bulk modulus. These figures show that presence of Anhydrite reduce both P- and S-wave velocities as anhydrite has the lowest bulk and shear moduli (Table 5.2) and mineralogy has remarkable influence in velocity. Another example will be shown later showed an influence of mineralogy in velocity.

Table 5.1: Petrological properties for sample 2-368, 3-05, 3-471 and 7-222.

Samples	2-368	3-05	3-471	7-222
Porosity (%)	3.5	5.0	3.3	3.3
Permeability (mD)	0.1	0.2	0.1	0.4
Grain density (g/cm ³)	2.83	2.87	2.74	2.82
Calcite (%)	21.5	2.0	71.5	0.0
Dolomite (%)	78	48	28	99
Anhydrite (%)	0.5	50	0.5	1.0

Table 5.2: Moduli and density of common mineral in carbonate.

Mineral	Bulk Modulus (GPa)	Bulk Modulus (GPa)	Density (g/cc)
Calcite	73.3	32	2.71
Dolomite	94.9	45.7	2.84
Anhydrite	54.9	29.2	2.96

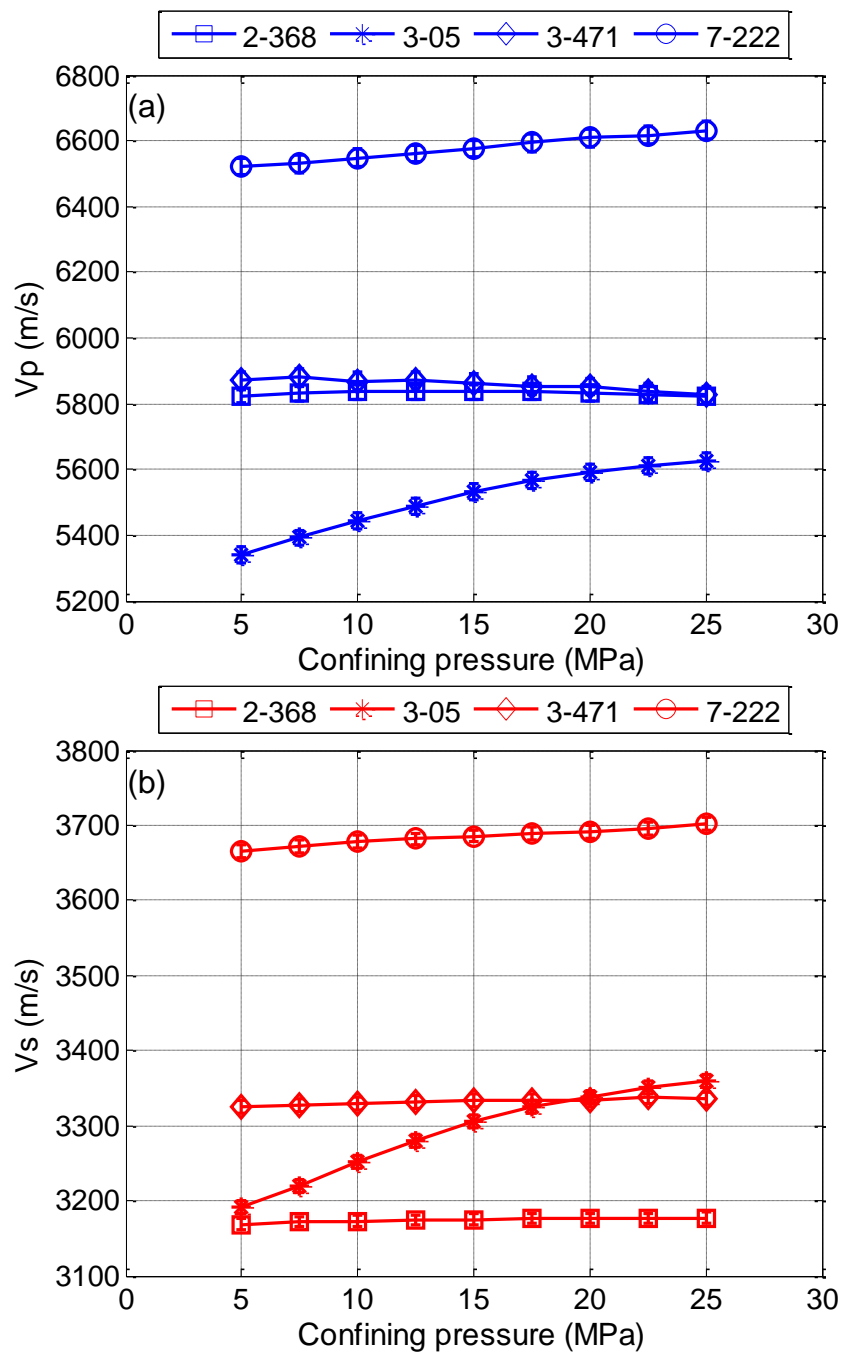


Figure 5.20: Dry P-(a) and S-(b) wave velocities for sample 2-368, 3-05, 3-471 and 7-222 at different confining pressure. Error bars are within the size of the marker.

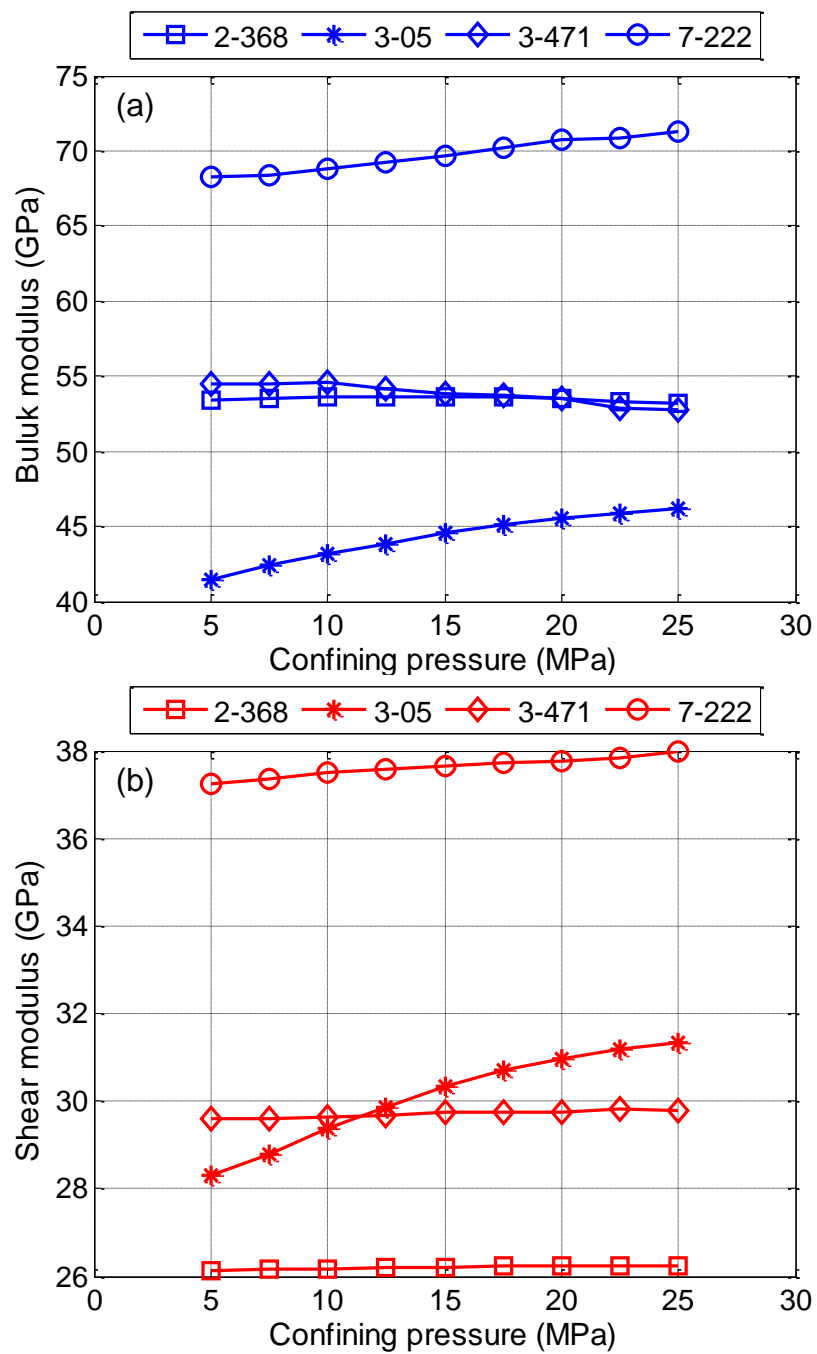


Figure 5.21: Dry bulk (a) and shear (b) moduli for sample 2-368, 3-05, 3-471 and 7-222 at different confining pressure.

5.7.5 Effect of porosity, pore type and texture in velocity

In general, P- and S-wave velocity of porous sample (i.e. rock) show an inverse correlation with porosity, velocity increases with decreasing porosity (Figure 5.22). What is interesting is that the velocities show a remarkable deviation with respect to the conventional velocity-porosity inverse relation and variability in velocity at a given porosity. Same observation was reported by Anselmetti and Eberli (1993), Assefa et al. (2003), and Baechle et al. (2005) which they attributed to the existence of different pore types.

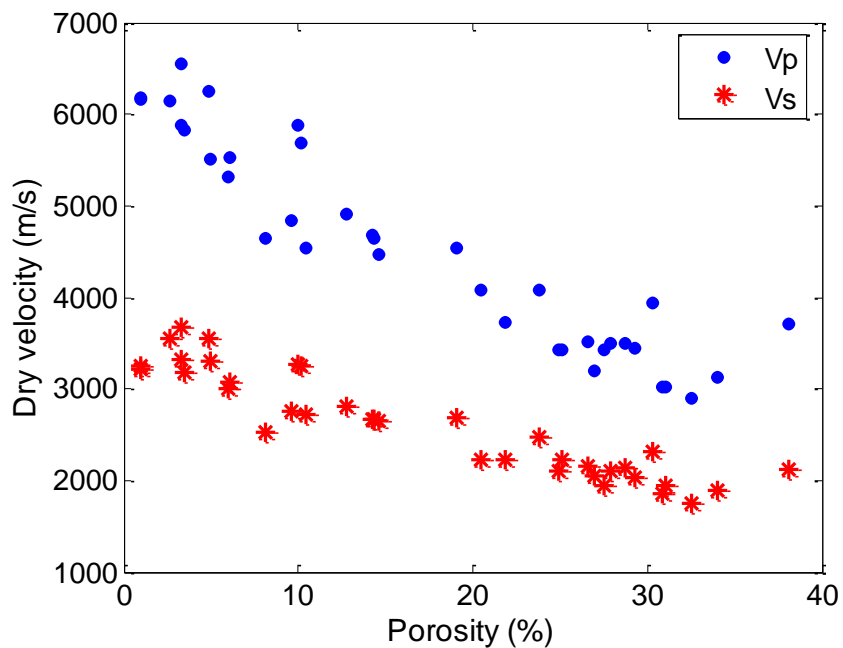


Figure 5.22: Velocity-porosity cross plot for dry P- and S-wave velocities.

Observe the inverse velocity-porosity relation.

For example near 10% porosity we observed variations of about 1700 m/s in P-wave and 1000 m/s in S-wave velocities (figure 5.23). The samples differ in

mineralogy and lithology (Table 5.3). First observation is that dolomite dominant samples (4-151, 3-429) have the highest velocities and then velocities decrease with the decrease of dolomite content. The differences in velocity between the two dolomite samples are 103 m/s at 5 MPa and 200 m/s at 25 MPa. These differences can be attributed to the differences in pore size difference between the two samples. The porosity of sample 4-151 classified in chapter 3 within the micropore samples and has higher velocities than sample 3-429, which was classified as a macropore sample. The difference in the average velocity between dolomite dominated samples and calcite dominated samples is 1000 m/s at 25 MPa confining pressure, suggesting the influence of mineralogy in velocity. Figure 5.24 shows theoretical end-member P- and S-wave velocities for isotropic, non-porous materials made of calcite and dolomite (figure 5.24a), calcite and anhydrite (figure 5.24b) and dolomite and anhydrite (figure 5.24c) calculated using Voigt (1928) and Reuss (1929) averages. The figures show that velocities do changes with mineralogy. The calcite dominated sample (1-304) has the slowest velocity compared to other calcite samples and the velocity dramatically increased with pressure by 880 m/s. The three calcite samples differ in texture and pore size distribution. The change in velocity with pressure in sample 2-383 is 83 m/s and in sample 4-09 is 350 m/s. This behaviour show a positive correlation with pore size distribution, in which the bi-model pore size sample (1-304) showed high velocity changes with pressure, and the micro porosity sample (2-383) showed the smallest change. Another remarkable observation is that S-wave velocities behave differently than the P-wave.

Another example that shows a deviation from the velocity-porosity inverse relation is the comparison between samples 1-132 and 2-33. Although, that sample 1-132 has high porosity (around 38% and sample 1-132 is 31%) but the velocity of sample 1-132 is higher by 810 m/s than sample 2-33 (figure 5.25). Sample 1-132 is constituted of two area boundstone and oolitic-peloidal grainstone. In the grainstone area the ooids and peloids are roughly equally present, however, the ooids grains are larger (0.5 – 1.0 mm), whereas the peloids are much smaller (0.1 – 0.25mm) (figure 5.26). Mercury intrusion curve shows that the dominant pore size is around 50 μm and small amount of mercury intruded in pore with size around 0.1 μm . Sample 2-33 is ooid grainstone, seventy percent of the constituent grains are oolites and about one third of the grains are skeletal (figure 5.27). The dominated pore size is around 20 μm . The differences in texture between the two samples have an influence on the stiffness of the sample. The boundstone in sample 1-132 is formed from sediments bound together during deposition producing close system. The boundstone area in this sample is a stromatoporid which formed a supported framework. The boundstone area and the absence of skeletal grains type in sample 1-132 increased the stiffness of the sample. In contrast, the existence of skeletal grains in sample 2-33 produce softer rock frame. As seen in the SEM images (figure 5.27 d and e) of this sample the skeletal grains are microporous which make the grains look a lot like a sponge which produce a soft texture.

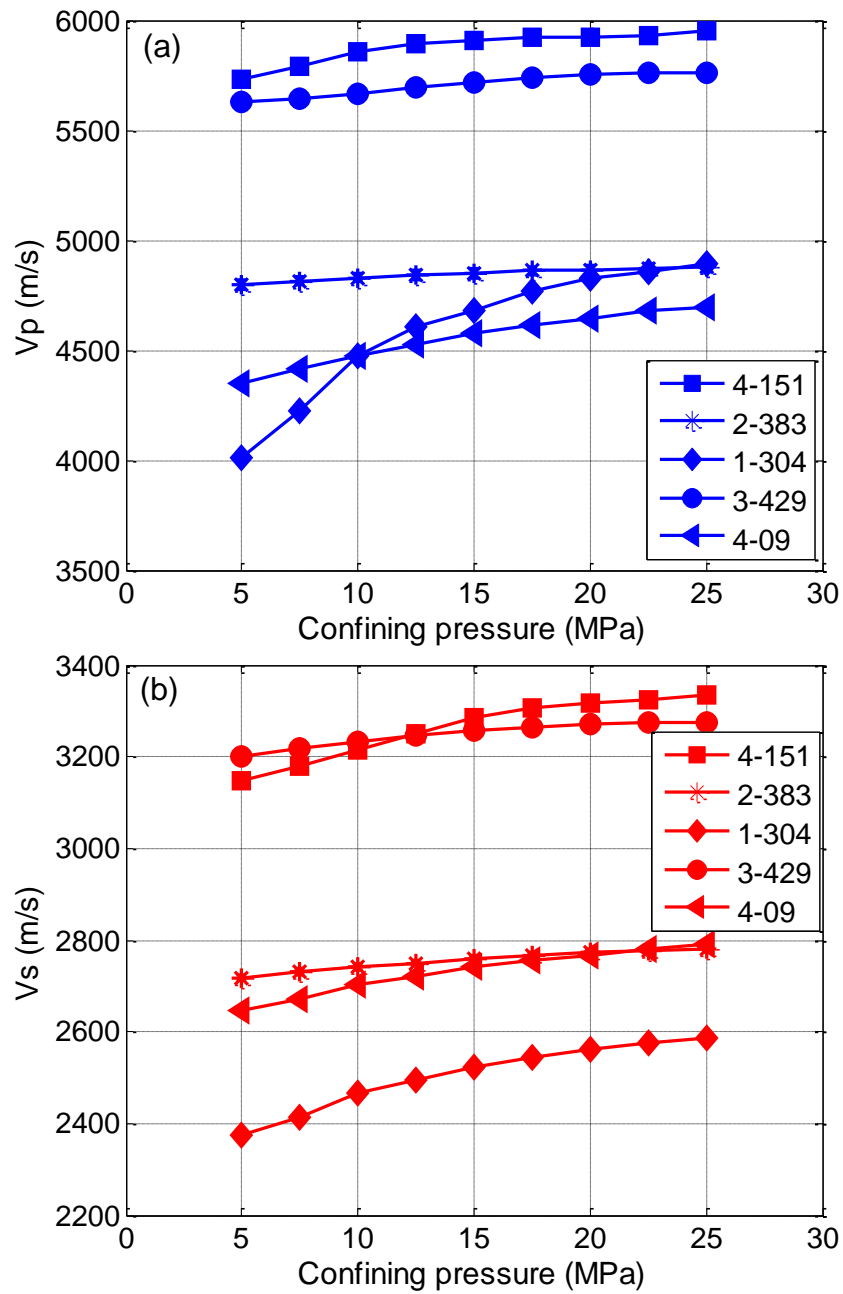


Figure 5.23: Dry P-(a) and S-(b) wave velocities for sample 4-151, 3-429, 2-383, 4-09 and 1-304 at different confining pressure. Error bars are within the size of the marker.

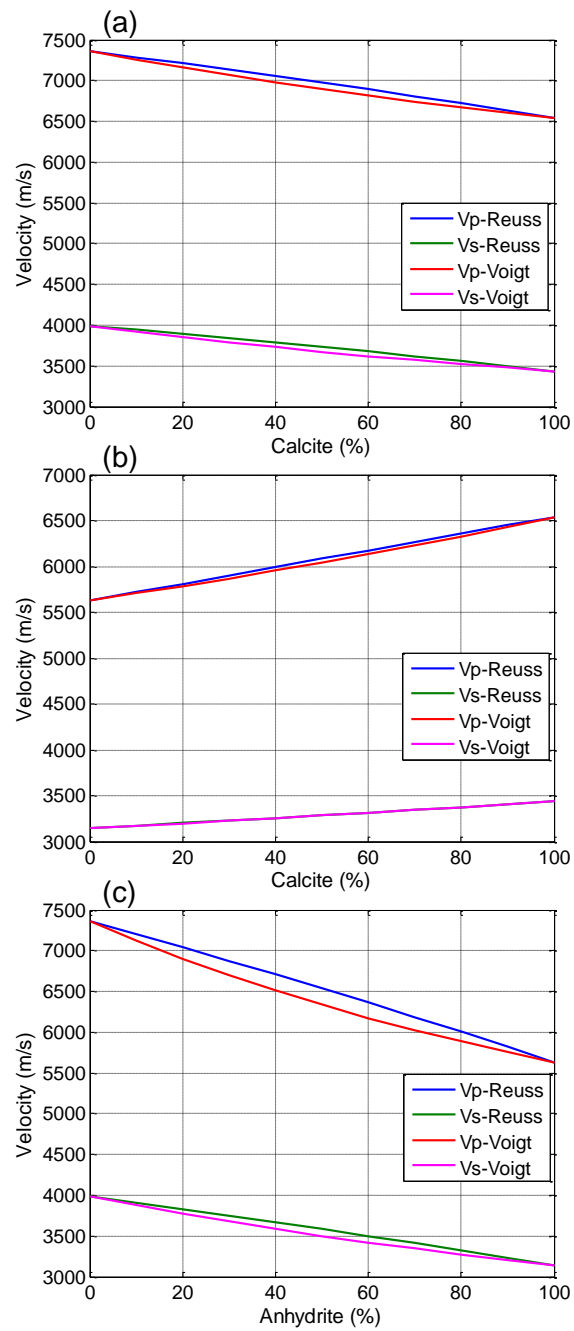


Figure 5.24: P- and S-wave velocities for non-porous material made of calcite and dolomite (a), calcite and anhydrite (b) and dolomite and anhydrite (c) calculated using Voigt (1928) and Reuss (1929) averages.

Table 5.3: Petrological properties for 5 samples.

Sample	4-151	3-429	2-383	4-09	1-304
Calcite (%)	6.0	0.0	70	92	99
Dolomite (%)	94	100	30	2.0	1.0
Anhydrite (%)	0.0	0.0	0.0	6.0	0.0
Lithology	NFP ¹ Dolomite	NFP ¹ Dolomite	Wackstone	Grainstone	Wackstone
Dominant pore size	Micro	Macro	Micro	Macro	Bi-model

¹ Non fabric preserved.

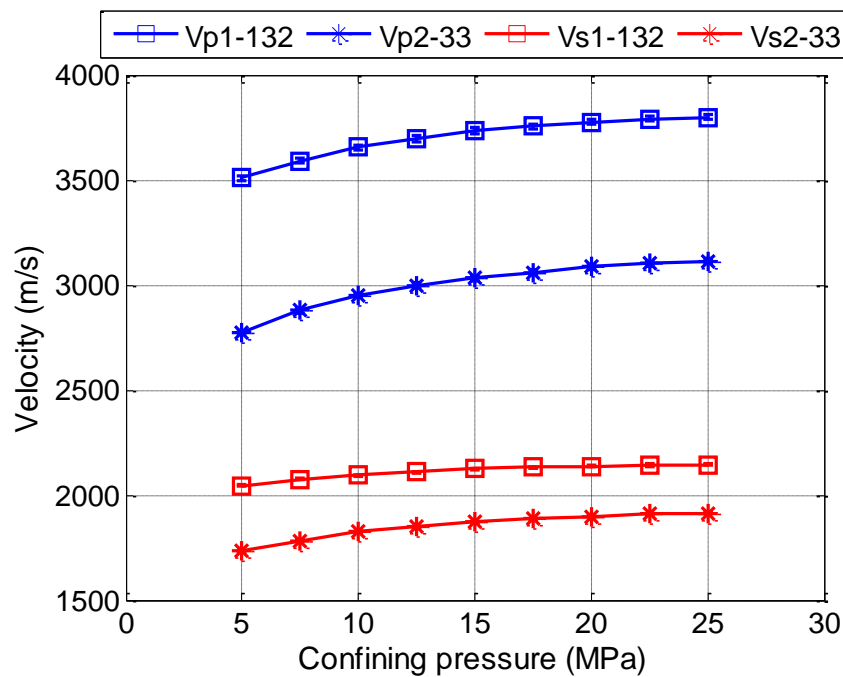


Figure 5.25: Dry P- (*blue*) and S- (*red*) wave velocities at different pressure for sample 2-33 and 1-132. Both P- and S-wave velocities for sample 1-132 ($\phi=38\%$) is higher than sample 2-33 ($\phi=31\%$). Error bars are within the size of the marker.

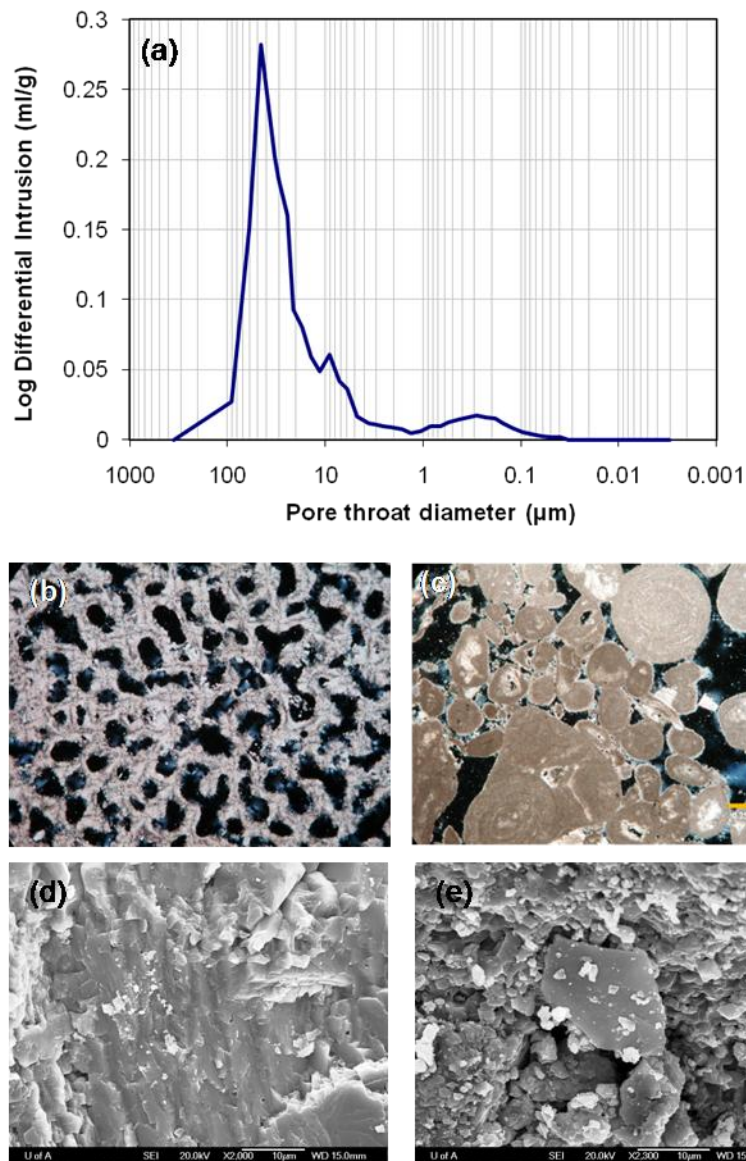


Figure 5.26: (a) Mercury intrusion curve, (b) thin section of boundstone area, (c) thin section of peloid-oolit grainstone area, (d) higher magnification view of boundstone (SEM) and (e) higher magnification view of grainstone area of sample 1-132. In thin section porosity is filled by blue-dyed epoxy.

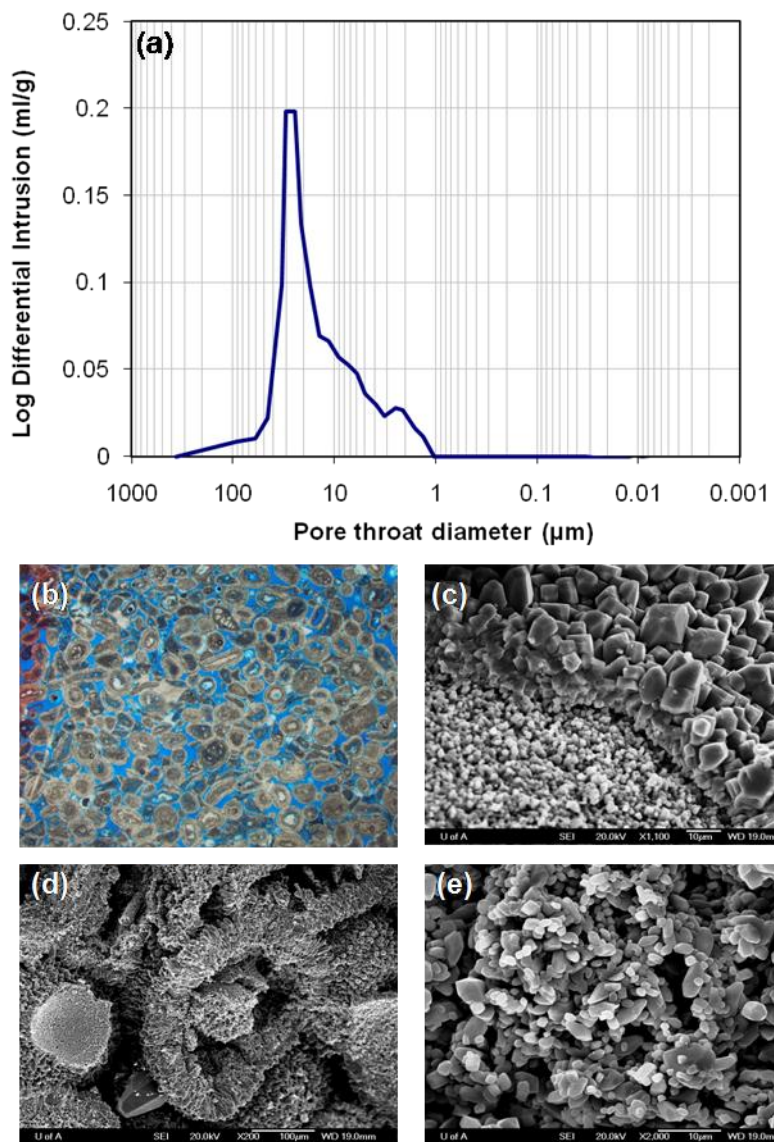


Figure 5.27: (a) Mercury intrusion curve, (b) thin section showing oolites and skeletal grains, (c) higher magnification SEM view of oolite grain, (d) higher magnification view of skeletal grain (SEM) and (e) higher magnification view inside skeletal grain of sample 2-33. In thin section porosity is filled by blue-dyed epoxy.

5.8 Conclusions

This chapter showed a detailed description of the experimental setup and the procedures that were conducted, to measure the ultrasonic velocity and the strain. For velocity measurements, the method that used to build the transducer and the acquisition system was shown. The velocity error analysis was calculated and found to be around 0.4%. The strain gauge technique was described and the use of the Wheatstone bridge to measure the small changes in resistance due to the strain was shown. A standard sample (fused quartz) is used to correct for the pressure effects on the strain gauges. The experimental procedure used in this project allows for simultaneous measurements of the P- and S-wave velocity as well as the quasi static strain measurements.

Examples of the effect of pressure, saturation, porosity, pore size and texture in velocity were presented. The initial velocity measurement conducted on one of high porosity samples to measure the strength of the sample. It shows that these carbonate rocks are very soft and the sample were physically deformed at pressure beyond 30 MPa. P- and S-wave velocities generally increase with pressure. As expected P-wave velocity increase after the sample is fully saturated with water and S-wave velocity decrease and increase with saturation. Shear modulus in most of the sample show an increase up to 15%. The presence of anhydrite mineral in the sample may decrease the velocity. The samples satisfied the conventional velocity-porosity relation with a remarkable deviation and variability in velocity at a given porosity. Texture of the sample may produce soft or stiff framework. The microporous grain in the skeletal and oolite grains seems

to produce a soft material which in turn increases the compressibility and decrease velocity of the sample. Similarly, Baechle et al. (2009) observed shear modulus weakening in samples with high amount of microporosity. In contrast with other studies, we observed velocity changes with mineralogy, velocity of dolomite dominated samples are higher than those with calcite dominated. Few samples show different behaviour in S-wave velocity from the P-wave velocities which might suggest that the induced deformation that produced by the passage of waves have influence the bulk and shear moduli differently.

Chapter 6

Fluid Saturated Ultrasonic Velocities in Carbonate Rocks

6.1 Introduction

Fluid saturation is one of the important factors that influence elastic properties of rocks. It is well documented that the seismic velocities of saturated rocks show significant changes with the wave frequency (e.g. Schmitt, 1999; Batzle et al., 2006; Winkler, 1983). Velocities of dry rock are usually assumed to be independent of frequency. Seismic velocities are measured over a wide range of frequencies from seismic (10-100 Hz) through sonic (~10 kHz to 20 kHz) up to ultrasonic (0.1-1 MHz); therefore corrections for the frequency dependence, so-called dispersion, are very important for an accurate comparison of the velocities acquired from different techniques.

Regardless of the frequency, the P-wave velocities generally increase and the S-wave velocities decrease upon complete saturation. This increase in P-wave velocity due to the changes of pore fluid bulk modulus from gas in case of the dry measurements to water in case of the water saturation measurements. The shear modulus of both water and gas are equal to zero, so the decrease of S-wave velocity is due to the increase of the overall bulk density of the porous rock upon saturation.

In general dispersion is manifest as an increase in velocity of the saturated rock with frequency. There are several theoretical models tried to explain the velocity dispersion of seismic waves in saturated rocks, but the primary cause of velocity dispersion is the interaction between the pore fluid and solid frame. Heuristically, the passage of longitudinal seismic wave globally induces pore pressure that resists pore compression. At low frequency this induced pressure has enough time to equilibrate due to fluid flow within the medium and will not cause any resistance to the compression of the pore. At high frequencies, pore pressure does not have enough time to equilibrate. Thus a resistance to pore compression will be produced, which in turn makes the rock stiffer (i.e., the moduli greater).

There are two popular fluid-solid interaction mechanisms that can describe the behaviour of the unrelaxed pressure: the global flow mechanism (Biot, 1956a, 1956b) and local or squirt-flow mechanism (e.g., Mavko and Jizba, 1991; Nie et al., 2008; Ba, et al., 2008; Diallo et al., 2003; Diallo and Appel, 2000; Dvorkin et al., 1994; Winkler, 1986; Oconnell and Budiansky, 1977; Oconnell and Budiansky, 1977). The Biot mechanism (global flow) generates by the

participation of the fluid in the solid motion through viscous friction and inertial coupling generally between the fluid and solid in the porous material. In contrast, squirt flow occurs at the pore scale when the fluid is squeezed in and out of thin pores (compliant soft pores) into more equant (stiffer) pores due to changes in pressure during passage of the wave. These soft pores will be isolated from the pore network and each other, which results in elastic moduli increase.

In this chapter the water saturated P- and S-wave velocities were measured and compared with those calculated using Gassmann's (1951) low frequency formula (Eqns. 4.17 and 4.18), Biot's (1956b) high frequency estimate as approximated by Geertsma and Smit (1961) of Eqns. 6.1 and 6.2, and what we refer to here as the squirt-Gassmann and squirt-Biot estimates that employ the bulk modulus of Mavko and Jizba (1991), as given by Eqns. 6.3 and 6.4. The predicted water saturated velocities were calculated using the dry velocity measurements. All the models used in this study assume full water saturation for the sample.

It is difficult to know if a rock is fully saturated, and most authors simply make this assumption after taking precautions during sample preparation. Rarely, however, is any additional evidence given support this contention. The same problem exists in these experiments and in order to satisfy this assumption a new quality control procedure was developed. After saturation the velocity was measured over pressures from 5 MPa to 25 MPa then the measurements carried out at constant differential pressure equal to 15 MPa. To keep a constant differential pressure the confining and pore pressure were increased with the same

rate. The chosen samples for models and observed comparison showed very little increase in the velocities within the error at constant differential pressure (figure 6.1). Changing velocity with constant effective pressure is taken to indicate saturation is not achieved, then some portion of the pore space must be filled with gas (likely water vapour as the pore space was initially under vacuum prior to introduction of the water). This vapour is highly compressible relative to the liquid and hence as the pore pressure is increased, the overall compressibility of the vapour-water mixture will also change, and this will also result in a variation of the overall velocity of the partially saturated rock. A contrasting example in which the velocity changes substantially at constant effective pressure is given in figure 6.1b and c. While this latter behaviour may also be indicative of other processes than partial vapour-water saturation (e.g. chemical reactions at the pore surfaces), it does lend confidence to selecting the set of 'high-quality' measurements that can be best compared to the various theories. Only seventeen such samples fit this criterion and are hence used in the analysis to follow.

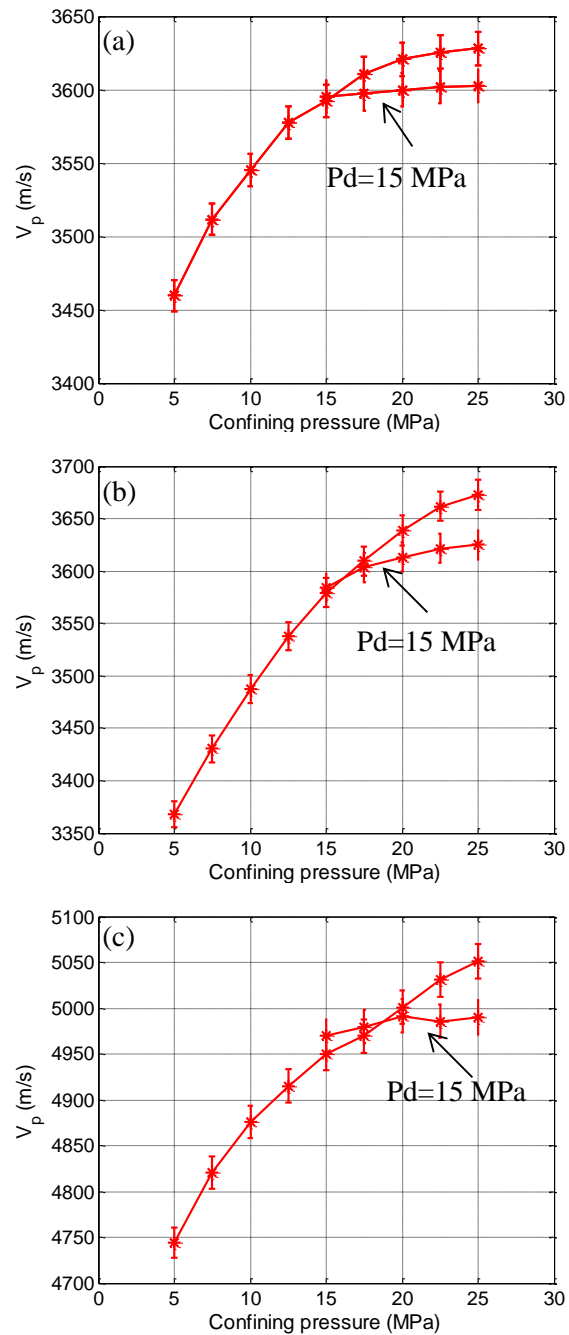


Figure 6.1: P-wave velocity as a function of confining and differential pressure for water saturated samples 4-55 (a), 8-23 (b) and 4-09 (c) (differential pressure equal to 15 MPa).

6.2 Velocity models in fully saturated rock

Biot (1956) developed a model to predict the frequency dependence of the saturated velocities due to the fluid-solid mechanical interaction. This model calculates the saturated velocity from the dry rock bulk and shear moduli, mineral bulk modulus, fluid bulk modulus, saturated density, porosity, fluid viscosity and the tortuosity. The tortuosity is a measure of the deviation of pore structure transit length from that for a straight tube; and its minimum value is 1 for perfect cylindrical pore. At low frequency Biot theory reduces to Gassmann's relations. In this study the high frequency limit of P-wave velocities were calculated using the Geertsma and Smit (1961) approximation:

$$V_p = \left\{ \frac{1}{\rho_0(1-\phi) + \phi\rho_{fl}(1-\alpha^{-1})} \left[\left(K_{fr} + \frac{4}{3}\mu_{fr} \right) + \frac{\phi \frac{\rho_b}{\rho_{fl}} \alpha^{-1} + \left(1 - \frac{K_{fr}}{K_m} \right) \left(1 - \frac{K_{fr}}{K_m} - 2\phi\alpha^{-1} \right)}{\left(1 - \frac{K_{fr}}{K_m} - \phi \right) \frac{1}{K_m} + \frac{\phi}{K_{fl}}} \right] \right\}^{1/2}, \quad (6.1)$$

$$V_s = \left(\frac{\mu_{fr}}{\rho_b - \phi\rho_{fl}\alpha^{-1}} \right), \quad (6.2)$$

where V_p and V_s are P- and S-wave velocities respectively, ρ_0 , ρ_{fl} and ρ_b are mineral, fluid and saturated bulk densities respectively, K_{fr} , K_m and K_{fl} are rock frame, mineral and fluid bulk moduli respectively, μ_{fr} is rock frame shear modulus, α is the tortuosity and ϕ is the porosity. The frame bulk K_{fr} and shear μ_{fr} moduli can be either the dry frame moduli obtained from ultrasonic velocity

measurements or the predicted unrelaxed moduli using Mavko-Jizba equations discussed shortly.

This approximation predicts velocities around 3-6% higher than Biot's (1956b) actual high frequency limit (Mavko et al., 1998) and hence must be considered an upper bound to the Biot value. Calculating the full Biot high frequency values requires that 17 different physical parameters be found. This is not easily done (see for example Bouzidi and Schmitt, 2009) and remains a goal for the future; and hence the simpler Geertsma-Smit expression above (Eqns. 6.1 and 6.2) is used here to bound the results.

In contrast, Mavko and Jizba (1991) developed a model that assumes squirt flow effects are active in rocks. In the model they defined an expression called unrelaxed frame bulk K_{uf} and shear μ_{uf} moduli based on the assumption that at high frequency the induced pore pressure occurs only in soft pores and the frame rock in this case is partially saturated. These expressions are:

$$\frac{1}{K_{uf}} \approx \frac{1}{K_h} + \left(\frac{1}{K_{fl}} - \frac{1}{K_m} \right) \phi_{soft} \quad (6.3)$$

$$\frac{1}{\mu_{uf}} - \frac{1}{\mu_{dry}} = \frac{4}{15} \left(\frac{1}{K_{uf}} - \frac{1}{K_{dry}} \right), \quad (6.4)$$

where K_{dry} and μ_{dry} are bulk and shear moduli of the dry rock, respectively, K_m and K_{fl} are fluid and mineral bulk moduli, respectively, K_h is dry bulk modulus at higher pressure and ϕ_{soft} is the 'soft' porosity.

Their model assumes that all soft pores will be closed at high pressure, so the unrelaxed bulk modulus is calculated from the measured high pressure dry bulk modulus plus a small correction for the bulk modulus of the fluid that exist in soft pores. The unrelaxed bulk modulus is then assumed to represent K dry and then substituted in both the Gassmann and the Geertsma-Smit equations to calculate the saturated bulk and shear moduli. We refer to these models as the squirt-Gassmann and the squirt-Biot respectively.

For each of the selected samples the Gassmann and Biot models were used to calculate the saturated velocities based on the dry moduli. The unrelaxed bulk and shear moduli were calculated using Mavko-Jizba models based on dry bulk and shear moduli obtained from dry velocity measurements and soft porosity as a function of pressure. The soft porosity is basically the difference between the total porosity and the linear extrapolation of high pressure trend (Mavko and Jizba, 1991). The porosity as a function of pressure was obtained using the measured change of the sample volume with pressure from the volumetric strain measurements (Schmitt and Li, 1995). Then the unrelaxed frame bulk and shear moduli were substituted in Gassmann and Biot models to compute squirt-Gassmann and squirt-Biot velocity predictions. Four model predictions are computed and compared: low frequency Gassmann, high frequency Biot, squirt-Gassmann and squirt-Biot.

6.3 Modeling results and discussions

In general P - and S -wave velocities predicted from the squirt-Biot model show a slight increase relative to the Biot model alone. Similarly, for S -wave velocities the squirt-Gassmann predictions slightly exceed the Gassmann predictions, whereas for P -wave few samples showed that Gassmann predicted velocities are higher than the squirt-Gassmann model. Figure 6.2 and 6.3 illustrate these observations for P -wave and S -wave velocities respectively.

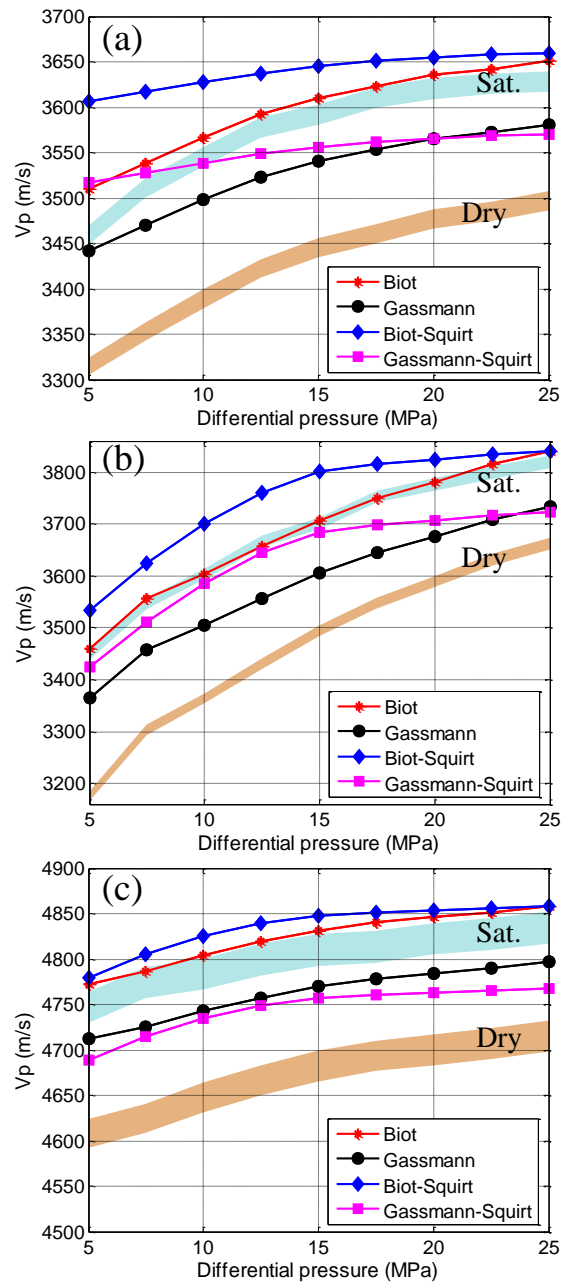


Figure 6.2: The observed dry (brown) and saturated (blue) velocities and model predictions for P-wave velocities of three different samples, (a) sample 4-55, (b) sample 4-97 and (c) sample 4-326.

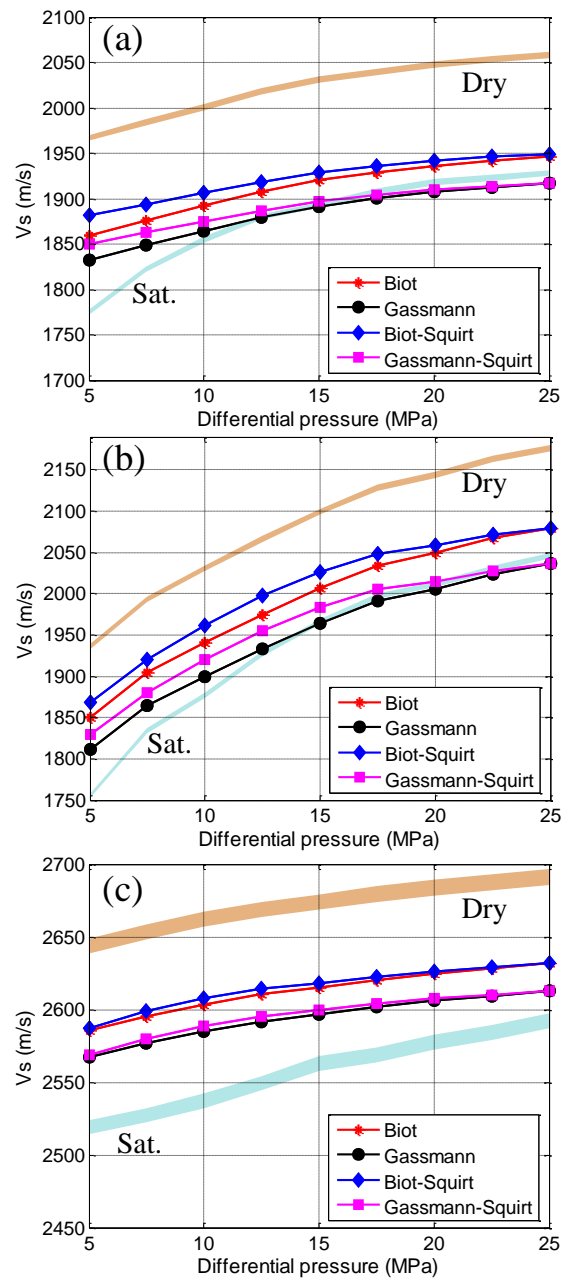


Figure 6.3: The observed dry (brown) and saturated (blue) velocities and model predictions for S-wave velocities of three different samples, (a) sample 4-55, (b) sample 4-97 and (c) sample 4-326.

6.3.1 P-wave velocities

The squirt-Biot model predictions are generally higher than the observed water saturated velocities; however two samples were showing agreements at low pressure and over-predicted at high pressure. From the comparison of the Biot and Gassmann model predictions with the measured water saturated velocities two different behaviours can be observed:

- Group one: Biot-predicted velocities are in agreement with the observed water saturated velocities, whereas the Gassmann formula always under predicts the velocities (figure 6.4),
- Group two: Biot and Gassmann models over-predict the saturated velocities (figure 6.5) and

The influence of mineral compositions can be neglected, and felt that it cannot be a reason for the different behaviour in the modeled velocities as all the samples are strongly calcite dominated (more than 95%). In order to better understand these different behaviours, thin section, scanning electron microscope (SEM) and Mercury Intrusion data are used to study the micro structure of the samples in each group. In group one, thin-section photomicrograph of sample 4-55 shows that the interparticle pore (pores between grains) is the dominant pore type with less than 15% intraparticle pores (figure 6.6a). Mercury intrusion data for the same sample (figure 6.6b) show the pore throat size distribution of the sample, it reveals that the dominant pore throat size is around 25 μm and there is little further contribution to the porosity by the micro-pores. SEM examination of the same sample shows microporous cements that occur between cement crystals

(figure 6.7). Samples that fall into this group showed a lack of intraparticle pores and less than 15% microporosity. Sample 2-33 is an example of group two with porosity around 30%. Thin-section photomicrography of the sample shows that almost half of this porosity is contributed by macropores, macro-porosity is 16% while the remaining comes from micro-pore (14%). The macropores are interparticle more than 60% and 40% is intraparticle (figure 6.8a). Mercury intrusion data also suggest that wide range of pores with dimensions of 60-1 micron exist (figure 6.8b). SEM photographs reveal that a variety of skeletal and non-skeletal grain types are microporous. The amount of micro-porosity within microporous grains is sometimes so high that the grains looks like a sponge, that produces a soft rock frame (figure 6.9). Almost all the samples in this group have more than 30% intraparticle porosity and the great contribution of microporous grains is very common.

The conclusion drawn from these result is that, as mentioned earlier the squirt predictions mostly over-predict the saturated velocities and suggest that the squirt mechanism in all of the studied samples is not active enough to produce dispersion. In group one, the Biot predictions reasonably match the measured velocities, and this suggests, the Biot global flow is the principle dispersion mechanism in these samples.

The over-predictions of Gassmann and Biot models in group two samples possibly have an experimental cause: that most likely the different behaviour of the dry and saturated cycles in which the first cycle might create inelastic deformation to the samples, as a mechanical break observed in SEM images as

illustrated in figure 6.9 (a). This conclusion is supported by the sponge like grains attributed to the samples in this group that discussed earlier.

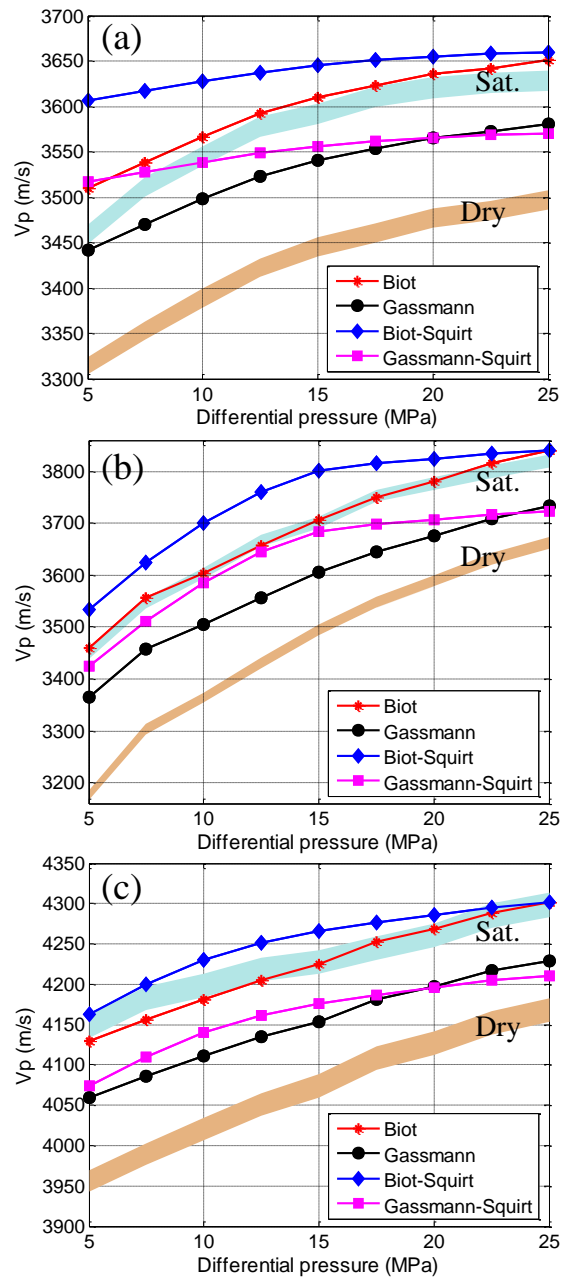


Figure 6.4: The observed dry (brown) and saturated (blue) velocities and model predictions for P-wave velocities of three samples from group one, (a) sample 4-55, (b) sample 4-97 and (c) sample 1-288.

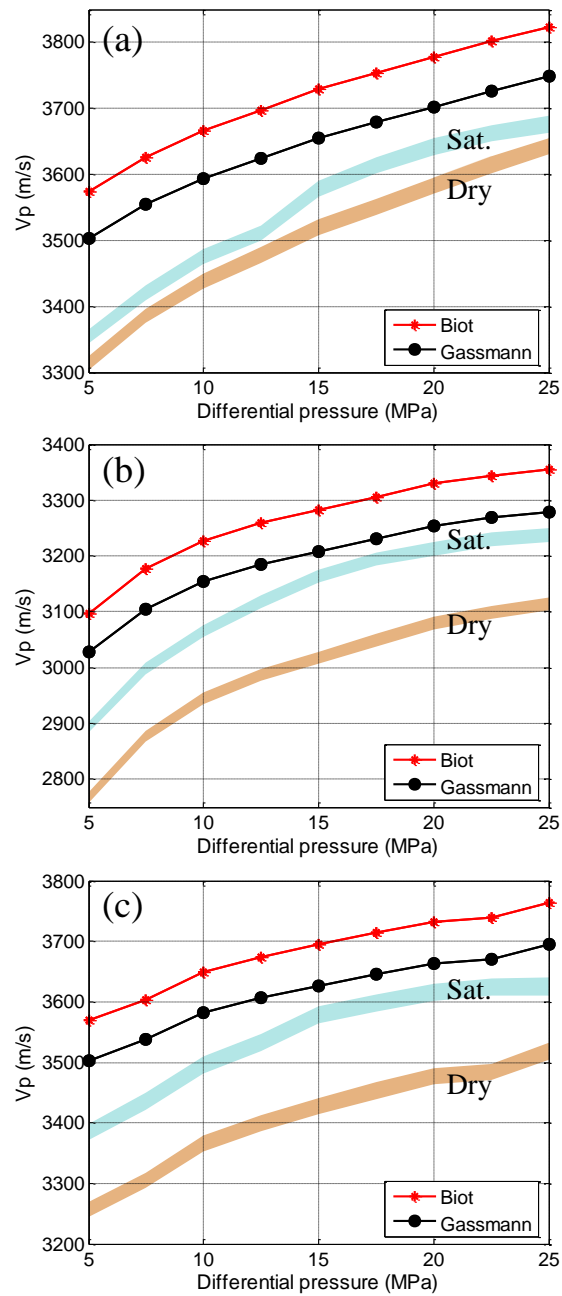


Figure 6.5: The observed dry (brown) and saturated (blue) velocities and model predictions for P-wave velocities of three samples from group two, (a) sample 2-160, (b) sample 2-33 and (c) sample 2-131.

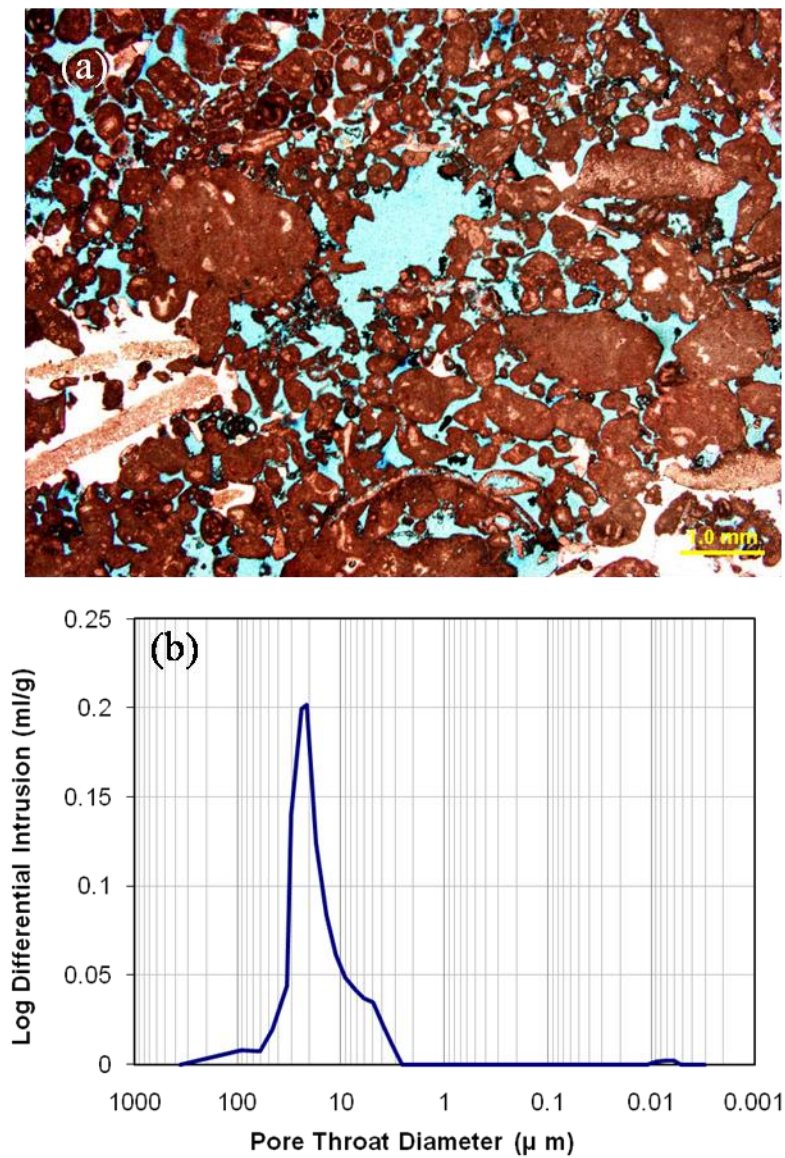


Figure 6.6: (a) Thin-section photomicrography of sample 4-55, the pores are filled by blue-dyed epoxy and calcite stained red, others are unstained. (b) Pore throat size distribution plot for sample 4-55 shows the dominant pore throat size (Peak) is around 25 μm and the smallest pore throat size around 2 μm .

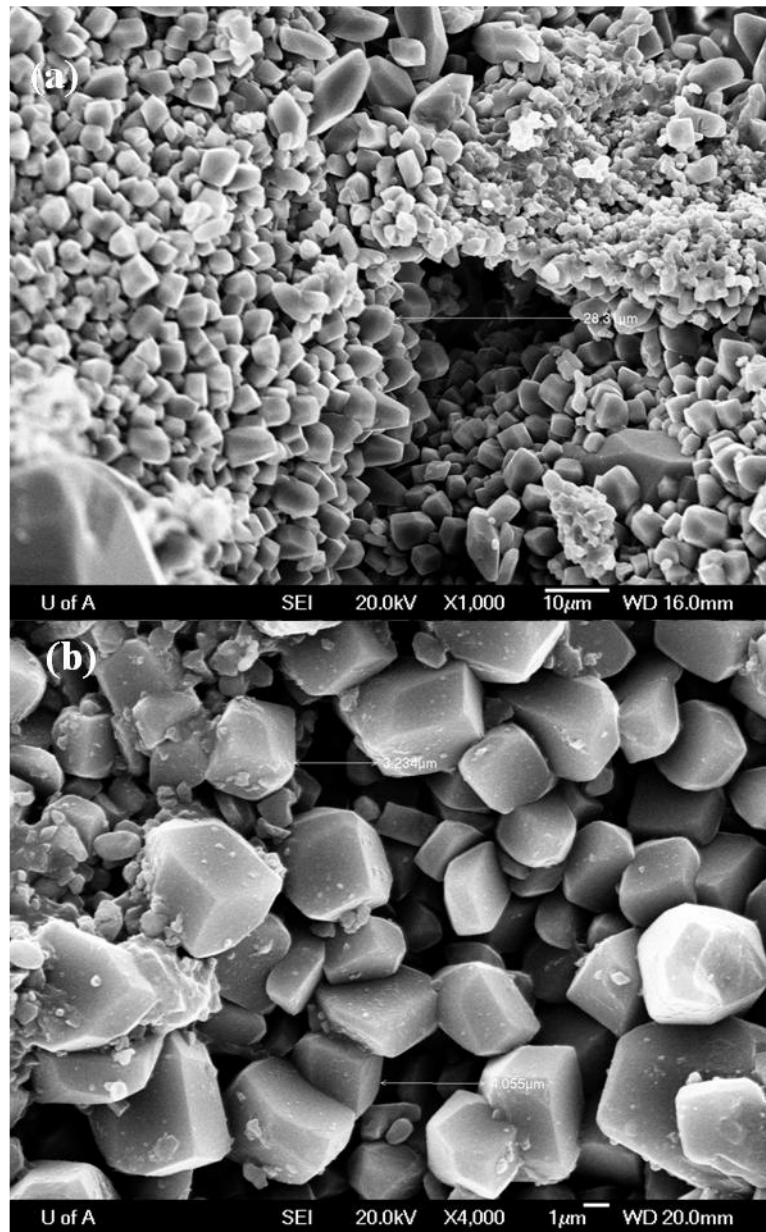


Figure 6.7: SEM images of sample 4-55 shows two types of pore size. (a) Shows interparticle macropore. (b) The micro size pores (4-5 μm) is formed between the calcite cement crystals.

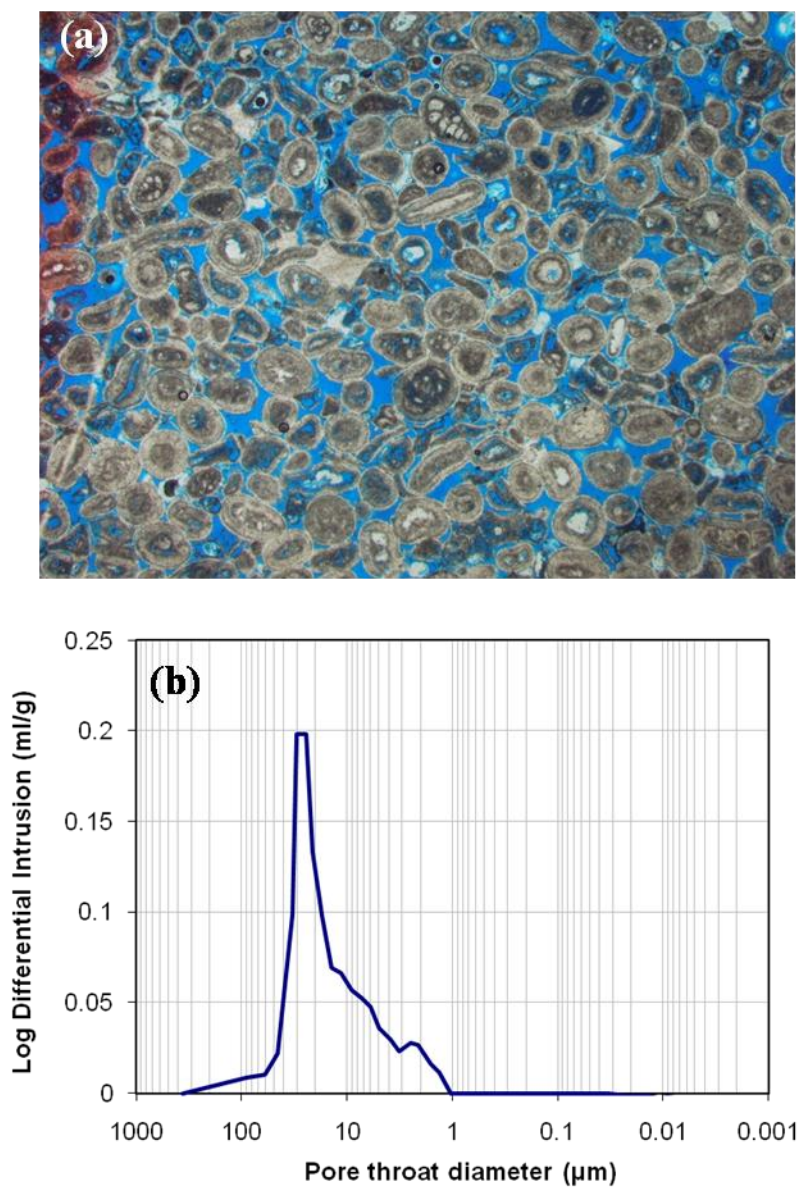


Figure 6.8: (a) Thin-section photomicrography of sample 2-33, the pores are filled by blue-dyed epoxy; interparticle and intraparticle pores are shown clearly. (b) Pore throat size distribution plot for sample 2-33 shows the dominant pore throat size (Peak) is around 30 μm and the smallest pore throat size around 1 μm .

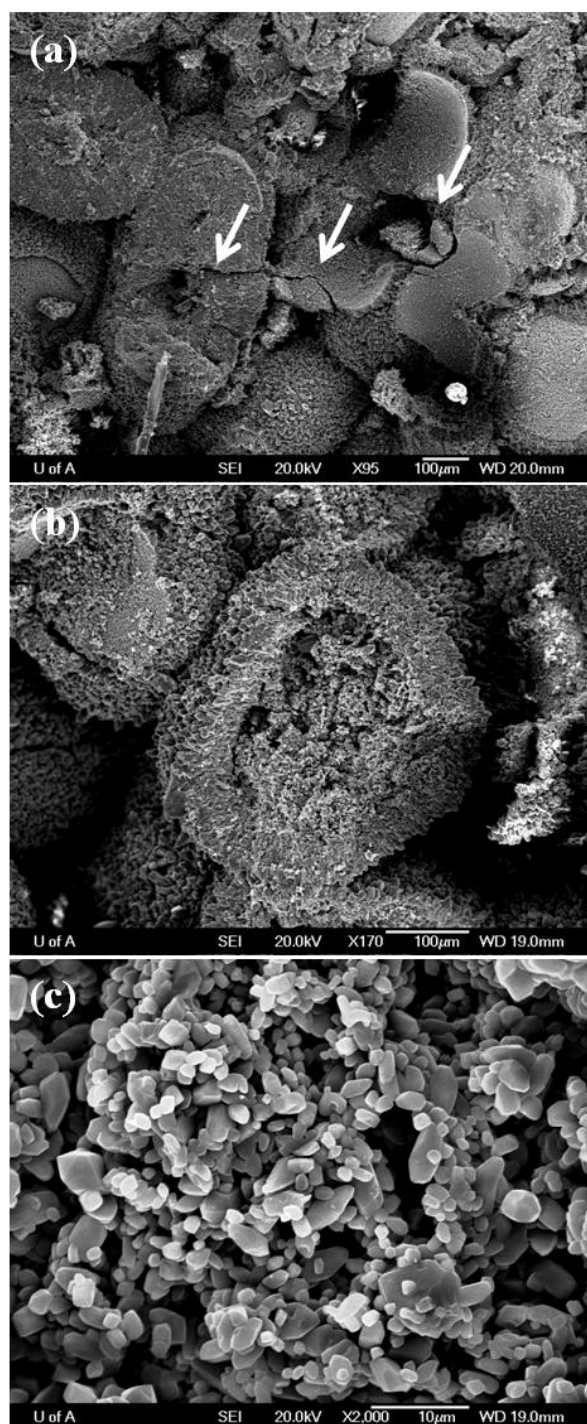


Figure 6.9: SEM images of sample 2-33 shows: (a) the mechanical breaks (white arrows) in the microporous grains. (b) Intraparticle macropore inside the

microporous grain, forming sponge like grains. (c) The micropores found between calcite crystals that formed microporous grains.

6.3.2 S-wave velocities

The Biot model over-predicted the S-wave velocities for most of the samples (figure 6.10). Two sample groups deviated from this trend.

The Biot calculated velocities for the low porosity samples ($\phi < 3\%$) are underpredicted. Another observation in this group is that the measured water saturated velocities are greater than the observed dry velocities (figure 6.11). This is unexpected as the increase in density upon liquid saturation should lead to a decline in the shear wave speed.

Another group of samples show that Biot predictions are reasonably close to the measured values. The mercury injection data show that the samples of this group have wide range of pore size distribution (figure 6.12-6.13). It was felt that type of pores here does not have any influence that can explain these behaviours.

In general Gassmann model over-predicts the saturated velocities at low pressure and lie close to the observed velocities at high pressure for most of the selected samples (figure 6.10). Gassmann predictions of the very low porosity samples under-predict the saturated velocities (figure 6.11).

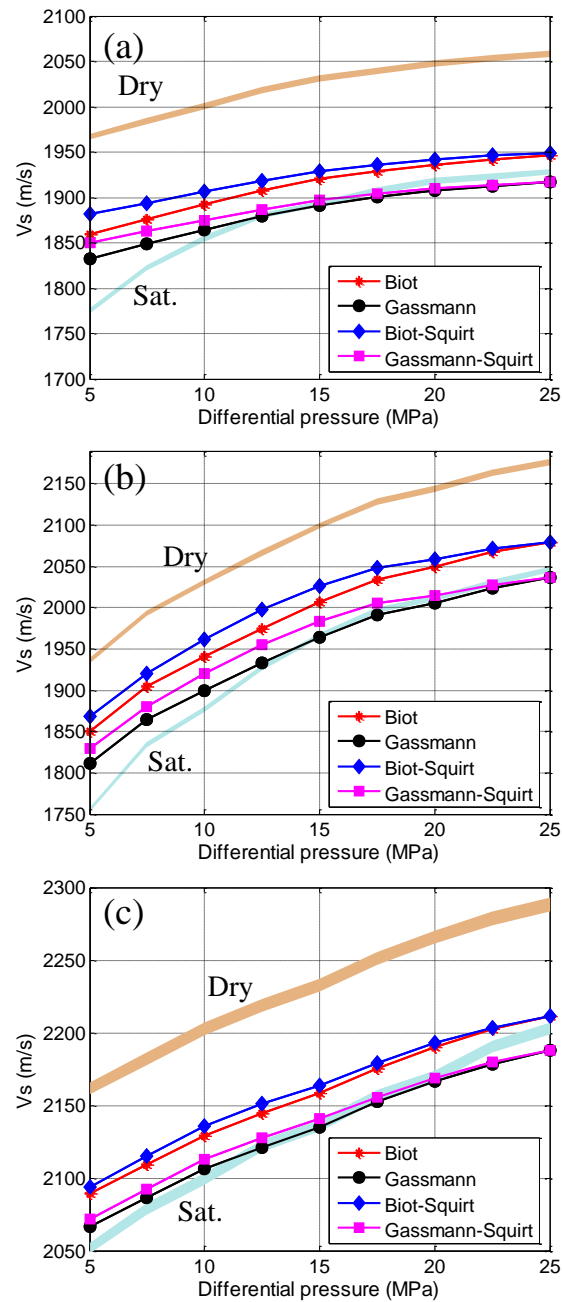


Figure 6.10: The observed dry (brown) and saturated (blue) velocities and model predictions for S-wave velocities of three different samples (a) sample 4-55, (b) sample 4-97 and (c) sample 1-288. Biot model over predicts the saturated S-wave velocities whereas Gassmann model over predicts the saturated velocities at low pressure and close to fit the observed velocities at high pressure.

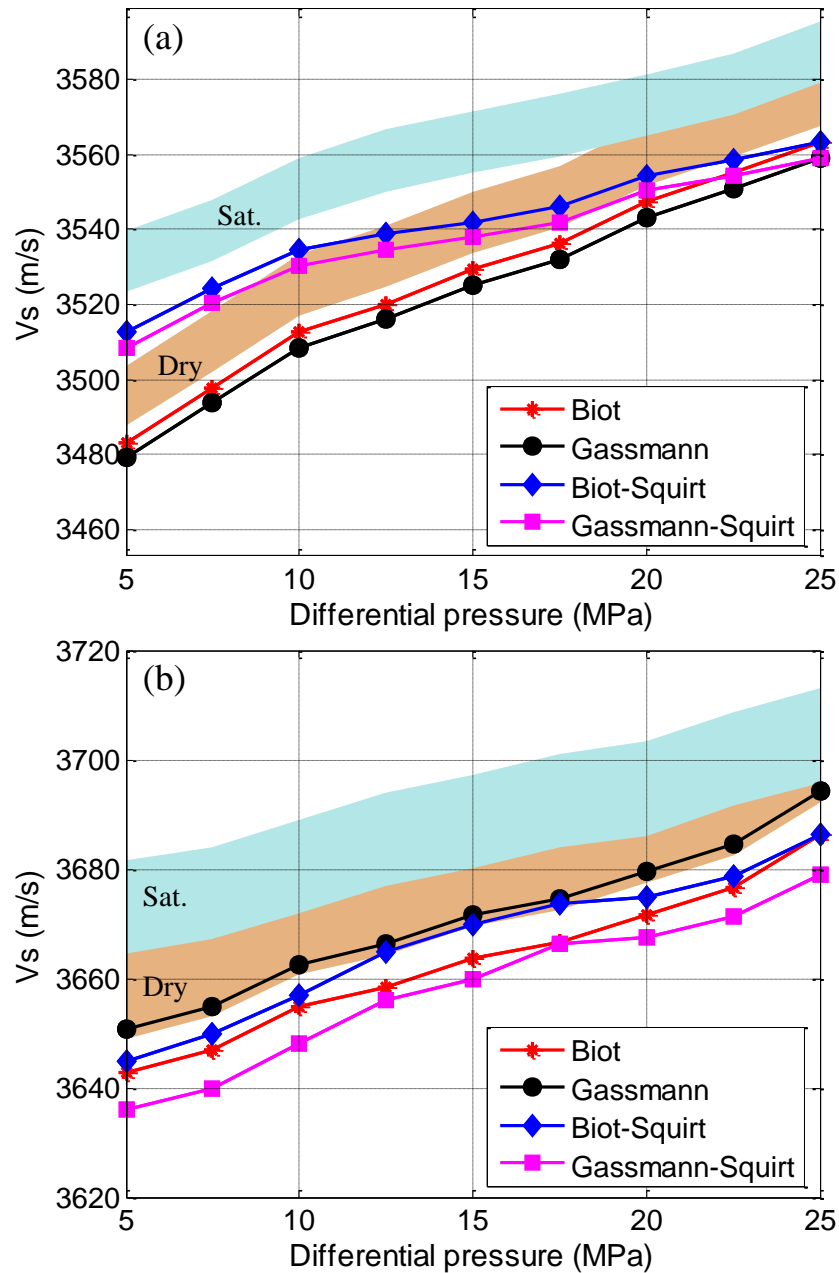


Figure 6.11: The observed dry (brown) and saturated (blue) velocities and model predictions for S-wave velocities of the very low porosity samples ($\phi < 3\%$), (a) sample 1-11 and (b) sample 7-222. Biot and Gassmann models under predict the saturated velocities and lie close to the observed dry velocities.

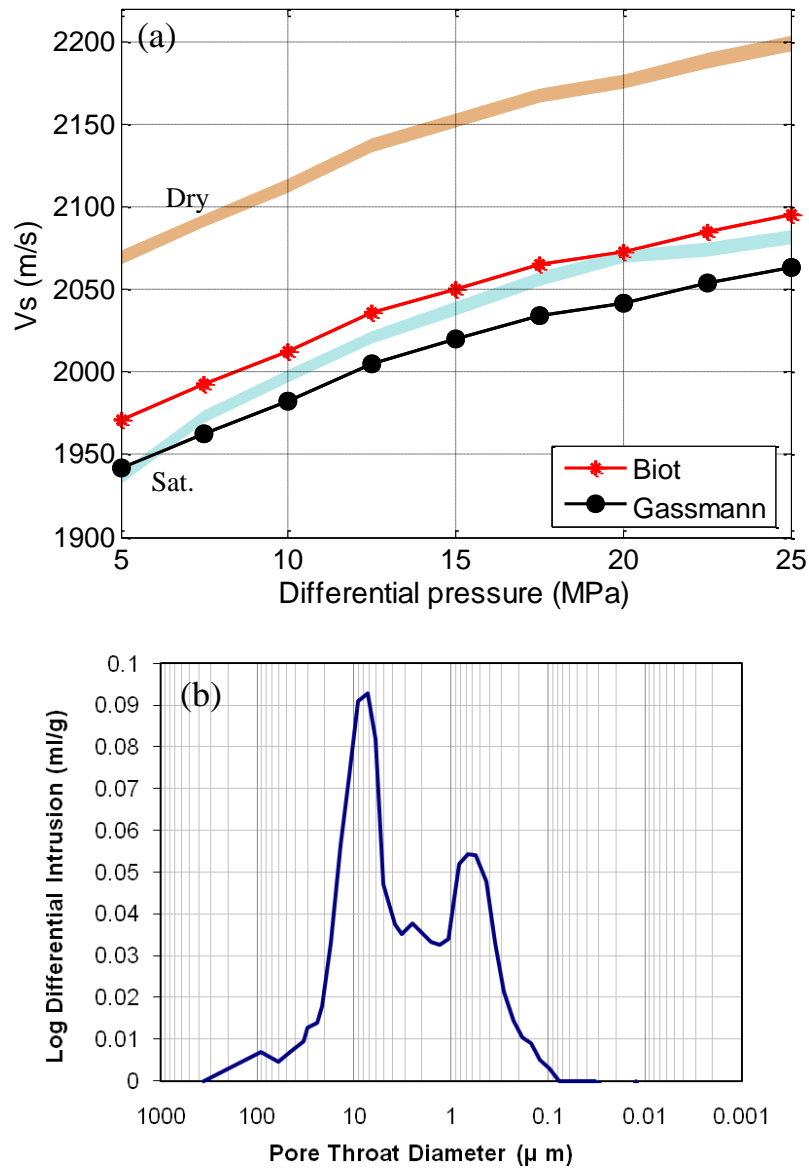


Figure 6.12: (a) The observed dry (brown) and saturated (blue) velocities and saturated velocity models for sample 2-160 Biot model predictions close to the observed velocities whereas Gassmann is under predict the velocities. (b) Mercury intrusion plot for same sample shows that the sample has a wide range of pore size distribution from 300 μm to 0.1 μm .

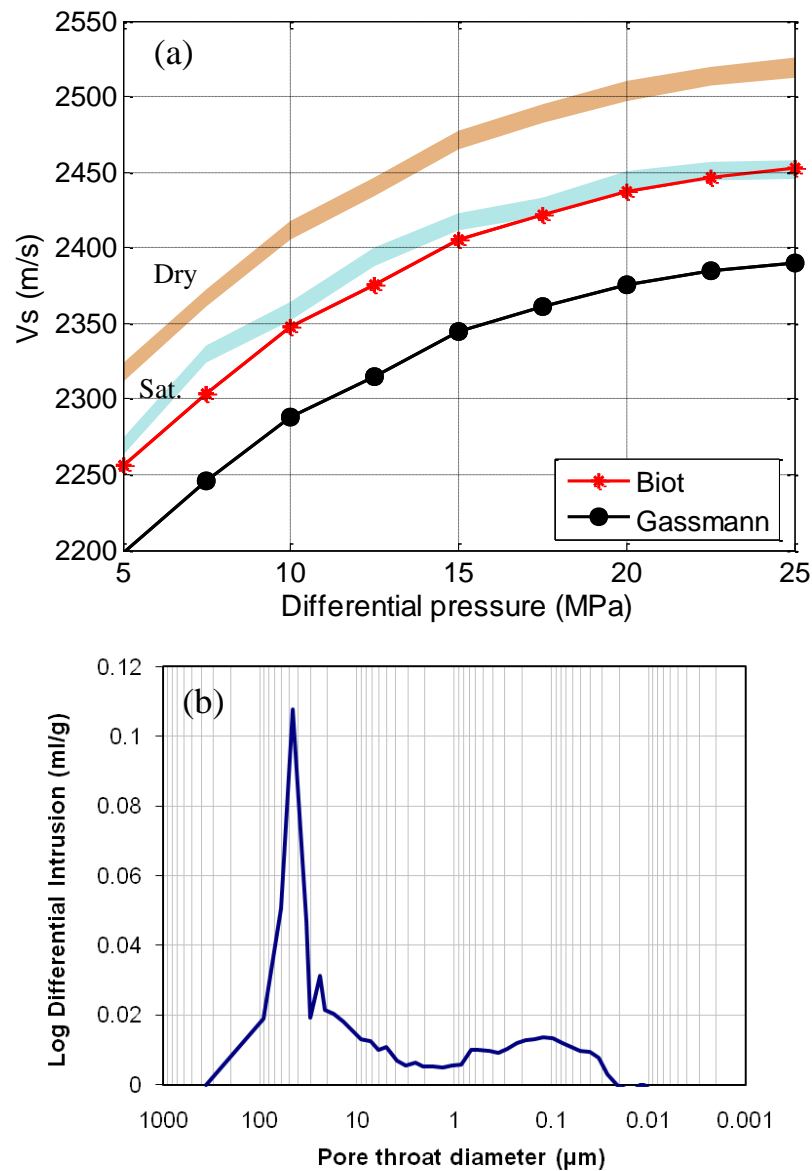


Figure 6.13: (a) The observed dry (brown) and saturated (blue) velocities and saturated velocity models, for a sample 3-331 Biot model, prediction close to the observed velocities whereas Gassmann is under predicts the velocities. (b) The mercury intrusion plot for the same sample shows that the sample has a wide range of pore size distribution from 45 μm to 0.013 μm .

6.4 Conclusions

Water-saturated P- and S-wave velocities were measured in thirty seven carbonate samples, only fifteen samples of them were selected for fluid model prediction study. The samples selected based on QC procedure developed in this study: that show almost no changes in saturated velocities at constant differential pressure. The measured velocities were compared to model predictions from dispersion-free Gassmann, Biot, squirt-Gassmann and squirt-Biot models. Only eight of the selected samples were used in squirt models as these were used in quasi-static data. The static data for these samples were used to calculate the porosity as function of confining pressure. We found that squirt mechanism is not active on all the studied samples. Biot mechanism is likely to be the principle dispersion mechanism in these samples. For S-wave velocities, Gassmann's model consistently over-predict the saturated at low pressure and closely fit the measured velocities at high pressure, whereas, Biot model over-predicts the saturated velocities in most of the studied samples.

Chapter 7

Static, dynamic and grain bulk moduli in Carbonate

7.1 Introduction

In general the bulk modulus describes the resistance of a material to compression, it can be obtained experimentally in two ways. The first, dynamic, measurement involves recording the P- and S-wave velocities and density; and then the bulk modulus can be calculated using equation (4.15) in chapter 4, which so-called the dynamic bulk modulus. The second, static, bulk modulus is obtained by directly measuring the volumetric strain for a given stress. This is accomplished with strain gauges as detailed in Chapter 5. The static bulk modulus is calculated from the volumetric strain and stress increment on each pair of consecutive measurements. The two methods differ substantially in the frequency of the applied loading and in the strain magnitude. The dynamic

measurements involve high loading frequency and extremely small strain magnitudes whereas the static measurements involve low loading frequency and high strain magnitude. The peak strain in dynamic measurement is of the order of 10^{-6} , while the static measurement is greater than 10^{-2} .

The static moduli are the real representation of the in situ mechanical activity. Therefore, it is very important to study the relation between the two bulk moduli as the dynamic bulk modulus can be easily obtained in situ by using, for example, the P and S wave sonic log velocities as measured in a borehole. In this way no actual material need be directly obtained. In contrast, the static modulus requires much more work and cost as core must be retrieved and then prepared for measurement in a laboratory.

Ideally, the static and dynamic moduli should be the same in an elastic material, but this is rarely the case for complex materials such as rock. Many studies have attempted to study the relationship between static and dynamic moduli. Zisman (1933) found that the static bulk modulus is always smaller than the dynamic modulus based on measurements made on different granite samples. He attributed this difference to the presence of cracks and cavities between the crystals that form the rock. He based his contention on the fact that the static and dynamic moduli are in good agreement in theunjacketed test (the rock opened to confining fluid). He also observed that the difference is high at low pressure and decreases with increasing pressure, suggesting that most of cracks are closed at high pressure. The same conclusions were drawn for a wide collection of rocks by many later workers (e.g., Birch, 1961; Ide, 1963; Simmons and Brace, 1965;

King, 1969; Cheng and Johnston, 1981; Fjaer, 2009). The differences between the static and the dynamic moduli is also possibly related to the differences of the strain amplitude between the two measurements (e.g., Cheng and Johnston, 1981; Fjaer, 2009).

Biot and Willis (1957) introduced theunjacketed test to measure grain or mineral modulus of the rock sample. In this test, the sample is uncovered and exposed to the confining fluid. The confining pressure fluid enters the pore spaces and after a period of time the confining pressure fluid will completely penetrate the pore spaces. In this case the changes in the pressure are the same inside the sample and equal to the changes in the confining pressure. If no isolated pores presented in the rock (all pores are connected) the unjacketed bulk modulus is identical to that for the minerals forming the rock.

This chapter shows the observation results of the static and dynamic bulk moduli, measured on the 15 carbonate samples for which strain was measured. Examples of the stress-strain curves in jacketed and unjacketed tests as well as the compressional and shear velocities for different samples will be shown. The relations between the dynamic and static bulk moduli are also discussed. Grain bulk modulus obtained from the unjacketed test will be shown as well.

7.2 Dynamic bulk modulus

Dynamic bulk modulus was calculated from the measured ultrasonic compressional and shear wave velocities. The P- and S-wave velocities (at 1 MHz) were calculated by dividing the length of the sample to the wave travel

time, which was obtained by picking the first arrival from the pulse-transmission signal. The measurements were made on dry and saturated samples with confining pressure ranging from 5 MPa to 25 MPa with 2.5 MPa incremental pressures in both during pressurization and depressurization cycles. The dynamic bulk modulus then was calculated from the observed P- and S-wave velocities and bulk density of the sample using equation 4.15 (see chapter 4).

Velocity and dynamic bulk modulus changes with pressure

The full set of normalized P- and S-wave waveforms of sample 2-33 ($\phi=31\%$) under dry condition are shown in figure 7.1. The samples were pressurized to the peak pressure of 25 MPa. Obviously, due to the closing of crack like pores and the sliding and the elastic and inelastic deformation of grain contacts, the travel times show remarkable reduction with the increase of confining pressure in both P- and S-wave. Figure 7.2 shows the effect of pressure on P- and S-wave velocities for samples 2-33. The sample shows general increase in velocity with pressure increase. The velocity readings taken during the pressurization cycle are slightly lower than the velocities taken during the depressurization cycle. This is due to the fact that during depressurization the closed microcracks and pores start to reopen once the pressure drops beyond the critical pressure that caused their initial closure. The velocities show a sharp increase with pressure at low pressure that is due to the fact that the compliant pores mostly close at low pressure. At higher pressure, the velocities show only a

relatively small further increase. Similarly, the dynamic bulk and shear moduli show general increase with pressure (figure 7.3).

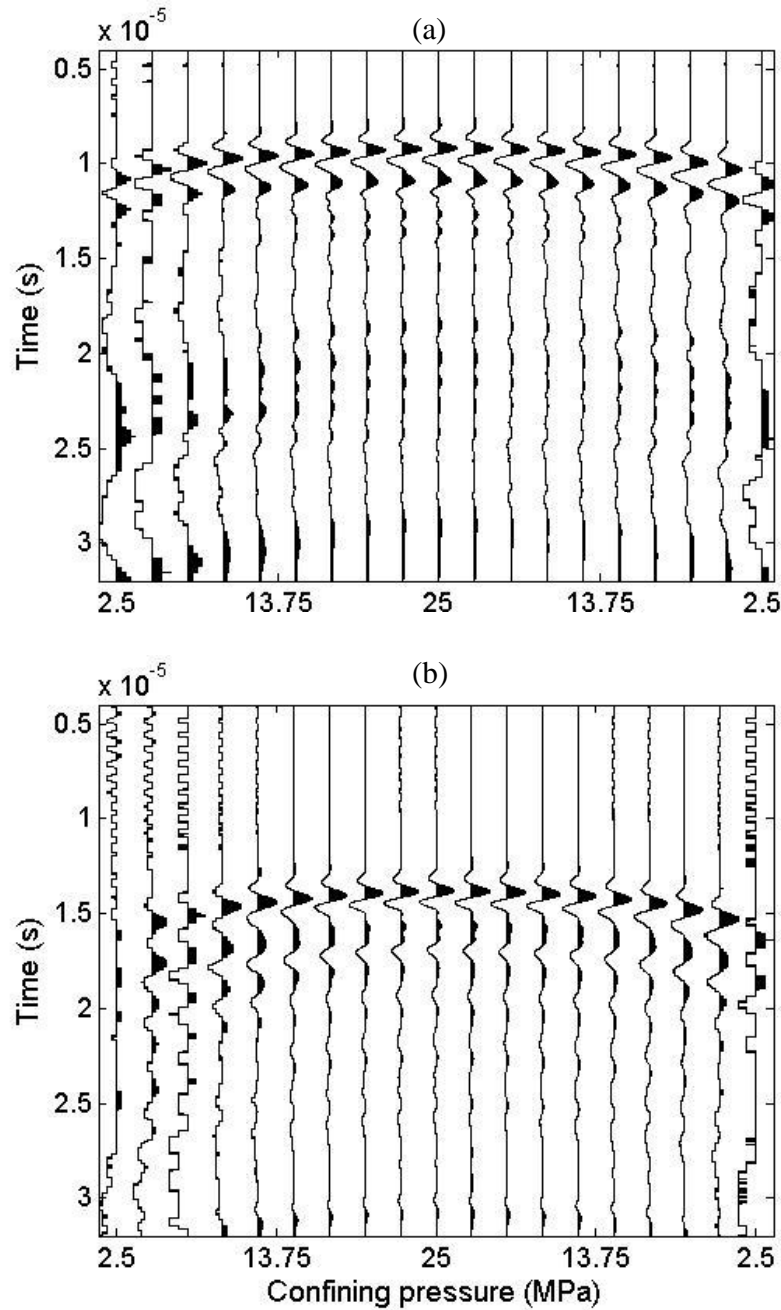


Figure 7.1: Normalized P- (a) and S- (b) wave waveforms for sample 2-33 at different confining pressure. Reductions of traveltimes with pressure are obvious in both P- and S-wave waveforms.

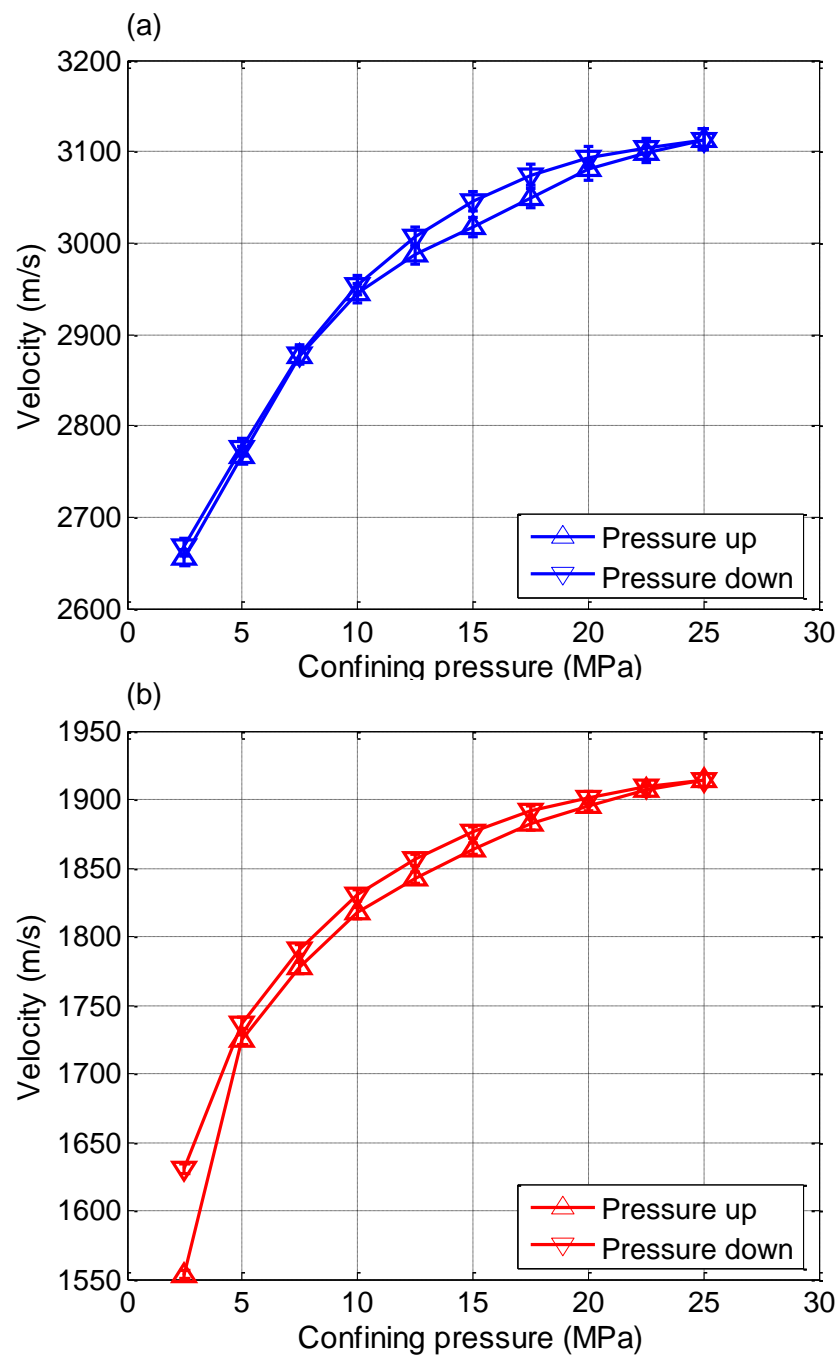


Figure 7.2: Dry P- (a) and S-wave (b) velocities of sample 2-33 at different confining pressure. The velocities in both P- and S-wave show sharp increase at low pressure.

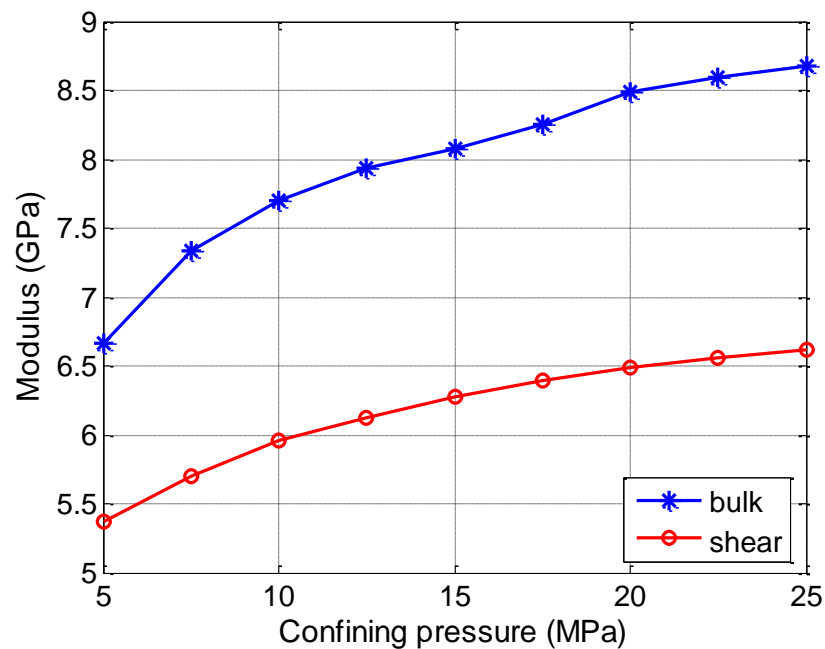


Figure 7.3: Bulk (*blue*) and shear (*red*) moduli of sample 2-33 at different confining pressures.

7.3 Static bulk modulus

The static bulk modulus was obtained from the quasi-static strain measurements using strain gauges technique. The sample with etched strain gauges was measured on dry and water saturated conditions with confining pressure varying from 5 MPa to 25 MPa with 2.5 MPa incremental pressures in both during pressurization and depressurization cycles. This was done simultaneously with the P and S wave velocity measurements described above. The rock sample and fused quartz strains were also measured simultaneously for calibration and pressure effect corrections. The stress-strain curves digitized and then 2nd or 3rd order polynomial were fitted to the digitized points to get a smooth

stress-strain curve and minimize the sharp fluctuation on the static bulk modulus. In some cases this curve fitting caused sharp and unrealistic increase in static bulk modulus at high pressure.

The stress-strain curve of the sample was corrected for the pressure effect using the differences between the measured and calculated stress-strain curves of fused quartz. The calculated stress-strain curve of the quartz obtained from its previously known bulk modulus (Bass, 1995). Then the static bulk modulus was calculated by computing the derivative of the stress-volumetric strain curve as described in chapter 5. The static moduli were measured from two different strain gauges bonded on the sample. One positioned parallel to the vertical axis of the sample which we called vertical component the other perpendicular to the vertical axis which referred to as horizontal component. The apparent bulk modulus calculated independently from each strain gauge. We considered the two moduli that calculated from each strain gauge represent the upper and lower bounds of the static bulk modulus on the studied samples.

The stress-strain curve of the dry jacketed test for sample 4-55 is shown in figure 7.4. The sample has 29% porosity and 930 mD permeability. The strains of the sample were observed using two independent strain gauges: one mounted vertically (parallel to the sample's axis) and the other horizontally (perpendicular to the sample vertical axis). These two strains differ by around 27%. The strains over the horizontal axis are higher than the vertical axis; suggesting that the majority of the compliant pores and crack-like pores are oriented almost in a direction parallel to the length of the sample. Similarly, the apparent static bulk

moduli calculated using only the horizontal component is greater than that calculated using only the vertical strains (figure 7.5). The stress-strain relations in both the vertical and horizontal directions are both nonlinear. In the vertical strain gauge, the observed strains during pressurization and depressurization cycle are very close. Whereas the horizontal strain gauge shows remarkable increase on strains made during the depressurization cycle. The hysteresis of the stress-strain curve can be explained by the absence of plastic deformation the crack-like pores closed and the grain contacts pushed together at certain pressure during the pressurization cycle value does not return to its initial state at exactly same pressure during depressurization cycle (Sharma and Tutuncu, 1994).

Figure 7.6 shows the stress-strain curves for sample 7-222. The sample has low porosity around 3% and permeability less than 0.1 mD. Strains from both vertical and horizontal strain gauges are almost identical suggesting the lack of anisotropy. In spite of the low porosity, the strains observed during the pressurization cycle are smaller than the strains observed during the depressurization. This observation might be due to the presence of the poorly interconnected leached dolomite pores that cannot be observed from the helium porosity test (see chapter 3).

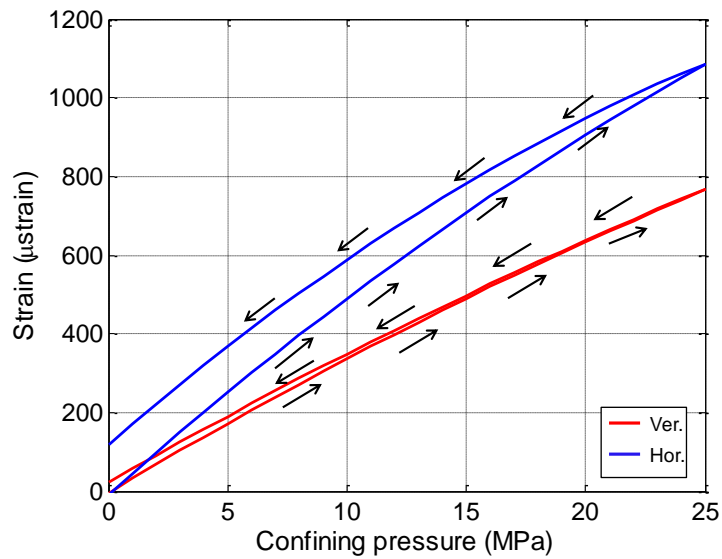


Figure 7.4: Stress-strain relations for sample 4-55, showing the vertical strain (*red*) and the horizontal strain (*blue*). Both were measured during pressurization and depressurization cycles indicated by arrows.

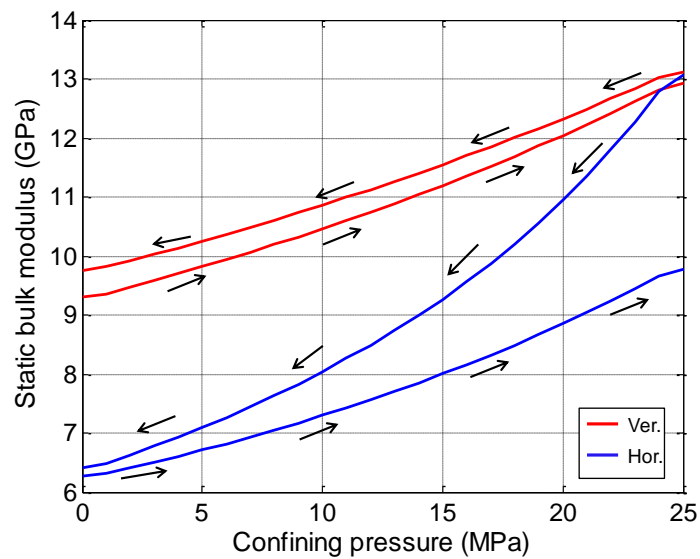


Figure 7.5: Static bulk moduli of sample 4-55 at different confining pressures. The red and blue curves show the static bulk modulus obtained from the vertical

and horizontal strain gauges. The pressurization and depressurization are indicated by arrows.

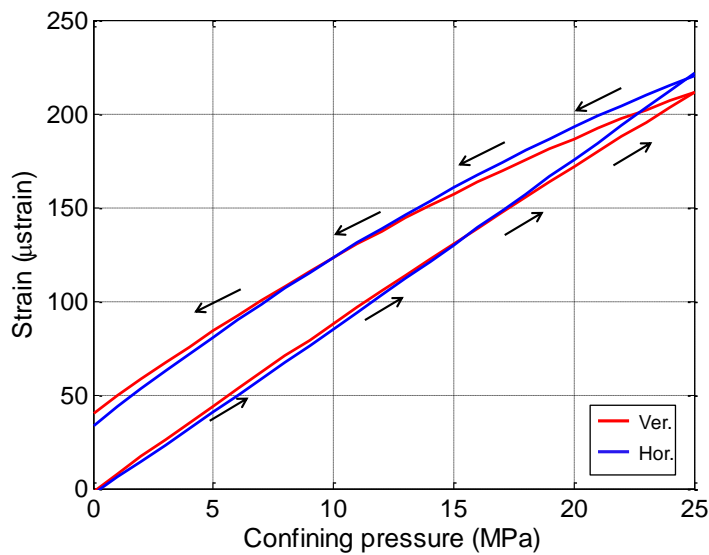


Figure 7.6: Stress-strain relations for sample 7-222, showing the vertical strain (*red*) and the horizontal strain (*blue*). Both were measured during pressurization and depressurization cycles indicated by arrows.

7.4 Comparison of static and dynamic bulk moduli

Figures 7.7 through 7.12 compare the static and dynamic bulk moduli for seven samples as an example. The area between upper and lower bounds of the static bulk moduli, mentioned earlier, are represented on the shaded area of the figures and the corresponding dynamic bulk moduli are shown by red asterisks in the same figure. The static modulus used in the static-dynamic ratio was calculated from the average of the vertical and horizontal moduli. First order observation from the comparison of the static and dynamic bulk moduli is that in

all the measured samples both moduli increase with pressure, suggesting that both are influenced by the changes that occur in the rock frame. The static bulk modulus is lower than the corresponding dynamic bulk modulus over pressure, indicating that there are some mechanisms that might exist in which each modulus has a different response. These differences between the bulk moduli decreased mostly at higher pressure. Similar observations were shown by Ide (1963) Brich (1961), Simmon and Brace (1965), King (1969), Cheng and Johnson (1981) and Fjaer (2009). Zisman (1933) suggested that the existence of cracks in the rock is the main reason for the differences between the two moduli. Simmon and Brace (1965) related these differences to the fact that elastic waves are less sensitive to the closing of cracks that produced by pressure than the strain. The major source of discrepancy is the difference in the strain amplitude between the two measurements (Tutuncu et al., 1995).

Figure 7.7 compares static and dynamic bulk moduli for sample 4-55. The sample has 29% porosity and permeability is equal to 930 mD. Calcite is the dominant mineral making up to 99% of the mineralogy. The sample shows large differences between the two static modulus bounds. Its static to dynamic ratio is around 0.7 at low pressure then it increased with pressure to 0.85 at 25 MPa. The dominant pore type is interparticle macropore and the sample lacks both intraparticle macropores and micropores. Despite the differences in porosity the static to dynamic ratio for sample 4-326 (figure 7.8) is very much close to the ratio in sample 4-55. Sample 4-326 has around 14% porosity and 55 mD permeability and static to dynamic ratio is close to 0.75 – 0.88. The static to

dynamic ratio of sample 1-288 ($\phi = 20\%$) varies from 0.5 at low pressure to 0.75 at high pressure (figure 7.9). Figures 7.10 to 7.12 compare static and dynamic moduli for three different samples (2-383, 4-09 and 3-429 respectively) have the same porosity around 10%. The samples differ in mineralogy, lithology and facies. Sample 2-383 is a lime mudstone with few dolomite crystals its mineralogy consist of 70% calcite and 30% dolomite. Sample 4-09 is a grainstone with 92% calcite, 6% anhydrite and traces of dolomite. Sample 3-429 is made of 100% dolomite crystals. There is no positive correlation between changes in mineralogy and the observed static and dynamic bulk moduli ratio. The observations that seem interesting are: the sample that made of 100% dolomite crystals and no grains (3-429) showed the lowest ratio between the three samples. Another interesting observation is that the relative changes on static and dynamic ratio with pressure increase with the increase of the amount of dolomite crystals. Figure 7.13 shows the static and dynamic moduli relation for sample 7-222 with around 3% porosity and less than 0.5 mD permeability. The static to dynamic ratio changes by 4% over pressure, from 0.55 at low pressure to 0.57 at high pressure.

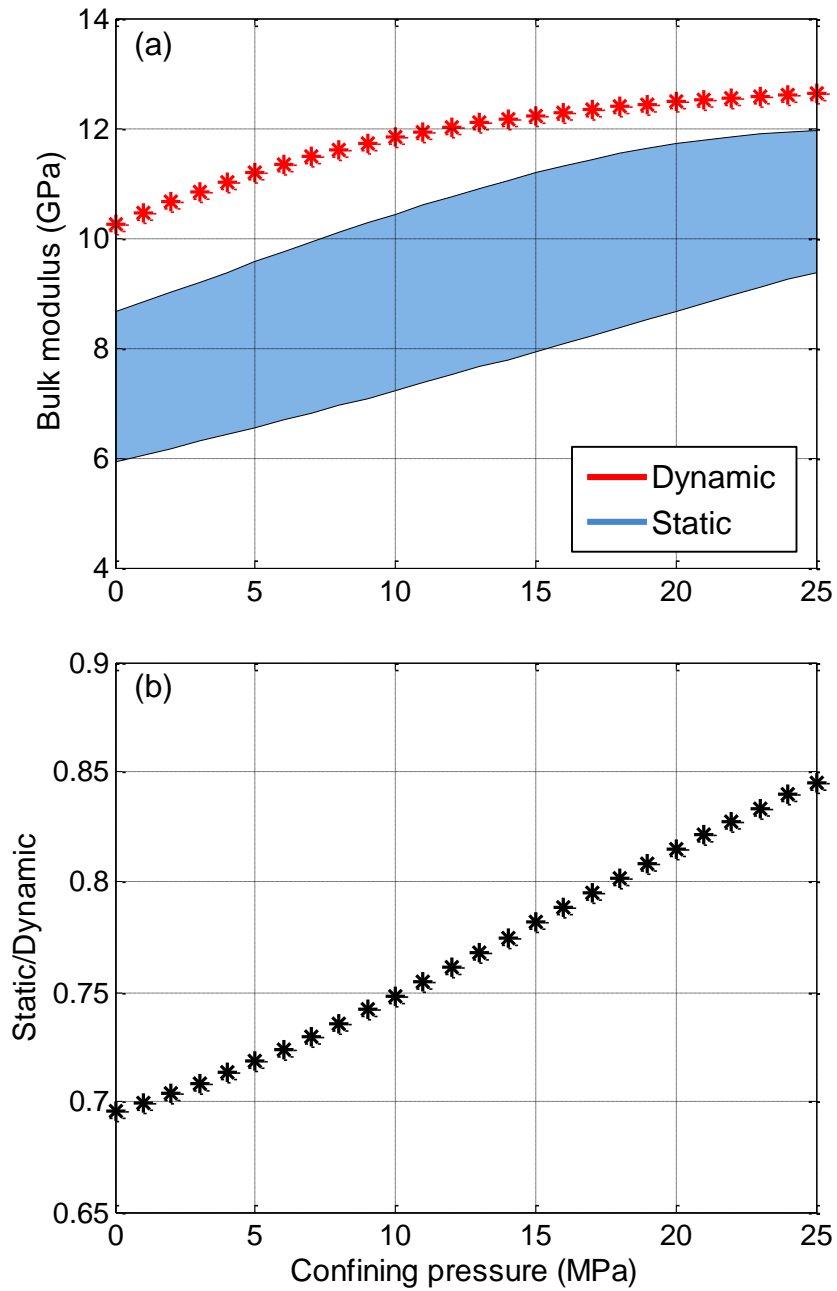


Figure 7.7: (a) Comparison of dynamic (asterisk) and static (blue shade) bulk moduli of sample 4-55. The blue shade is the area between the upper and lower bounds. (b) The ratio of static and dynamic moduli over the entire pressure.

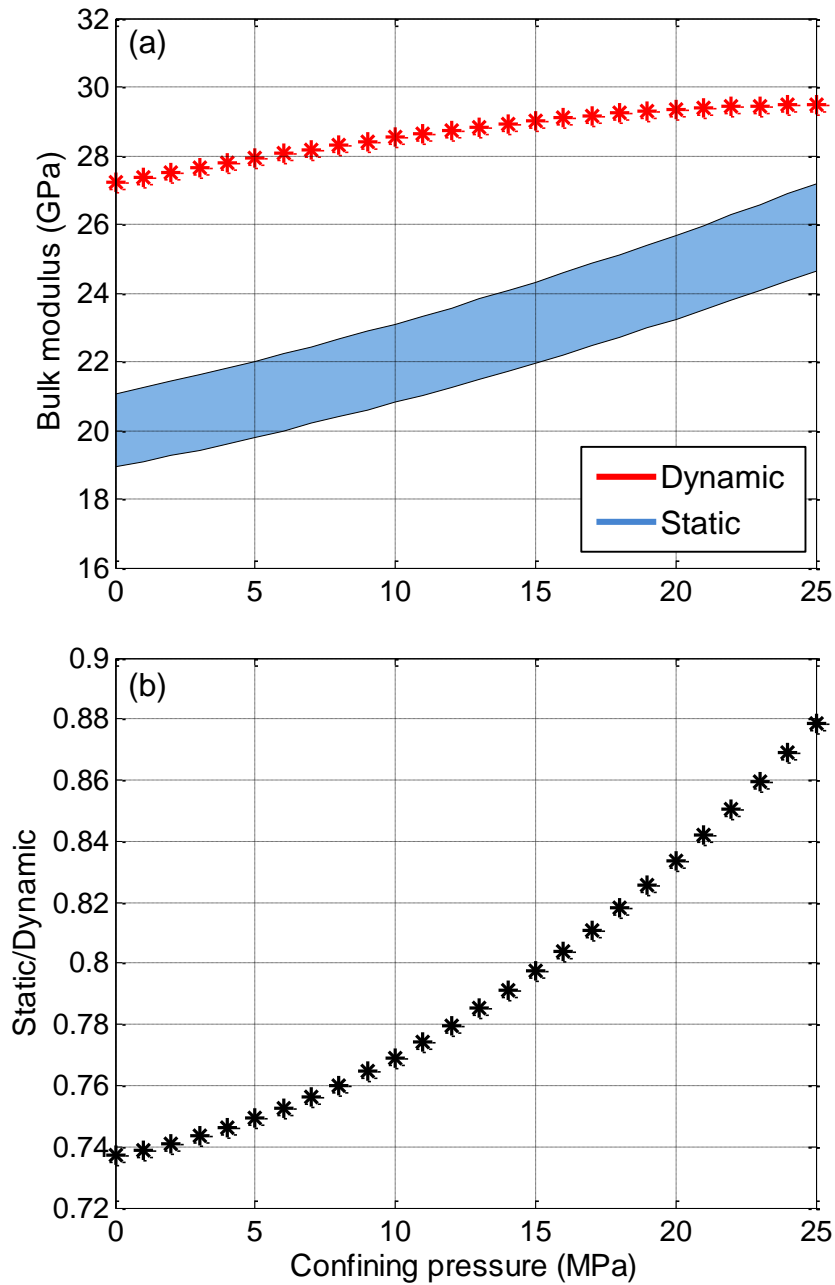


Figure 7.8: (a) Comparison of dynamic (asterisk) and static (blue shade) bulk moduli of sample 4-326. The blue shade is the area between the upper and lower bounds. (b) The ratio of static and dynamic moduli over the entire pressure.

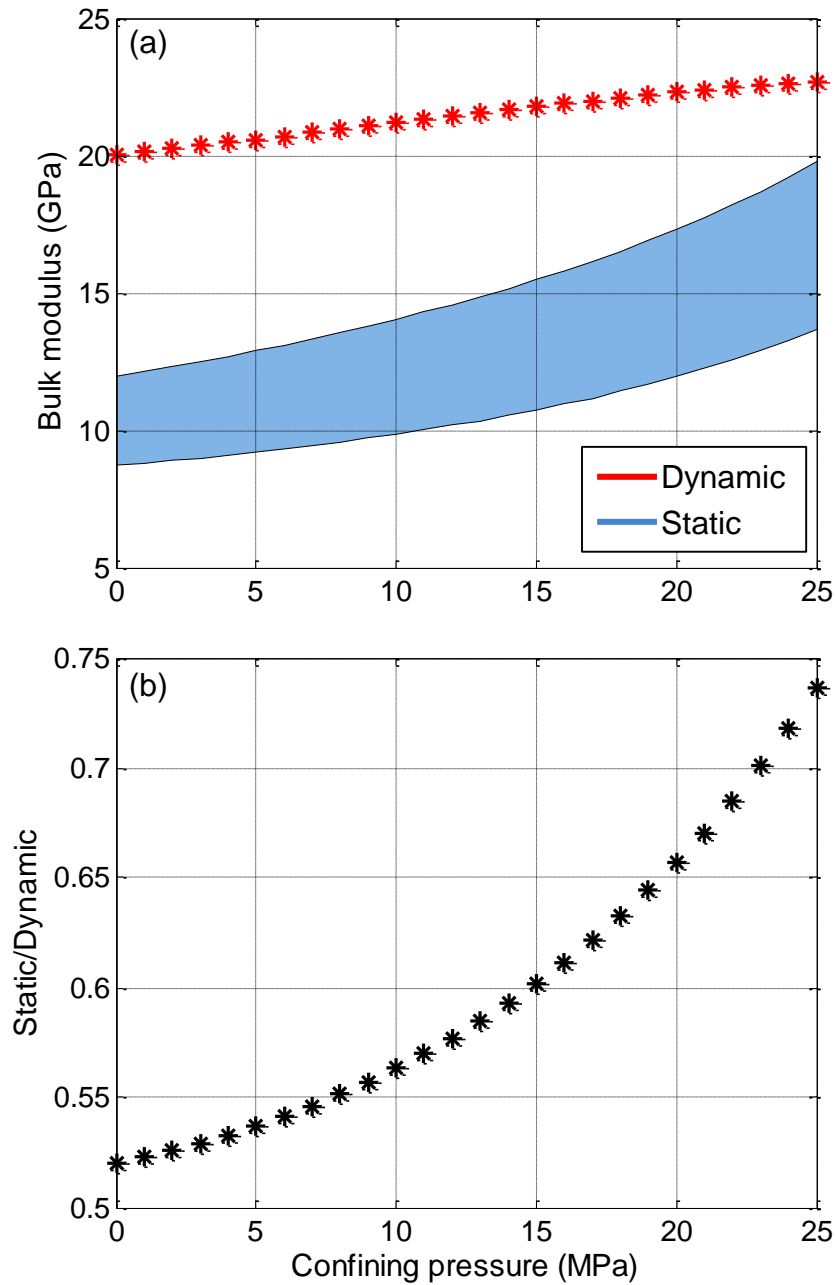


Figure 7.9: (a) Comparison of dynamic (asterisk) and static (blue shade) bulk moduli of sample 1-288. The blue shade is the area between the upper and lower bounds. (b) The ratio of static and dynamic moduli over the entire pressure.

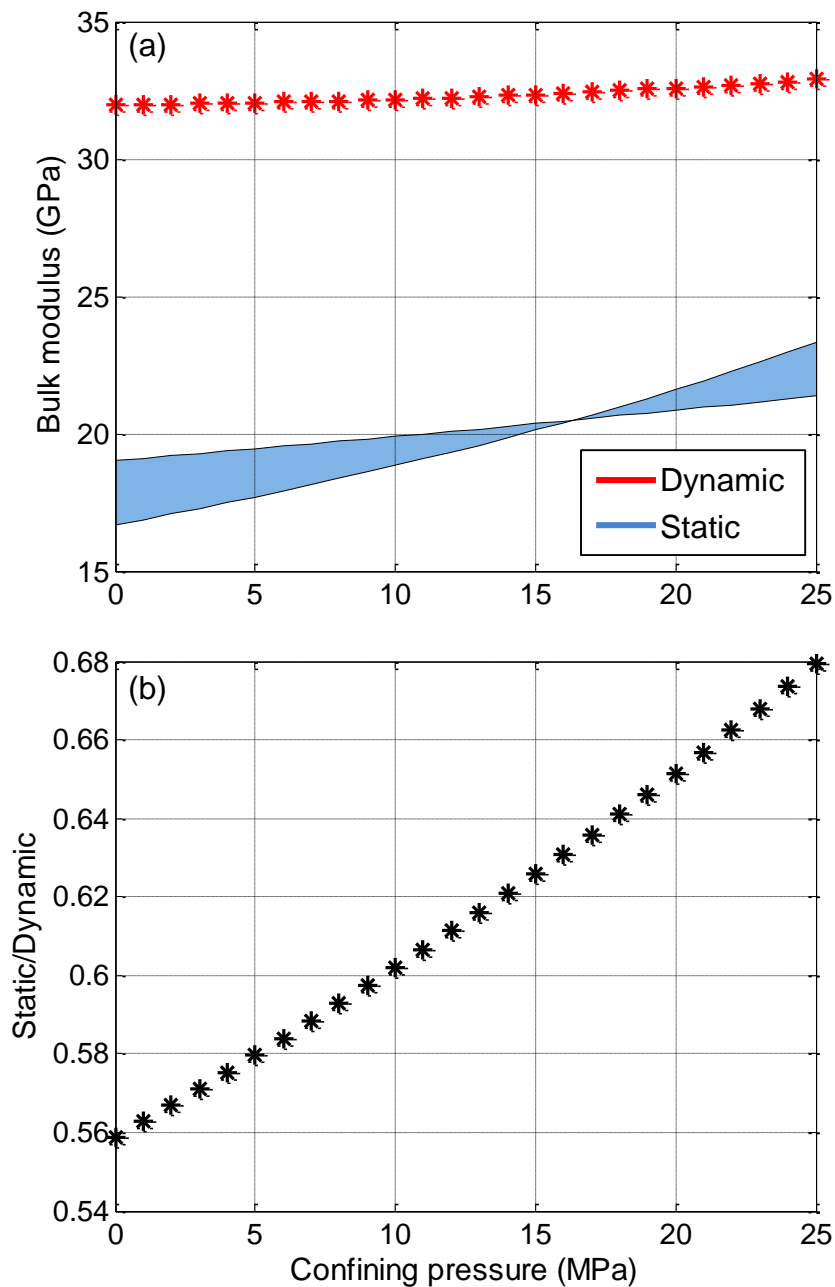


Figure 7.10: (a) Comparison of dynamic (asterisk) and static (blue shade) bulk moduli of sample 2-383. The blue shade is the area between the upper and lower bounds. (b) The ratio of static and dynamic moduli over the entire pressure.

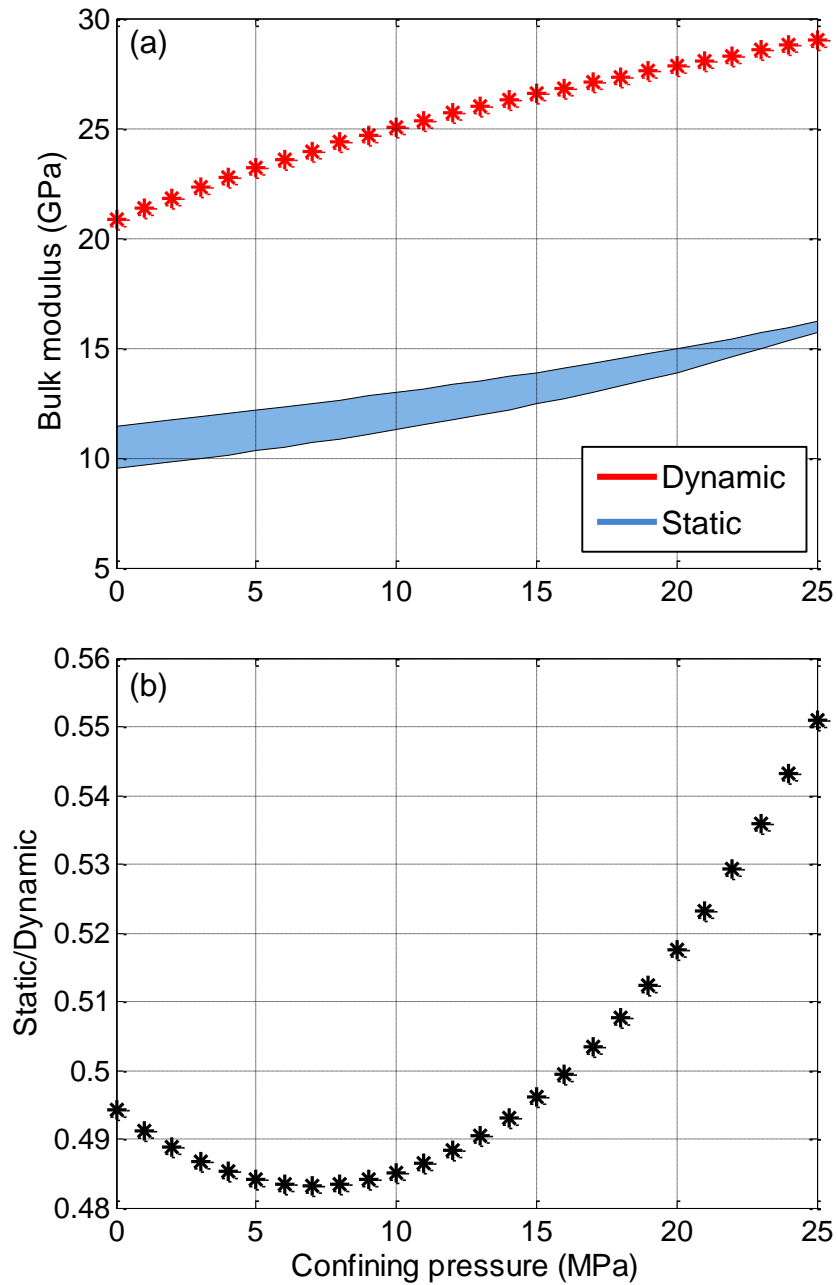


Figure 7.11: (a) Comparison of dynamic (asterisk) and static (blue shade) bulk moduli of sample 4-09. The blue shade is the area between the upper and lower bounds. (b) The ratio of static and dynamic moduli over the entire pressure.

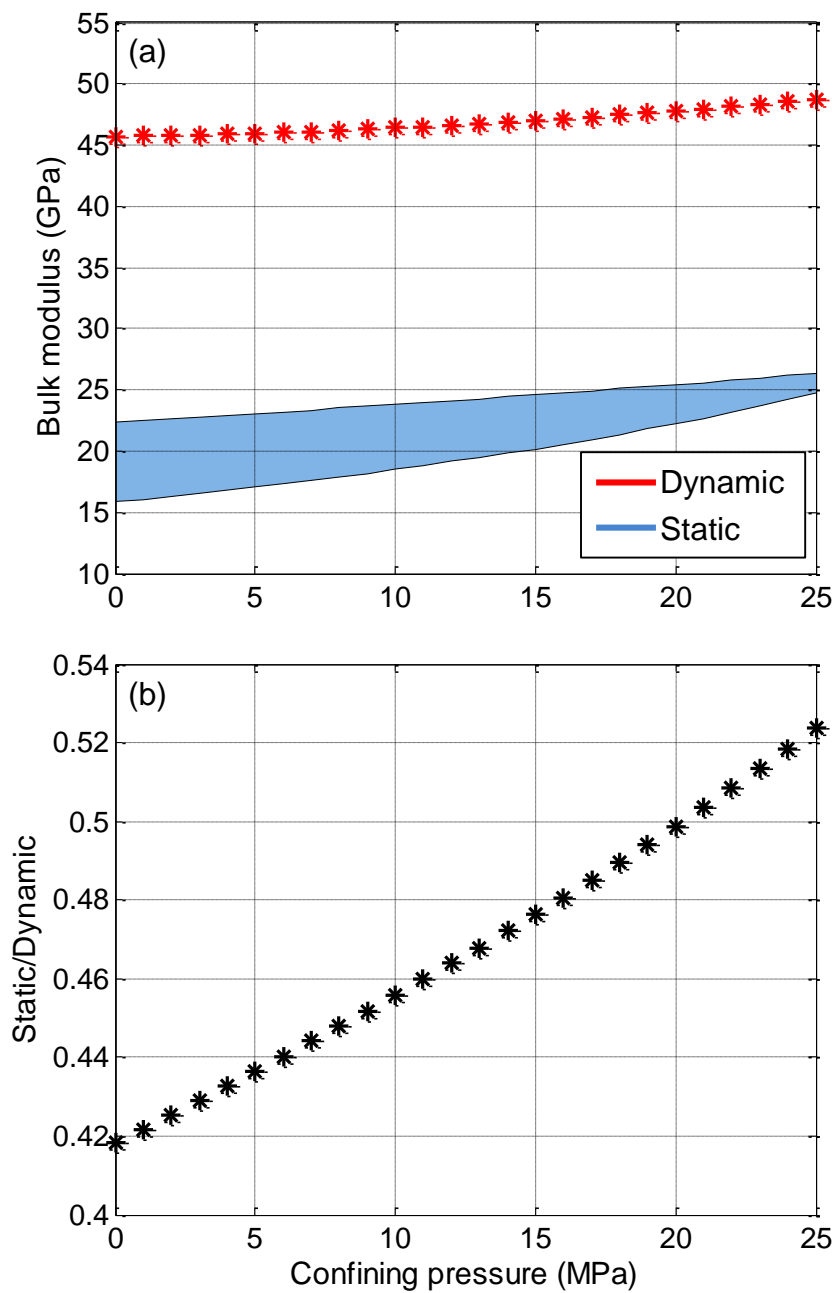


Figure 7.12: (a) Comparison of dynamic (asterisk) and static (blue shade) bulk moduli of sample 3-429. The blue shade is the area between the upper and lower bounds. (b) The ratio of static and dynamic moduli over the entire pressure.

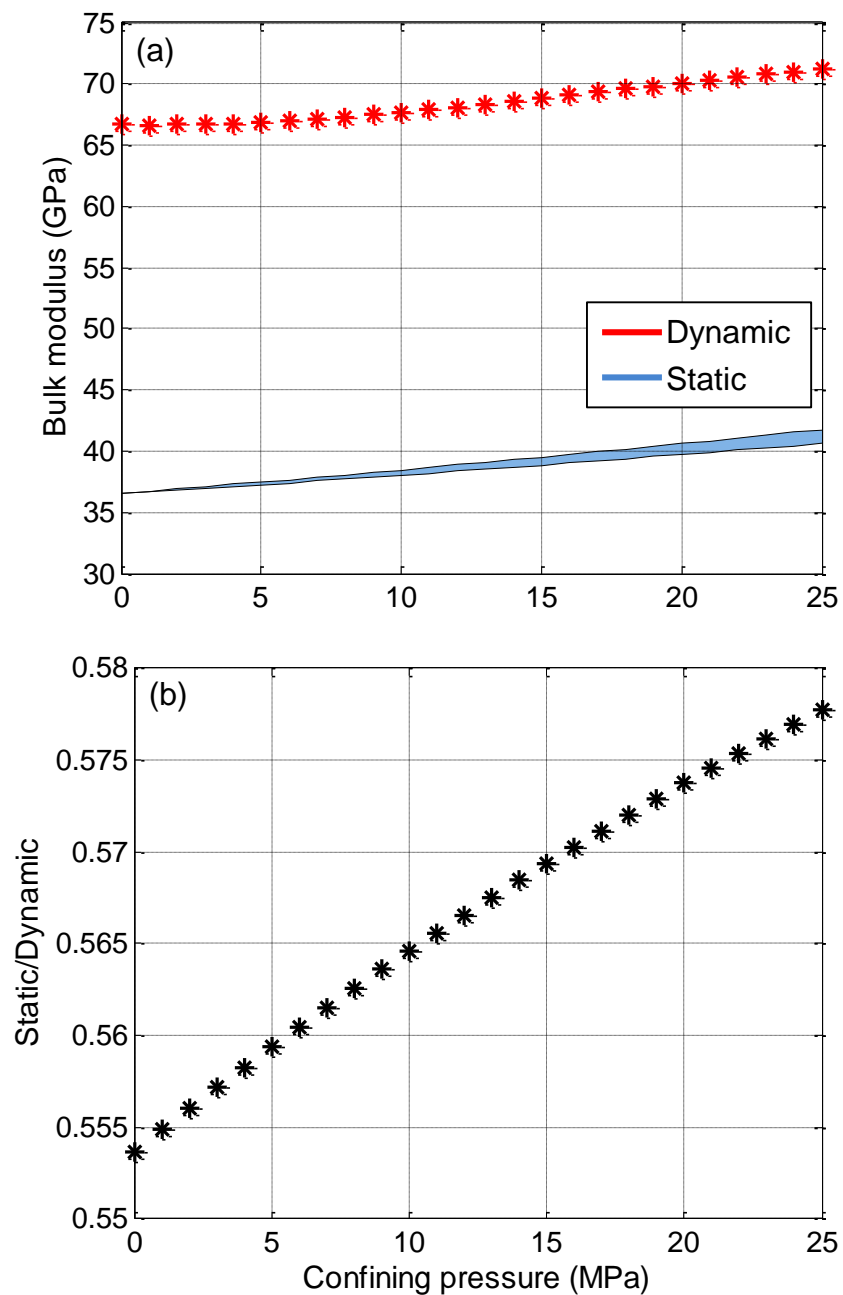


Figure 7.13: (a) Comparison of dynamic (asterisk) and static (blue shade) bulk moduli of sample 7-222. The blue shade is the area between the upper and lower bounds. (b) The ratio of static and dynamic moduli over the entire pressure.

Figure 7.14 illustrate the static-dynamic moduli relations at different pressure. At pressures from 5 to 15 MPa the static-dynamic ratio for high porosity samples scattered around 0.5-0.7 then the ratio increase at high pressure. One sample shows almost constant ratio over pressure. Low porosity samples at same pressure range (5-15 MPa) the ratio scattered between 0.4 and 0.5. At high pressures the ratios increase for all samples. There is no correlation between porosity and static-dynamic ratio. Figure 7.15 shows the changes of static modulus with saturation at different pressure. Most of the measured samples show increase of the static moduli after saturation, except three samples with porosity around 10%. The rates of increase show no correlation with porosity. The differences between the saturated and dry moduli decrease with pressure until the dry moduli far exceed the saturated moduli.

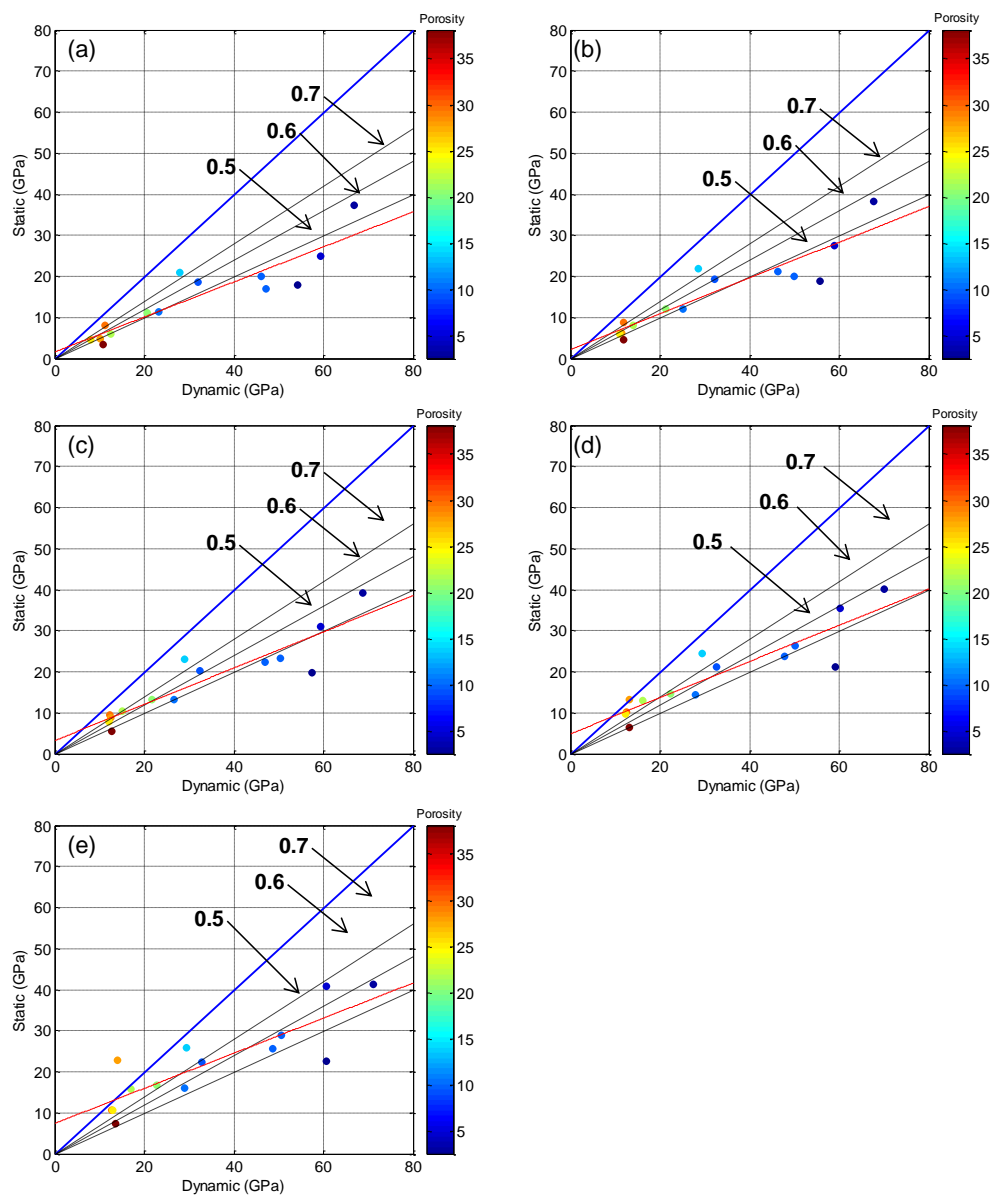


Figure 7.14: Cross plots of dry static against dry dynamic bulk moduli at 5 MPa (a), 10 MPa (b), 15 MPa (c), 20 MPa, (d) and 25 MPa (e) pressure, with linear fit (red line). The data points are color-coded with porosity. The blue line represents where the two moduli are equal and black dashed lines show different ratios.

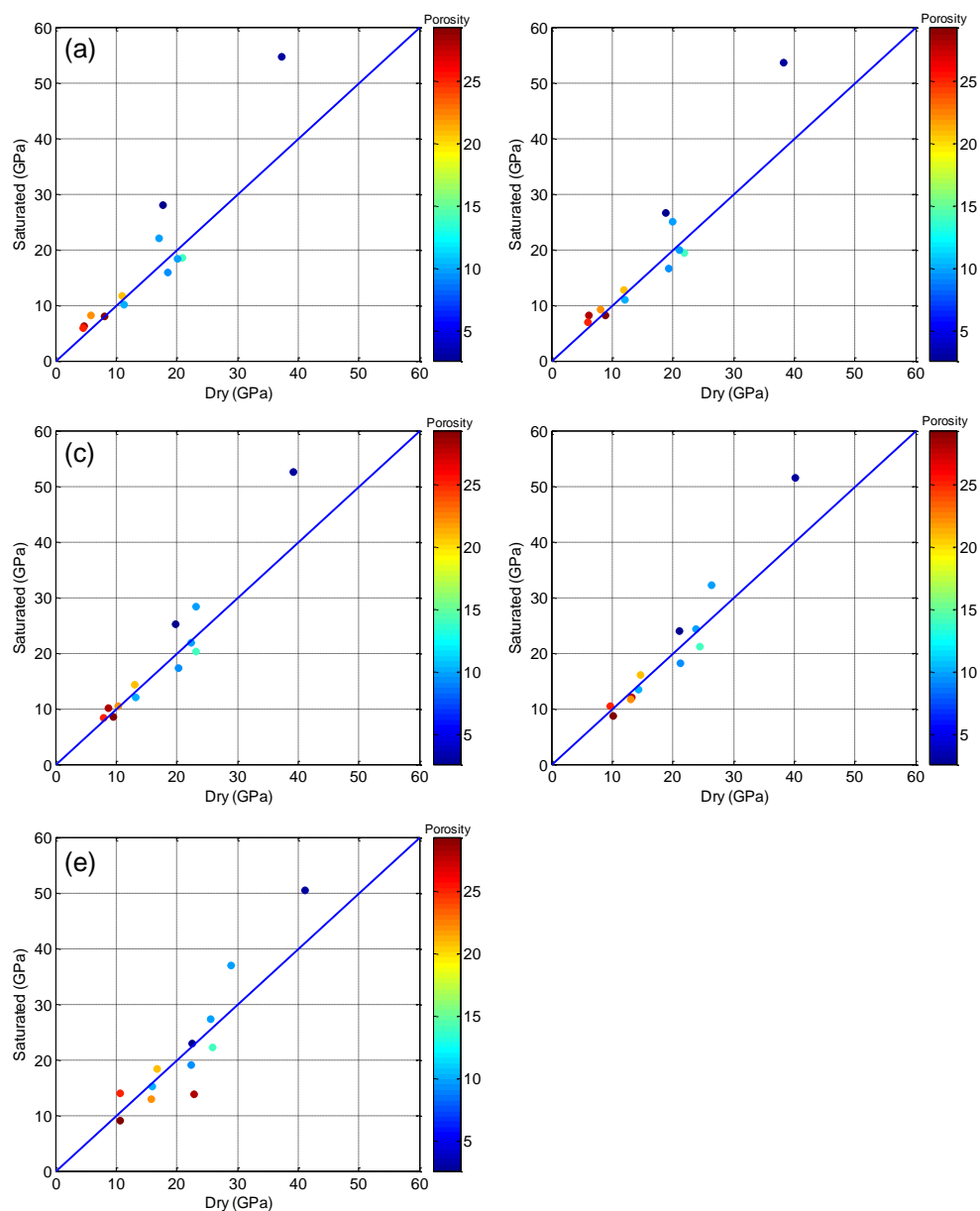


Figure 7.15: Cross plots of dry against saturated static bulk moduli at 5 MPa (a), 10 MPa (b), 15 MPa (c), 20 MPa, (d) and 25 MPa (e) pressure. The data points are color-coded with porosity. The blue line represents where the two moduli are equal.

7.5 Grain bulk modulus

In addition to the measurements of strain on the jacketed test shown in the previous sections, strain measurements were taken onunjacketed samples at pressures from 5 MPa to 65 MPa, to obtain the grain or rock forming minerals' bulk modulus. The rock sample and fused quartz strains were measured simultaneously for calibration and pressure effect corrections. The strains were measured from two different strain gauges bonded vertically and horizontally to the sample vertical axis. Then the static bulk modulus was calculated from the average of the two volumetric strains obtained from the strain gauges by computing the derivative of the stress-volumetric strain curve as described in chapter 5. As described in chapter 4, the (nonporous) grain bulk modulus can be estimated using Voigt-Reuss-Hill average (Hill, 1952). If no isolated pores are present in the rock the unjacketed bulk modulus is identical to the calculated grain bulk modulus.

Figure 7.16 shows the observed grain bulk modulus for sample 4-55 (a) and sample 2-383 (b). Sample 4-55 is almost pure calcite, composed of 99% calcite and 1% Dolomite with porosity equal to 29% and permeability equal to 930 mD. The observed grain bulk modulus vary with pressure and it is between 70 and 74 GPa and the calculated modulus is 73.4 GPa. The changes in the observed modulus with pressure can be ascribed as some small pores penetrated by confining oil at very high pressure. Sample 2-383 made out of 70% calcite and 30% dolomite with a porosity of 10% and 0.1 mD permeability. The observed bulk modulus is from 69-81 GPa and the calculated modulus is 79.5 GPa. The low

permeability value is a possible reason for a change in grain bulk modulus with pressure.

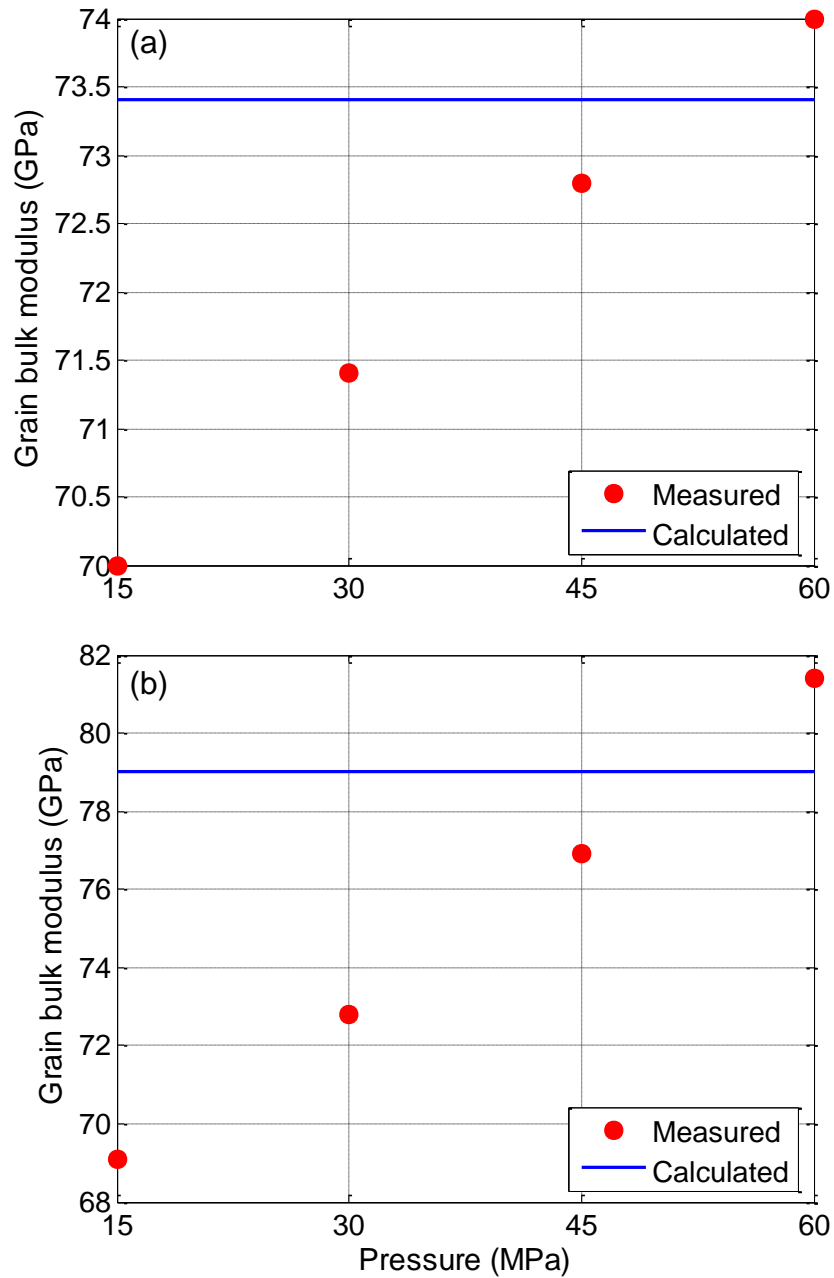


Figure 7.16: Grain bulk modulus for sample 4-55 (a) and sample 2-383 (b). The red dots are the observed grain moduli. The blue line is the grain bulk modulus calculated using Voigt-Reuss-Hill average (Hill, 1952).

7.6 Conclusions

Static and dynamic bulk moduli were measured on 15 samples. The strains were measured from two strain gauges glued parallel and perpendicular to the sample's vertical axis. The strains from the horizontal gauge are higher than the strain from the vertical gauge in most samples; suggesting that the majority of the compliant pores and crack-like pores are oriented, almost in a direction parallel to the cylindrical sample's axis.

In all measured samples both moduli increase with increasing pressure, suggesting that both are influenced by the changes that occur in the rock frame. The dynamic bulk modulus is always higher than static modulus, which might be result of the existence of cracks in the rock and the difference in strain amplitude between the two measurements. These differences between the bulk moduli decreased mostly at higher pressure. There is no correlation between porosity and static-dynamic ratio. The very low porosity samples (7-222, 4-180, 7-20 and 1-11) showed ratio between 0.4 and 0.5. The 100% dolomite showed the lowest static to dynamic. Most of the measured samples show increase of the static moduli after saturation, except three samples with porosity around 10%.

The measured grain bulk modulus obtained from theunjacketed test is reasonably close to the bulk modulus of the constituent mineral phases. The observed grain bulk modulus varies with pressure.

Chapter 8

Conclusion

8.1 Summary

This thesis has presented an extensive set of new measurements of the ultrasonic compressional and shear wave velocities and the quasi-static strain in a series of carbonate samples. The samples were measured under dry and saturation conditions at pressures from 2.5 MPa to 25 MPa. Furthermore, unjacketed quasi-static strain measurements were conducted on selected samples. Uniquely, this study further looked at detail a variety of factors such as the effects of saturation, mineralogy, and pore microstructure on the elastic properties on carbonate rocks.

The compositions of most of the samples are either calcite or dolomite dominant and only a few samples have mixed calcite-dolomite and anhydrite. The samples are free of clay and the additional complications such minerals would bring to the analyses. The pore types of the samples varie in size from macroporosity to microporosity. The macropore types include interparticle pores

(intergrain and intercrystalline), intraparticle, interskeletal, and a few moldic and leached dolomite. The samples can be categorized into three models to the respect of pore size, macropores samples (pore size greater than 10 microns), micropores samples (pore size less than 10 microns) and bi-modal samples that have distributions of both macro- and micropores. It is essential to study the carbonate samples in higher magnification such as SEM. The grains that appear solid in the microscope thin sections are revealed to be highly porous in SEM images, these grains looks more like a sponge.

As is found in nearly all rock types, the P- and S-wave velocities are highly dependent on pressure. The dry velocity dramatically increases with pressure for the most porous samples. As expected the P-wave velocity increases relative to the dry upon full water saturation. The S-wave velocities can either decrease or increase with saturation. Purely mechanical analyses (e.g. Gassmann (1951)) suggest that the S-wave should decrease with saturation; but at face value these results seem to indicate that the shear modulus increases in some cases.

The P- and S-wave velocities in general decrease with increasing porosity. However, a remarkable variability in velocity at a given porosity is observed. We observed velocity changes with mineralogy between calcite-dominant and dolomite-dominant samples, velocity of dolomite dominated samples are higher than those with calcite dominated. The S-wave velocity sometimes behaves different from the P-wave velocity in particular samples which might suggest that the induced deformation that produced by the passage of waves have influence the bulk and shear moduli differently. We believe that in order to accurately study the

factors that affect velocity in carbonate one should look at the texture, grain types, mineralogy, pore types and pore size of the rock as all these elements are contribute together and influence the velocity of the rock.

The comparisons of observed water saturated P-wave velocities to Gassmann (1951), the Biot high frequency (1956), and the Mavko-Jizba (1991) models appears to indicate that Biot global flow is active in these samples. The failure of the Mavko-Jizba (1991) to describe the observed velocities even given measured estimates of the 'soft' pore volume from strain gauges suggests that wave induced 'local' squirt mechanisms are not necessary for these materials. For S-wave velocities, Gassmann's model consistently over-predicts the saturated velocities at low pressure while closely agreeing with the measured velocities at high pressure. The Biot model over-predicts the saturated velocities in most of the studied samples.

Measurements of the static and dynamic bulk moduli in the studied samples demonstrate that both moduli increase with increasing pressure, suggesting that both are influenced by the changes that occur in the rock frame. Dynamic bulk modulus is always higher than static modulus, which might be result of the existence of cracks in the rock and the difference in strain amplitude between the two measurements. The result does not show any remarkable correlation between porosity and static-dynamic ratio, very low porosity samples showed a ratio between 0.4 and 0.5. In most of the studied samples, the static bulk moduli increased after water saturation. The measured grain bulk modulus

obtained from theunjacketed test is reasonably close to the bulk modulus of the constituent mineral phases.

The foremost unique contribution of the research presented here is the velocity and quasi-static strain data itself. With our work, we hope to increase the understanding of the factors that influence elastic properties in carbonate rocks. To our knowledge, these are the first simultaneous measurements of P- and S-wave velocities and quasi-static strain obtained on Arab-D carbonates under in situ pressure conditions.

8.2 Future Directions

The data presented in this work is a rather large and unique data set. The P- and S-wave data and the quasi-static strain data have been processed and analyzed for all the acquired data. In particular, beginning with simple cross plots of P- and S-wave velocities versus porosity. Comparisons between observed saturated velocities and fluid models were discussed. Differences between dynamic and static bulk moduli were investigated. Grain (mineral) bulk modulus was obtained from the results of the unjacketed test. Additional future work on this data set could include calculating of the attenuation as ultrasonic velocity and attenuation are both functions of porosity. Another future work that might lead to improved understanding of the relation between the elastic properties and petrophysical properties in this data set is to measure the pore network using CT scan images. It would be interesting if a low frequency measurement acquired on these samples and compared with the high frequency measurements presented

here. A velocity measured in the field (seismic, VSP and sonic) then could be compared with the lab measurements. Our strain results showed that the static bulk modulus changes with direction of measurements, the static bulk modulus obtained from the vertical gauge is different from the bulk modulus obtained from the horizontal gauge. Thus, it is very interesting to measure anisotropy of the samples using the dynamic measurements.

While these measurements provide some information on the behaviour of carbonate elastic properties, it must be remembered that these small samples are to some degree a biased representation of carbonate rock formations in general. Such formations are known to be highly complex with regards to their pore structures, and such laboratory experiments cannot study larger samples that will have greater pore 'vugs' that can be at the decimetre or larger scale. As such, these data should be seen as providing some insight into the 'intrinsic' properties of the frames of such formations; and the information obtained here should be useful in the development of reservoir scale models that would incorporate larger pores and heterogeneities.

References

- Adams, L . H., and Williamson, E. D., 1923, The compressibility of minerals and rocks at high pressures J. Franklin Inst., 195, 475-529.
- Adam, L., Batzle, M., and Brevik, I., 2006, Gassmann's fluid substitution and shear modulus variability in carbonates at laboratory seismic and ultrasonic frequencies: *Geophysics*, 71, no. 6, F173–F183.
- Adam, L., Batzle, M., Lewallen, K. T. and van Wijk, K., 2009, Seismic wave attenuation in carbonates: *Journal of Geophysical Research*, 114.
- Agersborg, R., Johansen, T., Jakobsen, M., Sothcott, J., and Best, A., 2008, Effects of fluids and dual-pore systems on pressure-dependent velocities and attenuations in carbonates: *Geophysics*, 73, no. 5, N35-N47.
- Alsharhan, A., and Kendall, G., 1986, Precambrian to Jurassic Rocks of Arabian Gulf and Adjacent Areas: Their Facies, Depositional Setting, and Hydrocarbon Habitat: *Bulletin of the American Association of Petroleum Geologists*, p. 977 – 1002.
- Anselmetti, F. S., and Eberli, G. P., 1993, Controls on sonic velocity in carbonates: *Pure and Applied Geophysics*, 141, 287–323.

- Anselmetti, F.S., and Eberli, G.P., 1997, Sonic velocity in carbonate sediments and rocks, in Palaz, I. and Marfurt K.J. (eds.): Carbonate Seismology: SEG Geophysical Developments Series, 6, 53-74.
- Archie, G. E., 1952, Classification of carbonate reservoir rocks and petrophysical considerations: AAPG Bulletin, v. 36, no. 2, p. 278– 298.
- Assefa, S., McCann, C., and Sothcott, J., 2003, Velocities of compressional and shear waves in limestones: Geophysical Prospecting, 51, 1-13.
- Ba, J., Cao, H., Yao, F., Nie, J. and Yang, H., 2008, Double-porosity rock model and squirt flow in the laboratory frequency band: Applied Geophysics, 5 (4): 261-276.
- Baechle, G. T., Weger, R., and Eberli, G. P., 2005, Changes of shear moduli in carbonate rocks: Implication for Gassmann applicability: The Leading Edge, 24, 507-510.
- Baechle, G. T., Eberli, G. P., Weger, R., and Massaferro, J., 2009, Changes of dynamic shear moduli of carbonate rocks with fluid substitution: Geophysics, 74, no. 3, E135-E147.
- Bass, J. D., 1995, Elasticity of minerals, glasses, and melts, *in* T.J. Ahrens, ed., Mineral Physics and Crystallography: A Handbook of Physical Constants: American Geophysical Union, Washington, D.C., 45-63.

- Bathurst, C., 1975, Carbonate sediments and their diagenesis, 2nd ed., Elsevier, Developments in Sedimentology no. 12: p. 39-69 and p. 70-76.
- Batzle, M. L., Simmons, G. and Siegfried, R. W., 1980, Microcrack closure in rocks under stress: direct observation: *Journal of Geophysical Research*, 85, 7072-7090.
- Batzle, M., Han, D., and Hofmann, R., 2006, Fluid mobility and frequency-dependent seismic velocity- direct measurements: *Geophysics*, 71, no. 1, N1-N9.
- Batzle, M. L. and Simmons, G., 1976, Microfractures in rocks from two geothermal areas: *Earth and Planetary Science Letters*, Vol. 30, p.71.
- Batzle, M. and Wang, Z., 1992, Seismic properties of pore fluids: *Geophysics*, 57, 1396-1408.
- Berryman, J. G., 1999, Origin of Gassmann's equations: *Geophysics*, 64, 1627-1629.
- Best, A., 1997, The effect of pressure on ultrasonic velocity and attenuation in near-surface sedimentary rocks: *Geophysical Prospecting*, 45, 345-364.
- Biot, M. A., 1956a, Theory of propagation of elastic waves in a fluid-saturated porous solid: I. Low frequency range: *Journal of the Acoustical Society of America*, 28, 168 -178.

- Biot, M. A., 1956b, Theory of propagation of elastic waves in a fluidsaturated porous solid. II. Higher frequency range: *J. Acoust. Soc. Am.*, 28(2), 179–191.
- Biot, M. A. 1962, Mechanics of deformation and acoustic propagation in porous media: *Journal of Applied Physics*, 34-9, 1254-1264.
- Biot, M. A. and Willis, D.G., 1957, The elastic coefficients of the theory of consolidation: *Journal of Applied Mechanics.*, 24, 594 601.
- Birch, F., 1961, The velocity of compressional waves in rocks to 10 kilobars: *Journal of Geophysical Research*, 66, 2199-2224.
- Brace, WF, 1964, Effect of pressure on electric-resistance strain gages: *Experimental Mechanics*, 4, 212-216.
- Brace, W. F., Silver, E., Hadley, K., and Goetze, C., 1972, Cracks and pores: A closer look: *Science*, 178, 162-764.
- Cantrell, D.L. and Hagerty, R.M., 1999, Microporosity in Arab Formation carbonates: *GeoArabia*, v. 4, p. 129-154.
- Cheng, C. H., and Johnston, D. H., 1981, Dynamic and static moduli: *Geophysical Research Letters*, 8, 39–42.
- Choquette, P.W. and Pray, L.C., 1970, Geological Nomenclature and Classification of Porosity in Sedimentary Carbonates: *American Association of Petroleum Geologists Bulletin*, v. 54, p. 207 250.

- Diallo, M., Prasad, M., and Appel, E., Comparison between experimental results and theoretical predictions for P-wave velocity and attenuation at ultrasonic frequency: *Wave Motion*, 37 (1): 1-16.
- Diallo, M. and Appel, E., 2000, Acoustic wave propagation in saturated porous media: reformulation of the Biot/Squirt flow theory: *Journal of Applied Geophysics*, 44 (4): 313-325.
- Dunham, R. J., 1962, Classification of carbonate rocks according to depositional texture, in W. E. Ham, ed., *Classifications of carbonate rocks symposium*, AAPG Memoir 1, 108-121.
- Dvorkin, J., Nolenhoeksema, R., and Nur, A., 1994, The squirt-flow mechanism-macroscopic description: *Geophysics*, 59 (3): 428-438.
- Ehrenberg, S. N., Nadeau, P. H., and Aqrabi, A. A. M., 2007, A comparison of Khuff and Arab reservoir potential throughout the Middle East: *AAPG Bulletin*, v. 91, p. 275–286.
- Folk, R.L., 1959, Practical petrographic classification of limestones: *American Association of Petroleum Geologists Bulletin*, v. 43, p. 1-38.
- Fjær, E., 2009, Static and dynamic moduli of a weak sandstone: *Geophysics*, 74, no. 2, WA103–WA112.

- Gassmann, F., 1951, Elasticity of porous media: *Über die Elastizität poroser Medien: Vierteljahrsschrift der Naturforschenden Gessellschaft in Zurich*, 96, 1-23.
- Green, D. H., and Wang, H. F, 1986, Fluid pressure response to undrained compression in saturated sedimentary rock: *Geophysics* 51, 948-956.
- Geertsma, J., and Smit, D. C., 1961, Some aspects of elastic wave propagation in fluid-saturated porous solids: *Geophysics*, 26, no. 2, 169-181.
- He, T., 2006, P- and S-wave velocity measurement and pressure sensitivity analysis of AVA response: M.Sc. thesis, University of Alberta.
- Hemsing, D. B., 2007, Laboratory determination of seismic anisotropy in sedimentary rock from the Western Canadian Sedimentary Basin: M.Sc. thesis, University of Alberta.
- Hill, R., 1952, The elastic behaviour of crystalline aggregate: *Proceedings of the Physical Society*, A65, 349-354.
- Ide, J. M., 1963, Comparison of statically and dynamically determined young's modulus of rocks: *Proc. Natl. Acad. Sci. U.S.*, 22(2), 81-92, 1936.
- Jansen, K. M. B., 1997, Effect of pressure on electrical resistance strain gages: *Experimental Mechanics*, 37, No. 3, 245-249.

- Katz, J. and Thompson, A. 1987, Prediction of rock electrical-conductivity from mercury injection measurements: *Journal of Geophysical Research-Solid Earth And Planets* 92 (B1): 599-607.
- Kenter, J. A. M., Braaksma, H., Verwer, K., and van Lanen, X. M. T., 2007, Acoustic behavior of sedimentary rocks: Geological properties versus Poisson's ratios: *The Leading Edge*, 26, 436-444.
- King, M. S., 1970, Static and dynamic elastic moduli of rocks under pressure: 11th U. S. Symposium on Rock Mechanics: American Rock Mechanics Association, Proceedings, 329-351.
- Kular, G. S., 1972, Use of foil strain gage at high hydrostatic pressure: *Experimental Mechanics*, 12, 311-316.
- Kumpel, K. J., 1991, Poroelasticity: parameters reviewed: *Geophysical Journal International*, 105, 783-799.
- Lay, T. and Wallace, T. C., 1995, *Modern global seismology*, vol. 58 of International Geophysics Series, Academic Press, San Diego.
- Lowell, S., and Shields, S., 1991, *Powder surface area and porosimetry: 2nd ed.*, Chapman and Hall, London.
- Lucia, F. J., 1983, Petrophysical parameters estimated from visual descriptions of carbonate rocks: A field classification of carbonate pore space: *Journal of Petroleum Technology*, v. 216, p. 221-224.

- Lucia, F. J., 1995, Rock-fabric/physical classification of carbonate pore space for reservoir characterization: AAPG Bulletin, v. 79, no. 9, p. 1275–1300.
- Lucia, F. J., 1999, Carbonate reservoir characterization: Berlin, Springer-Verlag, 226 p.
- Mah, M., and Schmitt, D. R., 2001a, Experimental determination of the elastic coefficients of an orthorhombic material: Geophysics, 66, 1217-1225.
- Mavko, G., and Jizba, D., 1991, Estimating grain-scale fluid effects on velocity dispersion in rocks: Geophysics, 56, 1940-1949.
- Mavko, G., Mukerji, T., and Dvorkin, J., 1998, The rock physics handbook: Tools for seismic analysis in porous media: Cambridge University Press.
- Milligan, R.V., 1967, The gross hydrostatic-pressure effect as related to foil and wire strain gages: Experimental Mechanics, 7, No. 2, 67-74.
- Molyneux, J. B., and D. R. Schmitt, 1999, First break timing: Arrival onset times by direct correlation: Geophysics: 64, 1492-1501.
- Nie, J., Yang, D., and Yang, H., 2008, A generalized viscoelastic Biot/squirt model for clay-bearing sandstones in a wide range of permeabilities: Applied Geophysics, 5 (4): 249-260.
- Oconnell, R., and Budiansk, B., 1974, Seismic velocities in dry and saturated cracked solids: Journal of Geophysical Research, 79 (35): 5412-5426.

- Oconnell, R., and Budiansky, B., 1977, Viscoelastic Properties of fluid-saturated cracked solids: *Journal of Geophysical Research*, 82 (36): 5719-5735.
- Pittman, E.D., 1971, Microporosity in Carbonate Rocks: *American Association of Petroleum Geologists Bulletin*, v. 55, p. 1873-1881.
- Potter, I., 2007, Alberta carbonates: Prime candidate for the 3rd trillion and beyond: SPE R&D conference.
- Rafavich, F., Kendall, C., and Todd, T., 1984, The relationship between acoustic properties and the petrographic character of carbonate rocks: *Geophysics*, 49, 1622-1636.
- Raymer, L. L., Hunt, E. R., and Gardner, J. S., 1980, An improved sonic transit-time-porosity transform: *Soc. Prof. Well Log Analysts, 21st Annual Logging Symposium Transactions*.
- Reuss, A., 1929, Berechnung der fließgrenze von mischkristallen auf grund der plastizitatbedingung fur einkristalle: *Zeitschrift fur Angewandte Mathematik aus Mechnik*, 9, 49–58.
- Rogen, B., Fabricius, I. L., Japsen, P., Hoier, C., Mavko, G., and Pedersen, J. M., 2005, Ultrasonic velocities of North Sea chalk samples: Influence of porosity, fluid content and texture: *Geophysics*, 53, 481–496.
- Schmitt, D.R., and Zoback, M., Poroelastic effects in the determination of the maximum horizontal principal stress in hydraulic fracturing tests: a proposed

breakdown equation employing a modified effective stress relation for tensile failure, *Int. J. Rock Mech. Mining Sci. & Geomech. Abstr.*, 26, 499-506, 1989.

Schmitt, D.R., and Li, Y.Y., A high pressure technique for determining the microcrack porosities of damaged brittle materials, *Can. J. Phys.*, 73, 330-337, 1995.

Schmitt, D. R., 1999, Seismic attributes for monitoring of a shallow heated heavy oil reservoir: A case study: *Geophysics*, 64, 368–377.

Schock, R. N., and Heard, H. C., 1974, Static mechanical properties and shock Loading Response of Granite *Journal of Geophysical Research*, vol. 79, issue 11, pp. 1662-1666

Scotellaro, C., Vanorio, T., and Mavko, G., 2007, The effect of mineral composition and pressure on carbonate rocks: Presented at the 77th Annual International Meeting, SEG.

Sharma, M.M. and Tutuncu, A.N., 1994, Grain contact adhesion hysteresis: A mechanism for attenuation of seismic waves: *Geophysical Research Letters*, vol. 21, no. 21, Pages 2323-2326.

Siggins, A. F. 1993: Dynamic elastic tests for rock engineering. In: Hudson, J. A. (ed.), *Comprehensive rock engineering*, 3(24). Pergamon Press, Oxford, 601-618.

- Simmons, G., and Brace, W. F., 1965, Comparison of static and dynamic measurements of compressibility of rocks: *Journal of Geophysical Research*, 70, 5649–5656.
- Thompson, A., Katz, A., and Raschke, R., 1987, Mercury injection in porous-media - a resistance devils staircase with percolation geometry: *Physical Review Letters* 58 (1): 29-32.
- Toksöz M. N., Cheng, C. H. and Timur, A., 1976, Velocities of seismic waves in porous rocks: *Geophysics*, 41, 621-645.
- Tutuncu A. N., Sharma, M. M., and Podio, A. L., 1995, Hysteresis observed in stress-strain diagrams and its relation to adhesion hysteresis and stick-slip sliding in sedimentary granular rocks, *in* J. J. K. Daemen, and R. A. Schultz, eds., *Rock mechanics: Proceedings of the 35th U.S. symposium*: Balkema, 801–806.
- Vanbrakel, J., Modry, S., and Svata, M., 1981, Mercury Porosimetry - state of the art: *Powder Technology* 29 (1): 1-12.
- Verwer, K., Kenter, J. A. M., Braaksma, H., and van Lanen, X. M. T., 2008, Acoustic properties of carbonates: Effects of rock texture and implications for fluid substitution, *Geophysics*, 73, B51-B65.
- Voigt, W., 1928, *Lehrbuch der Kristallphysik*: Teubner.

- Walsh, J., and Brace, W., 1972, Elasticity of rock in uniaxial strain: *International Journal of Rock Mechanics and Mining Sciences*, 9, no. 1, p. 7-15.
- Walsh, J. B., 1965, The effect of cracks on the compressibility of rock: *Journal of Geophysical Research*, 70, 381-389.
- Wang, Z., 1997, Seismic properties of carbonate rocks, in I. Palaz and K. J. Marfurt, eds., *Carbonate seismology: Geophysical Developments*, 6, 29-52.
- Washburn, E. W., 1921, Note on a method of determining the distribution of pore sizes in a porous material: *Proceedings of the National Academy of Sciences*: 7, 115-116.
- Winkler, K.W., 1983, Contact stiffness in granular porous materials: comparison between theory and experiment: *Geophys. Res. Lett.* 10, pp. 1073-1076.
- Winkler, K., 1986, Estimates of velocity dispersion between seismic and ultrasonic frequencies: *Geophysics*, 51 (1): 183-189.
- Wood, A. B., 1941, *A textbook of sound*: G. Bell and Sons.
- Wyllie, M. R. J., Gregory, A. R., and Gardner, G. H. F., 1958, An experimental investigation of factors affecting elastic wave velocities in porous media: *Geophysics*, 23, 459-493.

Qi, Xun (Pas), Simulation and laboratory measurements of velocity and attenuation in viscoelastic body: A frequency dependent study with respect to viscosities, Dept. of Physics, Univ. of Alberta, 208 pp., December, 2008.

Zisman, W. A., 1933, Comparison of statically and seismologically determined elastic constants of rocks: Pro. Natl. Acad. Sci., U.S., 19, 680-686.

Appendix A

Petrographic Descriptions and Petrophysical Data

A detail description of the samples is essential in order to fully understand and interpret the laboratory measurements. In the text we showed descriptions of few selected samples. In here we present a complete petrographic analysis using microscopic thin sections, SEM images and mercury intrusion data. Petrographic analysis using microscopic thin sections for most of the samples were obtained from Saudi Aramco, but for a subset additional thin sections were made in the Department of Earth and Atmospheric Sciences at the University of Alberta. Pore size distributions using mercury porosimetry (Micromeritics Autopore IV) on selected samples were measured in the rock physics lab in Department of Physics at University of Alberta. In addition SEM images (Scanning Electron Microscope)

on selected samples were obtained in Department of Earth and Atmospheric Sciences at the University of Alberta.

Sample 2-10 (2037.07 m)

Sample 2-10 (figure A.1) is dolomitic peloidal skeletal grainstone. The dominant mineral in this sample is dolomite making up to 94 % of the mineralogy followed by a small amount of anhydrite (4%) and negligible calcite content (1%). Two third of the grains in this rock are fine to medium peloids (62 %) and one third of the grains are skeletal (31 %). The majority of the skeletal grains are gastropod origin (70%) and the remaining 30 % is of aragonitic bivalve origin. The nature of the dolomitization suggests a fabric preserving dolomite.

Sample air permeability is 65.1 mD and the associated porosity is 30.3 %. The primary pore types (interparticles) are 25 % and the remaining 75 % are represented by secondary pores (moldic). The dominant pore size is micropores less than 10 micron (figure A.2).

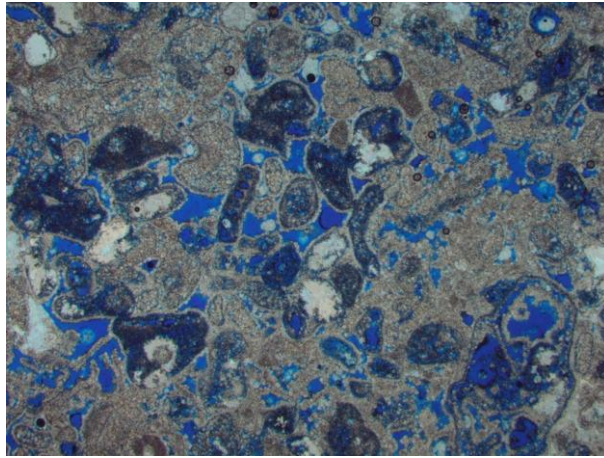


Figure A.1: Thin section photomicrograph of sample 2-10 depicting peloids and skeletal grains. Porosity is filled by blue-dyed epoxy (Mag. 1.5x).

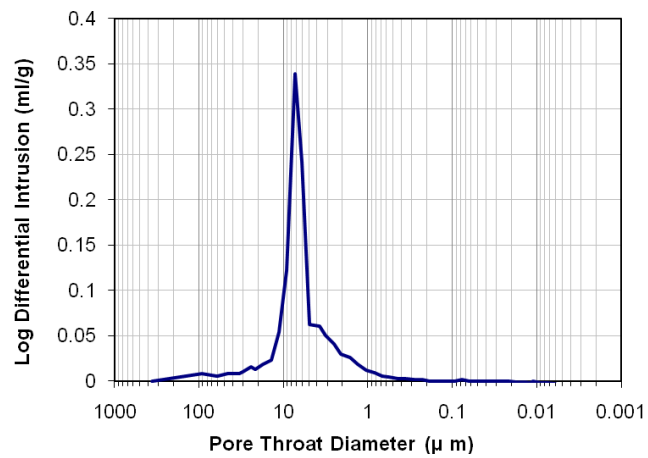


Figure A.2: Pore throat size distribution of sample 2-10, shows that the dominant pore size is less than 10 μm .

Sample 2-33 (2041.24 m)

Sample 2-33 (figure A.3) is ooid grainstone. The dominant mineral is calcite (99 %) with a negligible amount of anhydrite. Seventy percent of the constituent grains are oolites and about one third of the grains are skeletal (23 %). The bulk of the skeletal grains are forams (47%) and dasyclads (31%). In addition to these, there are echinoderms (13%), brachiopods (3%), gastropod (1%) and 5% undifferentiated remains. These grains are cemented by blocky and rim cements.

The sample is relatively of high permeability (1004.4 mD) and its porosity is 30.9 %. Almost more than half of this porosity is contributed by macropores (16.9%) while the remaining comes from micropore (figure A.4). Primary pore types (interparticles) are dominant 73%, and the additional present secondary pore types include intraskeletal (22%) and intaparticle (5%).

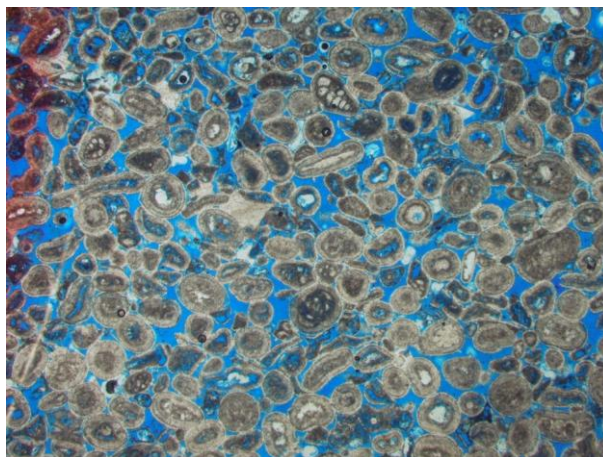


Figure A.3: Thin section photomicrograph of sample 2-33 showing ooids and skeletal grains with associated interparticle and intraparticle pore types. Porosity is filled by blue-dyed epoxy (Mag. 1.5x).

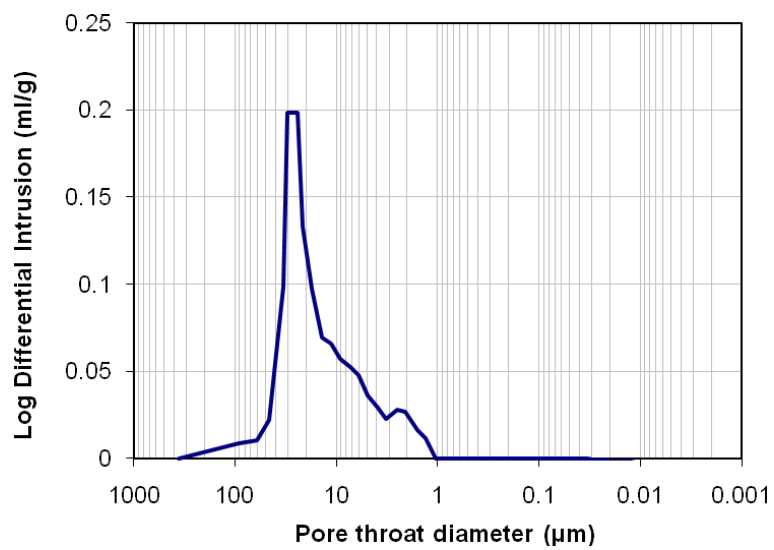


Figure A.4: Pore throat size distribution of sample 2-33, shows that the dominant pore size is greater than 10 μm .

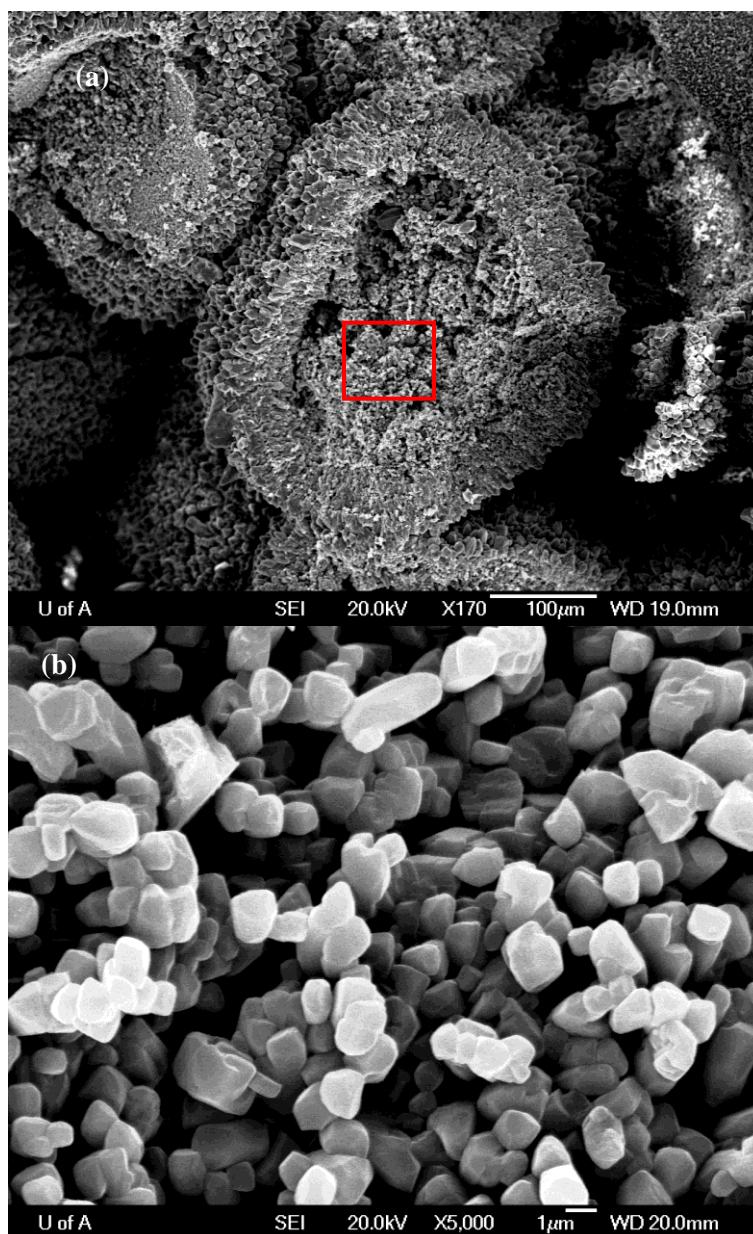


Figure A.5: (a) Microporous grains showing intraparticle pore, (b) higher magnification view of area outlined in (a), the microporous grain showing microporosity between calcite crystals.

Sample 2-59 (2045.39 m)

Sample 2-59 (figure A.6) is peloidal skeletal packstone. Calcite is the dominant mineral (95 %) and followed by 5% dolomite. Forty seven percent of the constituent grains are very fine to medium peloid, 35% skeletal and 12% lime mud. The skeletal grains are forams (21%), thau (21%), dasyclads (27%), echinoderms (13%), brachiopods (7%), bivalve (6%), sponge spicule (2%) and 3% undifferentiated remains. The cements are blocky and rim. The permeability is (33.7 mD) and the porosity is 32.5 %. Most of this porosity is of micropore (24.5%) and only eight percent is macropores (figure A.7). Interparticle pore types are the dominant 85%, and there are also intraskeletal (11%) and moldic (4%) pore types.

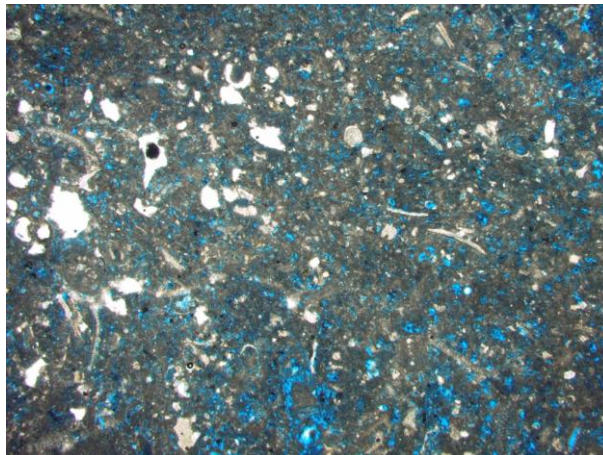


Figure A.6: Thin section photomicrograph of sample 2-59 showing peloids, skeletal and lime mud with associated interparticle, intraskeletal and moldic pore types. Porosity is filled by blue-dyed epoxy (Mag. 1.5x).

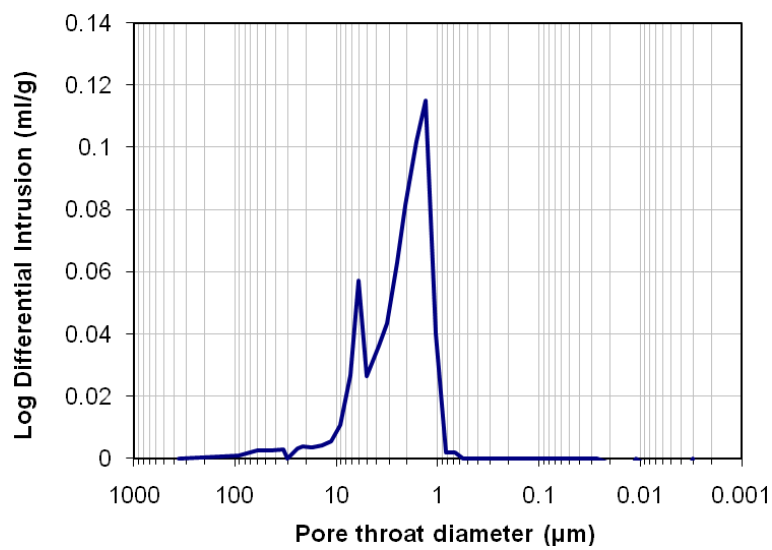


Figure A.7: Pore throat size distribution of sample 2-59, shows that the dominant pore size is less than 10 μm .

Sample 2-131 (2057.28 m)

Sample 2-131 (figure A.8) is peloidal skeletal packstone. Calcite is the dominant mineral (96 %) and followed by 4% dolomite. Forty percent of the constituent grains are fine to coarse peloids, 50% skeletal, 2% intraclasts and 6% lime mud. The skeletal grains are forams (35%), thaum (12%), dasyclads (47%), echinoderms (3%) and brachiopods (3%). The cement is blocky calcite.

The permeability is (469.1 mD) and the porosity is 25.1 %. This porosity is half micropores and the other half macropores. Interparticle pore types are the dominant 94%, and there are also intraparticle (4%) and intraskeletal (2%). SEM images show microporosity in side peloids and skeletal grains (figure A.9).

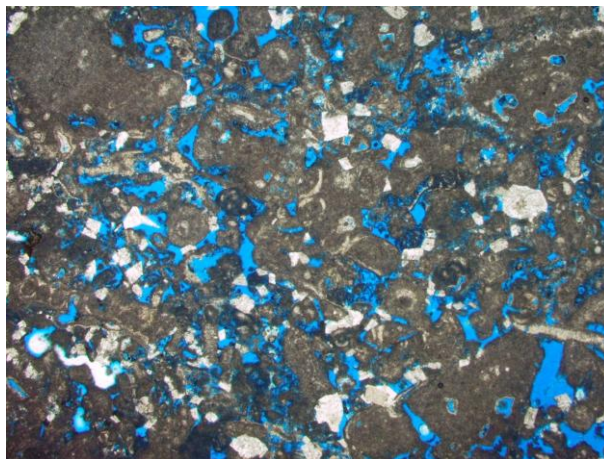


Figure A.8: Thin section photomicrograph of sample 2-131 showing peloids and skeletal grains with associated interparticle and intraskeletal pore types. Porosity is filled by blue-dyed epoxy (Mag. 1.5x).

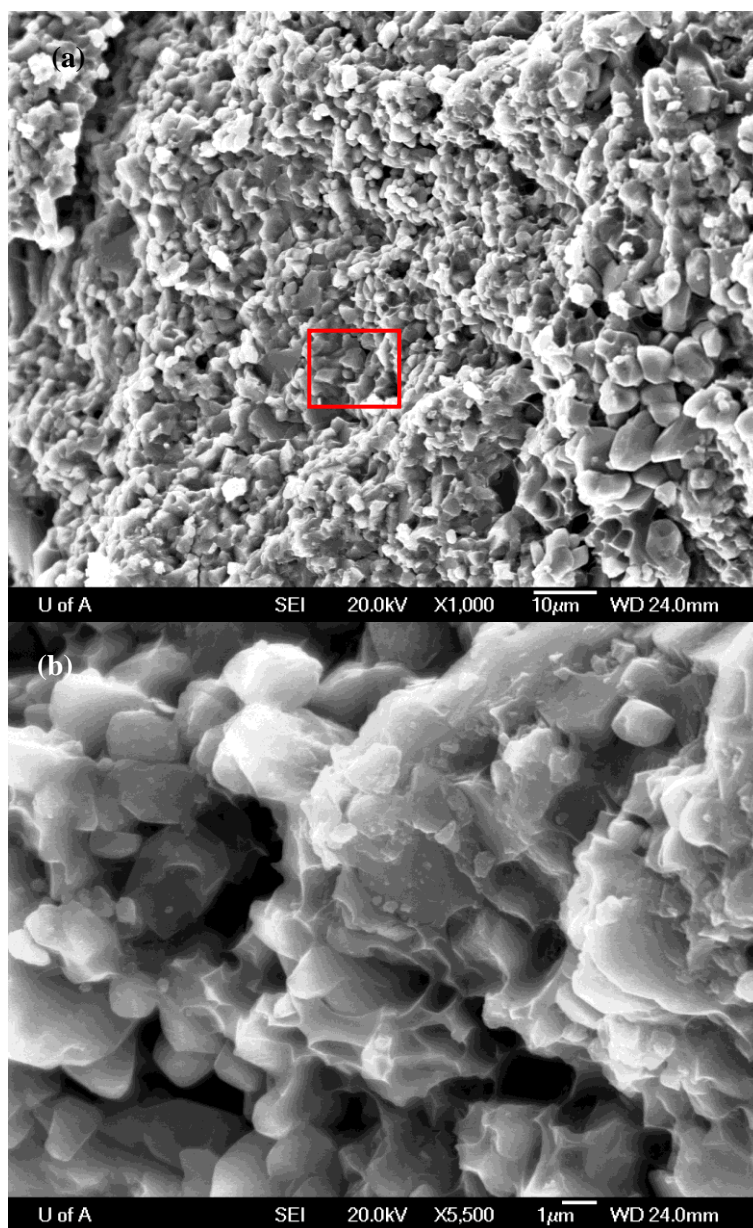


Figure A.9: (a) Microporous grains showing intraparticle pore, (b) higher magnification view of area outlined in (a) in the microporous grain showing microporosity between calcite crystals.

Sample 2-160 (2062.31 m)

Sample 2-160 (figure A.10) is peloidal skeletal packstone. Calcite is the dominant mineral (94 %) and followed by 6% dolomite. Twenty four percent of the constituent grains are fine to coarse peloids, 43% skeletal and 12% lime mud. The skeletal grains are forams (32%), cladocropsis (13%), thaum (13%), dasyclads (38%) and echinoderms (1%). The cements are rim and blocky calcite.

The permeability is (196.1 mD) and the porosity is 26.5 %. Interparticle pore types are the dominant 88%, and there are also moldic (5%), intraparticle (1%) and intraskeletal (6%). Mercury intrusion curve shows dual porosity model (figure A.11), and microporous skeletal grains shown in figure A.12.

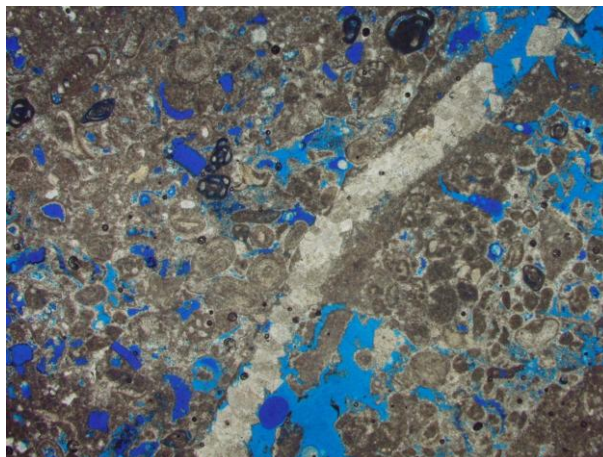


Figure A.10: Thin section photomicrograph of sample 2-160 showing peloids and skeletal grains with associated interparticle, moldic and intraskeletal pore types. Porosity is filled by blue-dyed epoxy (Mag. 1.5x).

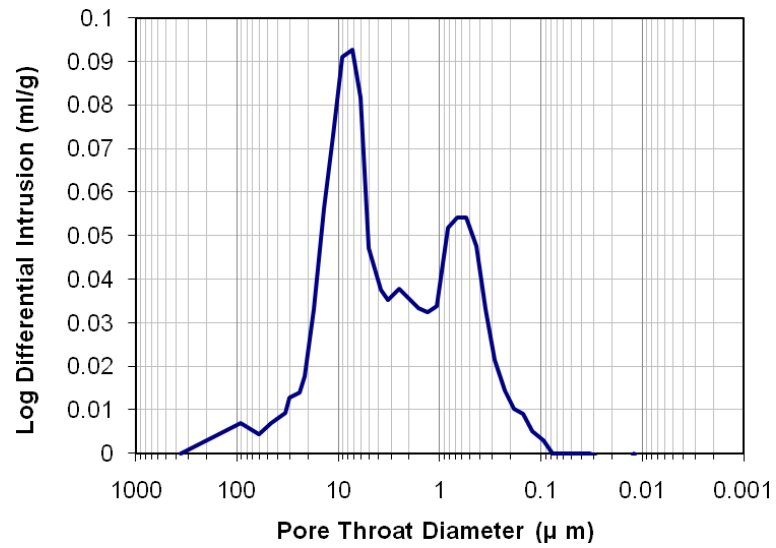


Figure A.11: Pore throat size distribution of sample 2-160, shows two peaks that fall on both sides of the 10 micron benchmark (Dual porosity).

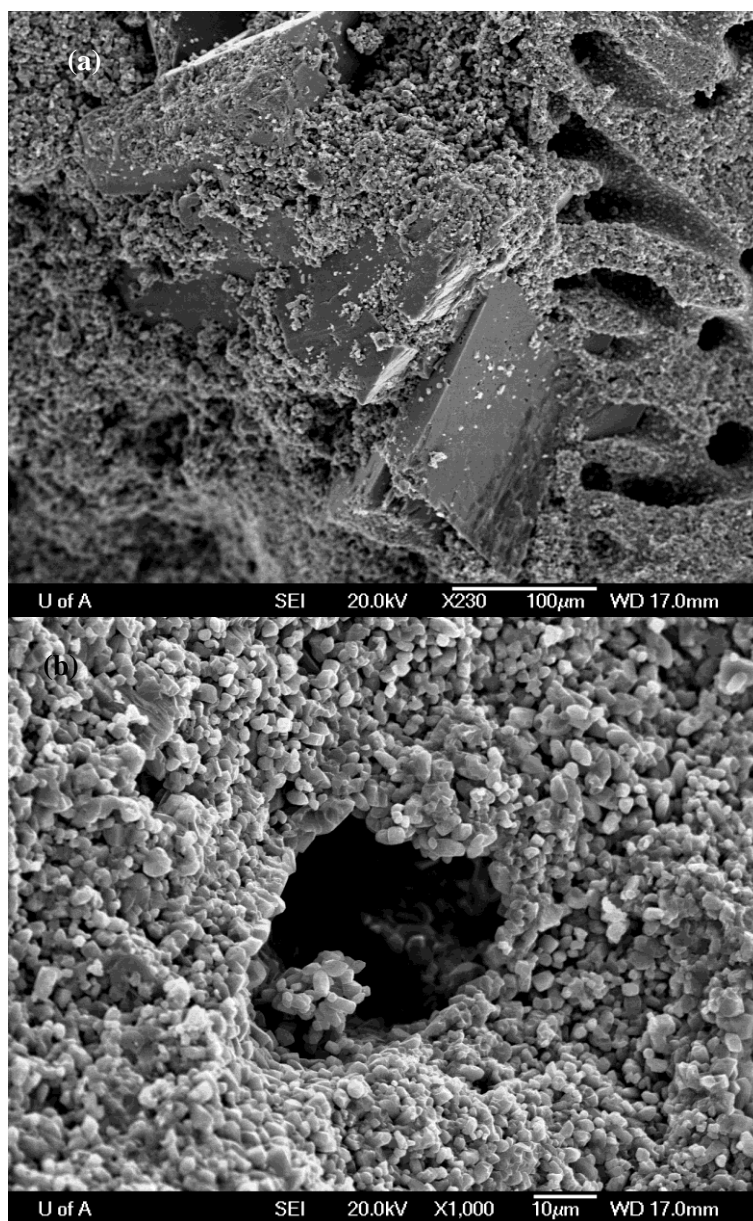


Figure A.12: (a) Microporous skeletal grain showing intraparticle pore, (b) higher magnification view of area outlined in (a) in the microporous grain showing microporosity between calcite crystals.

Sample 2-368 (2096.48 m)

Sample 2-368 (figure A.13) is dolomitic lime mudstone. Dolomite makes up of 78% of the minerals while calcite constitutes (21.5 %) and quartz 0.5%. There are no grains and the sample is exclusively dolo-lime mud.

The permeability is 0.01 mD and the porosity is 3.5 % mainly micropores (figure A.14).

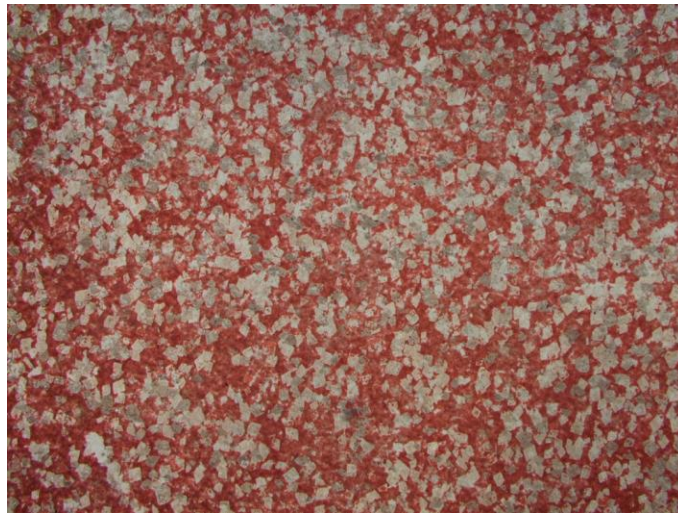


Figure A.13: Thin section photomicrograph of sample 2-368 showing fine dolomite crystals with associated intercrystal pore types. Calcite is stained red, other minerals are unstained (Mag. 1.5x).

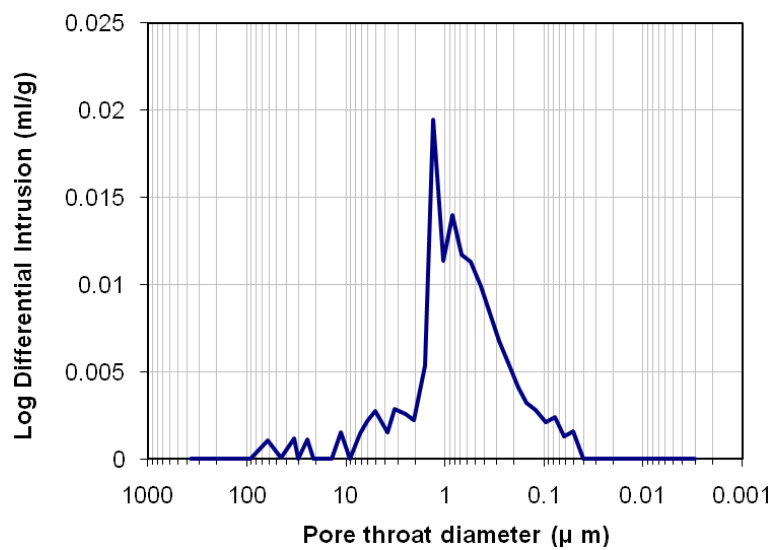


Figure A.14: Pore throat distribution of sample 2-368, shows the dominant pore size is less than $10 \mu m$.

Sample 2-383 (2098.88 m)

Sample 2-382 (figure A.15) is dolomitic coated grain lime mudstone. Calcite is (69.5 %) and dolomite is (30%) also there is a trace amount of quartz (0.5%). Fifty percent of the constituent grains are very fine to medium peloids, 27% coated grains and 23% skeletal. The skeletal grains are forams (22%), dasyclads (17%), echinoderms (38%), sponge spicules (8%) and undifferentiated fragments (15%). The permeability is 0.1 mD and the porosity is 9.6 %. This porosity is exclusively macropores.

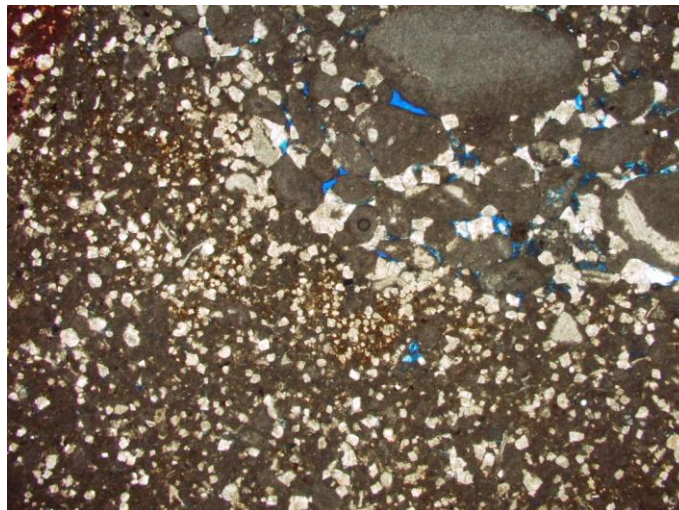


Figure A.15: Thin section photomicrograph of sample 2-383 showing coated grains, peloids and skeletal grains with associated interparticle pores. Porosity is filled by blue-dyed epoxy (Mag. 1.5x).

Sample 2-432 (2108.3 m)

Sample 2-432 (figure A.16) is sponge spicule wackestone. Calcite is (95.5 %) and dolomite is (4%) also there is a trace amount of quartz (0.5%). Eighty five percent of the sample is lime mud and the remaining 15% is skeletal. The permeability is less than 0.1 mD and the porosity is 6 %. This porosity is mainly micropores (4%) and macropores (2%). There are no fractures.

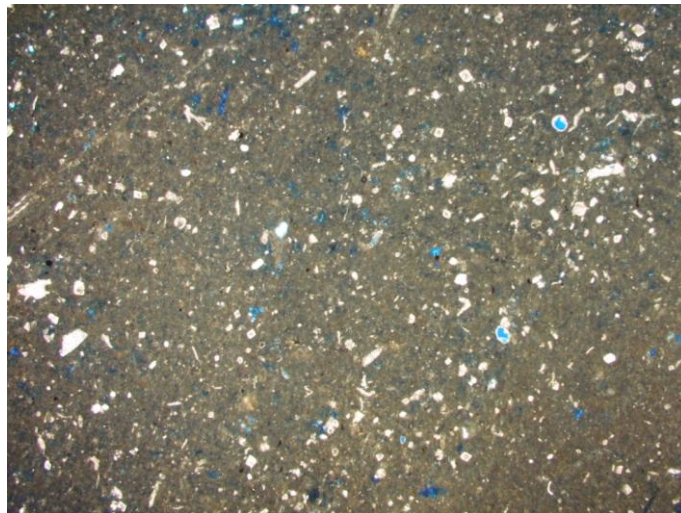


Figure A.16: Thin section photomicrograph of sample 2-432 showing grains and lime mud with associated prevalently moldic pores. Porosity is filled by blue-dyed epoxy (Mag. 1.5x).

Sample 3-05 (2175.42 m)

Sample 3-05 is dolomitized grainstone and wackestone. The sample is 48% dolomite, 2% calcite and 50% anhydrite. Fifty percent of the sample are bedded anhydrite, 18% coated grains, 6% very fine peloids, 8% skeletal and 10% lime mud. The skeletal grains are corals (40%), gastropods (35%), bivalve (20%) and forams (5%). The cements are rim and blocky calcites.

Permeability is very low (0.2 mD) and porosity is 5 %. Most of the porosity is macropores. The pore types are moldic (70%), intraparticle (15%) and intraskeletal (15%). Mercury intrusion curve shows dual porosity model (figure A.17).

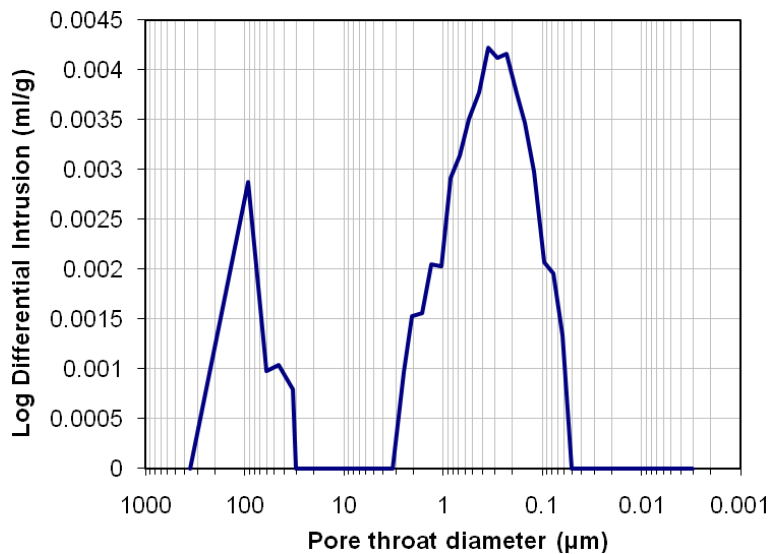


Figure A.17: Pore throat size distribution of sample 3-05, shows two peaks that fall on both sides of the 10 micron benchmark (dual porosity)..

Sample 3-90 (2188.37 m)

Sample 3-90 (figure A.18) is peloidal skeletal grainstone. Its mineralogy is 100% calcite. Fifty nine percent of the grains are fine to coarse peloids and thirty nine percent are skeletal. The skeletal grains are forams (46%), dasyclads (22%), echinoderms (22%) and thaum (10%). The cements are rim and blocky calcites.

The Sample is high permeability 2263 mD and the porosity is 32 %. Most of the porosity is macropores (27%) and small amount is micropores (5%). The pore types are interparticles 90%, intraparticle and intraskeletal 5% each with size greater than 10 microns (figure A.19). Figure A.20 shows Microporous skeletal grains.

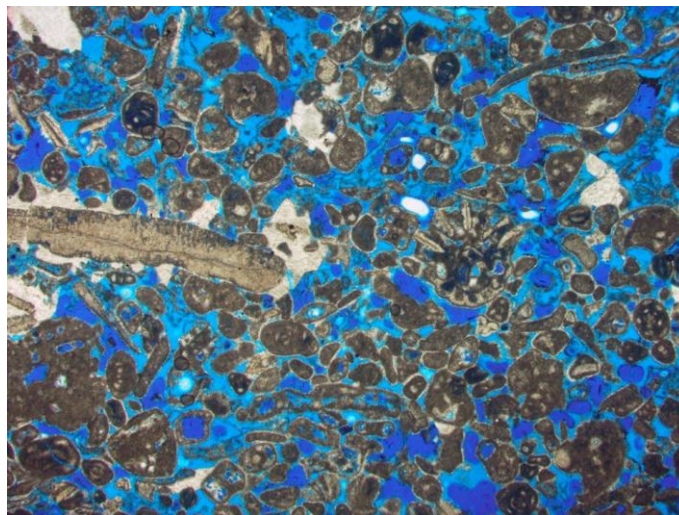


Figure A.18: Thin section photomicrograph of sample 3-90 showing peloids and skeletal grains with associated dominant pore types. Porosity is filled by blue-dyed epoxy (Mag. 1.5x).

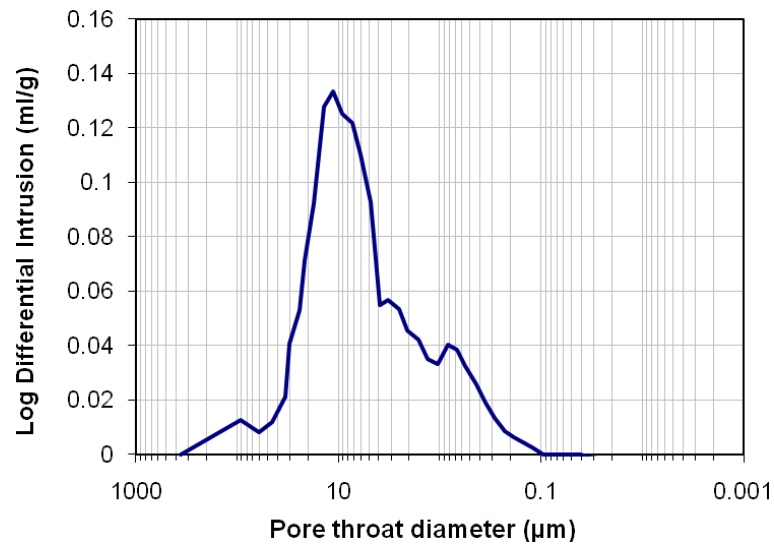


Figure A.19: Pore throat size distribution of sample 3-90, shows two peaks that fall on both sides of the 10 micron benchmark.

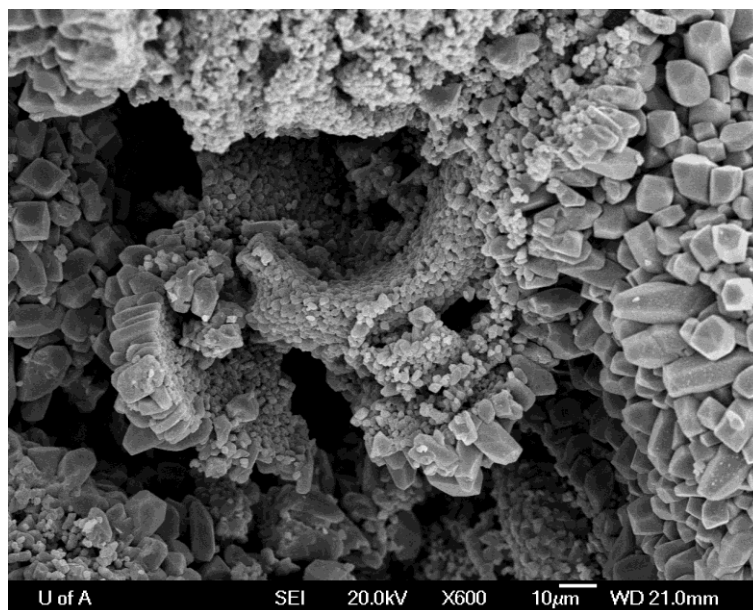


Figure A.20: Microporous skeletal grains.

Sample 3-104 (2190.5 m)

Sample 3-104 (figure A.21) is skeletal peloidal grainstone with 100% calcite. 42% of the grains are fine to coarse peloids and 45% are skeletal. The skeletal grains are forams (35%), dasyclads (28%), echinoderms (25%), thaum (6%) and fibrous (6%). Permeability is 766.6 mD and the porosity is 30.3 % mainly interparticle. Mercury intrusion curve shows dual porosity model (figure A.22).

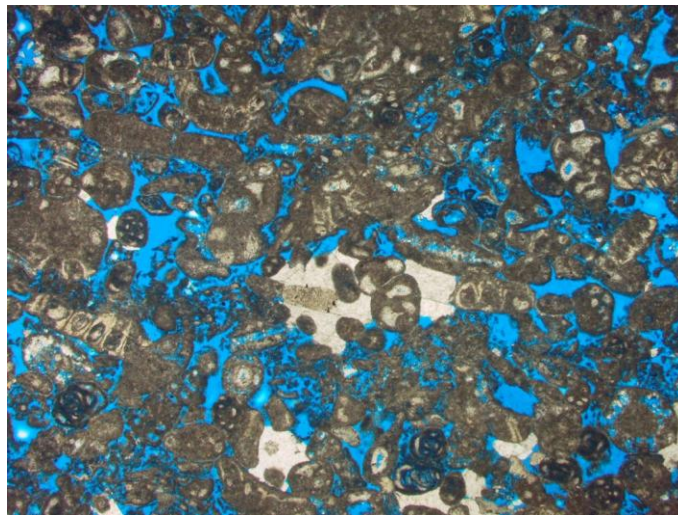


Figure A.21: Thin section photomicrograph of sample 3-104 showing peloids and skeletal grains. Porosity is filled by blue-dyed epoxy (Mag. 1.5x).

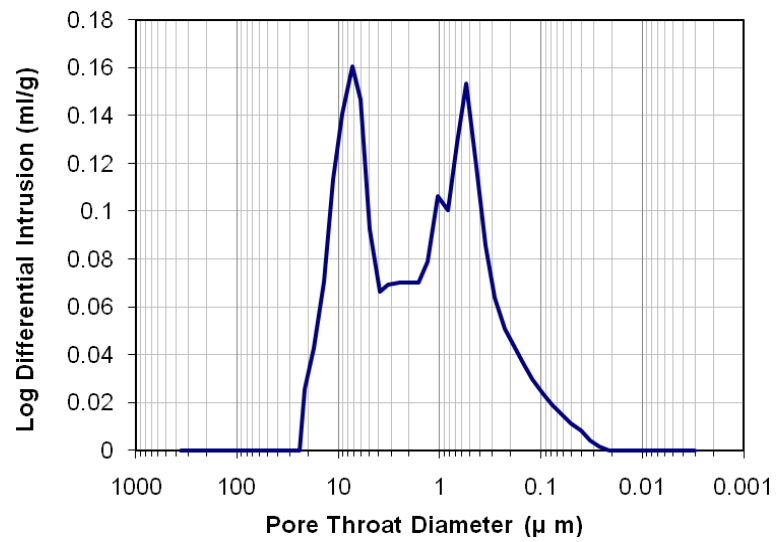


Figure A.22: Pore throat size distribution of sample 3-104, shows two peaks that fall on both sides of the 10 micron benchmark (Dual porosity).

Sample 3-146 (2196.75 m)

Sample 3-146 (figure A.23) is coral peloidal floatstone with 100% calcite. Forty two percent of the grains are fine to coarse peloids, forty eight percent are skeletal and six percent intraclasts. The skeletal grains are corals (60%), forams (26%), dasyclads (28%) and thaum (1%).

Permeability is 1193 mD and the porosity is 29 %. Most of the porosity is macropores (24%) and few are micropores (figure A.24). The pore types are interparticles 78%, intraparticle (5%) and intraskeletal 17%. Mercury intrusion curve shows dual porosity model (figure A.24).

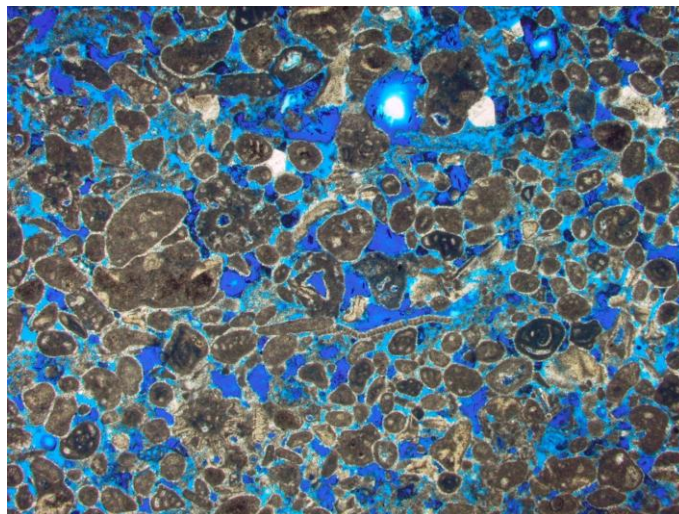


Figure A.23: Thin section photomicrograph of sample 3-146 showing peloids and skeletal grains. Porosity is filled by blue-dyed epoxy (Mag. 1.5x).

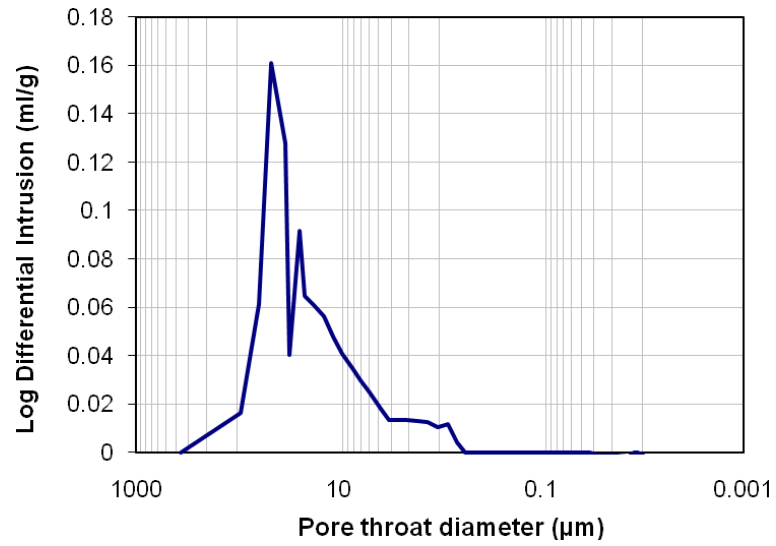


Figure A.24: Pore throat size distribution of sample 3-146, shows that the dominant pore size is greater than 10 μm .

Sample 3-331 (2224.796 m)

Sample 3-331 (figure A.25) is oncolite coated grains floatstone with 99% calcite with trace amounts of dolomite. Forty percent are coated grains, thirty five percent are oncolites, eleven percent skeletal and ten percent fine to coarse peloids.

Permeability is 3345.4 mD and the porosity is 23.8 %. Most of the porosity is macropores (figure A.26). The pore types are interparticles 90%, intraparticle 6% and intraskeletal 4% (figure A.27).

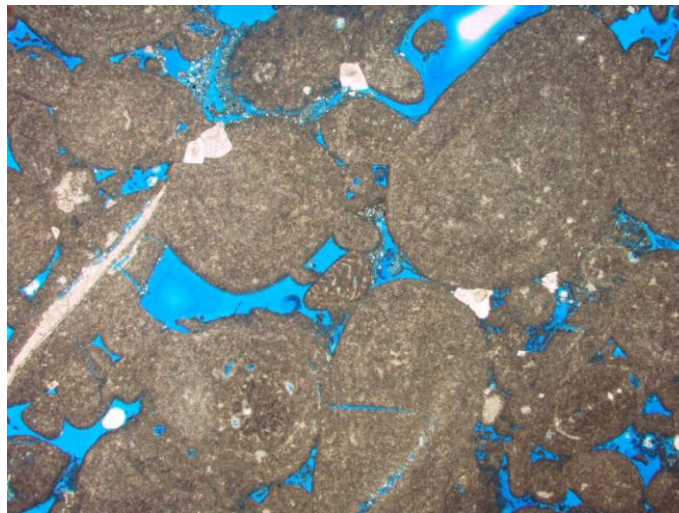


Figure A25: Thin section photomicrograph of sample 3-331 showing peloids and skeletal grains. Porosity is filled by blue-dyed epoxy (Mag. 1.5x).

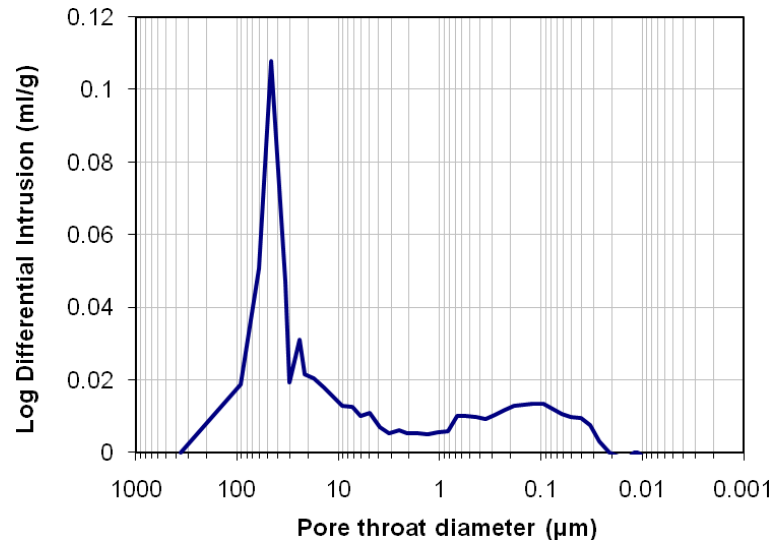


Figure A.26: Pore throat size distribution of sample 3-331, shows that the dominant pore size is around $50 \mu\text{m}$.

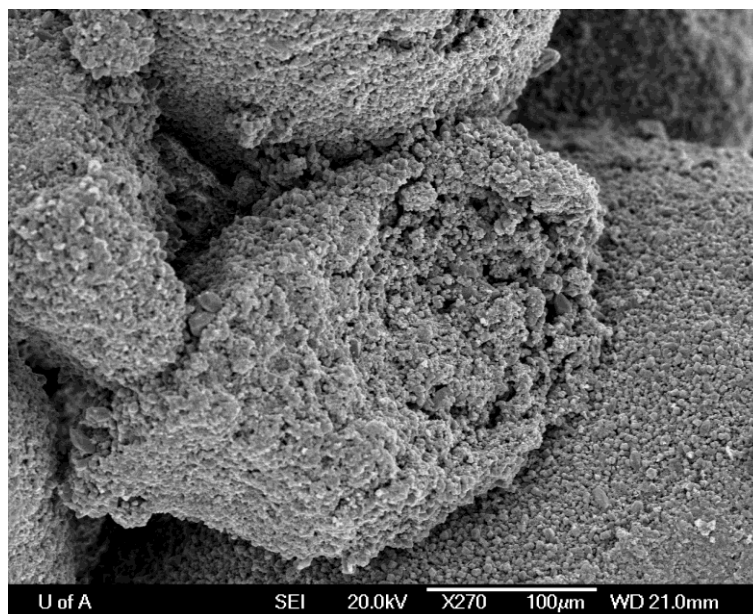


Figure A.27: SEM images showing the interparticle pores and micropores.

Sample 3-429 (2240 m)

Sample 3-429 (figure A.28) is dolo-wackestone consists of 100% dolomite crystals. Permeability is 0.1 mD and the porosity is 10.2 %. Most of the porosity is macropores (9%). The pore types are leached dolomites (85%) and intercrystalline (15%).

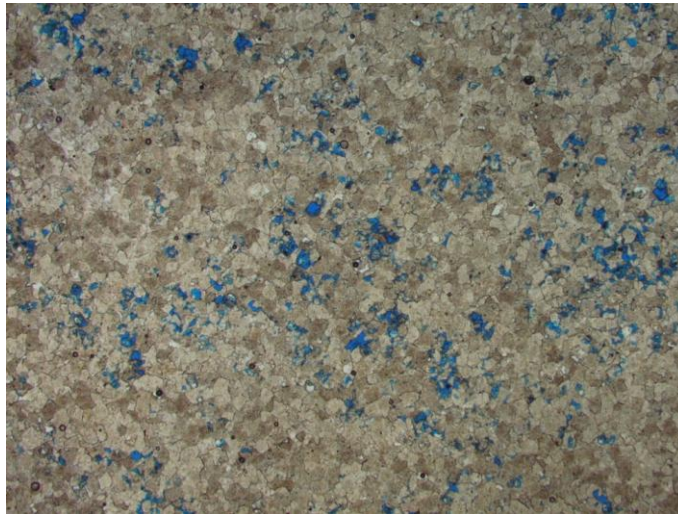


Figure A.28: Thin section photomicrograph of sample 3-429 showing dolomite crystals with leached dolomite pores. Porosity is filled by blue-dyed epoxy (Mag. 1.5x).

Sample 3-471 (2246.4 m)

Sample 3-471 (figure A.29) is lime mudstone. The dominant mineral is calcite 71.5% and 28% dolomite. The sample made of ninety two percent lime mud, seven percent skeletal and one percent coated grains. Permeability is less than 0.01 and the porosity is 3.3 %. The dominant pore type is micropores.

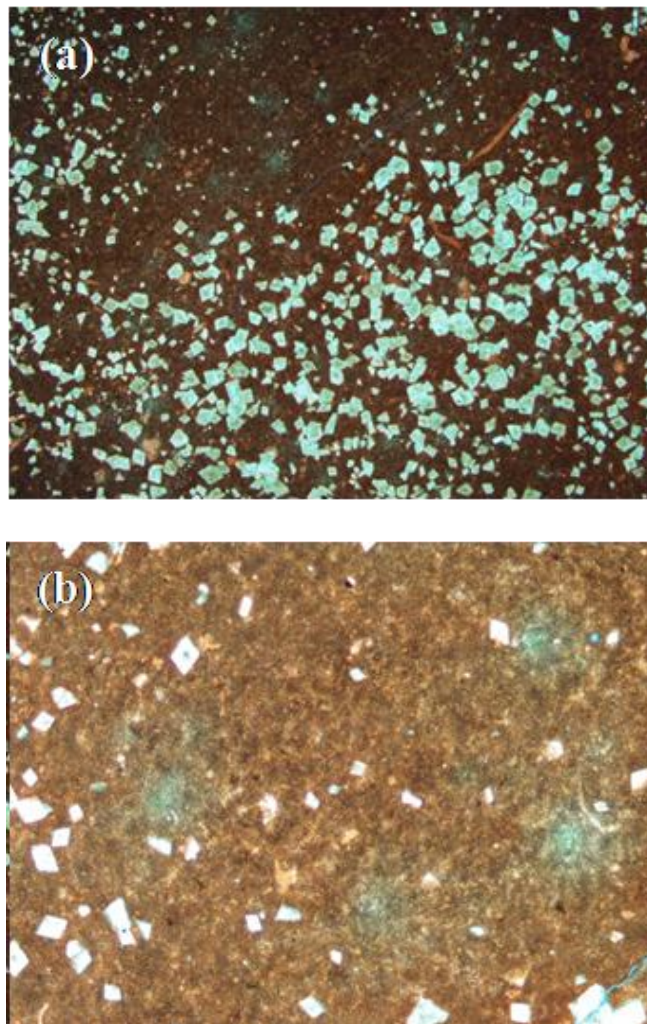


Figure A.29: (a) Thin section photomicrographs of sample 3-471 showing lime mud and dolomite crystals (Mag. 1.5x). (b) Higher magnification of (a) showing rhomb dolomite crystals (Mag. 2.5x). Porosity is filled by blue-dyed epoxy.

Sample 3-534 (2256 m)

Sample 3-534 (figure A.30) is coated grains skeletal grainstone/wackestone. The dominant mineral in this sample is calcite making up to 92%, 3% dolomite, 2% anhydrite and 1% quartz. Twenty two percent are coated grains; fifteen percent are fine to coarse peloids, twenty percent skeletal, fifteen percent pellets and twenty eight percent lime mud. The skeletal grains are stromatoporids (15%), corals (8%), fibrous (40%), bivalve (5%), echinoderms (10%) and sponge (12%). Permeability is 1.2 mD and the porosity is 3.8 %. Almost all of the porosity is micropores (figure A.31 and A.32).

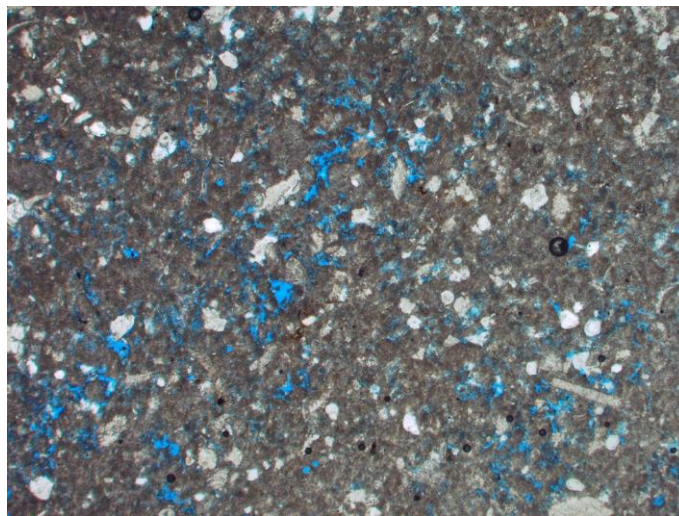


Figure A.30: Thin section photomicrographs of sample 3-534 showing peloids and skeletal grains with associated dominant pore types (Mag. 2.5x). Porosity is filled by blue-dyed epoxy.

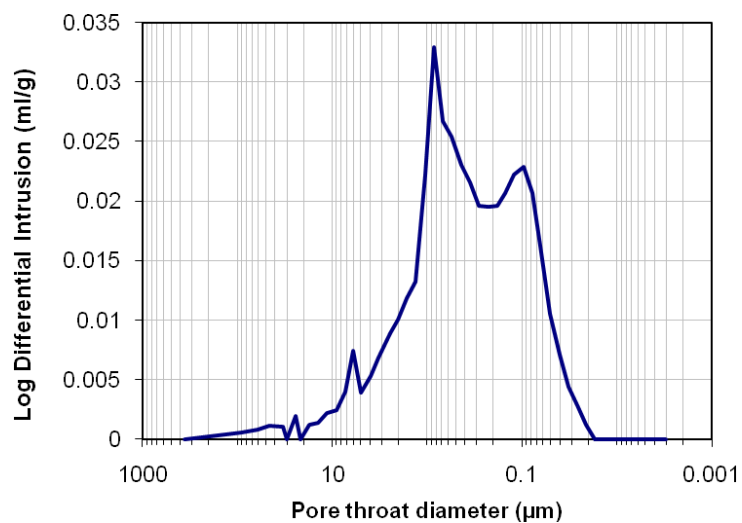


Figure A.31: Pore throat size distribution of sample 3-534, shows that the dominant pore size is less than $10 \mu\text{m}$.

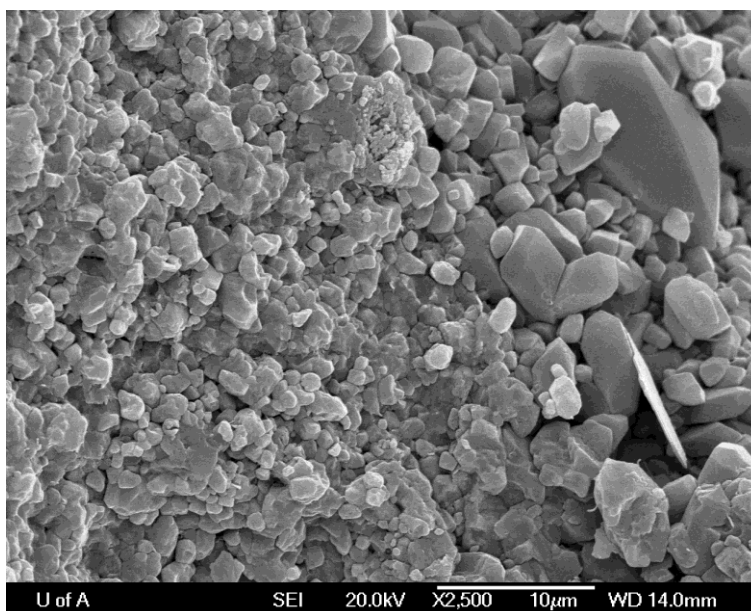


Figure A.32: SEM image showing two texture, relatively small crystals and larger crystals with the associated micropores.

Sample 4-09 (2036 m)

Sample 4-09 (figure A.33) is ooid coated grains-peloidal grainstone and GDP. The sample is 92% calcite, 2% dolomite and 6% anhydrite. Forty percent of the grains are peloids, thirty three percent are skeletal, ten percent coated grains, and another ten percent intraclasts. The skeletal grains are forams (75%), dasyclads (20%) and echinoderms (5%).

Permeability is 0.7 mD and porosity is 10.4 %. Most of the porosity is from macropores (9%) with the remaining (1.4%) from micropores. Pore types are interparticles (65%) and intercrystalline (35%).

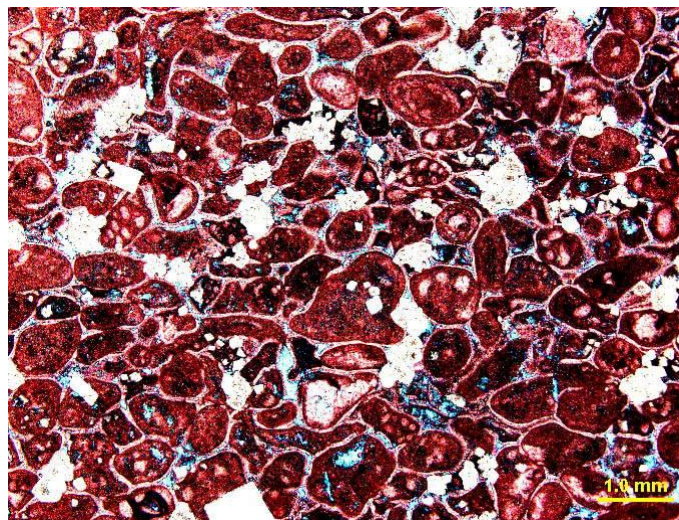


Figure A.33: Thin section photomicrographs of sample 4-09 depicting peloids and skeletal grains with associated dominant pore types. Porosity is filled by blue-dyed epoxy, calcite is stained red, other minerals are unstained (Mag. 1.5x).

Sample 4-55 (2043 m)

Sample 4-55 (figure A.34) is peloid skeletal grainstone and GDP. It is 99.5% calcite and 0.5% dolomite. Fifty one percent of the grains are peloids, forty percent are skeletal and 5% coated grains. The skeletal grains are forams (35%), cladocropsis (30%), dasyclads (15%) and echinoderms (20%). The cement is calcites.

Permeability is 930.7 mD and the porosity is 29.3 %. Most of the porosity is macropores (26%) and some are micropores (3.3%) (figures A.35 and A.36). The pore types are interparticles 85%, moldic (10%) and intraskeletal (5%).

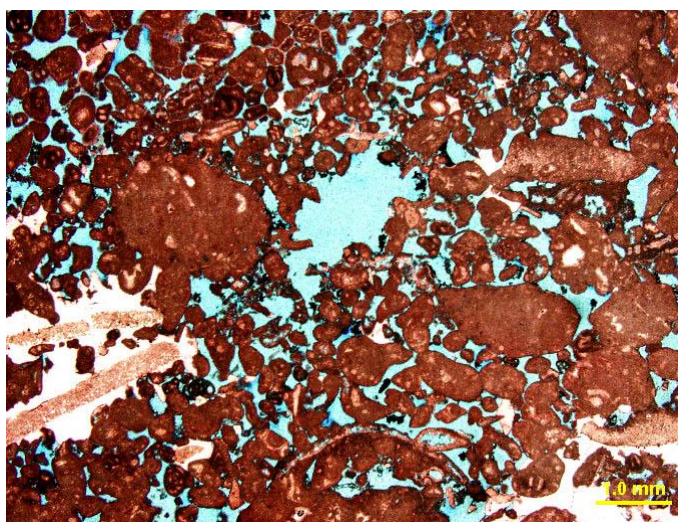


Figure A.34: Thin section photomicrograph of sample 4-55 showing peloids and skeletal grains Porosity is filled by blue-dyed epoxy (Mag. 1.5x).

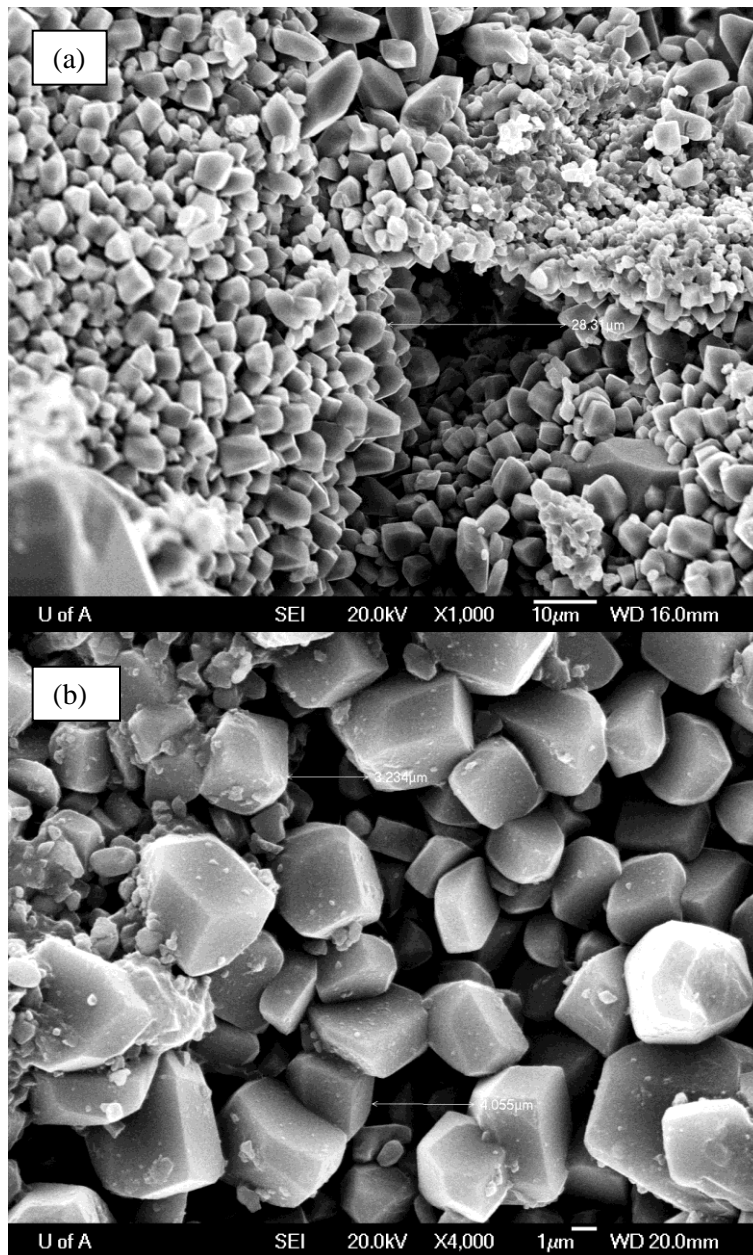


Figure A.35: SEM images of sample 4-55 shows two types of pore size, interparticle macropores (a) and the micro size pores (4-5 μm) is formed between the calcite cement crystals (b).

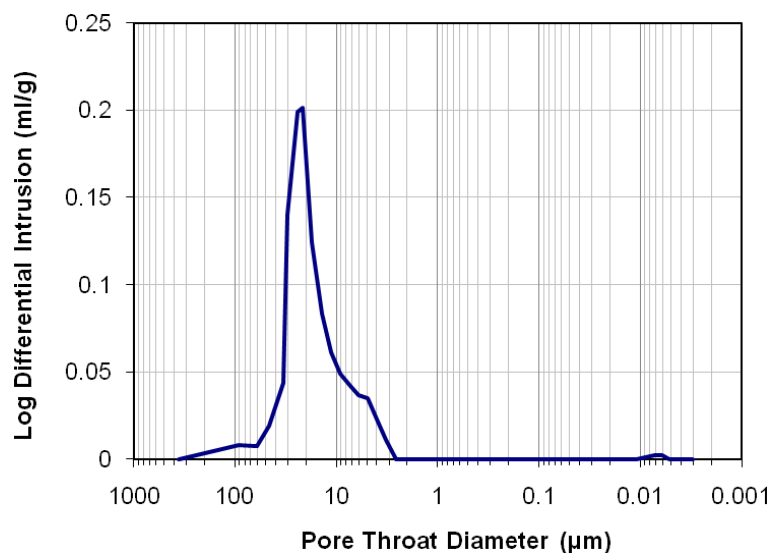


Figure A.36: Pore throat size distribution of sample 4-55, shows that the dominant pore size is greater than 10 μm .

Sample 4-97 (2049.5 m)

Sample 4-97 (figure A.37) is peloid skeletal grainstone and grain dominated packstone (GDP). It is 99.5% calcite and 0.5% dolomite. Thirty two percent of the grains are peloids and sixty seven percent are skeletal. The skeletal grains are forams (12%), stromatoporids (60%), dasyclads (8%), brachiopods (10%) and echinoderms (10%). The cement is calcites.

Permeability is 502.5 mD and the porosity is 27.5 %. The dominant pore size is macropores (25%) and few are micropores (figure A.38). The pore types are interparticles 60%, moldic (10%) and intraskeletal (30%).

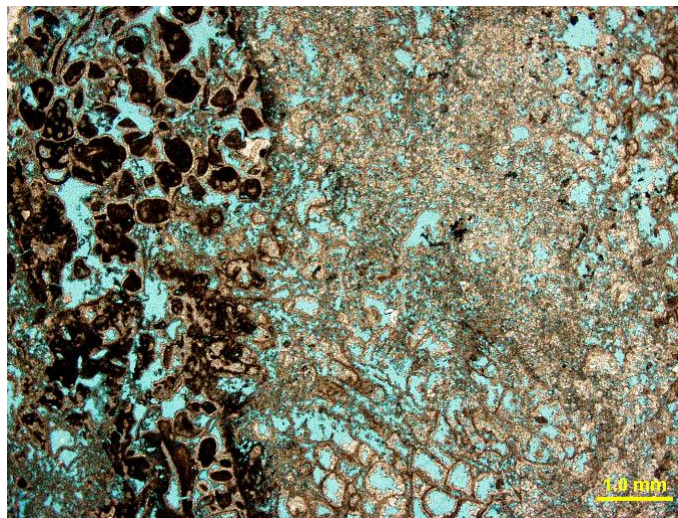


Figure A37: Thin section photomicrograph of sample 4-97 showing peloids and skeletal grains with associated dominant pore types. Porosity is filled by blue-dyed epoxy (Mag. 1.5x).

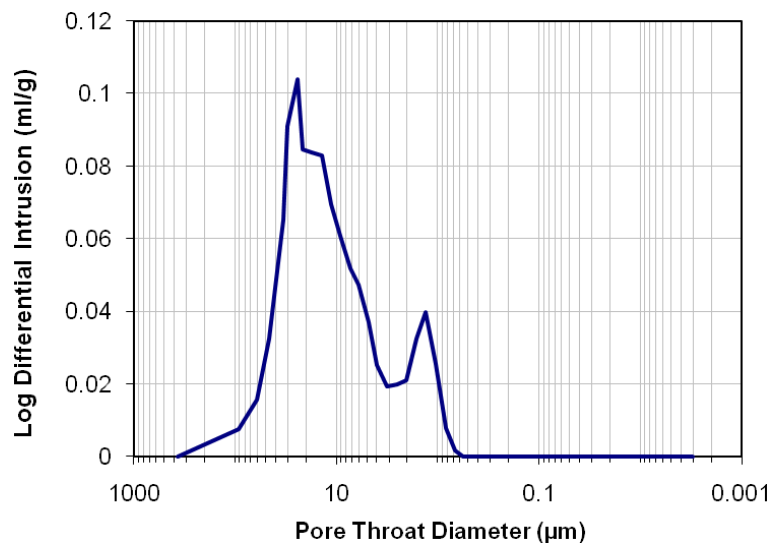


Figure A.38: Pore throat size distribution of sample 4-97, shows that the dominant pore size is greater than 10 μm .

Sample 4-151 (2057.76 m)

Sample 4-151 (figure A.39) is non fabric preserving dolomite. It is 94% dolomite and 6% calcite. Permeability is 0.8 mD and the porosity is 10 %. Most of the porosity is micropores (7%) and few are macropores (3%). The pore types are intercrystalline (65%), moldic (20%) and intraskeletal (15%).

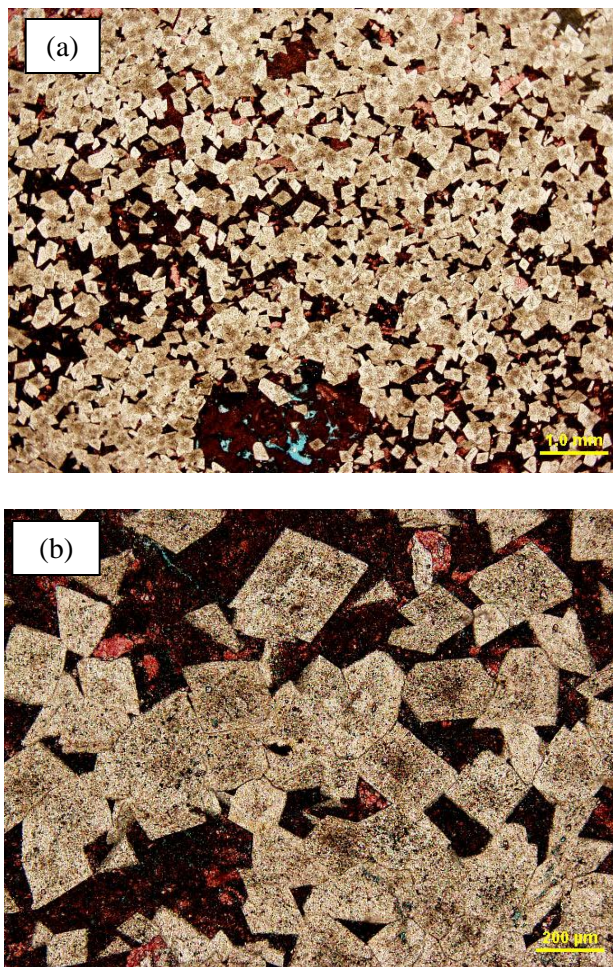


Figure A.39: (a) Thin section photomicrographs of sample 4-151 showing dolomite crystals with associated dominant pore types. (b) Higher magnification view of area in (a). Porosity is filled by blue-dyed epoxy, calcite is stained red, and other minerals are unstained.

Sample 4-180 (2062 m)

Sample 4-180 (figure A.40) is non fabric preserving dolomite. It is 99% dolomite and 1% anhydrite. Permeability is 0.0 mD and the porosity is 4.9 %. The pore types are intercrystalline (100%).

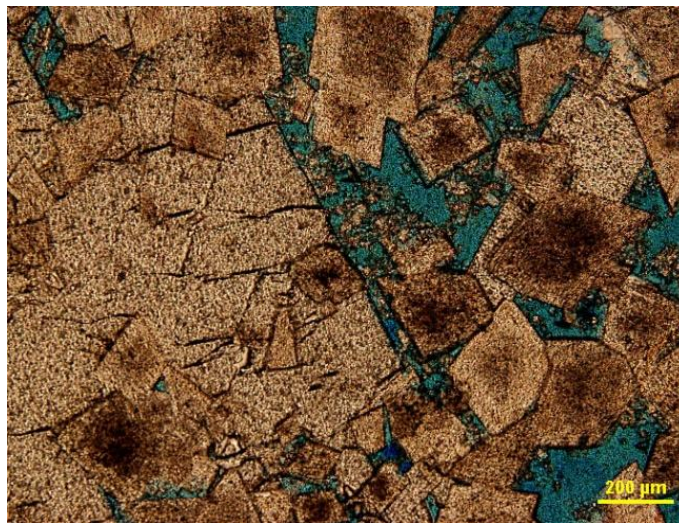


Figure A.40: Thin section photomicrographs of sample 4-180 showing non-fabric dolomite crystals and intercrystalline and leached dolomite pores. Porosity is filled by blue-dyed epoxy.

Sample 4-189 (2063.5 m)

Sample 4-189 (figure A.41) is peloid skeletal grainstone and GDP with 100% calcite. Seventy two percent of the grains are peloids and twenty eight percent are skeletal. The skeletal grains are forams (40%), dasyclads (50%) and echinoderms (10%). Permeability is 756.2 mD and the porosity is 24.9 %. Mercury injection curve (figure A.42) shows that the sample has dual porosity. The pore type is mostly interparticles and intraskeletal macropores and micropores between calcite cement crystals (figure A.43).

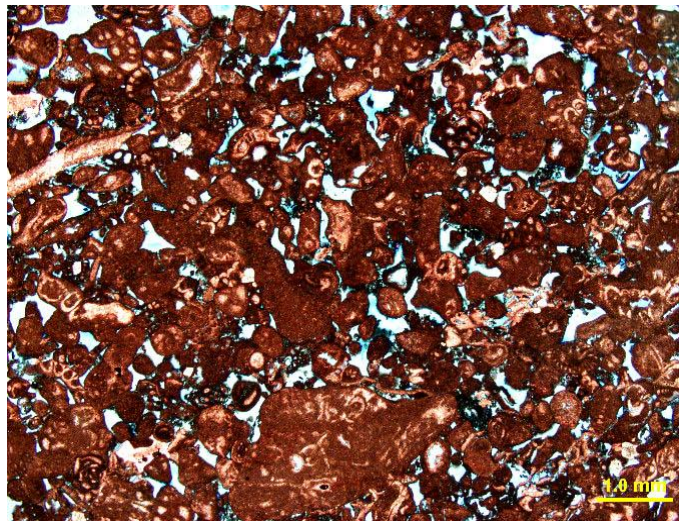


Figure A.41: Thin section photomicrograph of sample 4-189 showing peloids and skeletal grains and interparticles and intraskeletal pores. Porosity is filled by blue-dyed epoxy, calcite is stained red and other minerals are unstained.

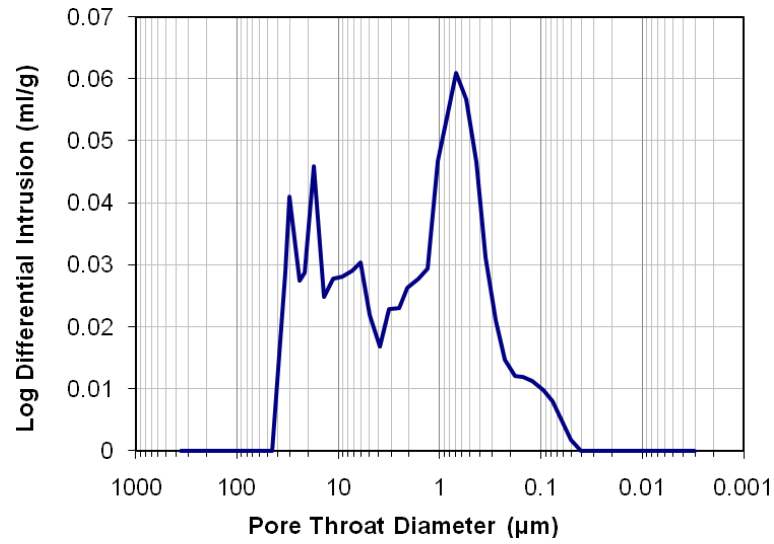


Figure A.42: Pore throat size distribution of sample 4-189, shows two peaks that fall on both sides of the 10 micron benchmark (dual porosity).

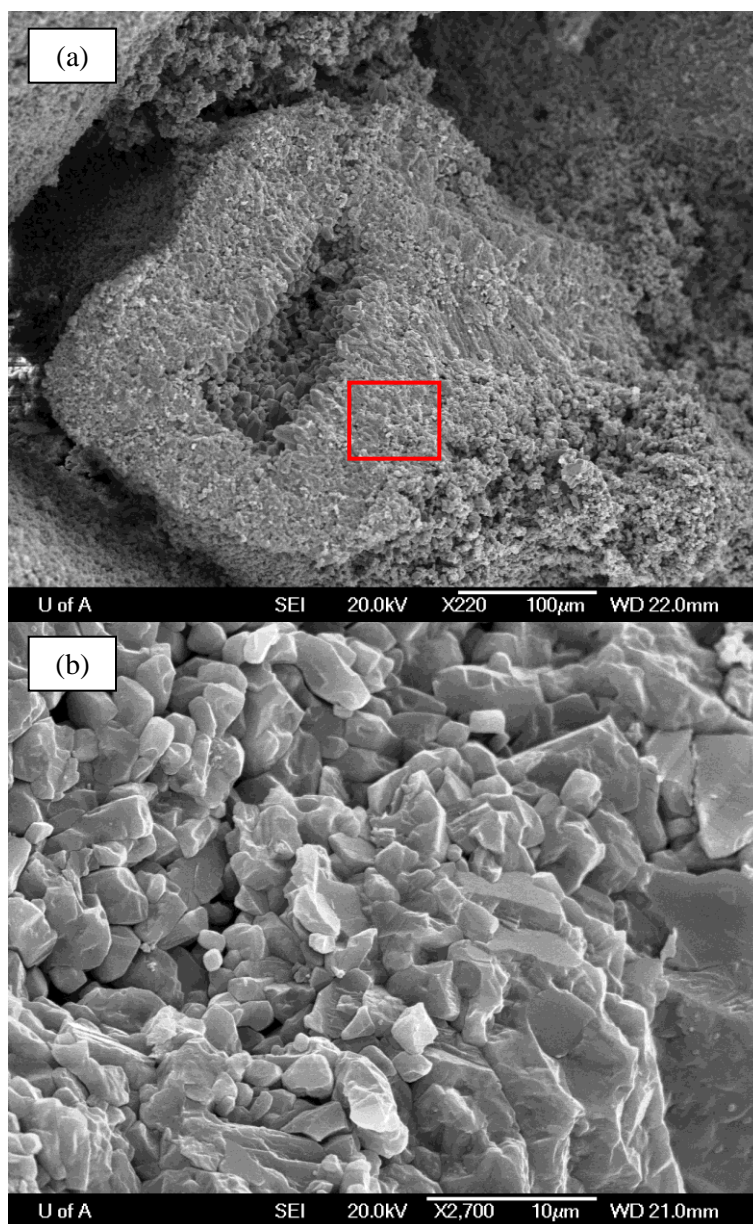


Figure A.43: (a) SEM images of sample 4-189 shows two types of macropores, interparticulate and intraskaletal. (b) Higher magnification view of are outlined in (a), the micro size pores is formed between the calcite crystals inside the grain.

Sample 4-326 (2084.4 m)

Sample 4-326 (figure A.44) is ooid coated grains peloidal grainstone and GDP. It is 99% calcite and 1% dolomite. Forty eight percent of the grains are coated grains, thirty six percent are peloids, ten percent are ooids and four percent are skeletal. The skeletal grains are stromatoporids (40%) and echinoderms (60%).

Permeability is 55.4 mD and the porosity is 14.2 %. The pore types are interparticle (95%) and intraskeletal (5%). Pore size mostly macropores with few micropores (figure A.45).

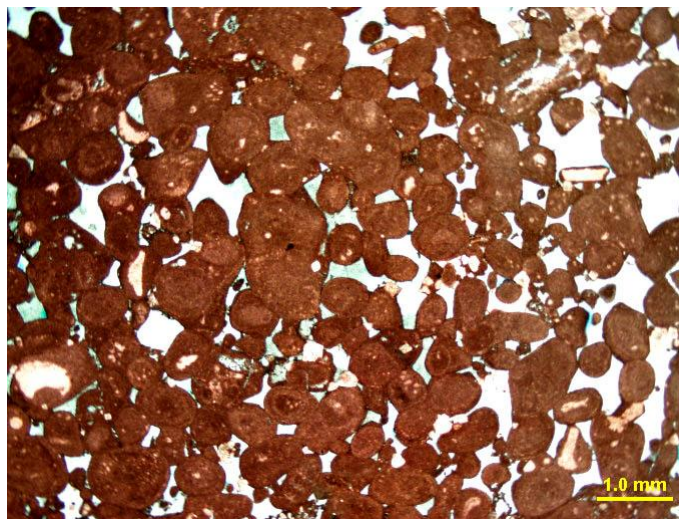


Figure A.44: Thin section photomicrograph of sample 4-326 showing peloids and skeletal grains with associated dominant pore types. Porosity is filled by blue-dyed epoxy.

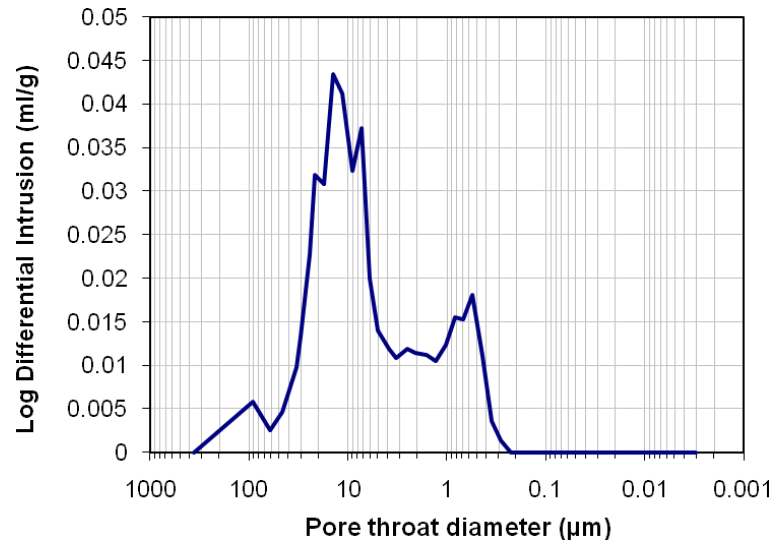


Figure A.45: Pore throat size distribution of sample 4-326, shows the dominant pore size is greater than 10 microns.

Sample 7-240 (2045.2 m)

Sample 7-240 is dolomitic peloidal packstone (figure A.46). The dominant mineral in this sample is calcite (97%) and 3% dolomite. The grains are overwhelmingly peloids with few coated grains. The dolomitization that produced the dolomites appear to have reduced in part the interparticle pores. Isopachous cement and probably leached peloids also are visible in some interparticels.

Permeability is 10.9 mD and porosity is 21.9 %. Macropores are reduced interparticels and small intraparticels. However, the majority are represented by micropores (figure 7-240).

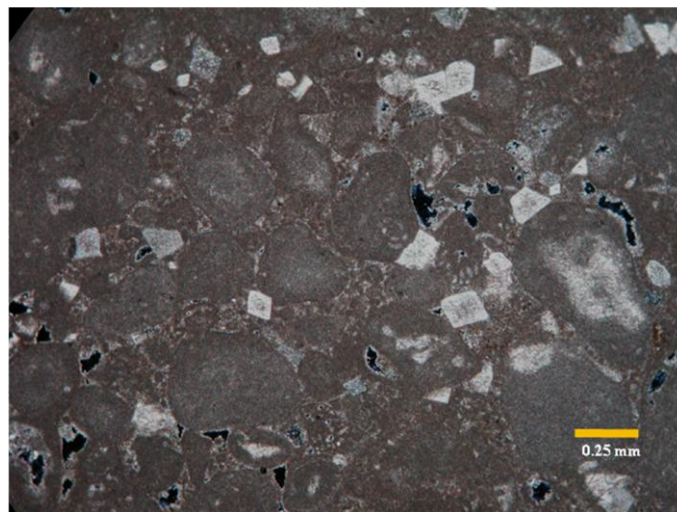


Figure A.46: Thin section photomicrograph of sample 7-240 showing peloids, lime mud and dolomite crystals. Porosity is filled by blue-dyed epoxy.

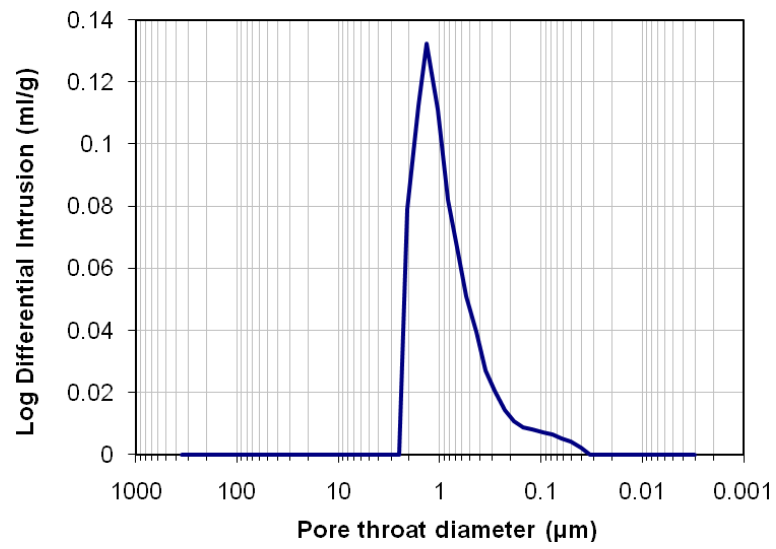


Figure A.47: Pore throat size distribution of sample 7-240, shows the dominant pore size is less than 10 microns.

Sample 7-20 (2088.9 m)

Sample 7-20 (figure A.48) is dolomitic lime mudstone. It is 90% calcite and 10% dolomite. Calcite is present as micrite while dolomite is present as minute scattered rhombus. Permeability is less than 0.01 mD and helium porosity is less than 1% however micropore is seen in SEM images (figure A.49).

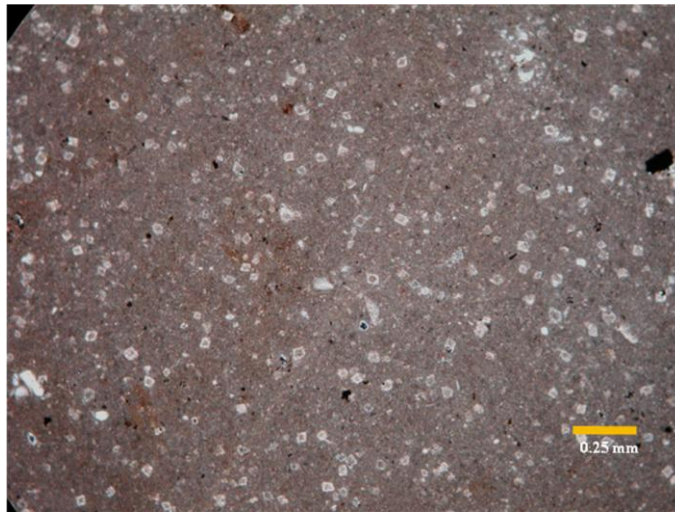


Figure A.48: Thin section photomicrograph of sample 7-20 showing lime mud and dolomite rhombus.

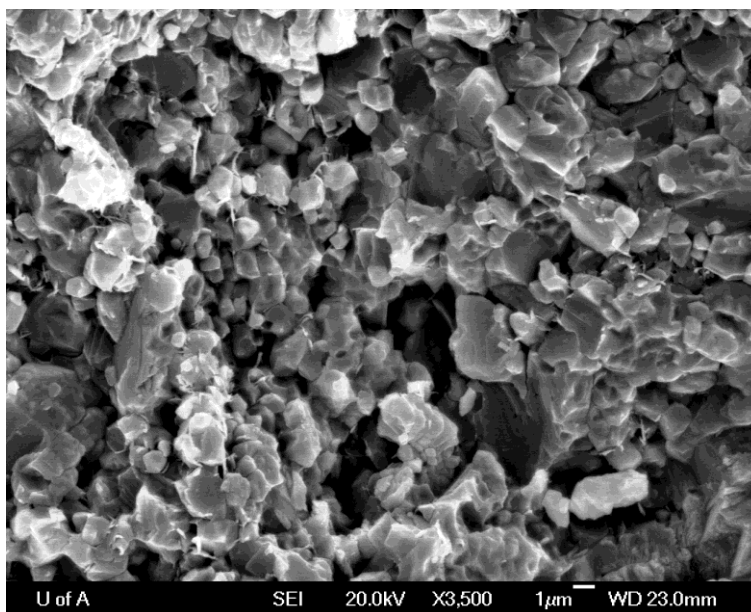


Figure A.49: SEM images of sample 7-20 shows the existence of micropores.

Sample 7-222 (2042.5 m)

Sample 7-222 (figure A.50) is non fabric preserving leached dolomite with 100% dolomite. The crystals vary between 1-3 mm. There are no appreciable intercrystalline pores and the pores are leached dolomites. These leached areas are not well interconnected. Hence porosity and permeability are very low respectively 3.3% and 0.4mD.



Figure A.50: Thin section photomicrograph of sample 7-222 showing non fabric preserved dolomite with some leached dolomite areas. Porosity is filled by blue-dyed epoxy.

Sample 7-16 (2100 m)

Sample 7-16 (figure A.51) is coated-grains peloidal skeletal grain dominated packstone, calcite dominated. Forty percent of the constituent grains are coated grains, 50% peloids whereas micrite makes up 10%. Some of the grains show mechanical breaking. Pores are mostly interparticle. Pore size is less than 10 microns (figure A.52). The permeability is 16.8 mD and the porosity is 12.8 %.

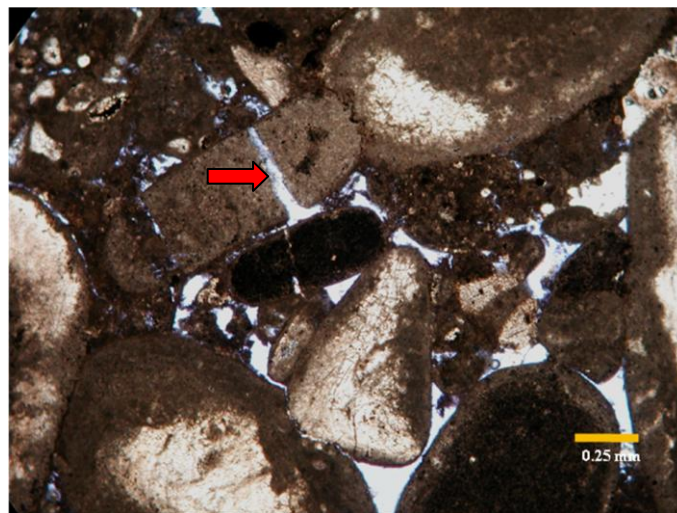


Figure A.51: Thin section photomicrograph of sample 7-16 peloids and coated-grain. Mechanical breaking is evident (red arrow). Porosity is filled by blue-dyed epoxy.

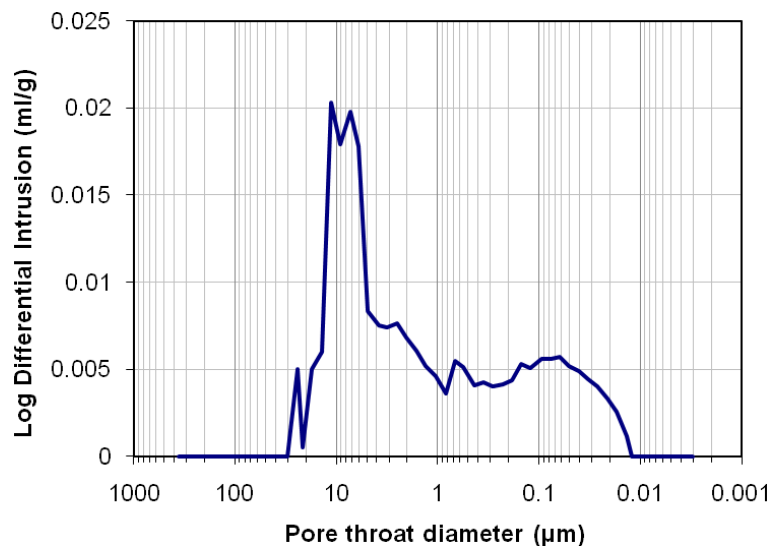


Figure A.52: Pore throat size distribution of sample 7-16, shows the dominant pore size is less than 10 microns.

Sample 5-289 (2264.42 m)

Sample 5-289 (figure A.53) is coated-grains peloidal skeletal packstone. Mineralogy is 100% calcite. Thirty percent are coated grains, thirty percent peloids, and forty percent micrite. The skeletal grains are forams.

The very few visible pores are filled with micrite and blocky cement. Permeability is nil and the porosity is 1.0 %.

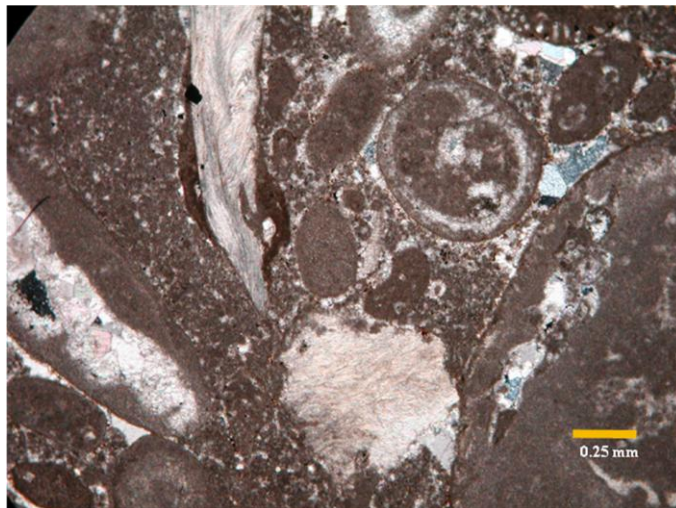


Figure A.53. Thin section photomicrograph of sample 5-289 shows peloids, skeletal and coated-grains and pores are filled with calcite cement. Porosity is filled by blue-dyed epoxy.

Sample 5-295 (2265.3 m)

Sample 5-295 (figure A.54) is dolomitic coated-grain peloidal packstone. Calcite is making up to 90% and dolomite is 10%. Fifty percent of the constituent grains are peloids, twenty percent leached peloids, coated grains are 10% and micrite is 20%. The permeability is 0.1 mD and the porosity is 6.1 %.

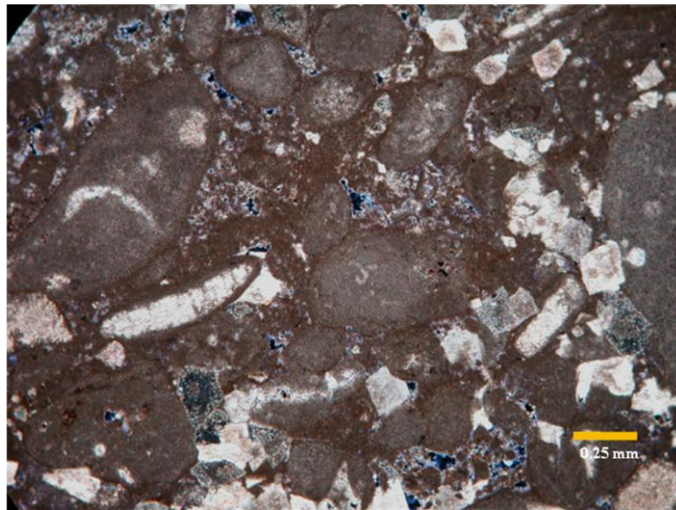


Figure A.54: Thin section photomicrograph of sample 5-295 shows peloids, coated-grains, lime-mud and dolomite rhombus. Porosity is filled by blue-dyed epoxy.

Sample 5-02 (2206.6 m)

Sample 5-295 (figure A.55) is skeletal peloidal grain dominated packstone. Calcite is the dominant mineral (100 %). Seventy percent of the constituent skeletal, 25% peloids and 5% lime mud. The skeletal grains are forams.

The permeability is 2.3 mD and the porosity is 14.3%. Most of this porosity is from reduced interparticle/intraparticle and micropores (figure A.56).

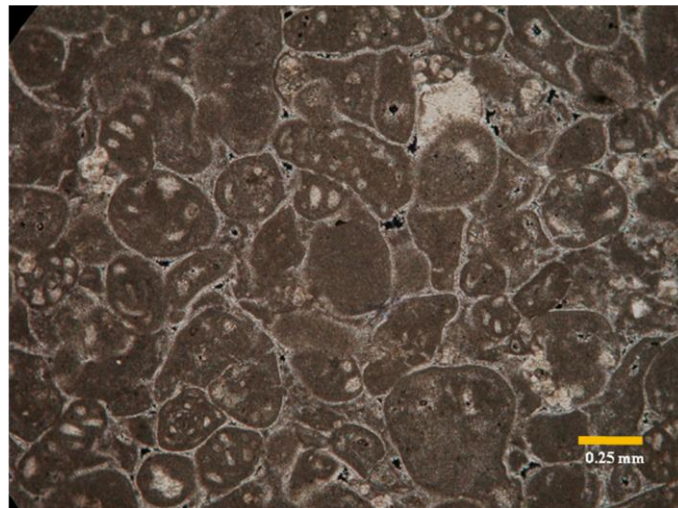


Figure A.55: Thin section photomicrograph of sample 5-02 showing abundant skeletal and some peloids. Porosity is filled by blue-dyed epoxy.

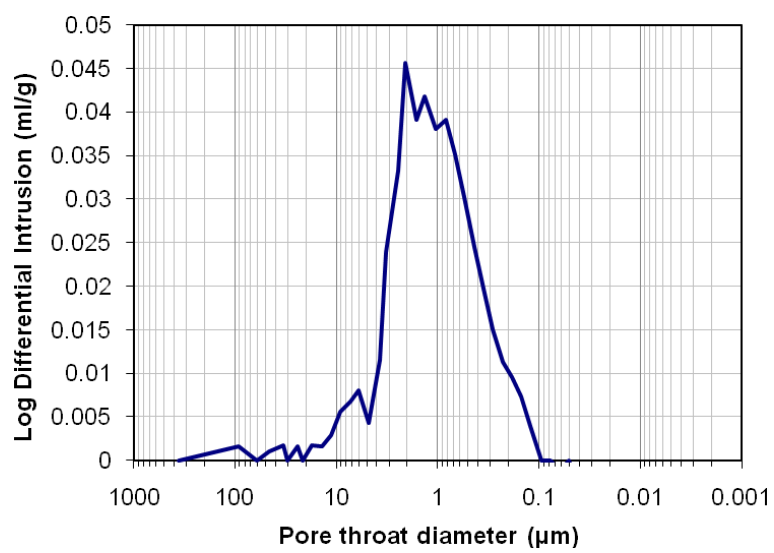


Figure A.56: Pore throat size distribution of sample 5-02, shows the dominant pore size is less than 10 microns.

Sample 1-132 (2155 m)

Sample 1-132 (figure A.57) is constituted of boundstone areas and oolitic-peloidal grainstone. The boundstone area is a stromatopoid and the remaining area is made up of ooids and peloids. Both areas show excellent pore systems. In the grainstone area the ooids and peloids are roughly equally present, however, the ooids grains are bigger in size (0.5 – 1.0 mm), whereas the peloids are much smaller in size (0.1 – 0.25 mm).

Both permeability (2251.2mD) and porosity (38.1%) are very high, and the sample with such a pore system and pore interconnection represents an excellent reservoir rock. Mercury intrusion curve shows that macropore is the dominant pore size (figure A.58).

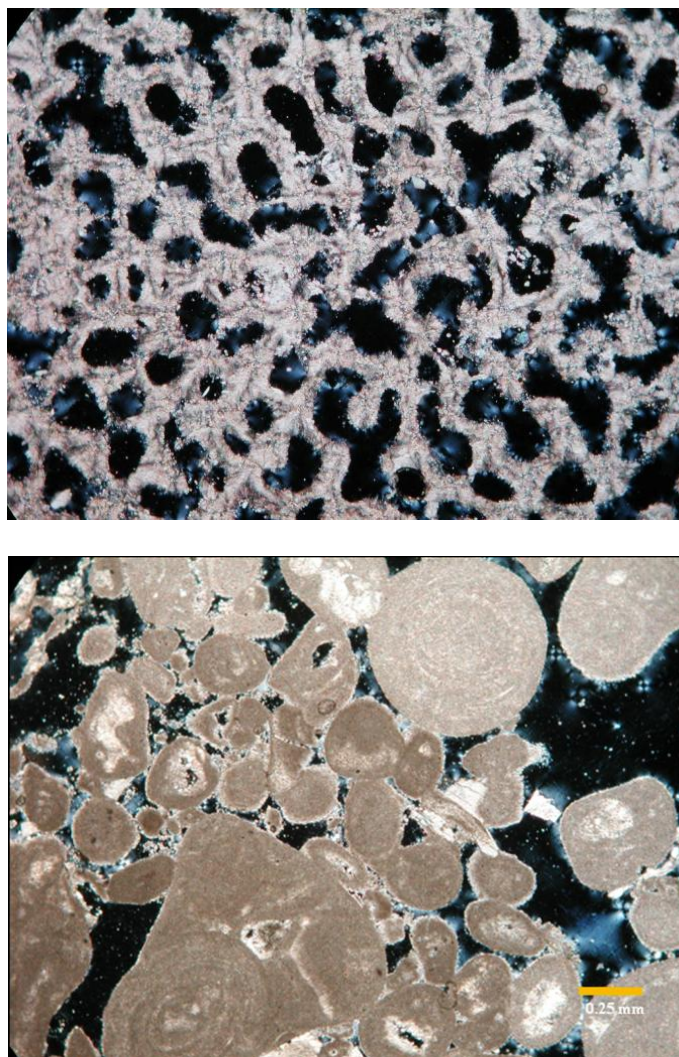


Figure A.57: Thin section photomicrographs (two areas) of sample 1-132. (a) The sample composed of stromatoporid boundstone area and (b) oolitic-peloidal grainstone. Porosity is filled by blue-dyed epoxy.

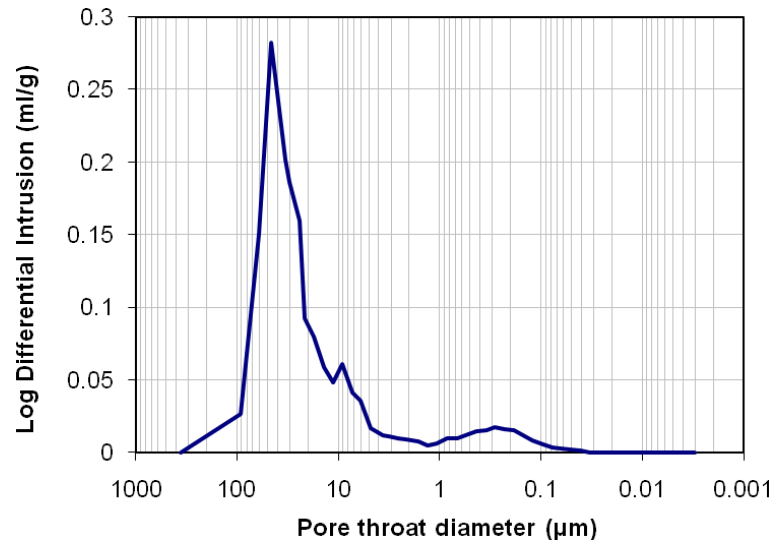


Figure A.58: Pore throat size distribution of sample 1-132, shows the dominant pore size is greater than 10 microns.

Sample 1-11 (2124.2 m)

Sample 1-11 (figure A.59) is dolomite crystals make up 98% and the rest is some anhydrite and calcite. The pore types are intercrystalline and leached dolomite.

Porosity is around 3% and permeability is less than 0.01 mD.

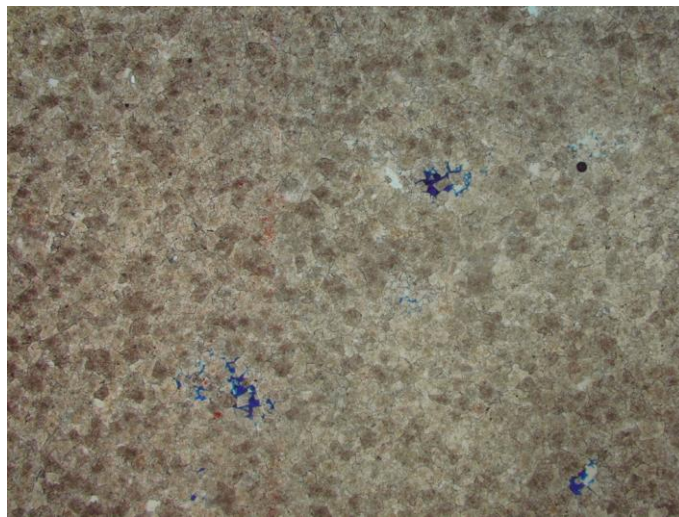


Figure A.59: Thin section photomicrograph of sample 1-11 showing dolomite with some leached dolomite areas. Porosity is filled by blue-dyed epoxy (Mag. 1.5x).

Sample 1-288 (2184.3 m)

Sample 1-288 (figure A.60) is grainstone and GDP. The sample is mainly calcite (99%). The grains are skeletal (38%), oncoids (22%), coated grains (21%), peloids (10%) some minor constituents. Pore types are interparticle (78%) and intraparticle (22%). Porosity is mainly macroporosity.

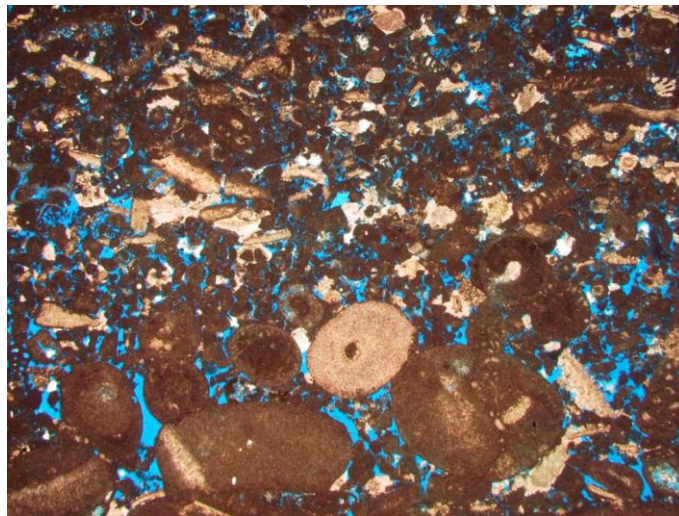


Figure A.60: Thin section photomicrograph of sample 1-288 shows skeletal grains, oncoids, coated grains and peloids. Interparticle pores are visible. Porosity is filled by blue-dyed epoxy (Mag. 1.5x).

Sample 1-304 (2189 m)

Sample 1-304 (figure A.61) is oncoïd spicule wackestone. The sample is 98.5% calcite and with some dolomite and silica. The major constituent is lime mud with some skeletal, peloids, coated grains, and oncoïds. The pores are moldic (80%) and interparticle (20%). Porosity is distributed equally between macro and micro pores.

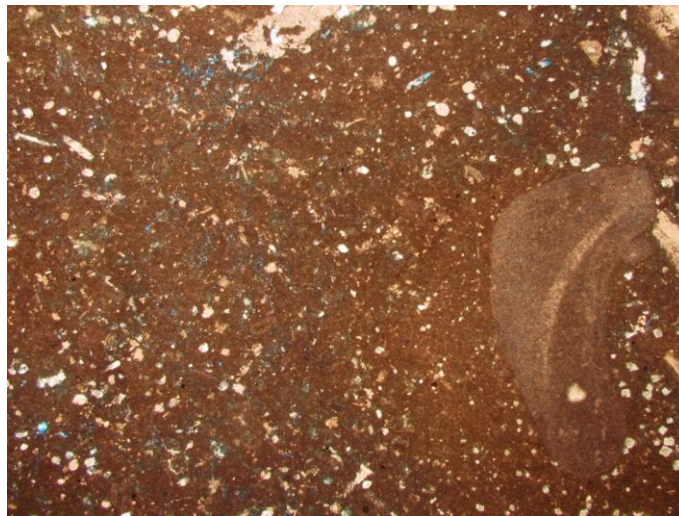


Figure A.61: Thin section photomicrograph of sample 1-304 showing grains and lime mud with associated prevalently moldic pores. Porosity is filled by blue-dyed epoxy (Mag. 1.5x).

Sample 8-91 (2239.6 m)

Sample 8-91 (figure A.62) is skeletal leached peloidal grainstone. Mineral is 100% calcite. Fifty percent of the constituent grains are skeletal and about equal amount is micritized/leached peloids. The skeletal grains are (100 %) forams.

The permeability is 1018.8 mD and the porosity is 27.0%. Most of this porosity is from solution enlarged interparticle pores and relatively abundant intraparticle. In addition the presence of micropores makes the sample another excellent reservoir rock (figure A.63). SEM images show skeletal and non skeletal calcite crystals (figure A.64).

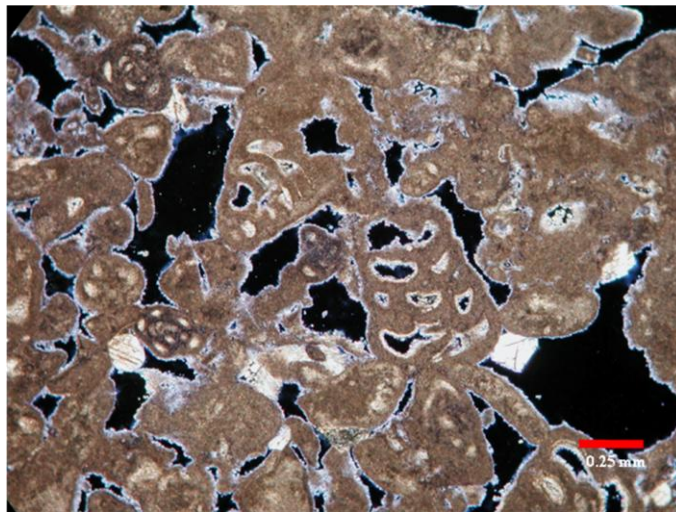


Figure A.62: Thin section photomicrograph of sample 8-91 skeletal and leached peloids grainstone. Isopachous cement, blocky cement, interparticle and intraparticle pores are visible. Porosity is filled by blue-dyed epoxy (Mag. 1.5x).

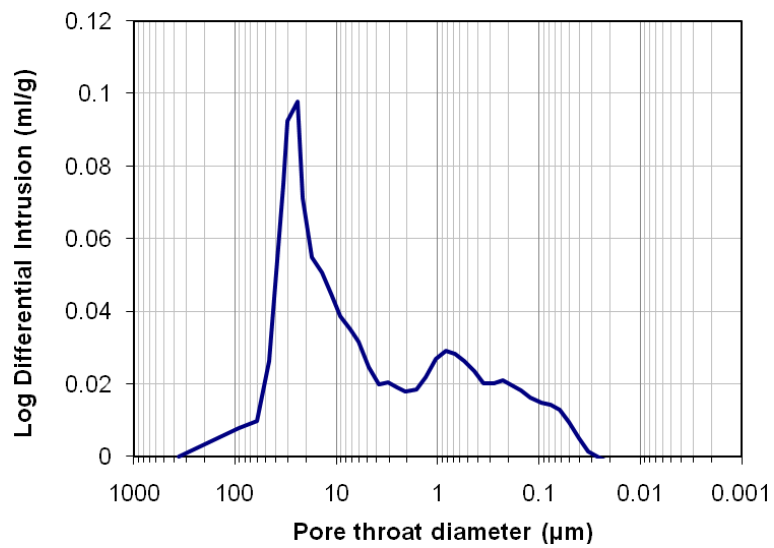


Figure A.63: Pore throat size distribution of sample 8-91, shows the dominant pore size is greater than 10 microns.

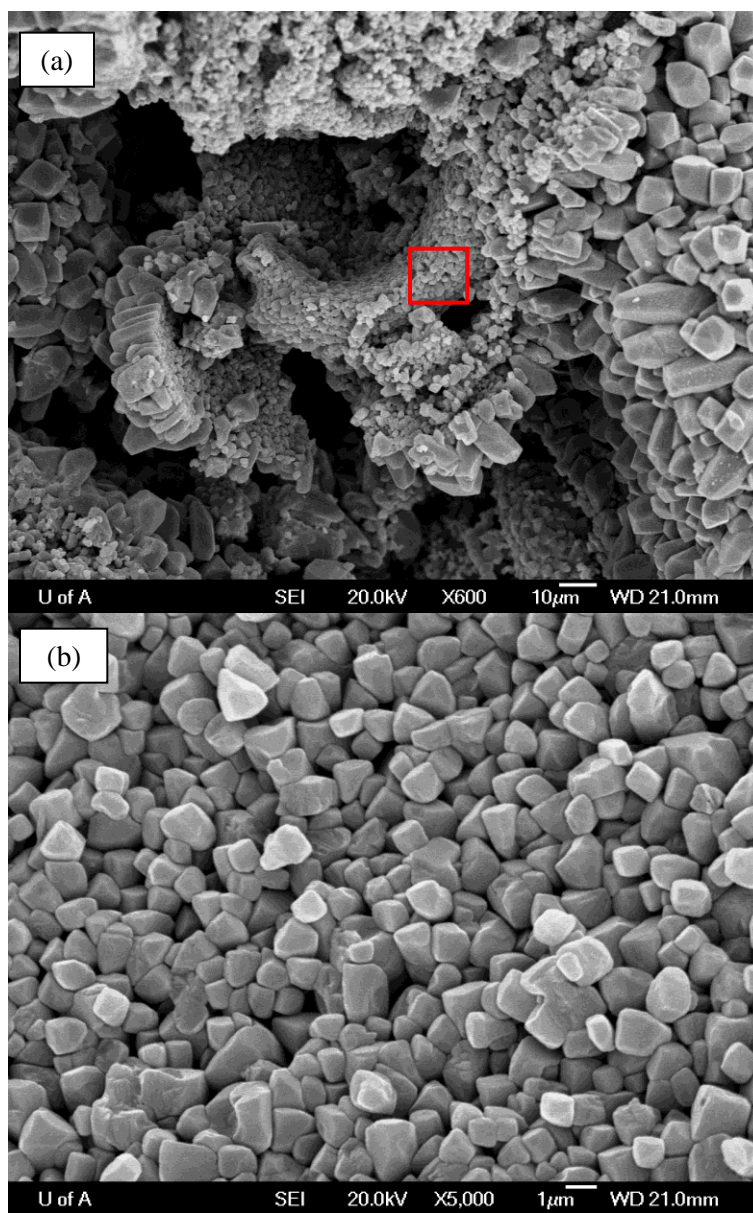


Figure A.64: (a) SEM image of sample 8-91 shows calcite crystals in skeletal grain. (b) Calcite crystals in peloids grains.

Sample 8-23 (2219 m)

Sample 8-23 (figure A.65) is ooid grainstone. Calcite makes up 98% and dolomite 3%. The grains are ooid and skeletal. Porosity is 29% and permeability is 315 mD. Pores are interparticle (92%) and intraparticle (28%). Mercury intrusion curve shows dual porosity model (figure A.66). SEM images show microporous skeletal and ooid grains (figure A.67).

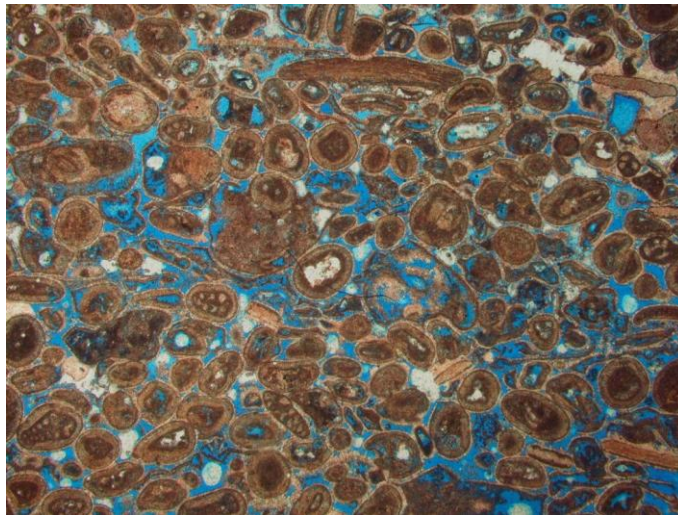


Figure A.65: Thin section photomicrograph of sample 8-23 showing ooid and skeletal grains and interparticle and intraparticle pores are visible. Porosity is filled by blue-dyed epoxy (Mag. 1.5x).

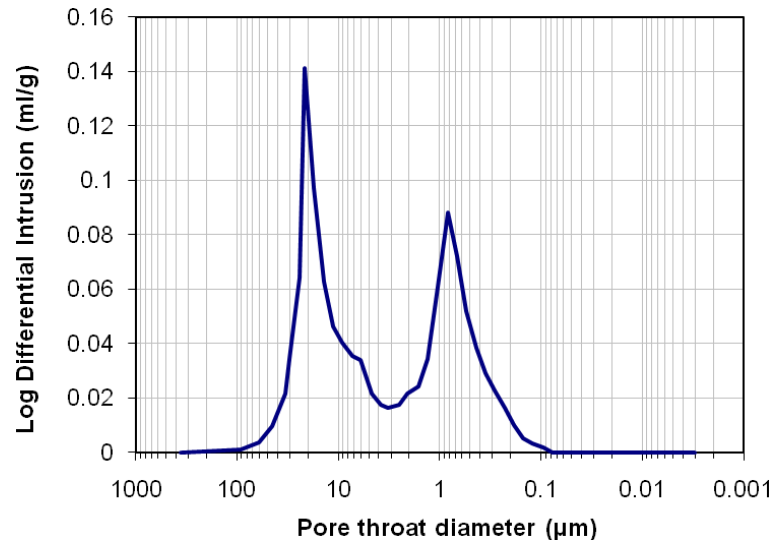


Figure A.66: Pore throat size distribution of sample 8-23, shows two peaks that fall on both sides of the 10 micron benchmark (dual porosity).

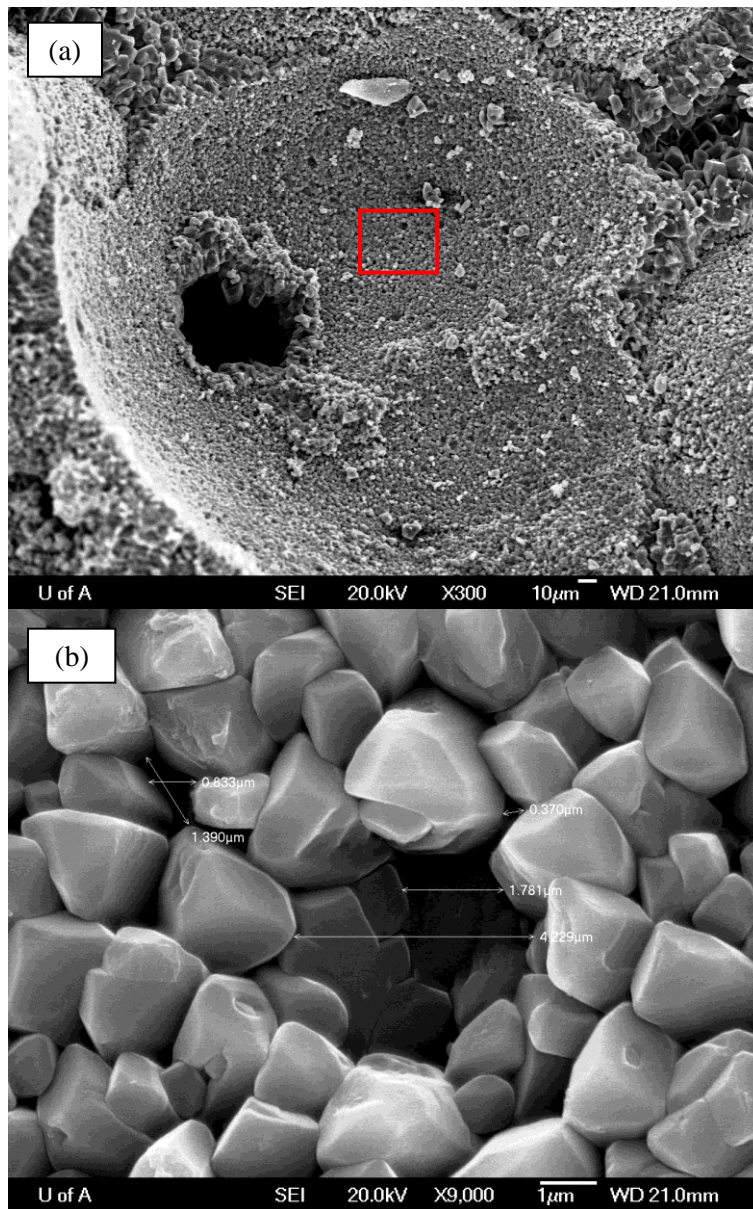


Figure A.67: SEM images show (a) micropore ooid grain surrounded by calcite cements and (b) higher magnification view of area outlined in (a) shows micropores inside the grain.

Sample 8-115 (m)

Sample 8-115 (figure A.68) is ooid dasyclad grainstone consists of 83% calcite and 17% dolomite. The grains are 42% skeletal, 22%, ooids 24%, 7% intraclasts and some minor constituents. Porosity is 19% and permeability is 117 mD. Pores are 96% interparticle and 4% intraparticle. Mercury intrusion curve shows dual porosity model (figure A.69).

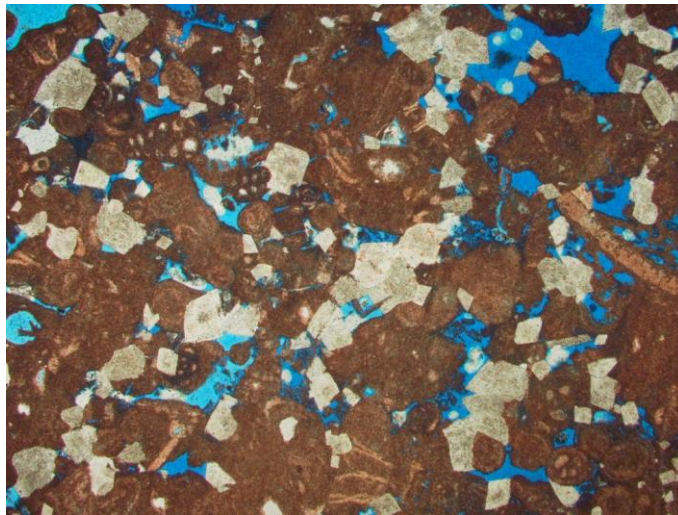


Figure A.68: Thin section photomicrograph of sample 8-115 showing ooid and skeletal grains. Interparticle pores are visible. Porosity is filled by blue-dyed epoxy (Mag. 1.5x).

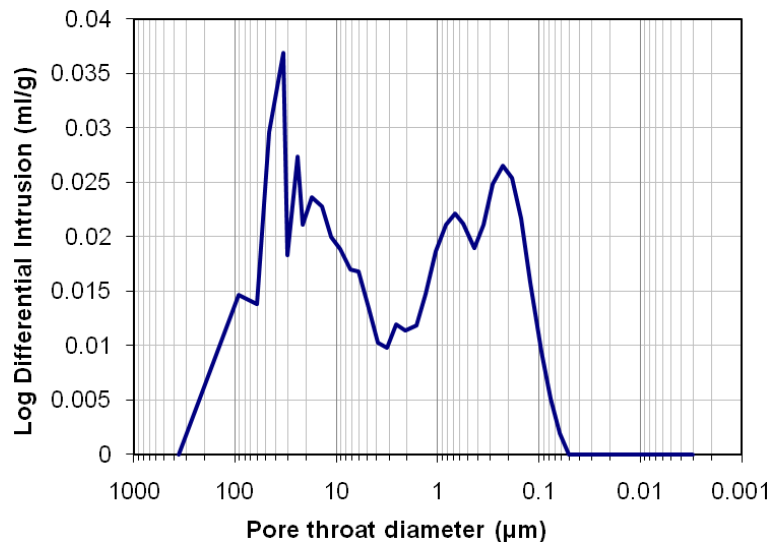


Figure A.69: Pore throat size distribution of sample 8-115, shows two peaks that fall on both sides of the 10 micron benchmark (dual porosity).

Appendix B:

Petrological Data

Table B.1: Petrological parameters of the studied samples.

Number	Sample	Depth (m)	Porosity (%)	Permeability (mD)	Bulk Density (g/cm ³)
1	1-11	2124.22	2.6	0.01	2.74
2	1-132	2155.06	38.1	2251.2	1.64
3	1-288	2184.26	20.5	3.1	2.18
4	1-304	2188.99	8.1	9.6	2.47
5	2-10	2037.08	30.3	65.1	1.97
6	2-33	2041.25	30.9	1004.4	1.81
7	2-59	2045.40	32.5	33.7	1.76
8	2-131	2057.28	25.1	469.1	2.01
9	2-160	2062.31	26.6	77.4	1.96
10	2-368	2096.48	3.5	0.01	2.60
11	2-382	2098.89	9.6	0.1	2.44
12	2-432	2108.31	6	0.01	2.48
13	3-05	2175.43	5	0.2	2.78
14	3-90	2188.38	34	328.9	1.85

Cont'd Table B.1: Petrological parameters of the studied samples.

Number	Sample	Depth (m)	Porosity (%)	Permeability (mD)	Bulk Density (g/cm ³)
15	3-104	2190.51	31	133.9	1.90
16	3-146	2196.76	27.5	1695.4	1.90
17	3-331	2224.80	23.8	3345.4	2.14
18	3-429	2240.04	10.2	0.1	2.57
19	3-471	2246.44	3.3	0.01	2.68
20	3-534	2256.05	14.6	1.2	2.30
21	4-09	2036.16	10.4	0.7	2.48
22	4-55	2043.14	29.3	930.7	1.92
23	4-97	2049.54	27.9	502.5	1.96
24	4-151	2057.77	10	0.8	2.48
25	4-180	2062.19	4.9	0.01	2.67
26	4-189	2063.56	24.9	756.2	2.02
27	4-326	2084.44	14.2	55.4	2.35
28	5-02	2206.67	14.3	2.3	2.31
29	5-289	2264.43	1.0	0.01	2.67
30	5-295	2265.34	6.1	0.1	2.53
34	7-16	2100.17	12.8	0.4	2.77
33	7-20	2088.92	1.0	10.9	2.09
31	7-222	2042.47	3.3	0.01	2.63
32	7-240	2045.18	21.9	16.8	2.42
35	8-23	2219.20	28.7	315.4	1.98
36	8-91	2239.59	27	1018.8	2.02
37	8-115	2243.46	19.1	117.4	2.26

The highlighted samples are those employed in the analysis in the main part of the thesis.

Appendix C

Velocity data

The P- and S-wave velocities for the Arab formation carbonate samples are measured as a function of differential pressure under both dry and water saturated conditions. In addition, the velocities are measured under constant differential pressure. In here, the full set of normalized waveforms of measured dry and water saturated P- and S-wave under differential pressure are shown. Tables of the measured P- and S-wave velocities under both dry and saturated conditions as a function of pressure as well as under constant differential pressure are also shown for all samples. Lastly, as discussed in chapter 5 calibration involved measuring the delay through the aluminum buffers so travel times obtained in later experiments could be adjusted. Five different buffer pairs were used in this project. Table C.72 list all buffer pairs and samples that measured with each pair. Tables showing P- and S-wave travel times of aluminum buffer pairs are also shown.

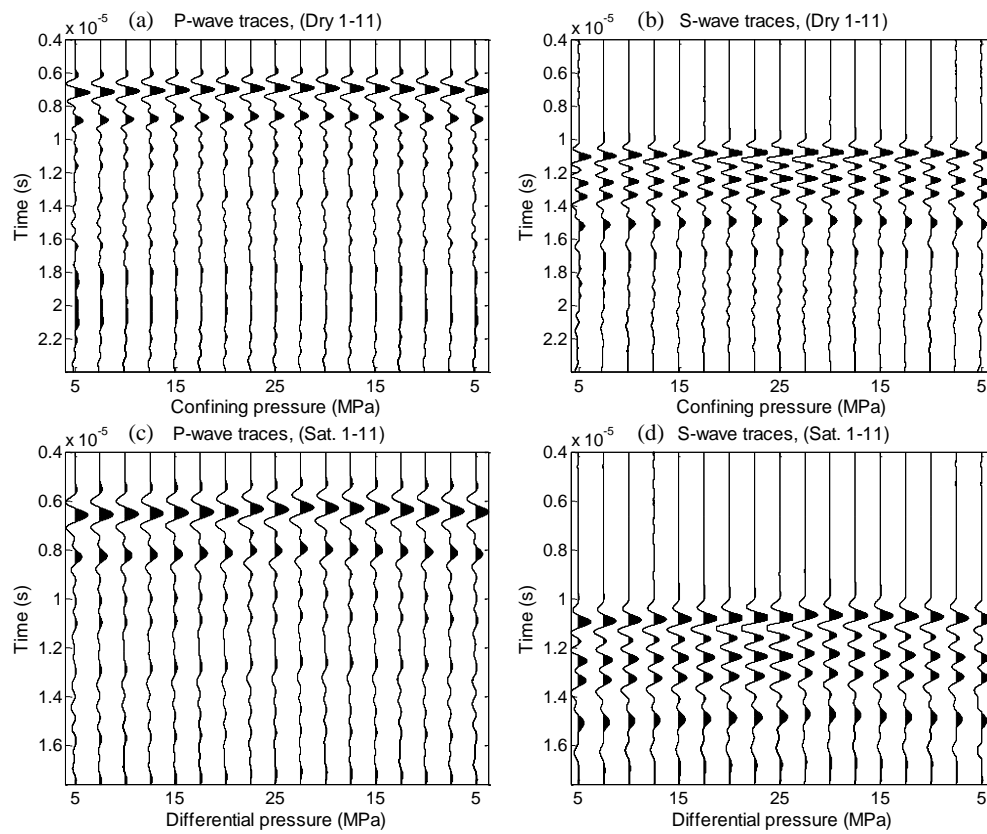


Figure C.1: Normalized waveforms of dry and saturated, P-wave (a and c respectively) and S-wave (b and d respectively) for sample 1-11 at different pressure.

Table C.1: Dry and saturated velocities of sample 1-11.

Pressure (MPa)	Dry		Saturated	
	Vp (m/s)	Vs (m/s)	Vp (m/s)	Vs (m/s)
5	6012 ± 24	3496 ± 8	6107 ± 24	3532 ± 8
7.5	6039 ± 24	3510 ± 8	6130 ± 25	3540 ± 8
10	6079 ± 24	3525 ± 8	6144 ± 25	3551 ± 8
12.5	6103 ± 24	3533 ± 8	6181 ± 25	3558 ± 8
15	6147 ± 25	3542 ± 8	6200 ± 25	3563 ± 8
17.5	6171 ± 25	3549 ± 8	6225 ± 25	3568 ± 8
20	6201 ± 25	3560 ± 8	6251 ± 25	3573 ± 8
22.5	6233 ± 25	3568 ± 8	6317 ± 26	3579 ± 8
25	6265 ± 25	3576 ± 8	6342 ± 26	3587 ± 8
22.5	6262 ± 25	3579 ± 8	6423 ± 26	3620 ± 8
20	6246 ± 25	3575 ± 8	6394 ± 26	3616 ± 8
17.5	6233 ± 25	3573 ± 8	6384 ± 26	3611 ± 8
15	6223 ± 25	3569 ± 8	6362 ± 26	3607 ± 8
12.5	6197 ± 25	3563 ± 8	6333 ± 26	3601 ± 8
10	6172 ± 25	3554 ± 8	6307 ± 25	3592 ± 8
7.5	6130 ± 25	3541 ± 8	6271 ± 25	3581 ± 8
5	6091 ± 24	3526 ± 8	6244 ± 25	3566 ± 8

Table C.2: Saturated velocities of sample 1-11 under constant differential pressure.

Confining pressure (MPa)	Pore pressure (MPa)	Vp (m/s)	Vs (m/s)
15	0	6319±26	3593±8
17.5	2.5	6336±26	3599±8
20	5	6354±26	3602±8
22.5	7.5	6370±26	3603±8
25	10	6390±26	3609±8

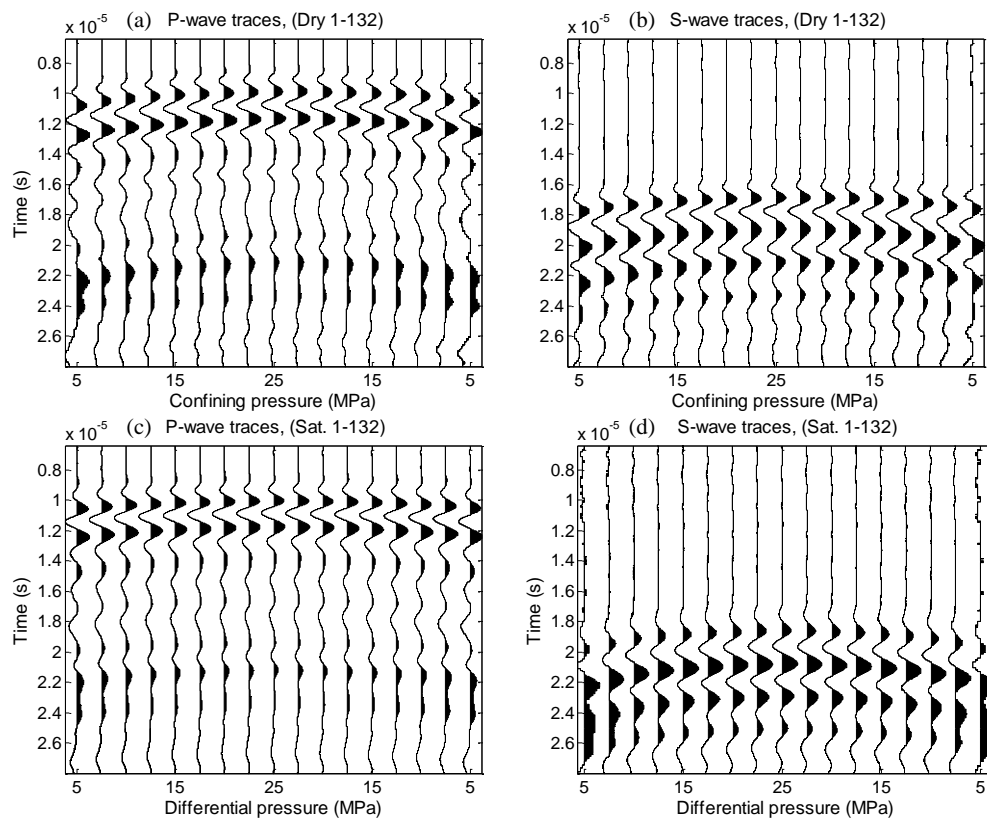


Figure C.2: Normalized waveforms of dry and saturated, P-wave (a and c respectively) and S-wave (b and d respectively) for sample 1-132 at different pressure.

Table C.3: Dry and saturated velocities of sample 1-132.

Pressure (MPa)	Dry		Saturated	
	V _p (m/s)	V _s (m/s)	V _p (m/s)	V _s (m/s)
5	3472 ± 11	2036 ± 4	3560 ± 12	1846 ± 3
7.5	3562 ± 12	2069 ± 4	3603 ± 12	1878 ± 4
10	3611 ± 12	2086 ± 4	3633 ± 12	1908 ± 4
12.5	3660 ± 12	2102 ± 4	3660 ± 12	1925 ± 4
15	3708 ± 13	2119 ± 4	3678 ± 12	1938 ± 4
17.5	3733 ± 13	2126 ± 4	3687 ± 13	1948 ± 4
20	3761 ± 13	2133 ± 4	3700 ± 13	1957 ± 4
22.5	3784 ± 13	2139 ± 4	3709 ± 13	1966 ± 4
25	3798 ± 13	2146 ± 4	3721 ± 13	1973 ± 4
22.5	3800 ± 13	2146 ± 4	3713 ± 13	1968 ± 4
20	3791 ± 13	2142 ± 4	3707 ± 13	1963 ± 4
17.5	3776 ± 13	2138 ± 4	3700 ± 13	1954 ± 4
15	3761 ± 13	2131 ± 4	3690 ± 13	1943 ± 4
12.5	3731 ± 13	2120 ± 4	3673 ± 12	1930 ± 4
10	3700 ± 13	2106 ± 4	3655 ± 12	1914 ± 4
7.5	3618 ± 12	2080 ± 4	3622 ± 12	1892 ± 4
5	3551 ± 12	2055 ± 4	3584 ± 12	1856 ± 3

Table C.4: Saturated velocities of sample 1-132 under constant differential pressure.

Confining pressure (MPa)	Pore pressure (MPa)	V _p (m/s)	V _s (m/s)
15	0	3683±12	1939±4
17.5	2.5	3675±12	1936±4
20	5	3676±12	1931±4
22.5	7.5	3674±12	1933±4
25	10	3678±12	1935±4

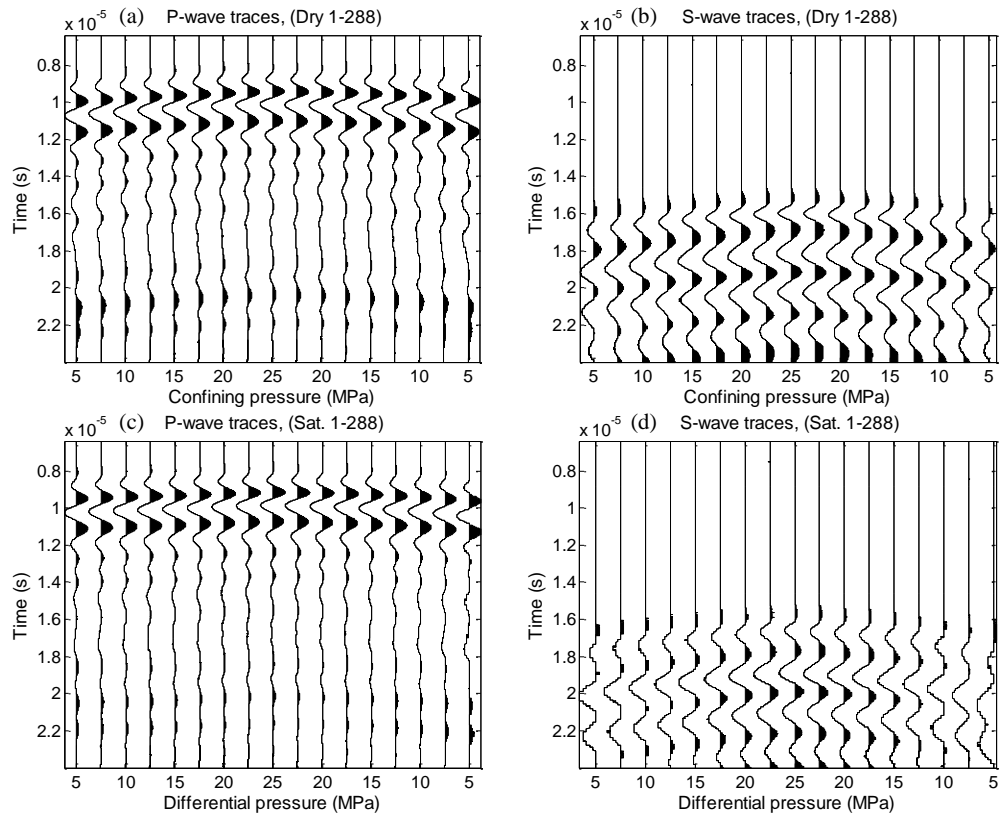


Figure C.3: Normalized waveforms of dry and saturated, P-wave (a and c respectively) and S-wave (b and d respectively) for sample 1-288 at different pressure.

Table C.5: Dry and saturated velocities of sample 1-288.

Pressure (MPa)	Dry		Saturated	
	Vp (m/s)	Vs (m/s)	Vp (m/s)	Vs (m/s)
5	3956 ± 14	2162 ± 4	4149 ± 14	2052 ± 4
7.5	3989 ± 14	2182 ± 4	4183 ± 15	2078 ± 4
10	4020 ± 14	2203 ± 4	4198 ± 15	2099 ± 4
12.5	4050 ± 14	2219 ± 4	4218 ± 15	2122 ± 4
15	4074 ± 14	2233 ± 4	4227 ± 15	2136 ± 4
17.5	4109 ± 14	2251 ± 4	4245 ± 15	2157 ± 4
20	4127 ± 14	2266 ± 4	4261 ± 15	2170 ± 4
22.5	4152 ± 15	2279 ± 5	4285 ± 15	2190 ± 4
25	4168 ± 15	2288 ± 5	4299 ± 15	2203 ± 4
22.5	4160 ± 15	2284 ± 5	4291 ± 15	2193 ± 4
20	4148 ± 15	2277 ± 5	4275 ± 15	2182 ± 4
17.5	4130 ± 14	2268 ± 4	4264 ± 15	2169 ± 4
15	4115 ± 14	2254 ± 4	4241 ± 15	2150 ± 4
12.5	4090 ± 14	2242 ± 4	4221 ± 15	2125 ± 4
10	4055 ± 14	2218 ± 4	4188 ± 15	2097 ± 4
7.5	4020 ± 14	2200 ± 4	4150 ± 14	2055 ± 4
5	3969 ± 14	2166 ± 4	4108 ± 14	1992 ± 4

Table C.6: Saturated velocities of sample 1-288 under constant differential pressure.

Confining pressure (MPa)	Pore pressure (MPa)	Vp (m/s)	Vs (m/s)
15	0	3990±14	2024±14
17.5	2.5	4020±14	2021±14
20	5	4023±14	2021±14
22.5	7.5	4021±14	2022±14
25	10	4018±14	2021±14

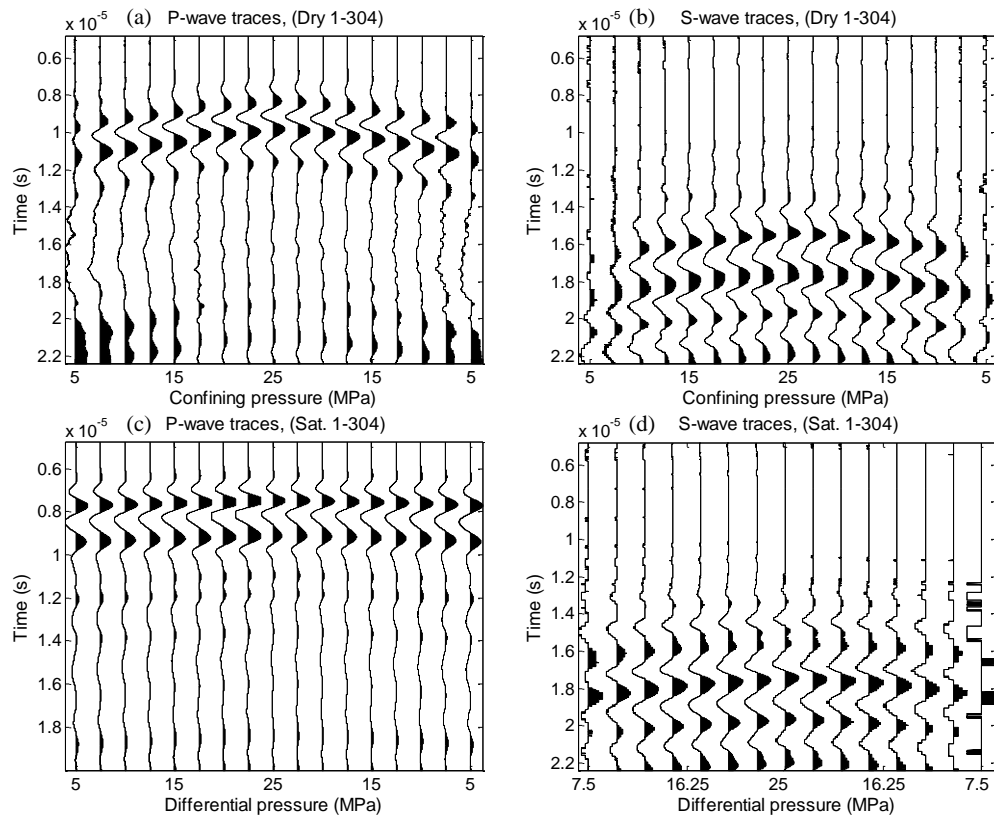


Figure C.4: Normalized waveforms of dry and saturated, P-wave (a and c respectively) and S-wave (b and d respectively) for sample 1-304 at different pressure.

Table C.7: Dry and saturated velocities of sample 1-304.

Pressure (MPa)	Dry				Saturated			
	Vp (m/s)		Vs (m/s)		Vp (m/s)		Vs (m/s)	
5	4002	± 14	-	-	5207	± 20	-	-
7.5	4214	± 15	2412	± 5	5226	± 20	2465	± 5
10	4449	± 16	2463	± 5	5242	± 20	2485	± 5
12.5	4593	± 17	2491	± 5	5260	± 20	2504	± 5
15	4645	± 17	2518	± 5	5271	± 20	2523	± 5
17.5	4737	± 17	2537	± 5	5296	± 20	2534	± 5
20	4811	± 18	2554	± 5	5309	± 20	2545	± 5
22.5	4846	± 18	2571	± 5	5329	± 20	2563	± 5
25	4891	± 18	2586	± 5	5344	± 20	2578	± 5
22.5	4861	± 18	2583	± 5	5343	± 20	2569	± 5
20	4837	± 18	2568	± 5	5336	± 20	2552	± 5
17.5	4806	± 18	2549	± 5	5326	± 20	2540	± 5
15	4708	± 17	2528	± 5	5305	± 20	2532	± 5
12.5	4627	± 17	2498	± 5	5287	± 20	2513	± 5
10	4499	± 16	2467	± 5	5268	± 20	2491	± 5
7.5	4234	± 15	2416	± 5	5247	± 20	2469	± 5
5	4023	± 14	-	-	5218	± 20	-	-

Table C.8: Saturated velocities of sample 1-304 under constant differential pressure.

Confining pressure (MPa)	Pore pressure (MPa)	Vp (m/s)	Vs (m/s)
15	0	5271±20	2529±5
17.5	2.5	5271±20	2530±5
20	5	5272±20	2524±5
22.5	7.5	5268±20	2517±5
25	10	5272±20	2524±5

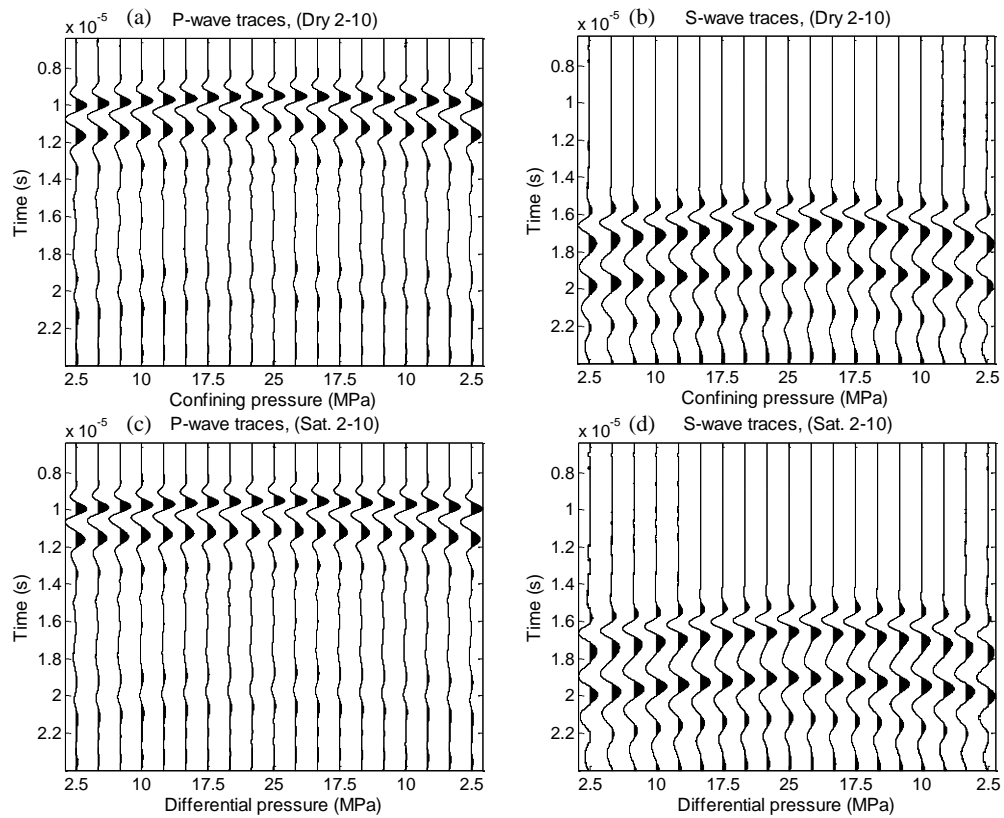


Figure C.5: Normalized waveforms of dry and saturated, P-wave (a and c respectively) and S-wave (b and d respectively) for sample 2-10 at different pressure.

Table C.9: Dry and saturated velocities of sample 2-10.

Pressure (MPa)	Dry		Saturated	
	V _p (m/s)	V _s (m/s)	V _p (m/s)	V _s (m/s)
2.5	3806 ± 13	2252 ± 5	3823 ± 13	2249 ± 4
5	3841 ± 13	2268 ± 5	3851 ± 13	2261 ± 5
7.5	3868 ± 13	2278 ± 5	3872 ± 13	2277 ± 5
10	3891 ± 13	2288 ± 5	3895 ± 13	2289 ± 5
12.5	3914 ± 14	2301 ± 5	3921 ± 14	2300 ± 5
15	3937 ± 14	2308 ± 5	3938 ± 14	2313 ± 5
17.5	3957 ± 14	2320 ± 5	3955 ± 14	2322 ± 5
20	3968 ± 14	2328 ± 5	3968 ± 14	2330 ± 5
22.5	3982 ± 14	2335 ± 5	3979 ± 14	2339 ± 5
25	3990 ± 14	2342 ± 5	3988 ± 14	2344 ± 5
22.5	3988 ± 14	2349 ± 5	3981 ± 14	2339 ± 5
20	3977 ± 14	2345 ± 5	3973 ± 14	2333 ± 5
17.5	3966 ± 14	2337 ± 5	3960 ± 14	2325 ± 5
15	3953 ± 14	2329 ± 5	3948 ± 14	2318 ± 5
12.5	3936 ± 14	2319 ± 5	3935 ± 14	2307 ± 5
10	3919 ± 14	2309 ± 5	3917 ± 14	2296 ± 5
7.5	3894 ± 13	2291 ± 5	3892 ± 13	2282 ± 5
5	3870 ± 13	2275 ± 5	3863 ± 13	2264 ± 5
2.5	3824 ± 13	2251 ± 4	3825 ± 13	2241 ± 4

Table C.10: Saturated velocities of sample 2-10 under constant differential pressure.

Confining pressure (MPa)	Pore pressure (MPa)	V _p (m/s)	V _s (m/s)
15	0	3299±11	1760±3
17.5	2.5	3293±11	1750±3
20	5	3305±11	1749±3
22.5	7.5	3299±11	1752±3
25	10	3306±11	1754±3

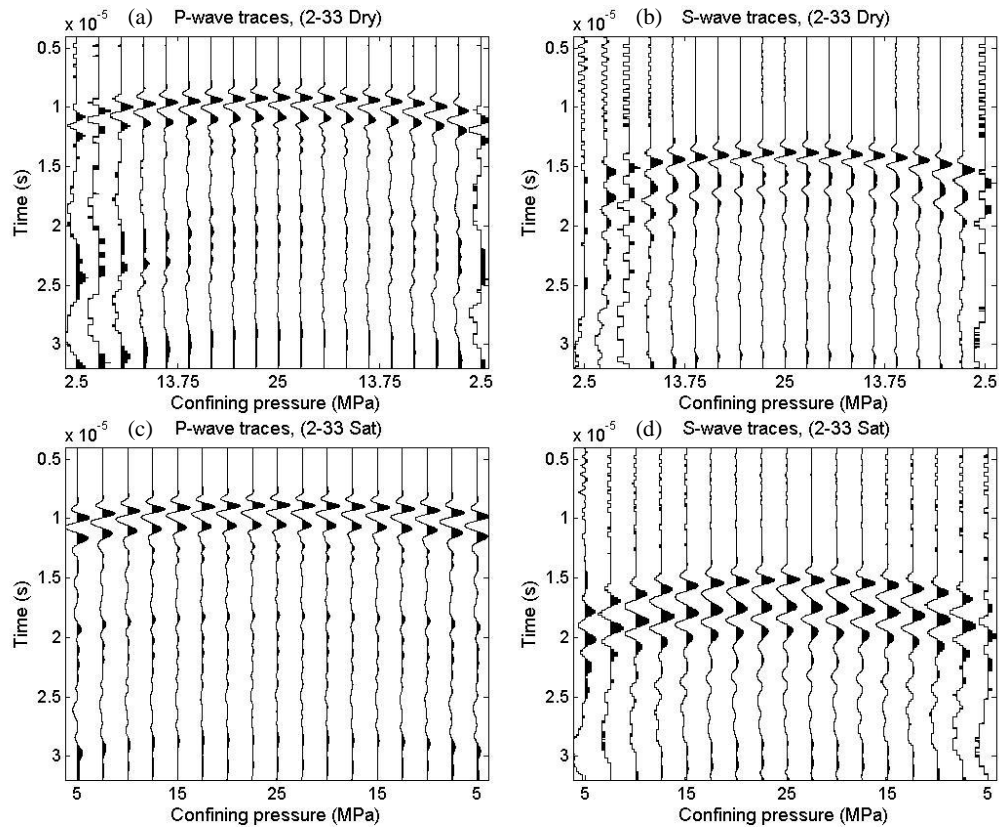


Figure C.6: Normalized waveforms of dry and saturated, P-wave (a and c respectively) and S-wave (b and d respectively) for sample 2-33 at different pressure.

Table C.11: Dry and saturated velocities of sample 2-33.

Pressure (MPa)	Dry				Saturated			
	Vp (m/s)		Vs (m/s)		Vp (m/s)		Vs (m/s)	
2.5	2655	± 9	1553	± 3	-	-	-	-
5	2767	± 10	1725	± 4	2894	± 10	1507	± 3
7.5	2877	± 10	1777	± 4	2999	± 11	1583	± 3
10	2944	± 11	1817	± 4	3065	± 11	1632	± 3
12.5	2987	± 11	1843	± 4	3119	± 11	1670	± 4
15	3017	± 11	1864	± 4	3163	± 12	1698	± 4
17.5	3049	± 11	1882	± 4	3194	± 12	1721	± 4
20	3081	± 11	1895	± 4	3213	± 12	1737	± 4
22.5	3099	± 11	1907	± 4	3230	± 12	1748	± 4
25	3113	± 11	1914	± 4	3238	± 12	1754	± 4
22.5	3104	± 11	1909	± 4	3231	± 12	1747	± 4
20	3094	± 11	1902	± 4	3216	± 12	1736	± 4
17.5	3074	± 11	1891	± 4	3196	± 12	1721	± 4
15	3045	± 11	1876	± 4	3170	± 12	1703	± 4
12.5	3007	± 11	1856	± 4	3131	± 12	1675	± 4
10	2954	± 11	1830	± 4	3088	± 11	1646	± 3
7.5	2879	± 10	1791	± 4	3017	± 11	1594	± 3
5	2776	± 10	1737	± 4	2929	± 10	1532	± 3
2.5	2667	± 9	1630	± 3	-	-	-	-

Table C.12: Saturated velocities of sample 2-33 under constant differential pressure.

Confining pressure (MPa)	Pore pressure (MPa)	Vp (m/s)	Vs (m/s)
15	0	3163±12	1698±4
17.5	2.5	3165±12	1695±4
20	5	3172±12	1697±4
22.5	7.5	3178±12	1700±4
25	10	3179±12	1700±4

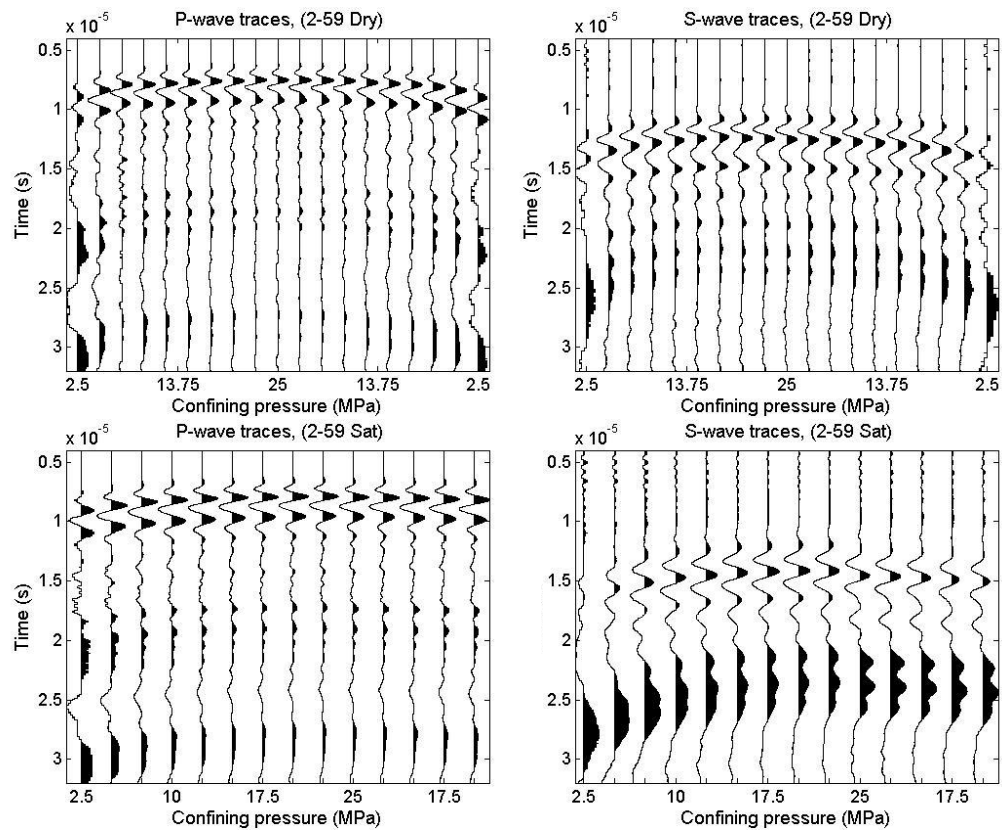


Figure C.7: Normalized waveforms of dry and saturated, P-wave (a and c respectively) and S-wave (b and d respectively) for sample 2-59 at different pressure.

Table C.13: Dry and saturated velocities of sample 2-59.

Pressure (MPa)	Dry		Saturated	
	Vp (m/s)	Vs (m/s)	Vp (m/s)	Vs (m/s)
2.5	2514 ± 10	1557 ± 4	2462 ± 9	1384 ± 3
5	2671 ± 10	1637 ± 4	2563 ± 10	1432 ± 3
7.5	2818 ± 11	1683 ± 4	2659 ± 10	1478 ± 3
10	2825 ± 11	1707 ± 4	2720 ± 11	1520 ± 4
12.5	2865 ± 11	1727 ± 4	2758 ± 11	1538 ± 4
15	2897 ± 12	1742 ± 4	2788 ± 11	1565 ± 4
17.5	2923 ± 12	1757 ± 4	2807 ± 11	1578 ± 4
20	2929 ± 12	1764 ± 4	2821 ± 11	1586 ± 4
22.5	2960 ± 12	1764 ± 4	2826 ± 11	1588 ± 4
25	2955 ± 12	1758 ± 4	2795 ± 11	1547 ± 4
22.5	2956 ± 12	1756 ± 4	2783 ± 11	1526 ± 4
20	2951 ± 12	1748 ± 4	2770 ± 11	1522 ± 4
17.5	2936 ± 12	1741 ± 4	2747 ± 11	1508 ± 4
15	2879 ± 12	1730 ± 4	2724 ± 11	1483 ± 3
12.5	2857 ± 11	1713 ± 4	-	-
10	2817 ± 11	1694 ± 4	-	-
7.5	2759 ± 11	1660 ± 4	-	-
5	2665 ± 10	1615 ± 4	-	-
2.5	2481 ± 9	1529 ± 4	-	-

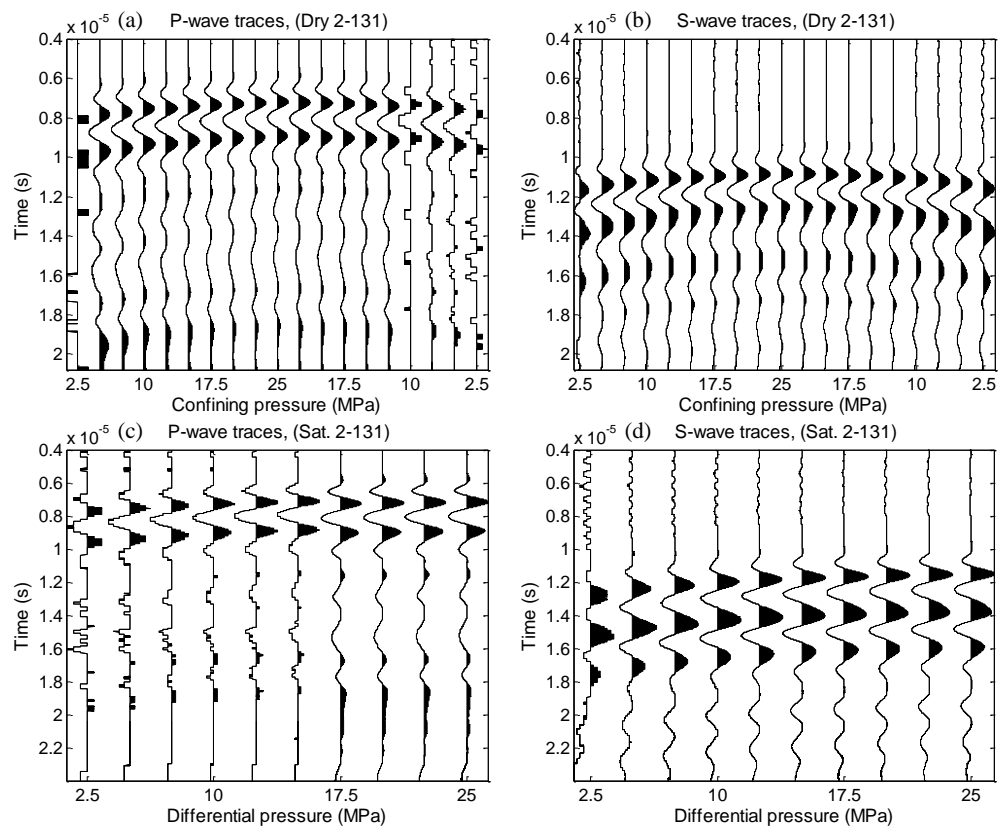


Figure C.8: Normalized waveforms of dry and saturated, P-wave (a and c respectively) and S-wave (b and d respectively) for sample 2-131 at different pressure.

Table C.14: Dry and saturated velocities of sample 2-131.

Pressure (MPa)	Dry		Saturated	
	Vp (m/s)	Vs (m/s)	Vp (m/s)	Vs (m/s)
2.5	3222 ± 12	2141 ± 5	3297 ± 13	1969 ± 5
5	3258 ± 13	2164 ± 5	3386 ± 13	2014 ± 5
7.5	3305 ± 13	2180 ± 5	3435 ± 14	2036 ± 5
10	3367 ± 13	2200 ± 5	3496 ± 14	2060 ± 5
12.5	3399 ± 13	2212 ± 5	3533 ± 14	2083 ± 5
15	3427 ± 14	2226 ± 5	3579 ± 14	2104 ± 5
17.5	3453 ± 14	2235 ± 5	3598 ± 14	2118 ± 5
20	3477 ± 14	2247 ± 5	3616 ± 14	2127 ± 5
22.5	3484 ± 14	2253 ± 5	3625 ± 14	2136 ± 5
25	3518 ± 14	2263 ± 6	3625 ± 14	2143 ± 5
22.5	3504 ± 14	2259 ± 5	-	-
20	3495 ± 14	2254 ± 5	-	-
17.5	3480 ± 14	2244 ± 5	-	-
15	3455 ± 14	2237 ± 5	-	-
12.5	3440 ± 14	2225 ± 5	-	-
10	3419 ± 13	2212 ± 5	-	-
7.5	3389 ± 13	2188 ± 5	-	-
5	3350 ± 13	2172 ± 5	-	-
2.5	3304 ± 13	2144 ± 5	-	-

Table C.15: Saturated velocities of sample 2-131 under constant differential pressure.

Confining pressure (MPa)	Pore pressure (MPa)	Vp (m/s)	Vs (m/s)
15	0	3596±14	2103±5
17.5	2.5	3593±14	2097±5
20	5	3592±14	2097±5
22.5	7.5	3595±14	2093±5
25	10	3599±14	2094±5

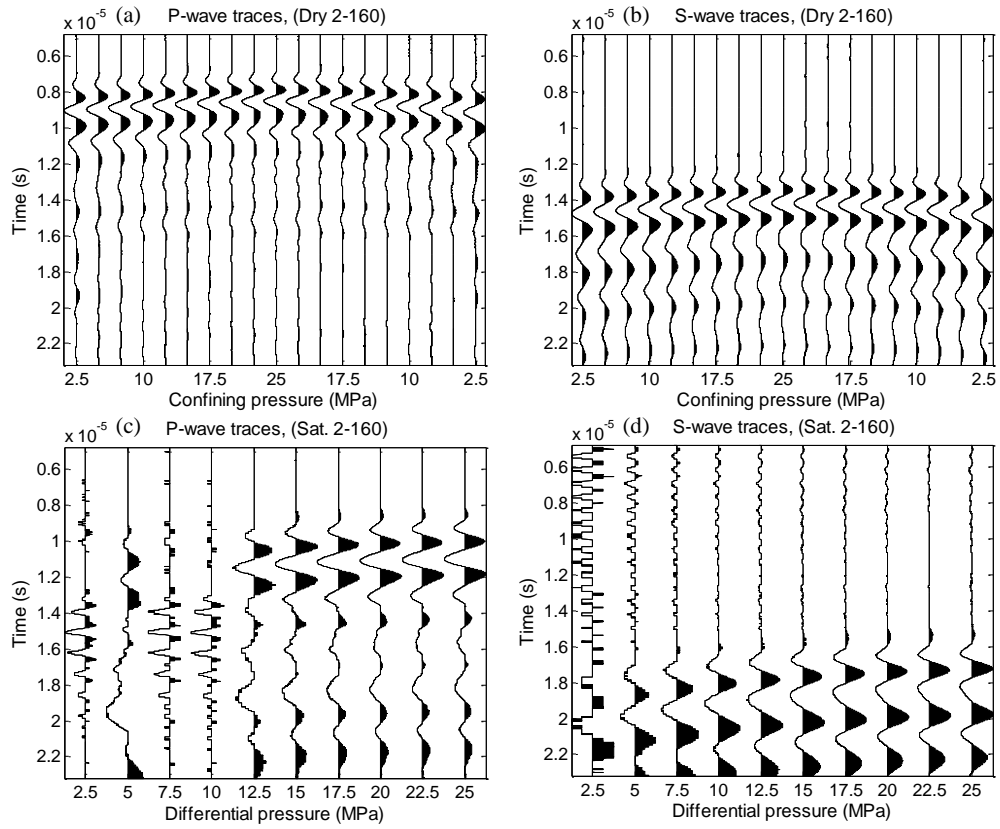


Figure C.9: Normalized waveforms of dry and saturated, P-wave (a and c respectively) and S-wave (b and d respectively) for sample 2-160 at different pressure.

Table C.16: Dry and saturated velocities of sample 2-160.

Pressure (MPa)	Dry		Saturated			
	Vp (m/s)	Vs (m/s)	Vp (m/s)		Vs (m/s)	
2.5	3233 ± 10	2040 ± 4	±		± 4	
5	3315 ± 11	2069 ± 4	3355 ± 11	1936 ± 4		
7.5	3386 ± 11	2092 ± 4	3420 ± 11	1973 ± 4		
10	3438 ± 11	2112 ± 4	3475 ± 12	1997 ± 4		
12.5	3478 ± 12	2137 ± 4	3511 ± 12	2021 ± 4		
15	3520 ± 12	2152 ± 4	3578 ± 12	2038 ± 4		
17.5	3551 ± 12	2168 ± 4	3614 ± 12	2056 ± 4		
20	3582 ± 12	2176 ± 4	3642 ± 12	2070 ± 4		
22.5	3615 ± 12	2188 ± 4	3662 ± 12	2074 ± 4		
25	3643 ± 12	2199 ± 4	3676 ± 13	2082 ± 4		
22.5	3630 ± 12	2193 ± 4	-	-	-	-
20	3611 ± 12	2186 ± 4	-	-	-	-
17.5	3591 ± 12	2177 ± 4	-	-	-	-
15	3558 ± 12	2172 ± 4	-	-	-	-
12.5	3523 ± 12	2149 ± 4	-	-	-	-
10	3480 ± 12	2136 ± 4	-	-	-	-
7.5	3431 ± 11	2106 ± 4	-	-	-	-
5	3383 ± 11	2077 ± 4	-	-	-	-
2.5	3336 ± 11	2054 ± 4	-	-	-	-

Table C.17: Saturated velocities of sample 2-160 under constant differential pressure.

Confining pressure (MPa)	Pore pressure (MPa)	Vp (m/s)	Vs (m/s)
15	0	3689±13	2029±4
17.5	2.5	3692±13	2037±4
20	5	3689±13	2037±4
22.5	7.5	3685±13	2037±4
25	10	3685±13	2035±4

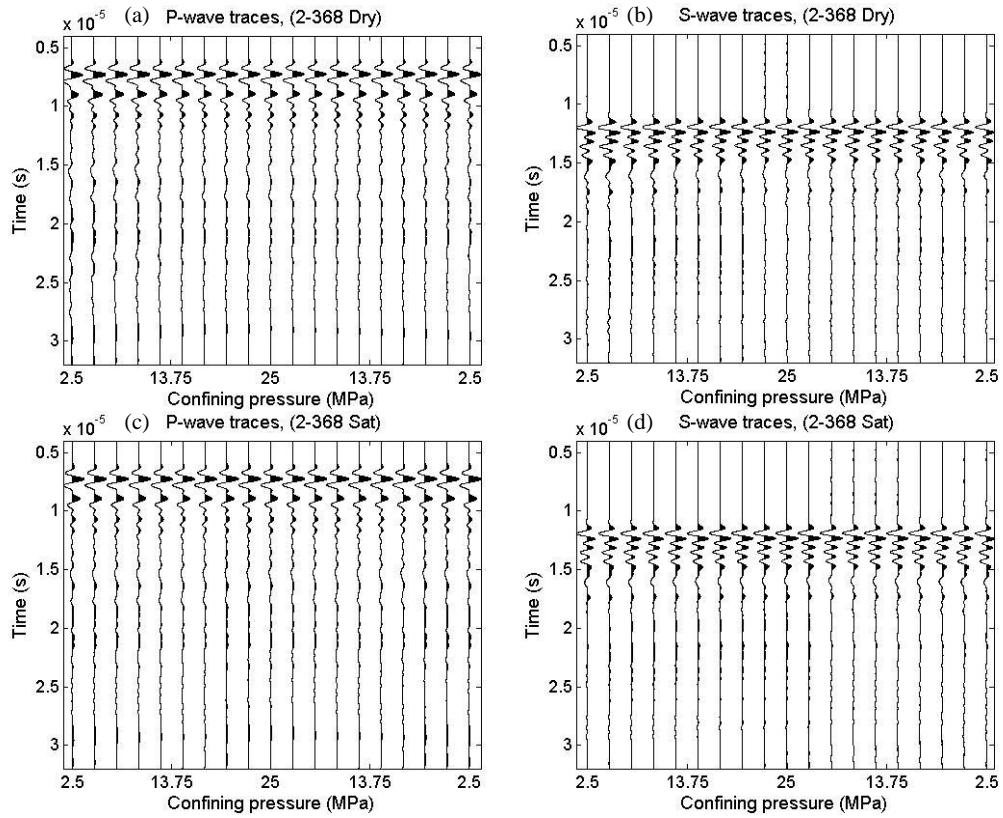


Figure C.10: Normalized waveforms of dry and saturated, P-wave (a and c respectively) and S-wave (b and d respectively) for sample 2-368 at different pressure.

Table C.18: Dry and saturated velocities of sample 2-368.

Pressure (MPa)	Dry		Saturated	
	Vp (m/s)	Vs (m/s)	Vp (m/s)	Vs (m/s)
2.5	5804 ± 23	3162 ± 7	5836 ± 23	3174 ± 7
5	5807 ± 23	3163 ± 7	5840 ± 23	3174 ± 7
7.5	5820 ± 23	3168 ± 7	5841 ± 23	3175 ± 7
10	5826 ± 23	3169 ± 7	5842 ± 23	3176 ± 7
12.5	5828 ± 23	3171 ± 7	5841 ± 23	3176 ± 7
15	5830 ± 23	3172 ± 7	5840 ± 23	3177 ± 7
17.5	5830 ± 23	3175 ± 7	5838 ± 23	3179 ± 7
20	5830 ± 23	3175 ± 7	5835 ± 23	3179 ± 7
22.5	5828 ± 23	3175 ± 7	5834 ± 23	3180 ± 7
25	5825 ± 23	3177 ± 7	5833 ± 23	3180 ± 7
22.5	5829 ± 23	3178 ± 7	5836 ± 23	3182 ± 7
20	5836 ± 23	3178 ± 7	5843 ± 23	3183 ± 7
17.5	5842 ± 23	3179 ± 7	5845 ± 23	3182 ± 7
15	5841 ± 23	3177 ± 7	5849 ± 23	3182 ± 7
12.5	5844 ± 23	3177 ± 7	5850 ± 23	3182 ± 7
10	5845 ± 23	3176 ± 7	5850 ± 23	3181 ± 7
7.5	5844 ± 23	3176 ± 7	5851 ± 23	3178 ± 7
5	5842 ± 23	3174 ± 7	5848 ± 23	3178 ± 7
2.5	5836 ± 23	3172 ± 7	5840 ± 23	3176 ± 7

Table C.19: Saturated velocities of sample 2-368 under constant differential pressure.

Confining pressure (MPa)	Pore pressure (MPa)	Vp (m/s)	Vs (m/s)
15	0	5855±23	3180±7
17.5	2.5	5852±23	3182±7
20	5	5863±23	3182±7
22.5	7.5	5874±23	3186±7
25	10	5874±23	3188±7

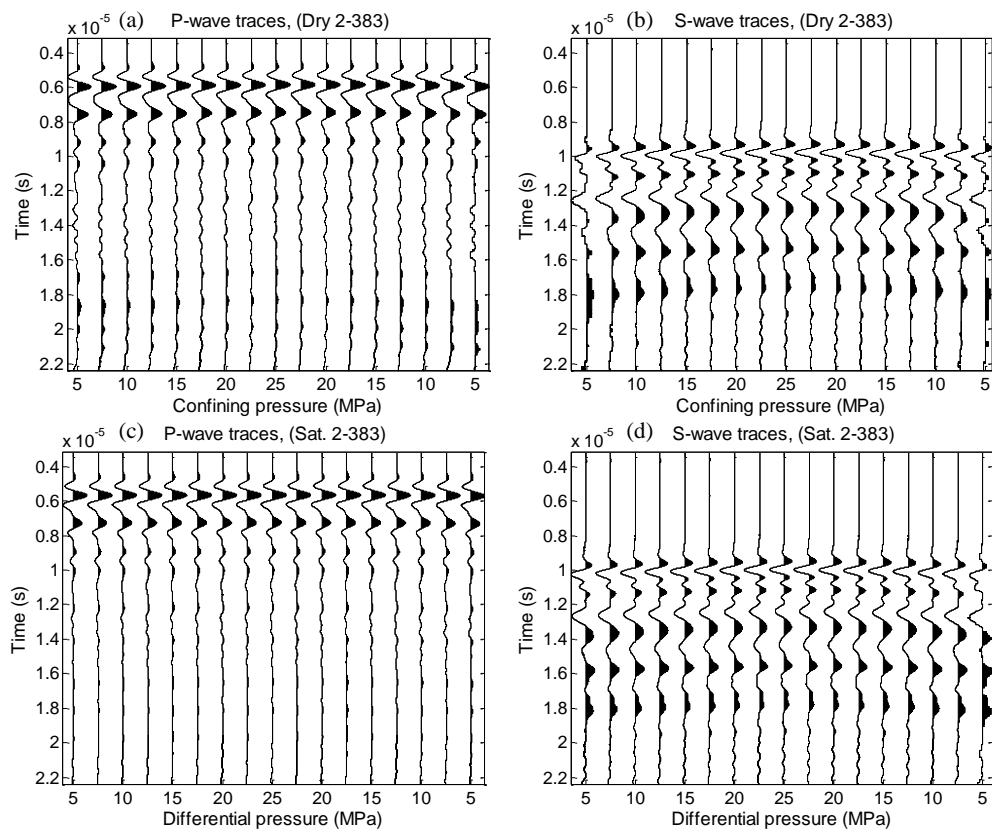


Figure C.11: Normalized waveforms of dry and saturated, P-wave (a and c respectively) and S-wave (b and d respectively) for sample 2-383 at different pressure.

Table C.20: Dry and saturated velocities of sample 2-383.

Pressure (MPa)	Dry		Saturated	
	Vp (m/s)	Vs (m/s)	Vp (m/s)	Vs (m/s)
5	4795 ± 20	2717 ± 7	5034 ± 22	2660 ± 6
7.5	4803 ± 20	2722 ± 7	5039 ± 22	2671 ± 6
10	4810 ± 20	2735 ± 7	5040 ± 22	2681 ± 7
12.5	4822 ± 20	2742 ± 7	5041 ± 22	2689 ± 7
15	4835 ± 20	2752 ± 7	5043 ± 22	2697 ± 7
17.5	4851 ± 21	2761 ± 7	5044 ± 22	2706 ± 7
20	4855 ± 21	2771 ± 7	5045 ± 22	2714 ± 7
22.5	4863 ± 21	2772 ± 7	5048 ± 22	2719 ± 7
25	4880 ± 21	2781 ± 7	5054 ± 22	2727 ± 7
22.5	4877 ± 21	2780 ± 7	5055 ± 22	2722 ± 7
20	4873 ± 21	2777 ± 7	5054 ± 22	2719 ± 7
17.5	4872 ± 21	2772 ± 7	5052 ± 22	2712 ± 7
15	4867 ± 21	2766 ± 7	5050 ± 22	2705 ± 7
12.5	4863 ± 21	2759 ± 7	5045 ± 22	2696 ± 7
10	4851 ± 21	2750 ± 7	5036 ± 22	2678 ± 7
7.5	4828 ± 20	2737 ± 7	5027 ± 21	2669 ± 6
5	4799 ± 20	2720 ± 7	5007 ± 21	2645 ± 6

Table C.21: Saturated velocities of sample 2-383 under constant differential pressure.

Confining pressure (MPa)	Pore pressure (MPa)	Vp (m/s)	Vs (m/s)
15	0	5049±22	2702±7
17.5	2.5	5057±22	2702±7
20	5	5053±22	2702±7
22.5	7.5	5046±22	2702±7
25	10	5047±22	2704±7

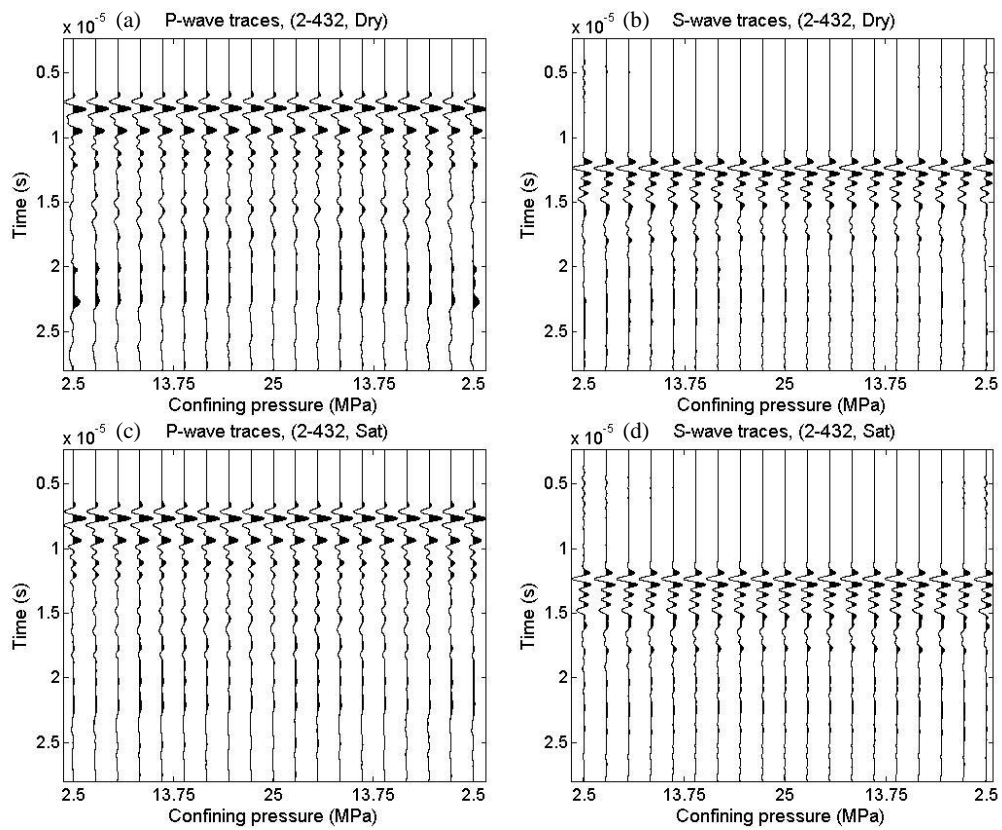


Figure C.12: Normalized waveforms of dry and saturated, P-wave (a and c respectively) and S-wave (b and d respectively) for sample 2-432 at different pressure.

Table C.22: Dry and saturated velocities of sample 2-432.

Pressure (MPa)	Dry		Saturated	
	Vp (m/s)	Vs (m/s)	Vp (m/s)	Vs (m/s)
2.5	5293 ± 21	2994 ± 7	5369 ± 21	2998 ± 7
5	5308 ± 21	2994 ± 7	5372 ± 21	2999 ± 7
7.5	5309 ± 21	2994 ± 7	5369 ± 21	2998 ± 7
10	5310 ± 21	2995 ± 7	5363 ± 21	2997 ± 7
12.5	5311 ± 21	2995 ± 7	5363 ± 21	2998 ± 7
15	5313 ± 21	2995 ± 7	5357 ± 21	2998 ± 7
17.5	5313 ± 21	2996 ± 7	5359 ± 21	2997 ± 7
20	5314 ± 21	2997 ± 7	5351 ± 21	2998 ± 7
22.5	5314 ± 21	2997 ± 7	5347 ± 21	2997 ± 7
25	5313 ± 21	2998 ± 7	5348 ± 21	2998 ± 7
22.5	5316 ± 21	3000 ± 7	5348 ± 21	2999 ± 7
20	5317 ± 21	3000 ± 7	5353 ± 21	2999 ± 7
17.5	5323 ± 21	3001 ± 7	5362 ± 21	2999 ± 7
15	5324 ± 21	3001 ± 7	5361 ± 21	2999 ± 7
12.5	5326 ± 21	3001 ± 7	5367 ± 21	2998 ± 7
10	5325 ± 21	3001 ± 7	5366 ± 21	2997 ± 7
7.5	5322 ± 21	2998 ± 7	5371 ± 21	2995 ± 7
5	5316 ± 21	2998 ± 7	5370 ± 21	2993 ± 7
2.5	5299 ± 21	2998 ± 7	5365 ± 21	2989 ± 7

Table C.23: Saturated velocities of sample 2-432 under constant differential pressure.

Confining pressure (MPa)	Pore pressure (MPa)	Vp (m/s)	Vs (m/s)
15	0	5323±21	2976±7
17.5	2.5	5323±21	2975±7
20	5	5327±21	2971±7
22.5	7.5	5325±21	2962±7
25	10	5319±21	2952±7

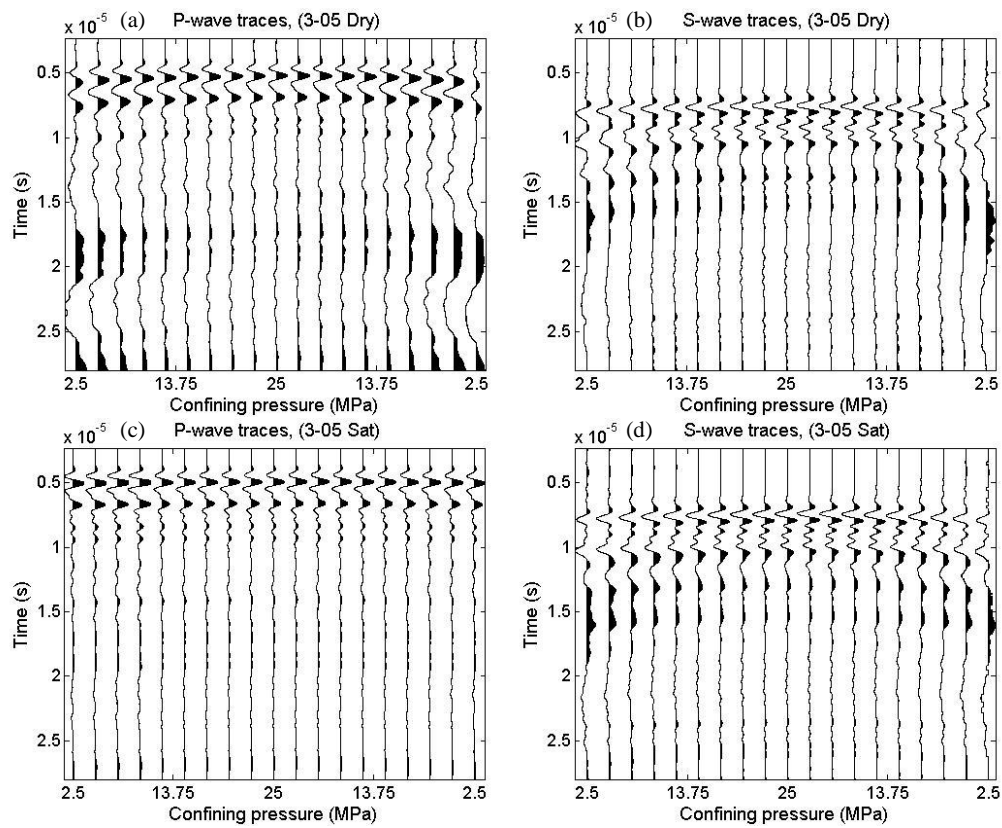


Figure C.13: Normalized waveforms of dry and saturated, P-wave (a and c respectively) and S-wave (b and d respectively) for sample 3-05 at different pressure.

Table C.24: Dry and saturated velocities of sample 3-05.

Pressure (MPa)	Dry		Saturated	
	V _p (m/s)	V _s (m/s)	V _p (m/s)	V _s (m/s)
2.5	5204 ± 23	3145 ± 8	5851 ± 27	3223 ± 9
5	5330 ± 24	3189 ± 8	5864 ± 27	3263 ± 9
7.5	5389 ± 24	3219 ± 9	5895 ± 27	3298 ± 9
10	5435 ± 25	3250 ± 9	5914 ± 27	3322 ± 9
12.5	5478 ± 25	3277 ± 9	5922 ± 27	3339 ± 9
15	5510 ± 25	3296 ± 9	5942 ± 27	3347 ± 9
17.5	5548 ± 25	3317 ± 9	5944 ± 28	3360 ± 9
20	5571 ± 25	3333 ± 9	5951 ± 28	3368 ± 9
22.5	5604 ± 26	3347 ± 9	5952 ± 28	3374 ± 9
25	5627 ± 26	3359 ± 9	5972 ± 28	3380 ± 9
22.5	5620 ± 26	3355 ± 9	5984 ± 28	3394 ± 9
20	5613 ± 26	3343 ± 9	5992 ± 28	3393 ± 9
17.5	5584 ± 25	3333 ± 9	5989 ± 28	3383 ± 9
15	5557 ± 25	3315 ± 9	5991 ± 28	3370 ± 9
12.5	5499 ± 25	3281 ± 9	5977 ± 28	3353 ± 9
10	5453 ± 25	3256 ± 9	5963 ± 28	3337 ± 9
7.5	5396 ± 24	3220 ± 9	5937 ± 27	3310 ± 9
5	5350 ± 24	3194 ± 8	5917 ± 27	3273 ± 9
2.5	5235 ± 23	3151 ± 8	5862 ± 27	3225 ± 9

Table C.25: Saturated velocities of sample 3-05 under constant differential pressure.

Confining pressure (MPa)	Pore pressure (MPa)	V _p (m/s)	V _s (m/s)
15	0	5942±27	3348±
17.5	2.5	5978±28	3355±9
20	5	5984±28	3357±9
22.5	7.5	5997±28	3359±9
25	10	5997±28	3363±9

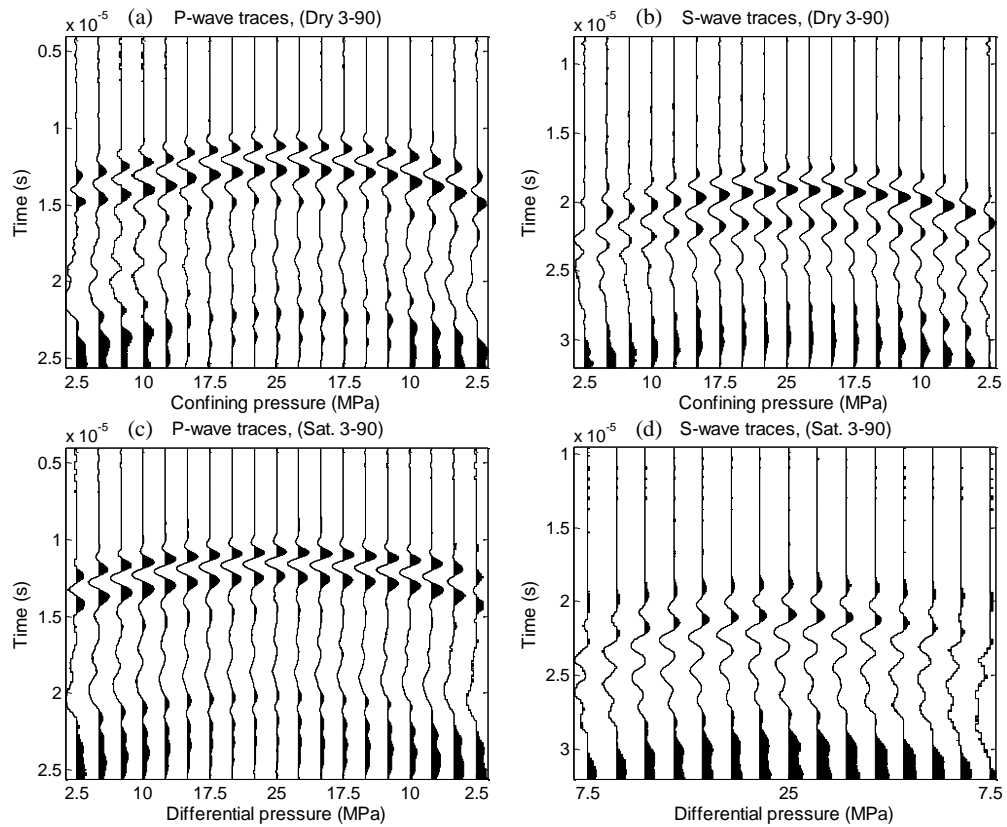


Figure C.14: Normalized waveforms of dry and saturated, P-wave (a and c respectively) and S-wave (b and d respectively) for sample 3-90 at different pressure.

Table C.26: Dry and saturated velocities of sample 3-90.

Pressure (MPa)	Dry		Saturated	
	Vp (m/s)	Vs (m/s)	Vp (m/s)	Vs (m/s)
2.5	2760 ± 8	1726 ± 3	2967 ± 9	-
5	2849 ± 9	1785 ± 3	3050 ± 10	1650 ± 3
7.5	2919 ± 9	1821 ± 3	3130 ± 10	1691 ± 3
10	2978 ± 9	1857 ± 4	3181 ± 10	1718 ± 3
12.5	3046 ± 10	1880 ± 4	3238 ± 10	1744 ± 3
15	3135 ± 10	1894 ± 4	3286 ± 11	1769 ± 3
17.5	3182 ± 10	1913 ± 4	3311 ± 11	1784 ± 3
20	3215 ± 10	1930 ± 4	3336 ± 11	1797 ± 3
22.5	3248 ± 11	1945 ± 4	3353 ± 11	1807 ± 3
25	3266 ± 11	1956 ± 4	3381 ± 11	1814 ± 3
22.5	3255 ± 11	1951 ± 4	3366 ± 11	1810 ± 3
20	3236 ± 10	1945 ± 4	3347 ± 11	1802 ± 3
17.5	3216 ± 10	1935 ± 4	3326 ± 11	1793 ± 3
15	3196 ± 10	1921 ± 4	3298 ± 11	1777 ± 3
12.5	3155 ± 10	1902 ± 4	3263 ± 11	1758 ± 3
10	3075 ± 10	1882 ± 4	3216 ± 10	1731 ± 3
7.5	3005 ± 9	1854 ± 3	3154 ± 10	1703 ± 3
5	2932 ± 9	1814 ± 3	3074 ± 10	-
2.5	2786 ± 8	1745 ± 3	2993 ± 9	-

Table C.27: Saturated velocities of sample 3-90 under constant differential pressure.

Confining pressure (MPa)	Pore pressure (MPa)	Vp (m/s)	Vs (m/s)
15	0	3299±11	1760±3
17.5	2.5	3293±11	1750±3
20	5	3305±11	1749±3
22.5	7.5	3299±11	1752±3
25	10	3306±11	1754±3

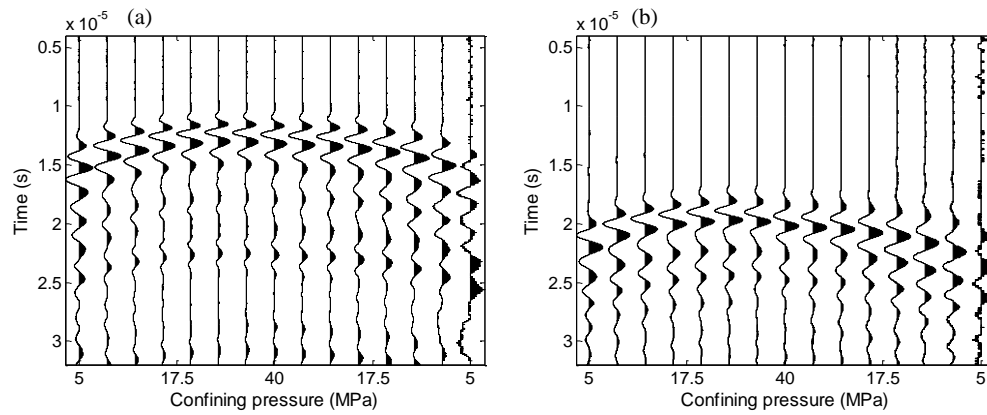


Figure C.15: Normalized waveforms of dry and saturated, P-wave (a and c respectively) and S-wave (b and d respectively) for sample 3-104 at different pressure.

Table C.28: Dry and saturated velocities of sample 3-104.

Pressure (MPa)	Dry		Saturated	
	Vp (m/s)	Vs (m/s)	Vp (m/s)	Vs (m/s)
5	2754 ± 8	1824 ± 3	2788 ± 8	1226 ± 2
10	2942 ± 9	1894 ± 4	2887 ± 9	1552 ± 3
15	3027 ± 10	1937 ± 4	2976 ± 9	1600 ± 3
20	3107 ± 10	1970 ± 4	3044 ± 10	1641 ± 3
25	3154 ± 10	1992 ± 4	3076 ± 10	1669 ± 3
30	3181 ± 10	2009 ± 4	3099 ± 10	1679 ± 3
35	3178 ± 10	2007 ± 4	3040 ± 10	1595 ± 3
40	3171 ± 10	1989 ± 4	3068 ± 10	1612 ± 3
35	3146 ± 10	1981 ± 4	-	-
30	3119 ± 10	1969 ± 4	-	-
25	3080 ± 10	1961 ± 4	-	-
20	3032 ± 10	1937 ± 4	-	-
15	2939 ± 9	1908 ± 4	-	-
10	2828 ± 9	1859 ± 3	-	-
5	2534 ± 7	1762 ± 3	-	-

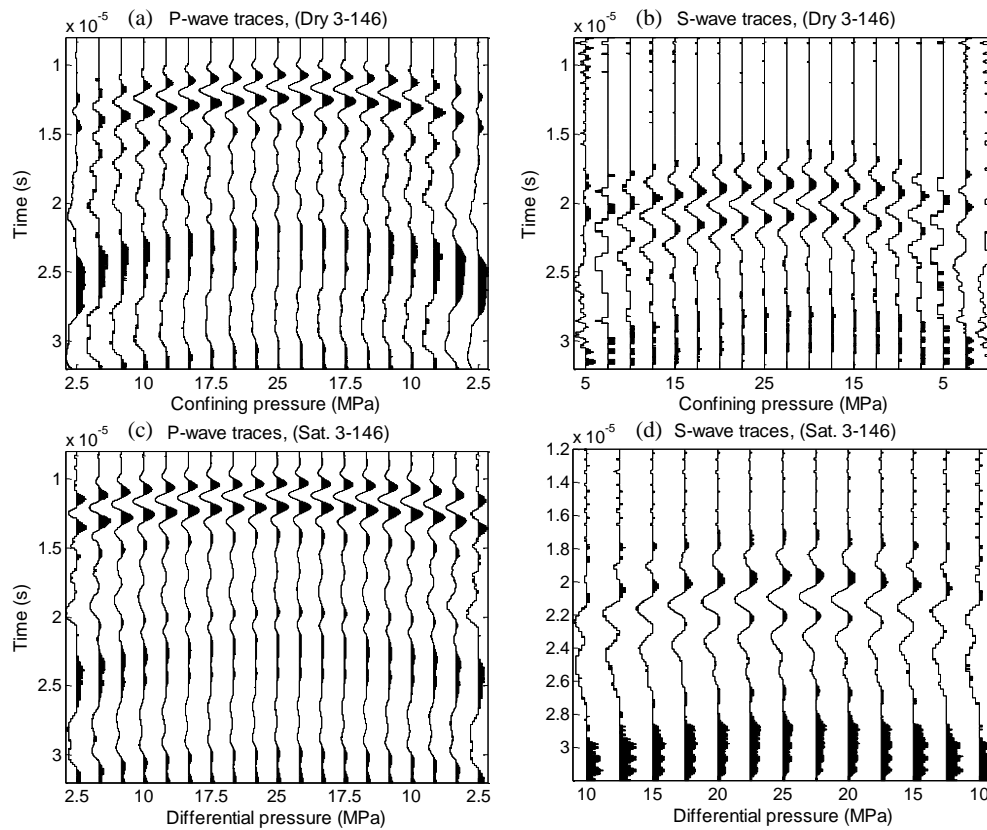


Figure C.16: Normalized waveforms of dry and saturated, P-wave (a and c respectively) and S-wave (b and d respectively) for sample 3-146 at different pressure.

Table C.29: Dry and saturated velocities of sample 3-146.

Pressure (MPa)	Dry				Saturated			
	Vp (m/s)		Vs (m/s)		Vp (m/s)		Vs (m/s)	
2.5	3060	± 9	1771	± 3	3357	± 11	-	-
5	3156	± 10	1828	± 3	3447	± 11	-	-
7.5	3238	± 10	1860	± 3	3491	± 12	-	-
10	3323	± 11	1903	± 4	3541	± 12	1771	± 3
12.5	3374	± 11	1925	± 4	3579	± 12	1816	± 3
15	3425	± 11	1948	± 4	3615	± 12	1841	± 3
17.5	3458	± 11	1977	± 4	3640	± 12	1858	± 3
20	3486	± 12	1989	± 4	3658	± 12	1878	± 4
22.5	3516	± 12	2001	± 4	3671	± 12	1891	± 4
25	3536	± 12	2011	± 4	3685	± 12	1919	± 4
22.5	3527	± 12	2005	± 4	3688	± 12	1914	± 4
20	3510	± 12	1997	± 4	3672	± 12	1897	± 4
17.5	3487	± 12	1991	± 4	3653	± 12	1872	± 3
15	3463	± 11	1972	± 4	3623	± 12	1847	± 3
12.5	3441	± 11	1946	± 4	3591	± 12	1825	± 3
10	3395	± 11	1920	± 4	3557	± 12	1784	± 3
7.5	3319	± 11	1888	± 4	3504	± 12	-	-
5	3216	± 10	1854	± 3	3461	± 11	-	-
2.5	3106	± 10	1799	± 3	3386	± 11	-	-

Table C.30: Saturated velocities of sample 3-146 under constant differential pressure.

Confining pressure (MPa)	Pore pressure (MPa)	Vp (m/s)	Vs (m/s)
15	0	4350±16	1840±3
17.5	2.5	4350±16	1844±3
20	5	4357±16	1846±3
22.5	7.5	4359±16	1843±3
25	10	4360±16	1846±3

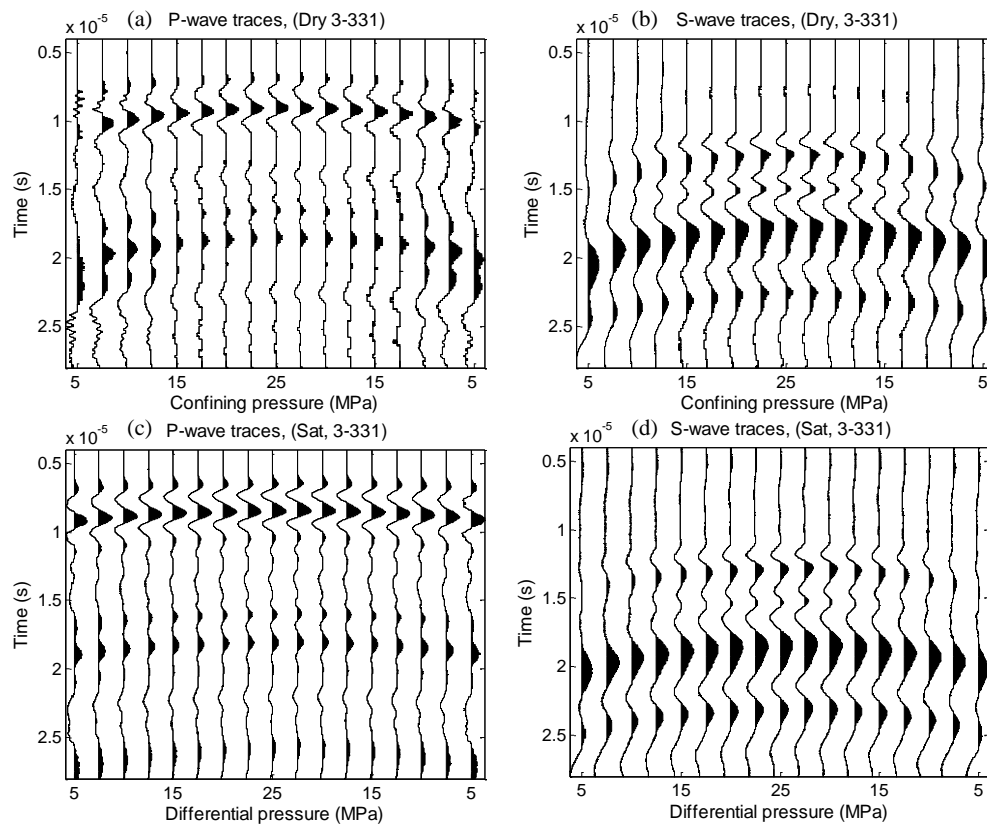


Figure C.17: Normalized waveforms of dry and saturated, P-wave (a and c respectively) and S-wave (b and d respectively) for sample 3-331 at different pressure.

Table C.31: Dry and saturated velocities of sample 3-331.

Pressure (MPa)	Dry		Saturated	
	Vp (m/s)	Vs (m/s)	Vp (m/s)	Vs (m/s)
5	3522 ± 14	2318 ± 6	4242 ± 19	2269 ± 6
7.5	3696 ± 15	2367 ± 6	4294 ± 19	2330 ± 6
10	3873 ± 16	2412 ± 6	4360 ± 19	2358 ± 6
12.5	4006 ± 17	2440 ± 6	4395 ± 20	2394 ± 6
15	4076 ± 18	2471 ± 6	4420 ± 20	2417 ± 6
17.5	4136 ± 18	2489 ± 6	4437 ± 20	2427 ± 6
20	4166 ± 18	2504 ± 6	4456 ± 20	2445 ± 6
22.5	4208 ± 19	2514 ± 6	4466 ± 20	2451 ± 6
25	4235 ± 19	2519 ± 6	4476 ± 20	2452 ± 6
22.5	4221 ± 19	2520 ± 6	4492 ± 20	2466 ± 6
20	4204 ± 19	2511 ± 6	4487 ± 20	2458 ± 6
17.5	4184 ± 18	2502 ± 6	4469 ± 20	2450 ± 6
15	4140 ± 18	2490 ± 6	4450 ± 20	2432 ± 6
12.5	4063 ± 18	2464 ± 6	4422 ± 20	2412 ± 6
10	3992 ± 17	2433 ± 6	4387 ± 20	2377 ± 6
7.5	3811 ± 16	2392 ± 6	4337 ± 19	2342 ± 6
5	3570 ± 15	2335 ± 6	4264 ± 19	2284 ± 6

Table C.32: Saturated velocities of sample 3-331 under constant differential pressure.

Confining pressure (MPa)	Pore pressure (MPa)	Vp (m/s)	Vs (m/s)
15	0	4441±20	2421±6
17.5	2.5	4445±20	2424±6
20	5	4444±20	2422±6
22.5	7.5	4442±20	2419±6
25	10	4447±20	2427±6

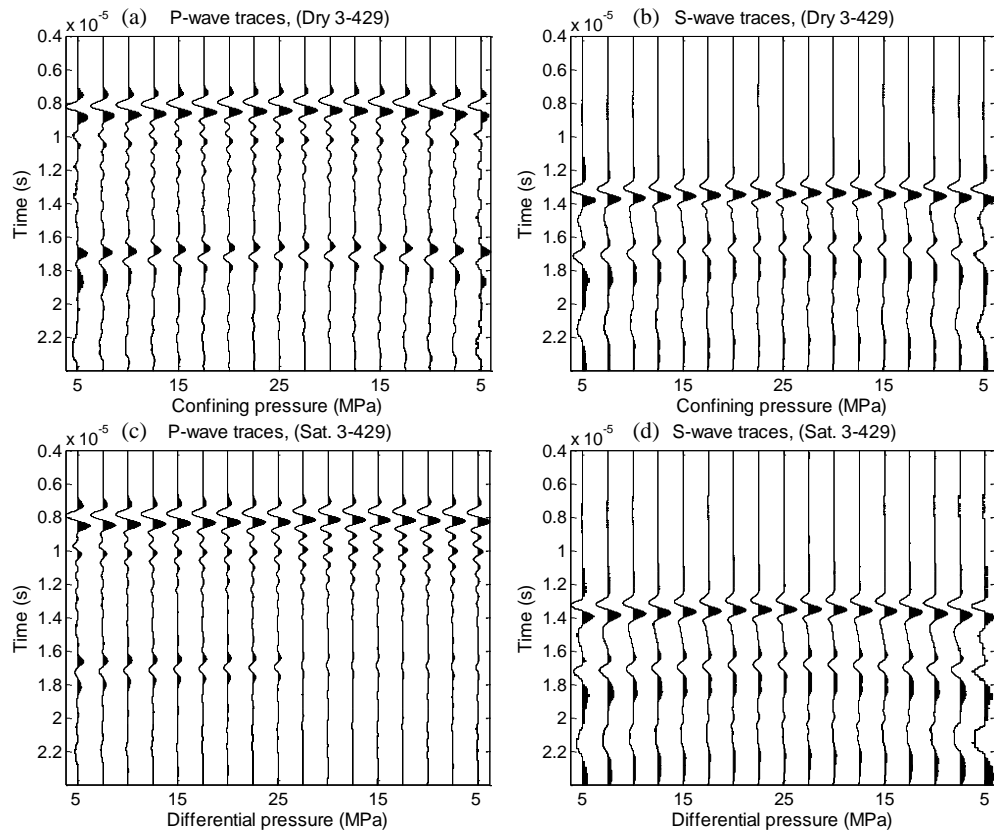


Figure C.18: Normalized waveforms of dry and saturated, P-wave (a and c respectively) and S-wave (b and d respectively) for sample 3-429 at different pressure.

Table C.33: Dry and saturated velocities of sample 3-429.

Pressure (MPa)	Dry		Saturated	
	V _p (m/s)	V _s (m/s)	V _p (m/s)	V _s (m/s)
5	5614 ± 24	3194 ± 8	5783 ± 25	3177 ± 8
7.5	5619 ± 24	3204 ± 8	5804 ± 25	3193 ± 8
10	5637 ± 24	3219 ± 8	5831 ± 25	3206 ± 8
12.5	5660 ± 24	3232 ± 8	5839 ± 25	3216 ± 8
15	5683 ± 24	3241 ± 8	5858 ± 25	3228 ± 8
17.5	5705 ± 24	3254 ± 8	5877 ± 25	3239 ± 8
20	5722 ± 24	3259 ± 8	5889 ± 25	3249 ± 8
22.5	5744 ± 25	3266 ± 8	5892 ± 25	3253 ± 8
25	5759 ± 25	3273 ± 8	5901 ± 26	3256 ± 8
22.5	5781 ± 25	3284 ± 8	5971 ± 26	3257 ± 8
20	5789 ± 25	3282 ± 8	5973 ± 26	3254 ± 8
17.5	5777 ± 25	3276 ± 8	5970 ± 26	3245 ± 8
15	5754 ± 25	3270 ± 8	5967 ± 26	3237 ± 8
12.5	5734 ± 24	3262 ± 8	5958 ± 26	3224 ± 8
10	5694 ± 24	3247 ± 8	5945 ± 26	3209 ± 8
7.5	5669 ± 24	3230 ± 8	5932 ± 26	3198 ± 8
5	5641 ± 24	3211 ± 8	5900 ± 25	3186 ± 8

Table C.34: Saturated velocities of sample 3-429 under constant differential pressure.

Confining pressure (MPa)	Pore pressure (MPa)	V _p (m/s)	V _s (m/s)
15	0	5961±26	3231±8
17.5	2.5	5977±26	3225±8
20	5	5988±26	3229±8
22.5	7.5	5991±26	3235±8
25	10	5991±26	3228±8

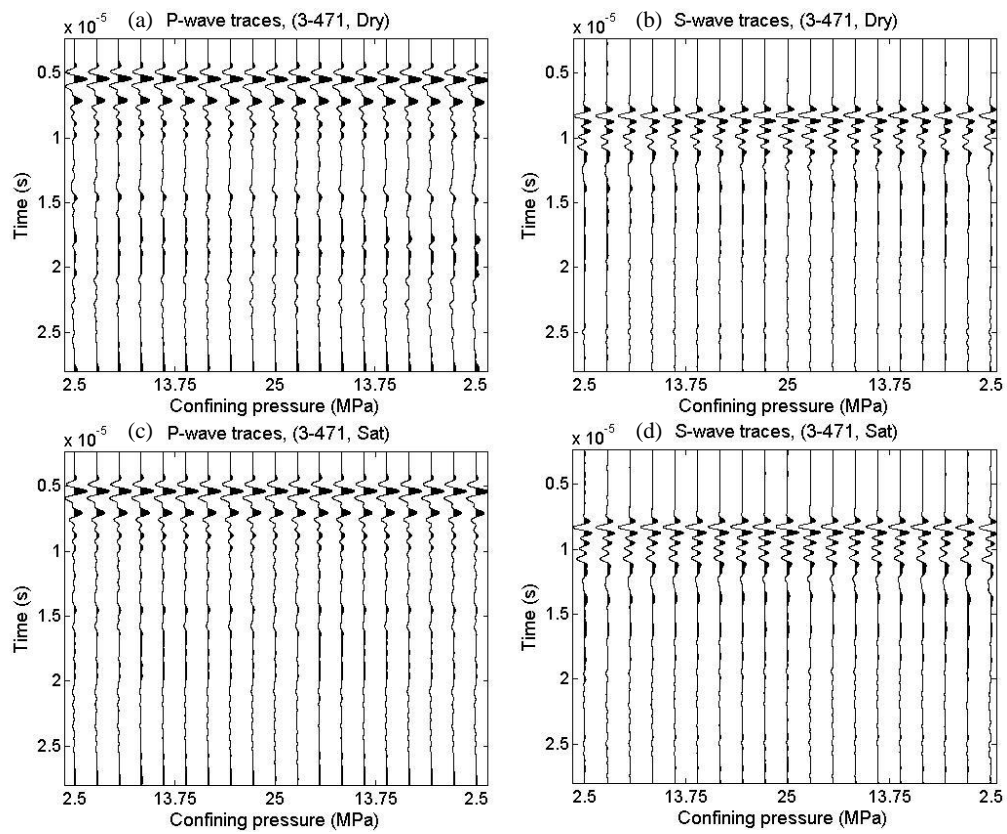


Figure C.19: Normalized waveforms of dry and saturated, P-wave (a and c respectively) and S-wave (b and d respectively) for sample 3-471 at different pressure.

Table C.35: Dry and saturated velocities of sample 3-471.

Pressure (MPa)	Dry		Saturated	
	Vp (m/s)	Vs (m/s)	Vp (m/s)	Vs (m/s)
2.5	5883 ± 26	3319 ± 9	5979 ± 27	3310 ± 8
5	5916 ± 26	3322 ± 9	5976 ± 27	3314 ± 9
7.5	5923 ± 26	3325 ± 9	5982 ± 27	3313 ± 9
10	5898 ± 26	3325 ± 9	5968 ± 27	3320 ± 9
12.5	5899 ± 26	3327 ± 9	5969 ± 27	3320 ± 9
15	5884 ± 26	3329 ± 9	5976 ± 27	3321 ± 9
17.5	5875 ± 26	3330 ± 9	5966 ± 27	3323 ± 9
20	5866 ± 26	3332 ± 9	5968 ± 27	3325 ± 9
22.5	5831 ± 26	3337 ± 9	5964 ± 27	3325 ± 9
25	5827 ± 26	3336 ± 9	5965 ± 27	3326 ± 9
22.5	5841 ± 26	3339 ± 9	5969 ± 27	3327 ± 9
20	5840 ± 26	3337 ± 9	5979 ± 27	3328 ± 9
17.5	5833 ± 26	3338 ± 9	5989 ± 27	3330 ± 9
15	5842 ± 26	3340 ± 9	5982 ± 27	3328 ± 9
12.5	5846 ± 26	3336 ± 9	5985 ± 27	3325 ± 9
10	5839 ± 26	3334 ± 9	5984 ± 27	3320 ± 9
7.5	5838 ± 26	3330 ± 9	5983 ± 27	3314 ± 9
5	5826 ± 26	3329 ± 9	5970 ± 27	3309 ± 8
2.5	5814 ± 26	3325 ± 9	5947 ± 27	3297 ± 8

Table C.36: Saturated velocities of sample 3-471 under constant differential pressure.

Confining pressure (MPa)	Pore pressure (MPa)	Vp (m/s)	Vs (m/s)
15	0	5975±27	3321±9
17.5	2.5	5983±27	3323±9
20	5	5996±27	3323±9
22.5	7.5	6014±27	3324±9
25	10	6021±27	3322±9

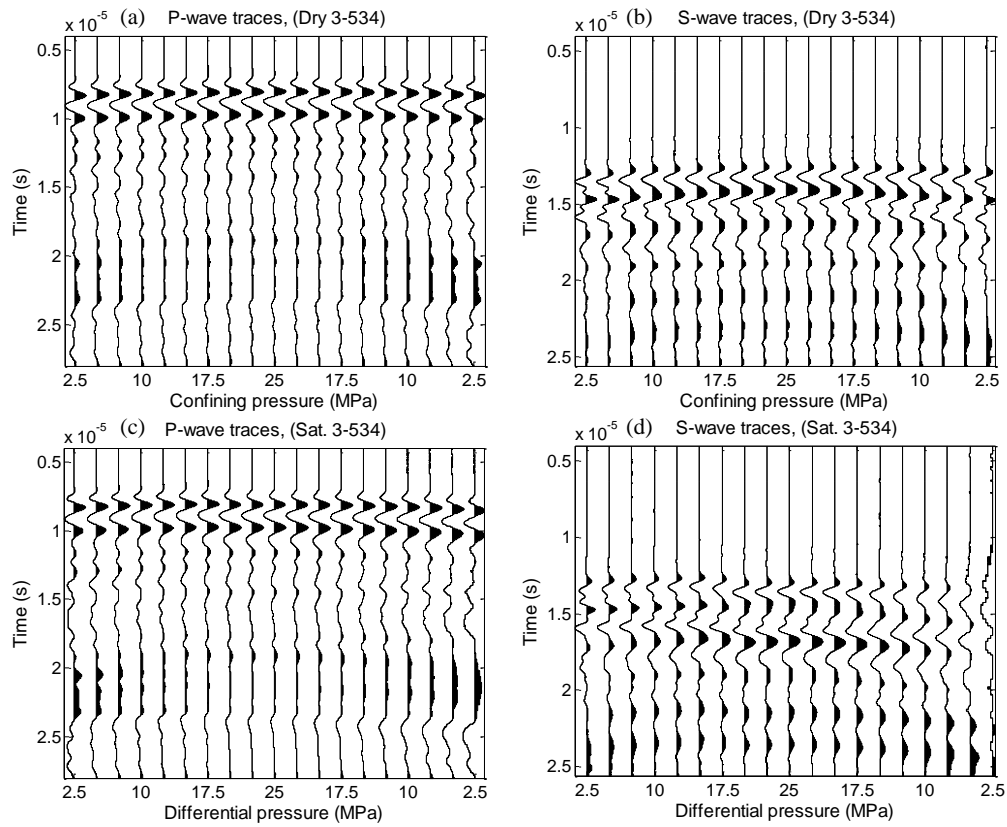


Figure C.20: Normalized waveforms of dry and saturated, P-wave (a and c respectively) and S-wave (b and d respectively) for sample 3-534 at different pressure.

Table C.37: Dry and saturated velocities of sample 3-534.

Pressure (MPa)	Dry		Saturated	
	Vp (m/s)	Vs (m/s)	Vp (m/s)	Vs (m/s)
2.5	4345 ± 16	2567 ± 6	4357 ± 16	2600 ± 6
5	4383 ± 16	2596 ± 6	4396 ± 16	2617 ± 6
7.5	4410 ± 16	2617 ± 6	4422 ± 16	2628 ± 6
10	4430 ± 17	2628 ± 6	4443 ± 17	2637 ± 6
12.5	4447 ± 17	2634 ± 6	4457 ± 17	2644 ± 6
15	4462 ± 17	2641 ± 6	4476 ± 17	2651 ± 6
17.5	4472 ± 17	2648 ± 6	4493 ± 17	2629 ± 6
20	4485 ± 17	2654 ± 6	4466 ± 17	2579 ± 6
22.5	4495 ± 17	2659 ± 6	4468 ± 17	2583 ± 6
25	4505 ± 17	2664 ± 6	4474 ± 17	2586 ± 6
22.5	4505 ± 17	2663 ± 6	4466 ± 17	2583 ± 6
20	4497 ± 17	2660 ± 6	4458 ± 17	2577 ± 6
17.5	4491 ± 17	2656 ± 6	4436 ± 17	2567 ± 6
15	4483 ± 17	2651 ± 6	4428 ± 17	2559 ± 6
12.5	4464 ± 17	2645 ± 6	4406 ± 16	2547 ± 5
10	4446 ± 17	2638 ± 6	4381 ± 16	2532 ± 5
7.5	4425 ± 16	2626 ± 6	4351 ± 16	2513 ± 5
5	4398 ± 16	2614 ± 6	4317 ± 16	2483 ± 5
2.5	4357 ± 16	2589 ± 6	4267 ± 16	2411 ± 5

Table C.38: Saturated velocities of sample 3-534 under constant differential pressure.

Confining pressure (MPa)	Pore pressure (MPa)	Vp (m/s)	Vs (m/s)
15	0	3299±11	1760±3
17.5	2.5	3293±11	1750±3
20	5	3305±11	1749±3
22.5	7.5	3299±11	1752±3
25	10	3306±11	1754±3

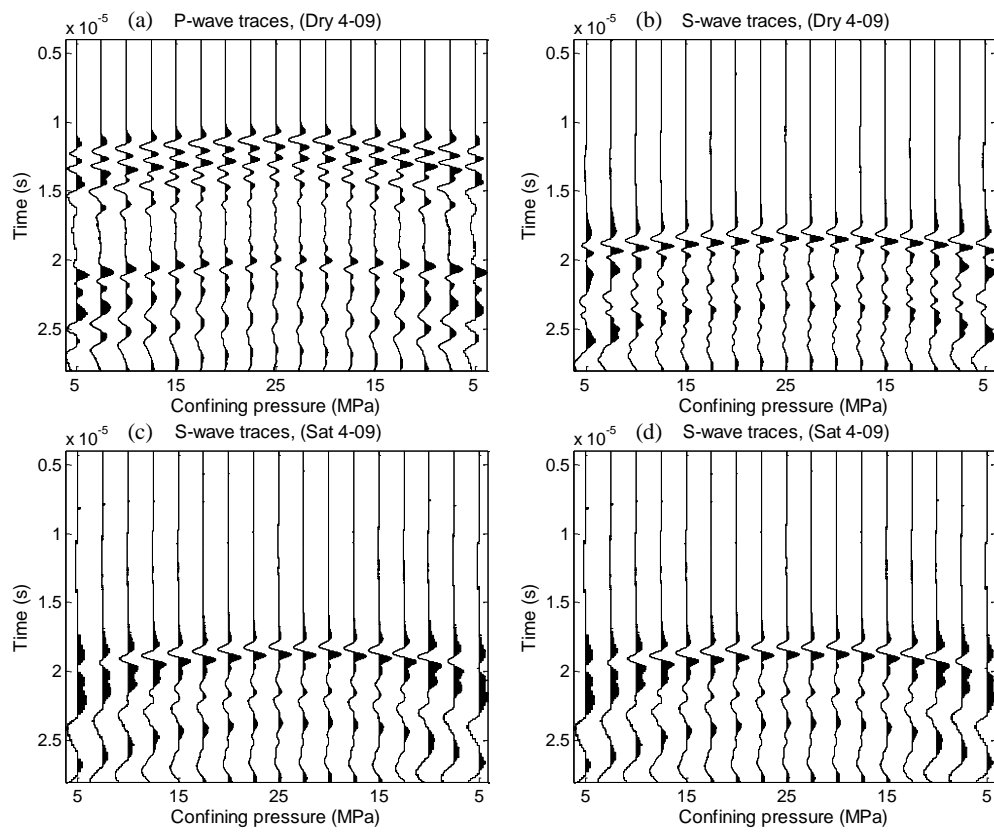


Figure C.21: Normalized waveforms of dry and saturated, P-wave (a and c respectively) and S-wave (b and d respectively) for sample 4-09 at different pressure.

Table C.39: Dry and saturated velocities of sample 4-09.

Pressure (MPa)	Dry		Saturated	
	Vp (m/s)	Vs (m/s)	Vp (m/s)	Vs (m/s)
5	4307 ± 15	2631 ± 5	4744 ± 17	2524 ± 5
7.5	4375 ± 15	2654 ± 5	4821 ± 17	2575 ± 5
10	4448 ± 15	2686 ± 5	4876 ± 18	2617 ± 5
12.5	4484 ± 16	2705 ± 5	4915 ± 18	2649 ± 5
15	4539 ± 16	2726 ± 6	4950 ± 18	2679 ± 5
17.5	4584 ± 16	2742 ± 6	4970 ± 18	2693 ± 5
20	4623 ± 16	2757 ± 6	5001 ± 18	2717 ± 6
22.5	4664 ± 17	2775 ± 6	5031 ± 19	2737 ± 6
25	4697 ± 17	2790 ± 6	5051 ± 19	2748 ± 6
22.5	4690 ± 17	2786 ± 6	5043 ± 19	2743 ± 6
20	4666 ± 17	2778 ± 6	5038 ± 19	2734 ± 6
17.5	4646 ± 16	2769 ± 6	5024 ± 19	2730 ± 6
15	4620 ± 16	2756 ± 6	4996 ± 18	2706 ± 5
12.5	4564 ± 16	2737 ± 6	4955 ± 18	2676 ± 5
10	4507 ± 16	2717 ± 6	4906 ± 18	2637 ± 5
7.5	4462 ± 15	2691 ± 5	4845 ± 17	2592 ± 5
5	4390 ± 15	2660 ± 5	4757 ± 17	2531 ± 5

Table C.40: Saturated velocities of sample 4-09 under constant differential pressure.

Confining pressure (MPa)	Pore pressure (MPa)	Vp (m/s)	Vs (m/s)
15	0	4970±18	2685±5
17.5	2.5	4979±18	2694±5
20	5	4992±18	2699±5
22.5	7.5	4986±18	2696±5
25	10	4990±18	2692±5

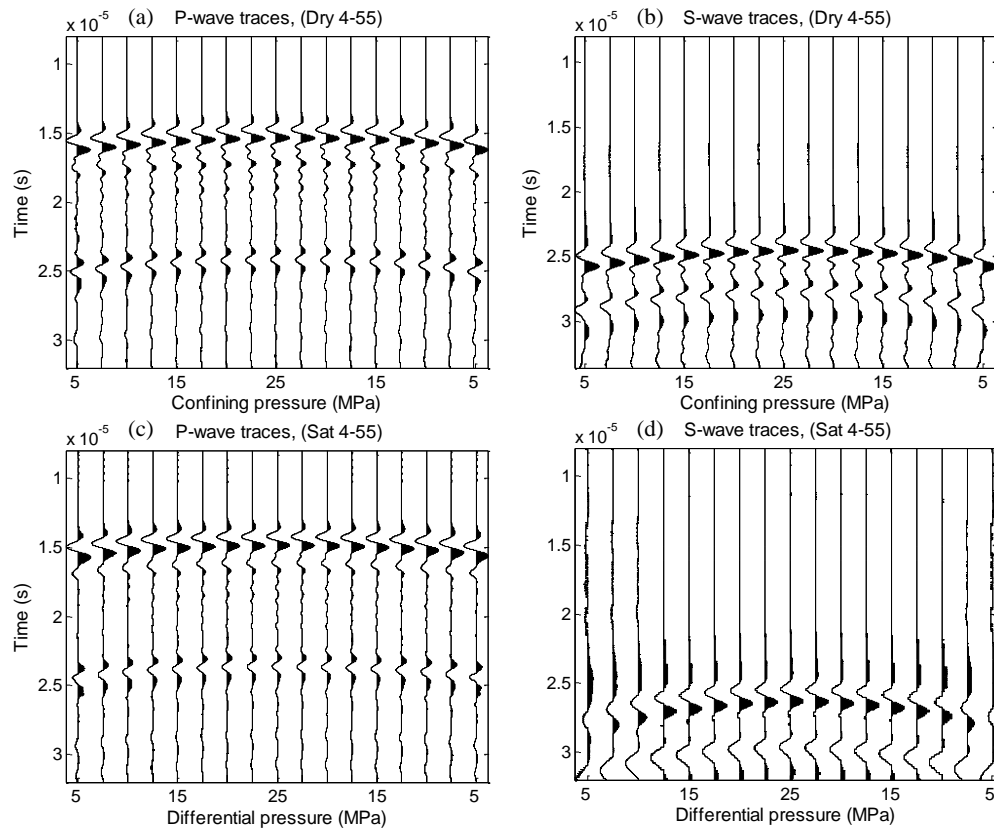


Figure C.22: Normalized waveforms of dry and saturated, P-wave (a and c respectively) and S-wave (b and d respectively) for sample 4-55 at different pressure.

Table C.41: Dry and saturated velocities of sample 4-55.

Pressure (MPa)	Dry		Saturated	
	V _p (m/s)	V _s (m/s)	V _p (m/s)	V _s (m/s)
5	3315 ± 10	1967 ± 3	3460 ± 10	1775 ± 3
7.5	3353 ± 10	1984 ± 3	3512 ± 11	1822 ± 3
10	3389 ± 10	2001 ± 3	3545 ± 11	1855 ± 3
12.5	3422 ± 10	2018 ± 4	3578 ± 11	1880 ± 3
15	3445 ± 10	2031 ± 4	3592 ± 11	1893 ± 3
17.5	3461 ± 10	2040 ± 4	3611 ± 11	1908 ± 3
20	3477 ± 11	2048 ± 4	3621 ± 11	1918 ± 3
22.5	3485 ± 11	2053 ± 4	3626 ± 11	1923 ± 3
25	3497 ± 11	2058 ± 4	3628 ± 11	1928 ± 3
22.5	3492 ± 11	2056 ± 4	3626 ± 11	1925 ± 3
20	3485 ± 11	2052 ± 4	3624 ± 11	1919 ± 3
17.5	3475 ± 11	2047 ± 4	3614 ± 11	1910 ± 3
15	3464 ± 10	2040 ± 4	3597 ± 11	1899 ± 3
12.5	3443 ± 10	2030 ± 4	3582 ± 11	1883 ± 3
10	3411 ± 10	2012 ± 4	3548 ± 11	1861 ± 3
7.5	3381 ± 10	1997 ± 3	3516 ± 11	1829 ± 3
5	3330 ± 10	1974 ± 3	3475 ± 10	1787 ± 3

Table C.42: Saturated velocities of sample 4-55 under constant differential pressure.

Confining pressure (MPa)	Pore pressure (MPa)	V _p (m/s)	V _s (m/s)
15	0	3595±11	1896±3
17.5	2.5	3597±11	1898±3
20	5	3600±11	1894±3
22.5	7.5	3603±11	1897±3
25	10	3603±11	1895±3

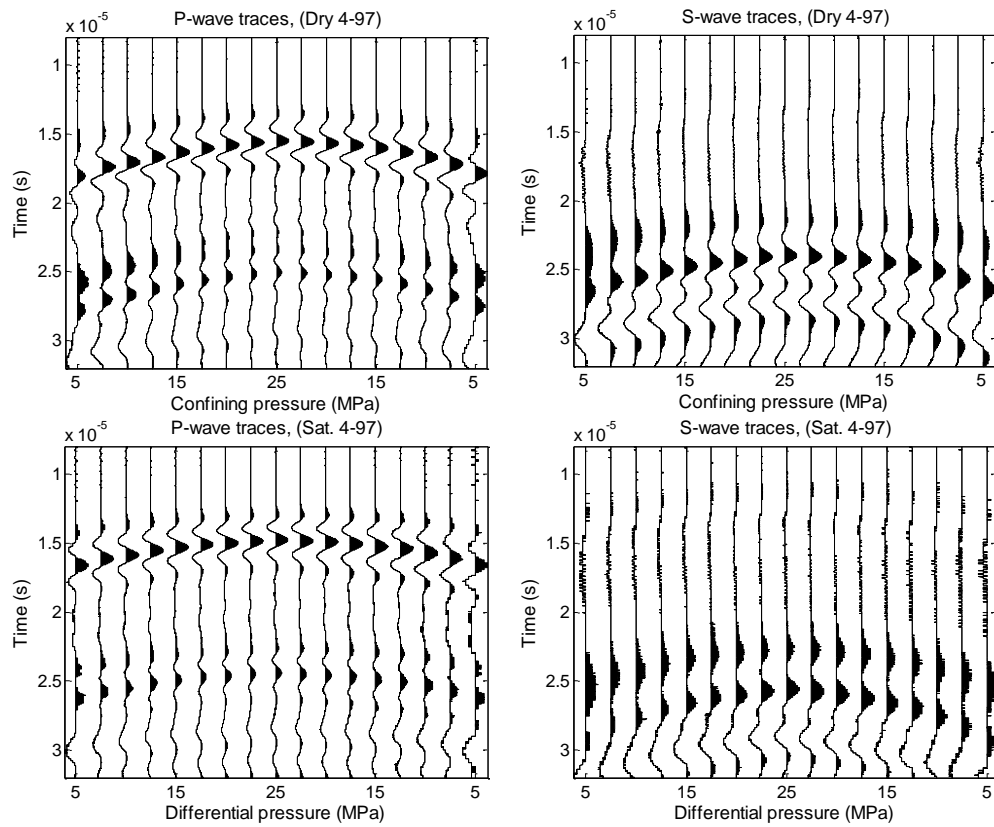


Figure C.23: Normalized waveforms of dry and saturated, P-wave (a and c respectively) and S-wave (b and d respectively) for sample 4-97 at different pressure.

Table C.43: Dry and saturated velocities of sample 4-97.

Pressure (MPa)	Dry		Saturated	
	V _p (m/s)	V _s (m/s)	V _p (m/s)	V _s (m/s)
5	3177 ± 9	1937 ± 3	3450 ± 10	1756 ± 3
7.5	3303 ± 10	1993 ± 3	3546 ± 11	1834 ± 3
10	3364 ± 10	2031 ± 4	3604 ± 11	1877 ± 3
12.5	3431 ± 10	2067 ± 4	3667 ± 11	1927 ± 3
15	3495 ± 11	2099 ± 4	3701 ± 12	1966 ± 3
17.5	3548 ± 11	2128 ± 4	3753 ± 12	1997 ± 3
20	3589 ± 11	2144 ± 4	3776 ± 12	2011 ± 4
22.5	3631 ± 11	2163 ± 4	3799 ± 12	2030 ± 4
25	3663 ± 11	2176 ± 4	3821 ± 12	2046 ± 4
22.5	3657 ± 11	2170 ± 4	3812 ± 12	2033 ± 4
20	3626 ± 11	2157 ± 4	3803 ± 12	2019 ± 4
17.5	3589 ± 11	2144 ± 4	3782 ± 12	1997 ± 3
15	3557 ± 11	2129 ± 4	3753 ± 12	1965 ± 3
12.5	3511 ± 11	2106 ± 4	3705 ± 12	1937 ± 3
10	3436 ± 10	2077 ± 4	3665 ± 11	1893 ± 3
7.5	3353 ± 10	2024 ± 4	3580 ± 11	1839 ± 3
5	3241 ± 9	1967 ± 3	3468 ± 10	1777 ± 3

Table C.44: Saturated velocities of sample 4-97 under constant differential pressure.

Confining pressure (MPa)	Pore pressure (MPa)	V _p (m/s)	V _s (m/s)
15	0	3746±12	1966±3
17.5	2.5	3744±12	1962±3
20	5	3745±12	1966±3
22.5	7.5	3744±12	1963±3
25	10	3747±12	1964±3

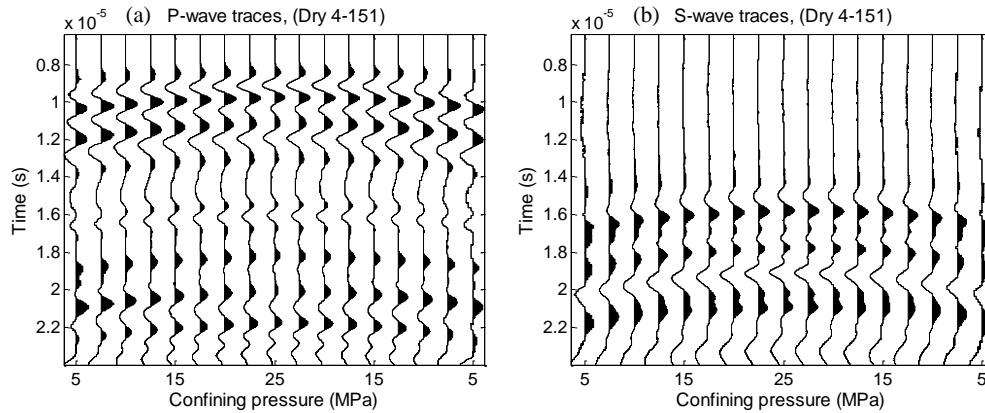


Figure C.24: Normalized waveforms of dry and saturated, P-wave (a and c respectively) and S-wave (b and d respectively) for sample 4-151 at different pressure.

Table C.45: Dry and saturated velocities of sample 4-151.

Pressure (MPa)	Dry		Saturated	
	V _p (m/s)	V _s (m/s)	V _p (m/s)	V _s (m/s)
5	5676 ± 22	3139 ± 7	5730 ± 22	3124 ± 7
7.5	5751 ± 23	3165 ± 7	5792 ± 23	3168 ± 7
10	5805 ± 23	3198 ± 7	5839 ± 23	3203 ± 7
12.5	5864 ± 23	3233 ± 7	5897 ± 23	3245 ± 7
15	5882 ± 23	3272 ± 7	5910 ± 24	3278 ± 7
17.5	5898 ± 23	3291 ± 7	5924 ± 24	3299 ± 7
20	5904 ± 24	3309 ± 7	5931 ± 24	3315 ± 7
22.5	5916 ± 24	3322 ± 7	5936 ± 24	3328 ± 7
25	5951 ± 24	3333 ± 7	5956 ± 24	3331 ± 7
22.5	5948 ± 24	3329 ± 7	5953 ± 24	3333 ± 7
20	5947 ± 24	3326 ± 7	5950 ± 24	3328 ± 7
17.5	5942 ± 24	3318 ± 7	5943 ± 24	3318 ± 7
15	5938 ± 24	3298 ± 7	5933 ± 24	3299 ± 7
12.5	5926 ± 24	3270 ± 7	5919 ± 24	3272 ± 7
10	5908 ± 23	3228 ± 7	5898 ± 23	3235 ± 7
7.5	5833 ± 23	3191 ± 7	5821 ± 23	3196 ± 7
5	5788 ± 23	3155 ± 7	5776 ± 23	3143 ± 7

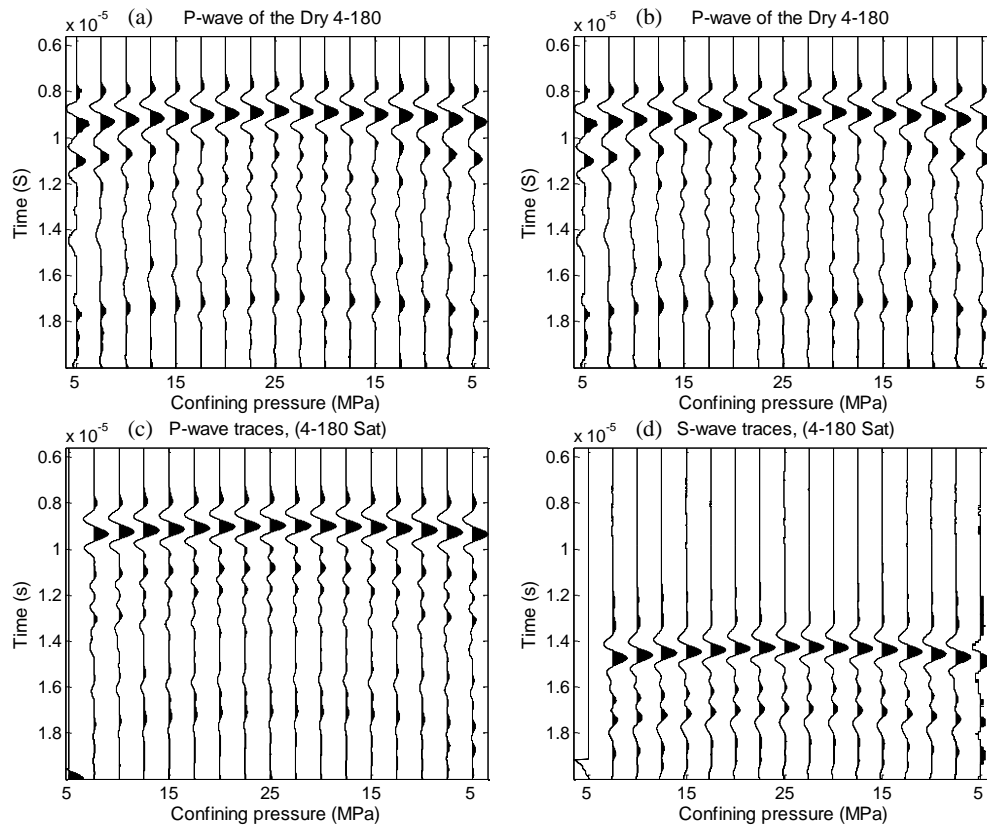


Figure C.25: Normalized waveforms of dry and saturated, P-wave (a and c respectively) and S-wave (b and d respectively) for sample 4-180 at different pressure.

Table C.46: Dry and saturated velocities of sample 4-180.

Pressure (MPa)	Dry		Saturated	
	Vp (m/s)	Vs (m/s)	Vp (m/s)	Vs (m/s)
5	6166 ± 25	3443 ± 8	6167 ± 25	3467 ± 8
7.5	6183 ± 25	3487 ± 8	6194 ± 25	3503 ± 8
10	6203 ± 25	3519 ± 8	6219 ± 25	3528 ± 8
12.5	6225 ± 26	3536 ± 8	6259 ± 26	3553 ± 8
15	6259 ± 26	3556 ± 8	6281 ± 26	3567 ± 8
17.5	6273 ± 26	3572 ± 8	6296 ± 26	3583 ± 8
20	6302 ± 26	3585 ± 8	6321 ± 26	3601 ± 8
22.5	6314 ± 26	3598 ± 8	6333 ± 26	3609 ± 8
25	6335 ± 26	3611 ± 8	6359 ± 26	3618 ± 8
22.5	6330 ± 26	3607 ± 8	6354 ± 26	3614 ± 8
20	6322 ± 26	3603 ± 8	6348 ± 26	3608 ± 8
17.5	6314 ± 26	3591 ± 8	6335 ± 26	3599 ± 8
15	6302 ± 26	3581 ± 8	6323 ± 26	3585 ± 8
12.5	6288 ± 26	3562 ± 8	6291 ± 26	3566 ± 8
10	6257 ± 26	3536 ± 8	6254 ± 26	3538 ± 8
7.5	6226 ± 25	3509 ± 8	6220 ± 25	3513 ± 8
5	6203 ± 25	3470 ± 8	6196 ± 25	3473 ± 8

Table C.47: Saturated velocities of sample 4-180 under constant differential pressure.

Confining pressure (MPa)	Pore pressure (MPa)	Vp (m/s)	Vs (m/s)
15	0	6312±26	3585±8
17.5	2.5	6329±26	3593±8
20	5	6355±26	3607±8
22.5	7.5	6408±26	3623±8
25	10	6451±26	3636±8

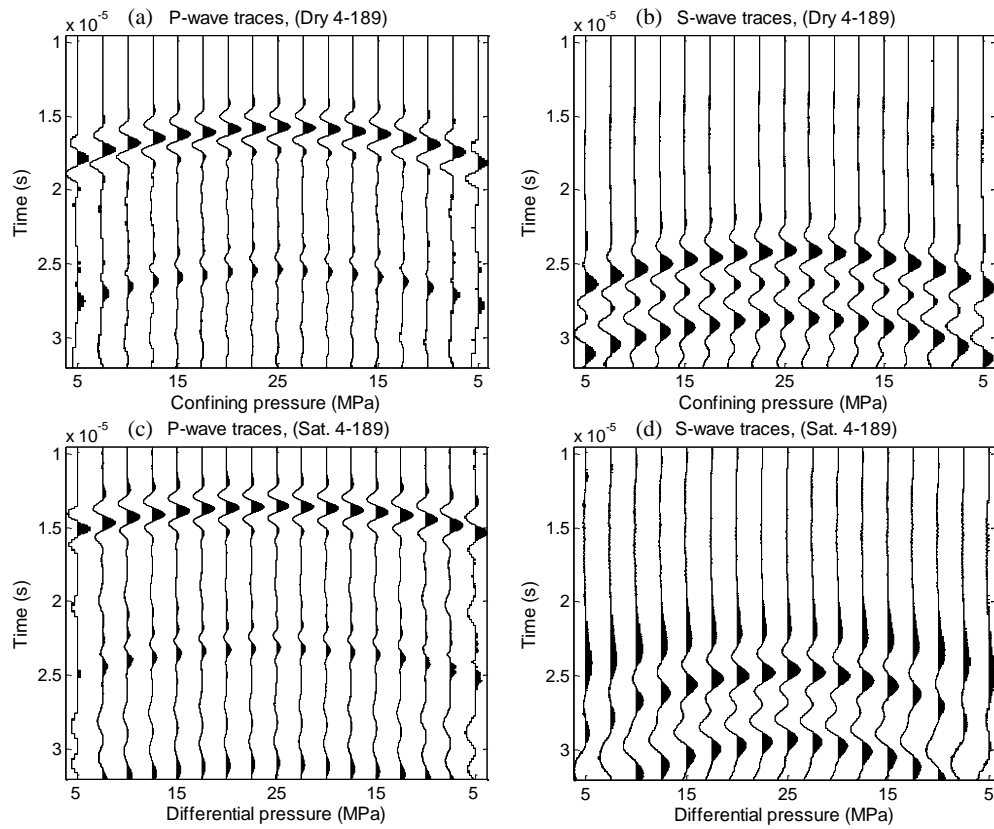


Figure C.26: Normalized waveforms of dry and saturated, P-wave (a and c respectively) and S-wave (b and d respectively) for sample 4-189 at different pressure.

Table C.48: Dry and saturated velocities of sample 4-189.

Pressure (MPa)	Dry		Saturated	
	Vp (m/s)	Vs (m/s)	Vp (m/s)	Vs (m/s)
5	2999 ± 8	1974 ± 3	3256 ± 9	1720 ± 3
7.5	3235 ± 9	2012 ± 4	3453 ± 10	1784 ± 3
10	3323 ± 10	2046 ± 4	3513 ± 11	1842 ± 3
12.5	3375 ± 10	2073 ± 4	3553 ± 11	1874 ± 3
15	3426 ± 10	2096 ± 4	3583 ± 11	1912 ± 3
17.5	3457 ± 10	2106 ± 4	3629 ± 11	1936 ± 3
20	3493 ± 11	2128 ± 4	3639 ± 11	1951 ± 3
22.5	3509 ± 11	2137 ± 4	3657 ± 11	1966 ± 3
25	3527 ± 11	2148 ± 4	3668 ± 11	1981 ± 3
22.5	3513 ± 11	2138 ± 4	3657 ± 11	1966 ± 3
20	3494 ± 11	2130 ± 4	3636 ± 11	1948 ± 3
17.5	3472 ± 10	2118 ± 4	3610 ± 11	1929 ± 3
15	3430 ± 10	2101 ± 4	3576 ± 11	1903 ± 3
12.5	3382 ± 10	2076 ± 4	3535 ± 11	1869 ± 3
10	3311 ± 10	2046 ± 4	3492 ± 11	1818 ± 3
7.5	3228 ± 9	2006 ± 3	3419 ± 10	1752 ± 3
5	3079 ± 9	1958 ± 3	3324 ± 10	1670 ± 3

Table C.49: Saturated velocities of sample 4-189 under constant differential pressure.

Confining pressure (MPa)	Pore pressure (MPa)	Vp (m/s)	Vs (m/s)
15	0	3585±11	1898±3
17.5	2.5	3582±11	1898±3
20	5	3589±11	1906±3
22.5	7.5	3586±11	1903±3
25	10	3583±11	1899±3

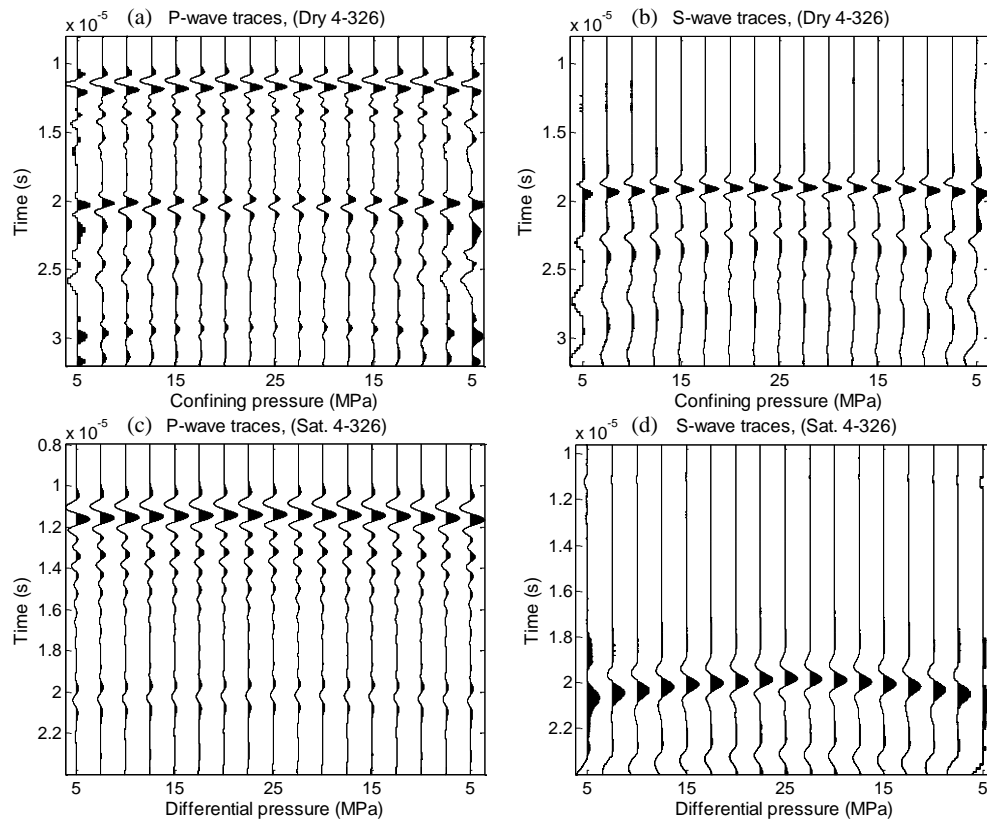


Figure C.27: Normalized waveforms of dry and saturated, P-wave (a and c respectively) and S-wave (b and d respectively) for sample 4-326 at different pressure.

Table C.50: Dry and saturated velocities of sample 4-326.

Pressure (MPa)	Dry		Saturated	
	Vp (m/s)	Vs (m/s)	Vp (m/s)	Vs (m/s)
5	4608 ± 16	2644 ± 5	4747 ± 17	2519 ± 5
7.5	4625 ± 16	2653 ± 5	4774 ± 17	2527 ± 5
10	4648 ± 16	2662 ± 5	4783 ± 17	2537 ± 5
12.5	4666 ± 17	2669 ± 5	4800 ± 17	2549 ± 5
15	4682 ± 17	2674 ± 5	4810 ± 17	2563 ± 5
17.5	4693 ± 17	2679 ± 5	4813 ± 17	2569 ± 5
20	4700 ± 17	2684 ± 5	4822 ± 17	2577 ± 5
22.5	4707 ± 17	2687 ± 5	4828 ± 17	2584 ± 5
25	4715 ± 17	2691 ± 5	4835 ± 18	2592 ± 5
22.5	4713 ± 17	2691 ± 5	4833 ± 17	2588 ± 5
20	4709 ± 17	2688 ± 5	4830 ± 17	2582 ± 5
17.5	4706 ± 17	2685 ± 5	4826 ± 17	2575 ± 5
15	4698 ± 17	2681 ± 5	4818 ± 17	2566 ± 5
12.5	4685 ± 17	2676 ± 5	4805 ± 17	2553 ± 5
10	4663 ± 16	2669 ± 5	4784 ± 17	2540 ± 5
7.5	4637 ± 16	2659 ± 5	4769 ± 17	2527 ± 5
5	4615 ± 16	2649 ± 5	4744 ± 17	2516 ± 5

Table C.51: Saturated velocities of sample 4-326 under constant differential pressure.

Confining pressure (MPa)	Pore pressure (MPa)	Vp (m/s)	Vs (m/s)
15	0	4814±17	2565±5
17.5	2.5	4814±17	2563±5
20	5	4820±17	2564±5
22.5	7.5	4821±17	2568±5
25	10	4822±17	2567±5

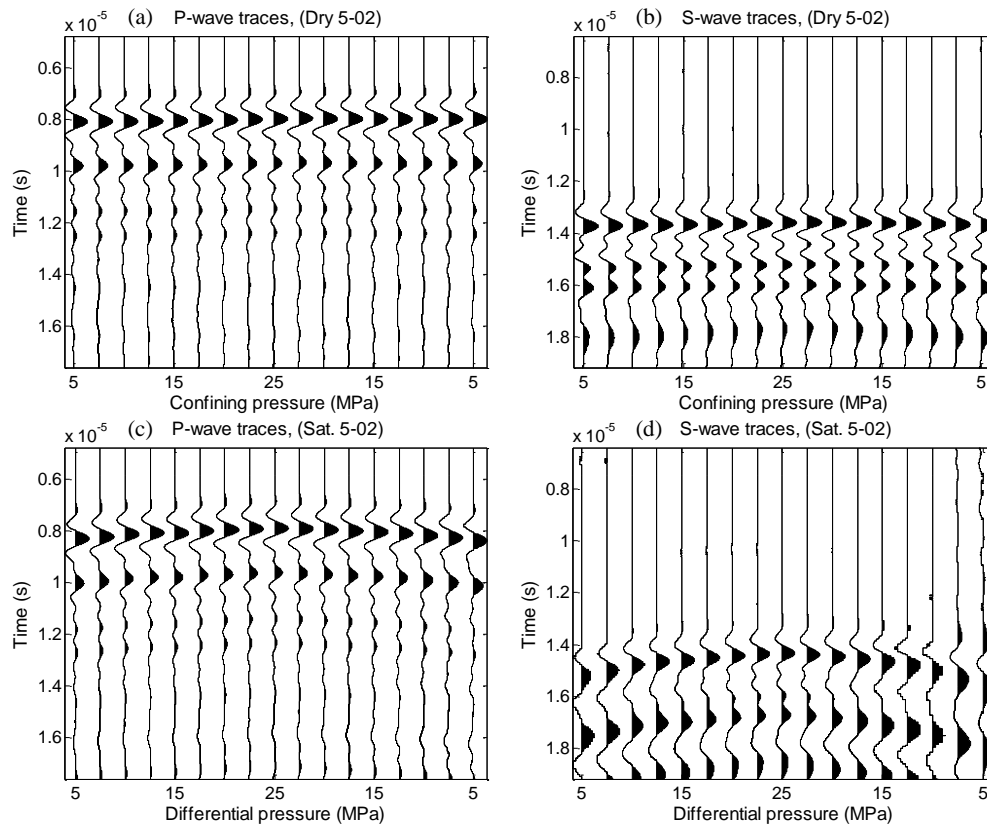


Figure C.28: Normalized waveforms of dry and saturated, P-wave (a and c respectively) and S-wave (b and d respectively) for sample 5-02 at different pressure.

Table C.52: Dry and saturated velocities of sample 5-02

Pressure (MPa)	Dry		Saturated	
	Vp (m/s)	Vs (m/s)	Vp (m/s)	Vs (m/s)
5	4625 ± 17	2651 ± 6	4511 ± 16	2412 ± 5
7.5	4628 ± 17	2654 ± 6	4532 ± 17	2435 ± 5
10	4633 ± 17	2656 ± 6	4585 ± 17	2469 ± 5
12.5	4638 ± 17	2657 ± 6	4619 ± 17	2486 ± 5
15	4645 ± 17	2660 ± 6	4632 ± 17	2495 ± 5
17.5	4655 ± 17	2660 ± 6	4657 ± 17	2509 ± 5
20	4660 ± 17	2663 ± 6	4680 ± 17	2522 ± 5
22.5	4671 ± 17	2666 ± 6	4704 ± 18	2532 ± 5
25	4681 ± 17	2669 ± 6	4716 ± 18	2539 ± 5
22.5	4691 ± 17	2672 ± 6	4702 ± 18	2530 ± 5
20	4688 ± 17	2671 ± 6	4683 ± 17	2521 ± 5
17.5	4682 ± 17	2669 ± 6	4661 ± 17	2508 ± 5
15	4681 ± 17	2668 ± 6	4635 ± 17	2494 ± 5
12.5	4678 ± 17	2665 ± 6	4609 ± 17	2472 ± 5
10	4675 ± 17	2664 ± 6	4568 ± 17	2447 ± 5
7.5	4673 ± 17	2661 ± 6	4520 ± 17	2412 ± 5
5	4670 ± 17	2657 ± 6	4463 ± 16	2371 ± 5

Table C.53: Saturated velocities of sample 5-02 under constant differential pressure.

Confining pressure (MPa)	Pore pressure (MPa)	Vp (m/s)	Vs (m/s)
15	0	4611±17	2488±5
17.5	2.5	4645±17	2489±5
20	5	4648±17	2484±5
22.5	7.5	4644±17	2489±5
25	10	4650±17	2481±5

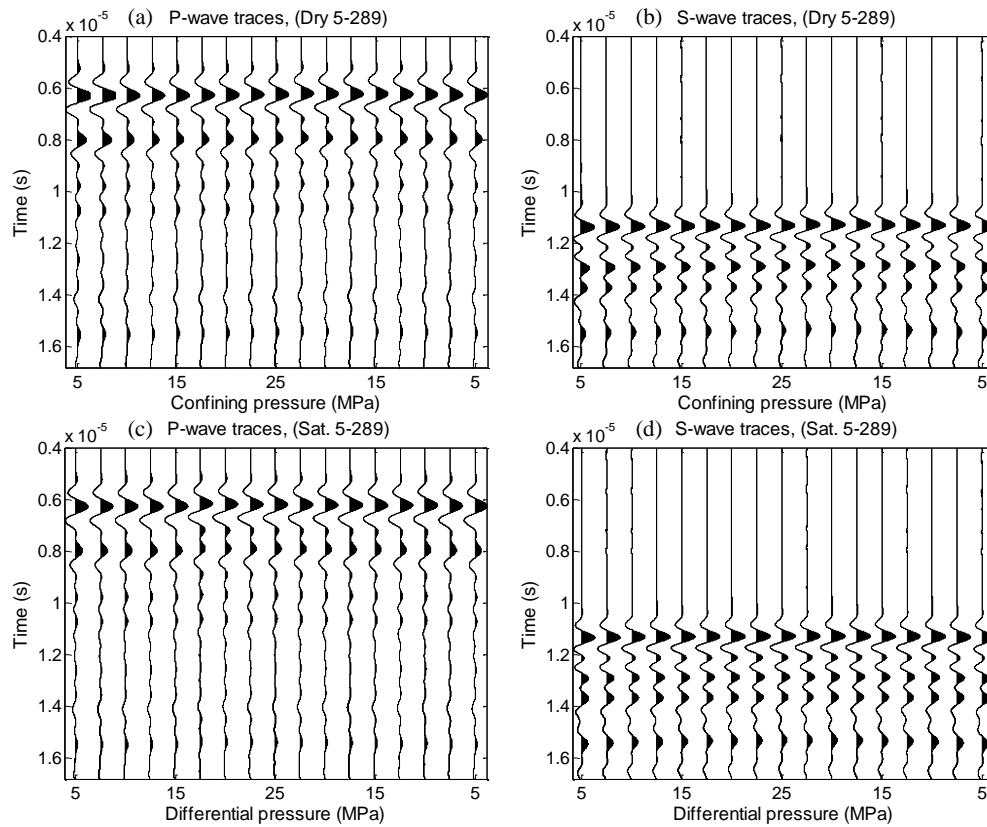


Figure C.29: Normalized waveforms of dry and saturated, P-wave (a and c respectively) and S-wave (b and d respectively) for sample 5-289 at different pressure.

Table C.54: Dry and saturated velocities of sample 5-289.

Pressure (MPa)	Dry		Saturated	
	Vp (m/s)	Vs (m/s)	Vp (m/s)	Vs (m/s)
5	6147 ± 25	3250 ± 7	6178 ± 25	3260 ± 7
7.5	6151 ± 25	3252 ± 7	6176 ± 25	3262 ± 7
10	6151 ± 25	3255 ± 7	6178 ± 25	3264 ± 7
12.5	6156 ± 25	3255 ± 7	6173 ± 25	3264 ± 7
15	6155 ± 25	3257 ± 7	6185 ± 25	3267 ± 7
17.5	6163 ± 25	3257 ± 7	6272 ± 26	3267 ± 7
20	6173 ± 25	3259 ± 7	6260 ± 26	3267 ± 7
22.5	6179 ± 25	3259 ± 7	6231 ± 25	3269 ± 7
25	6186 ± 25	3261 ± 7	6230 ± 25	3269 ± 7
22.5	6214 ± 25	3272 ± 7	6227 ± 25	3270 ± 7
20	6216 ± 25	3272 ± 7	6225 ± 25	3271 ± 7
17.5	6210 ± 25	3272 ± 7	6215 ± 25	3271 ± 7
15	6204 ± 25	3271 ± 7	6215 ± 25	3271 ± 7
12.5	6199 ± 25	3270 ± 7	6207 ± 25	3271 ± 7
10	6194 ± 25	3268 ± 7	6217 ± 25	3268 ± 7
7.5	6185 ± 25	3264 ± 7	6193 ± 25	3265 ± 7
5	6182 ± 25	3259 ± 7	6187 ± 25	3264 ± 7

Table C.55: Saturated velocities of sample 5-289 under constant differential pressure.

Confining pressure (MPa)	Pore pressure (MPa)	Vp (m/s)	Vs (m/s)
15	0	6207±25	3268±25
17.5	2.5	6215±25	3267±25
20	5	6216±25	3265±25
22.5	7.5	6222±25	3266±25
25	10	6234±25	3267±25

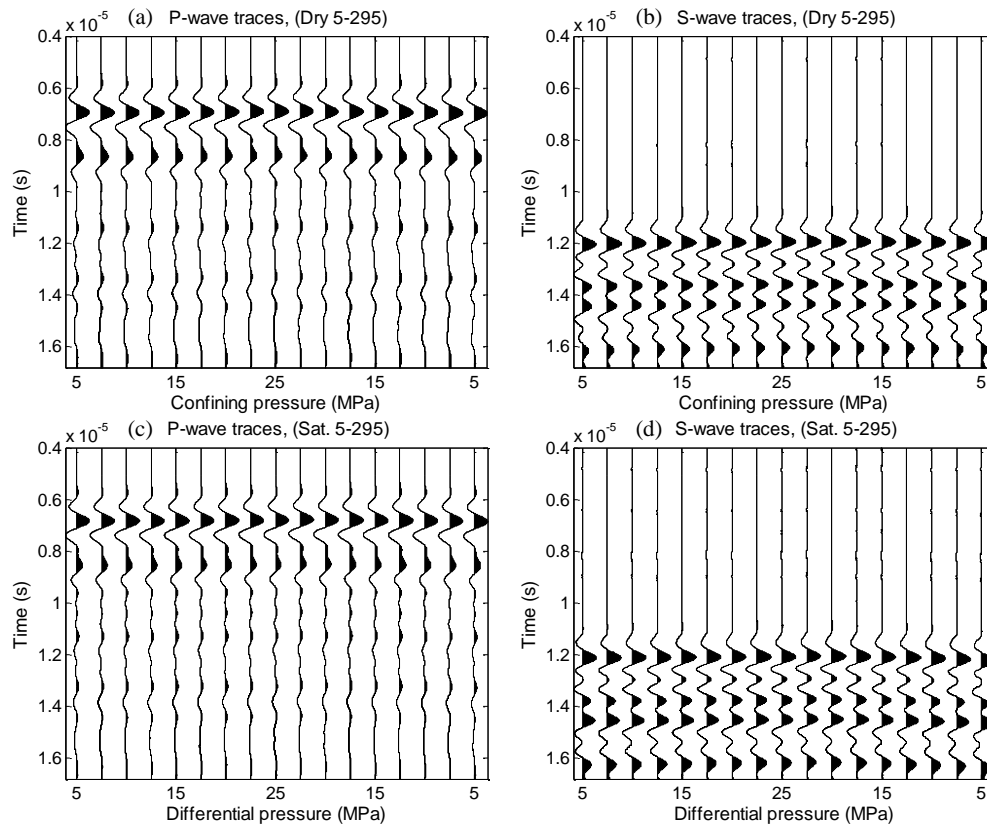


Figure C.30: Normalized waveforms of dry and saturated, P-wave (a and c respectively) and S-wave (b and d respectively) for sample 5-295 at different pressure.

Table C.56: Dry and saturated velocities of sample 5-295.

Pressure(MPa)	Dry		Saturated	
	Vp (m/s)	Vs (m/s)	Vp (m/s)	Vs (m/s)
5	5540 ± 22	3069 ± 7	5624 ± 22	3063 ± 7
7.5	5521 ± 22	3072 ± 7	5620 ± 22	3056 ± 7
10	5519 ± 22	3075 ± 7	5621 ± 22	3052 ± 7
12.5	5523 ± 22	3078 ± 7	5618 ± 22	3053 ± 7
15	5525 ± 22	3079 ± 7	5623 ± 22	3055 ± 7
17.5	5532 ± 22	3082 ± 7	5627 ± 22	3056 ± 7
20	5536 ± 22	3084 ± 7	5631 ± 22	3058 ± 7
22.5	5545 ± 22	3086 ± 7	5639 ± 22	3059 ± 7
25	5557 ± 22	3089 ± 7	5643 ± 22	3061 ± 7
22.5	5553 ± 22	3088 ± 7	5652 ± 22	3063 ± 7
20	5548 ± 22	3087 ± 7	5649 ± 22	3061 ± 7
17.5	5545 ± 22	3086 ± 7	5645 ± 22	3060 ± 7
15	5539 ± 22	3084 ± 7	5638 ± 22	3057 ± 7
12.5	5528 ± 22	3083 ± 7	5632 ± 22	3053 ± 7
10	5523 ± 22	3080 ± 7	5627 ± 22	3050 ± 7
7.5	5511 ± 22	3078 ± 7	5613 ± 22	3041 ± 7
5	5502 ± 22	3075 ± 7	5603 ± 22	3032 ± 7

Table C.57: Saturated velocities of sample 5-295 under constant differential pressure.

Confining pressure (MPa)	Pore pressure (MPa)	Vp (m/s)	Vs (m/s)
15	0	5638±22	3027±7
17.5	2.5	5649±22	3024±7
20	5	5653±22	3026±7
22.5	7.5	5655±22	3025±7
25	10	5650±22	3023±7

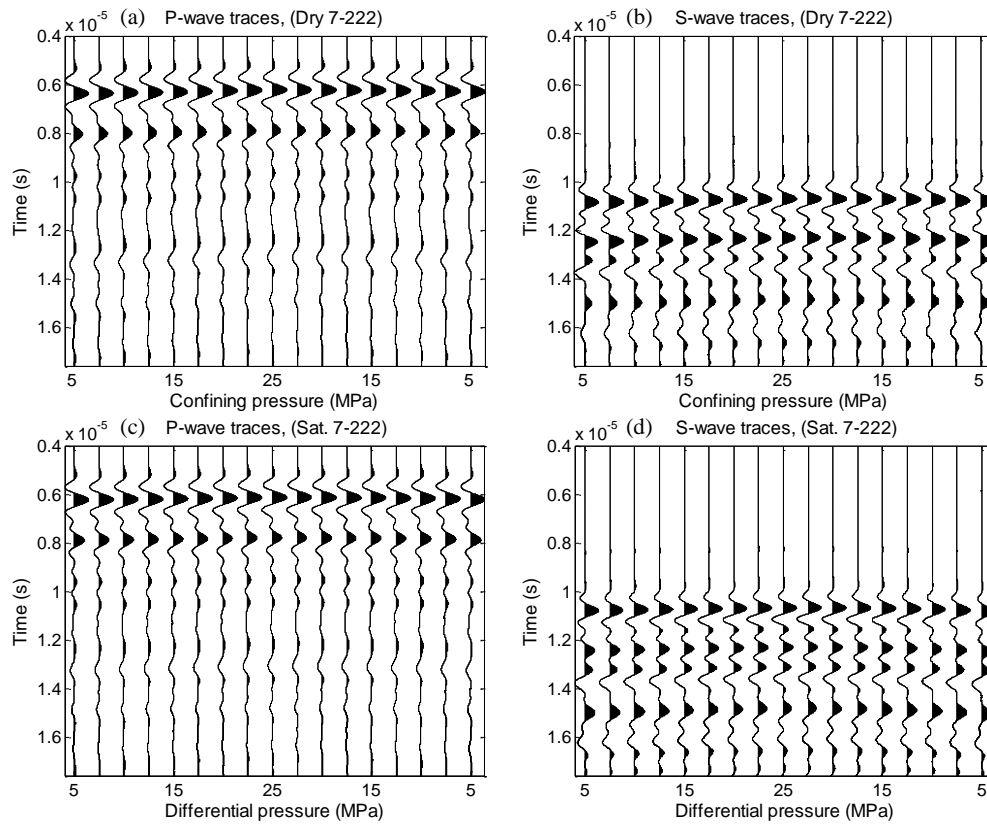


Figure C.31: Normalized waveforms of dry and saturated, P-wave (a and c respectively) and S-wave (b and d respectively) for sample 7-222 at different pressure.

Table C.58: Dry and saturated velocities of sample 7-222.

Pressure(MPa)	Dry		Saturated	
	Vp (m/s)	Vs (m/s)	Vp (m/s)	Vs (m/s)
5	6479 ± 26	3657 ± 8	6620 ± 27	3673 ± 8
7.5	6487 ± 26	3661 ± 8	6625 ± 27	3676 ± 8
10	6510 ± 26	3669 ± 8	6639 ± 27	3681 ± 9
12.5	6529 ± 26	3673 ± 8	6653 ± 27	3685 ± 9
15	6546 ± 27	3678 ± 9	6671 ± 27	3689 ± 9
17.5	6564 ± 27	3681 ± 9	6685 ± 27	3693 ± 9
20	6593 ± 27	3686 ± 9	6695 ± 27	3695 ± 9
22.5	6604 ± 27	3691 ± 9	6712 ± 28	3700 ± 9
25	6631 ± 27	3701 ± 9	6726 ± 28	3704 ± 9
22.5	6630 ± 27	3699 ± 9	6725 ± 28	3703 ± 9
20	6628 ± 27	3698 ± 9	6722 ± 28	3702 ± 9
17.5	6623 ± 27	3696 ± 9	6718 ± 28	3701 ± 9
15	6606 ± 27	3694 ± 9	6704 ± 27	3697 ± 9
12.5	6594 ± 27	3690 ± 9	6696 ± 27	3694 ± 9
10	6586 ± 27	3686 ± 9	6682 ± 27	3688 ± 9
7.5	6573 ± 27	3682 ± 9	6671 ± 27	3683 ± 9
5	6565 ± 27	3673 ± 8	6649 ± 27	3677 ± 8

Table C.59: Saturated velocities of sample 7-222 under constant differential pressure.

Confining pressure (MPa)	Pore pressure (MPa)	Vp (m/s)	Vs (m/s)
15	0	6695±27	3690±9
17.5	2.5	6718±28	3692±9
20	5	6758±28	3696±9
22.5	7.5	6779±28	3697±9
25	10	6822±28	3701±9

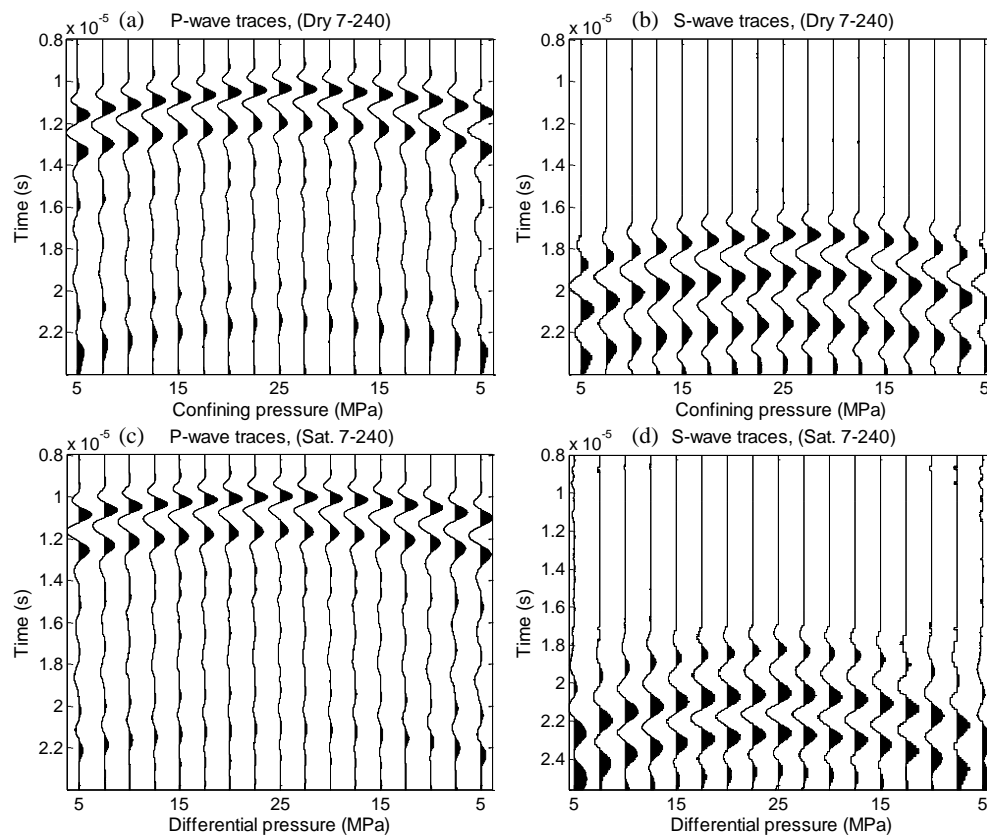


Figure C.32: Normalized waveforms of dry and saturated, P-wave (a and c respectively) and S-wave (b and d respectively) for sample 7-240 at different pressure.

Table C.60: Dry and saturated velocities of sample 7-240.

Pressure(MPa)	Dry		Saturated	
	Vp (m/s)	Vs (m/s)	Vp (m/s)	Vs (m/s)
5	3452 ± 11	2110 ± 4	3698 ± 12	1975 ± 4
7.5	3541 ± 11	2149 ± 4	3771 ± 12	2037 ± 4
10	3604 ± 12	2181 ± 4	3830 ± 13	2074 ± 4
12.5	3662 ± 12	2203 ± 4	3872 ± 13	2099 ± 4
15	3719 ± 12	2224 ± 4	3912 ± 13	2122 ± 4
17.5	3754 ± 12	2237 ± 4	3946 ± 13	2134 ± 4
20	3794 ± 13	2248 ± 4	3968 ± 13	2147 ± 4
22.5	3834 ± 13	2260 ± 4	3992 ± 13	2158 ± 4
25	3865 ± 13	2269 ± 4	4014 ± 14	2165 ± 4
22.5	3850 ± 13	2268 ± 4	3994 ± 13	2156 ± 4
20	3834 ± 13	2261 ± 4	3972 ± 13	2146 ± 4
17.5	3802 ± 13	2253 ± 4	3947 ± 13	2129 ± 4
15	3762 ± 12	2239 ± 4	3905 ± 13	2115 ± 4
12.5	3714 ± 12	2219 ± 4	3863 ± 13	2093 ± 4
10	3664 ± 12	2199 ± 4	3813 ± 13	2057 ± 4
7.5	3579 ± 11	2167 ± 4	3737 ± 12	2017 ± 4
5	3490 ± 11	2123 ± 4	3657 ± 12	1950 ± 4

Table C.61: Saturated velocities of sample 7-240 under constant differential pressure.

Confining pressure (MPa)	Pore pressure (MPa)	Vp (m/s)	Vs (m/s)
15	0	3903±13	2096±4
17.5	2.5	3924±13	2096±4
20	5	3925±13	2096±4
22.5	7.5	3928±13	2101±4
25	10	3931±13	2101±4

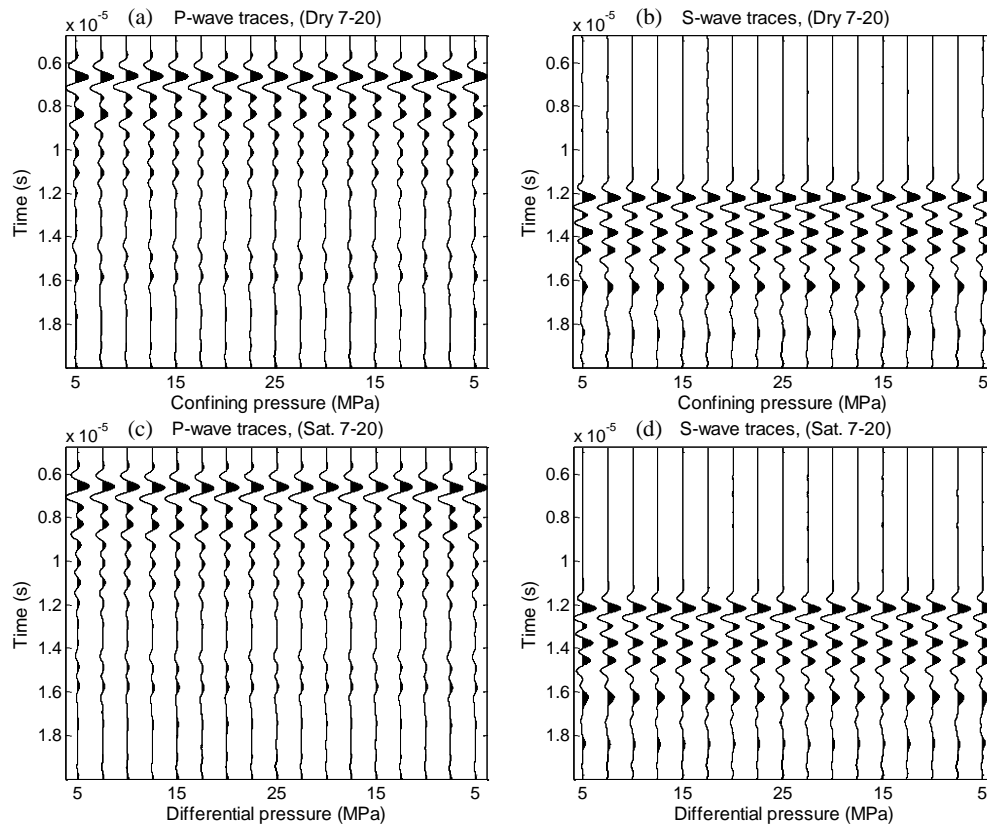


Figure C.33: Normalized waveforms of dry and saturated, P-wave (a and c respectively) and S-wave (b and d respectively) for sample 7-20 at different pressure.

Table C.62: Dry and saturated velocities of sample 7-20.

Pressure(MPa)	Dry		Saturated	
	Vp (m/s)	Vs (m/s)	Vp (m/s)	Vs (m/s)
5	6139 ± 24	3228 ± 7	6256 ± 25	3236 ± 7
7.5	6137 ± 24	3221 ± 7	6235 ± 25	3234 ± 7
10	6203 ± 25	3219 ± 7	6223 ± 25	3233 ± 7
12.5	6187 ± 25	3219 ± 7	6179 ± 25	3231 ± 7
15	6178 ± 25	3218 ± 7	6181 ± 25	3229 ± 7
17.5	6173 ± 25	3216 ± 7	6161 ± 25	3229 ± 7
20	6158 ± 25	3214 ± 7	6198 ± 25	3227 ± 7
22.5	6172 ± 25	3216 ± 7	6193 ± 25	3228 ± 7
25	6167 ± 25	3215 ± 7	6212 ± 25	3226 ± 7
22.5	6168 ± 25	3218 ± 7	6205 ± 25	3219 ± 7
20	6171 ± 25	3218 ± 7	6211 ± 25	3219 ± 7
17.5	6173 ± 25	3218 ± 7	6214 ± 25	3231 ± 7
15	6177 ± 25	3223 ± 7	6216 ± 25	3232 ± 7
12.5	6183 ± 25	3224 ± 7	6220 ± 25	3234 ± 7
10	6199 ± 25	3225 ± 7	6223 ± 25	3236 ± 7
7.5	6205 ± 25	3225 ± 7	6162 ± 25	3228 ± 7
5	6171 ± 24	3238 ± 7	6187 ± 25	3238 ± 7

Table C.63: Saturated velocities of sample 7-20 under constant differential pressure.

Confining pressure (MPa)	Pore pressure (MPa)	Vp (m/s)	Vs (m/s)
15	0	6145±24	3220±7
17.5	2.5	6133±24	3220±7
20	5	6146±25	3224±7
22.5	7.5	6137±24	3224±7
25	10	6143±24	3225±7

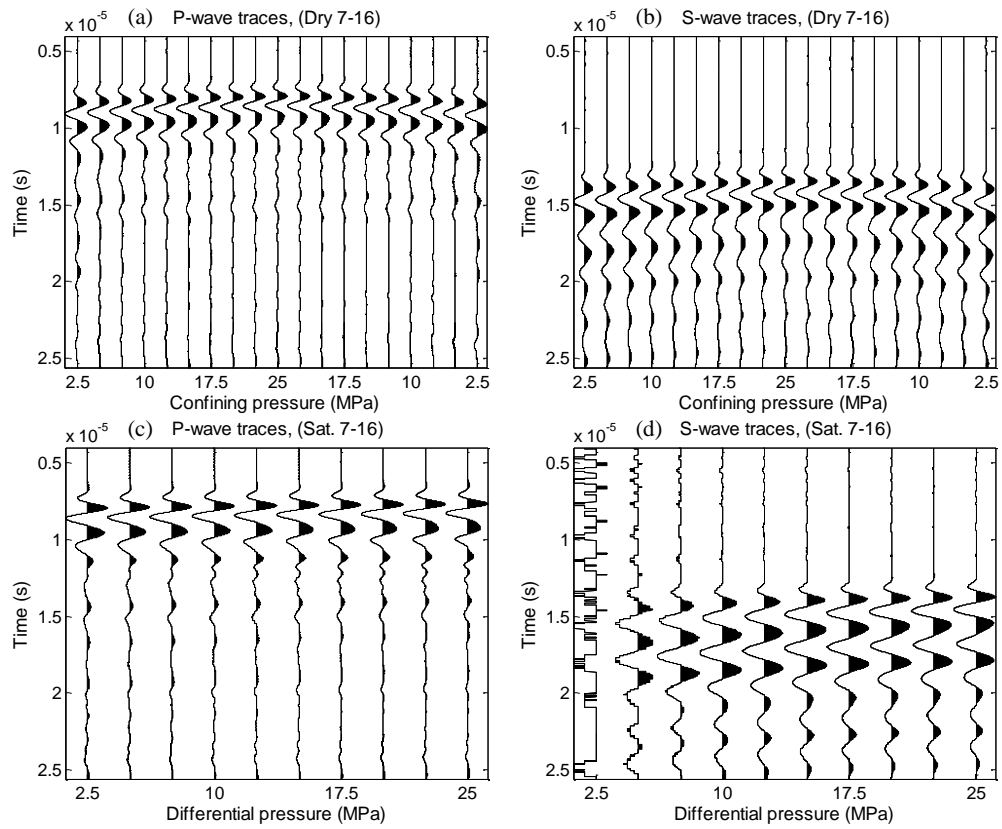


Figure C.34: Normalized waveforms of dry and saturated, P-wave (a and c respectively) and S-wave (b and d respectively) for sample 7-16 at different pressure.

Table C.64: Dry and saturated velocities of sample 7-16.

Pressure(MPa)	Dry		Saturated	
	Vp (m/s)	Vs (m/s)	Vp (m/s)	Vs (m/s)
2.5	4817 ± 18	2773 ± 6	5025 ± 19	2692 ± 6
5	4813 ± 18	2778 ± 6	5036 ± 19	2707 ± 6
7.5	4846 ± 18	2787 ± 6	5053 ± 19	2716 ± 6
10	4875 ± 18	2796 ± 6	5075 ± 19	2726 ± 6
12.5	4897 ± 18	2805 ± 6	5097 ± 19	2741 ± 6
15	4916 ± 18	2814 ± 6	5114 ± 19	2754 ± 6
17.5	4945 ± 19	2822 ± 6	5124 ± 19	2769 ± 6
20	4981 ± 19	2831 ± 6	5136 ± 20	2776 ± 6
22.5	5001 ± 19	2836 ± 6	5141 ± 20	2782 ± 6
25	5009 ± 19	2845 ± 6	5152 ± 20	2793 ± 6
22.5	5006 ± 19	2842 ± 6	-	-
20	4987 ± 19	2838 ± 6	-	-
17.5	4970 ± 19	2830 ± 6	-	-
15	4925 ± 18	2824 ± 6	-	-
12.5	4901 ± 18	2815 ± 6	-	-
10	4893 ± 18	2804 ± 6	-	-
7.5	4852 ± 18	2787 ± 6	-	-
5	4822 ± 18	2776 ± 6	-	-
2.5	4763 ± 18	2758 ± 6	-	-

Table C.65: Saturated velocities of sample 7-16 under constant differential pressure.

Confining pressure (MPa)	Pore pressure (MPa)	Vp (m/s)	Vs (m/s)
15	0	5129±19	2769±6
17.5	2.5	5130±19	2769±6
20	5	5131±20	2769±6
22.5	7.5	5129±19	2768±6
25	10	5129±19	2769±6

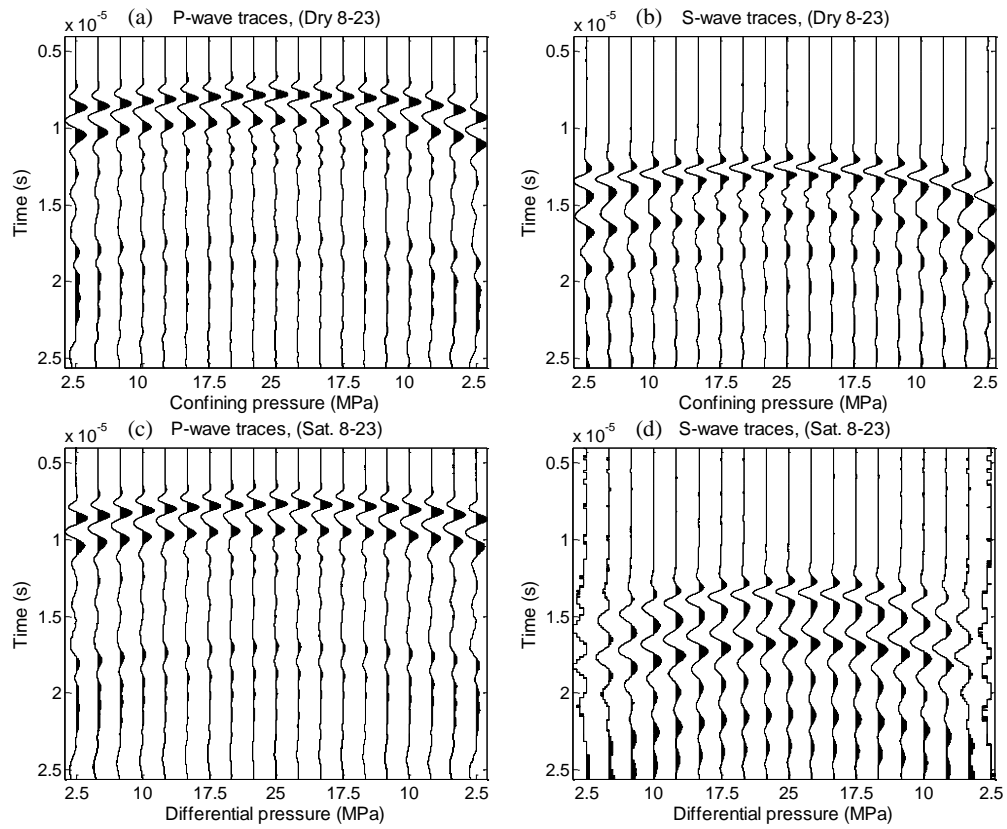


Figure C.35: Normalized waveforms of dry and saturated, P-wave (a and c respectively) and S-wave (b and d respectively) for sample 8-23 at different pressure.

Table C.66: Dry and saturated velocities of sample 8-23.

Pressure(MPa)	Dry		Saturated	
	Vp (m/s)	Vs (m/s)	Vp (m/s)	Vs (m/s)
2.5	3283 ± 12	2060 ± 5	3312 ± 12	1771 ± 4
5	3301 ± 12	2065 ± 5	3368 ± 13	1822 ± 4
7.5	3353 ± 12	2081 ± 5	3430 ± 13	1874 ± 4
10	3420 ± 13	2111 ± 5	3487 ± 13	1915 ± 4
12.5	3466 ± 13	2130 ± 5	3538 ± 13	1949 ± 4
15	3495 ± 13	2141 ± 5	3579 ± 14	1982 ± 4
17.5	3531 ± 13	2155 ± 5	3610 ± 14	2004 ± 4
20	3555 ± 14	2168 ± 5	3639 ± 14	2021 ± 4
22.5	3583 ± 14	2177 ± 5	3662 ± 14	2037 ± 5
25	3604 ± 14	2189 ± 5	3673 ± 14	2045 ± 5
22.5	3587 ± 14	2180 ± 5	3664 ± 14	2038 ± 5
20	3561 ± 14	2170 ± 5	3649 ± 14	2028 ± 5
17.5	3537 ± 13	2157 ± 5	3625 ± 14	2012 ± 4
15	3495 ± 13	2138 ± 5	3599 ± 14	1992 ± 4
12.5	3451 ± 13	2115 ± 5	3558 ± 14	1965 ± 4
10	3390 ± 13	2087 ± 5	3507 ± 13	1930 ± 4
7.5	3301 ± 12	2046 ± 5	3451 ± 13	1889 ± 4
5	3195 ± 12	1995 ± 4	3381 ± 13	1837 ± 4
2.5	3029 ± 11	1916 ± 4	3271 ± 12	1736 ± 4

Table C.67: Saturated velocities of sample 8-23 under constant differential pressure.

Confining pressure (MPa)	Pore pressure (MPa)	Vp (m/s)	Vs (m/s)
15	0	3584±14	1983±4
17.5	2.5	3603±14	1980±4
20	5	3613±14	1983±4
22.5	7.5	3622±14	1987±4
25	10	3618±14	1982±4

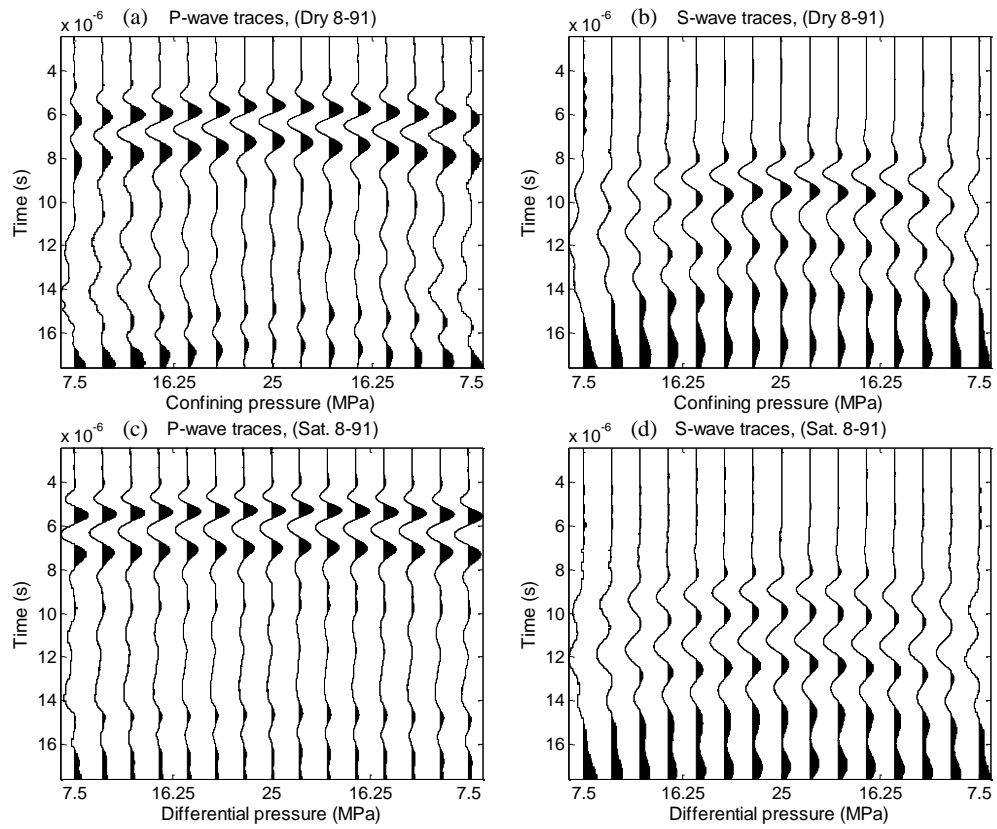


Figure C.36: Normalized waveforms of dry and saturated, P-wave (a and c respectively) and S-wave (b and d respectively) for sample 8-91 at different pressure.

Table C.68: Dry and saturated velocities of sample 8-91.

Pressure(MPa)	Dry		Saturated	
	Vp (m/s)	Vs (m/s)	Vp (m/s)	Vs (m/s)
7.5	3065 ± 13	1973 ± 5	3459 ± 15	1955 ± 5
10	3126 ± 14	1993 ± 5	3485 ± 16	1971 ± 5
12.5	3166 ± 14	2016 ± 5	3515 ± 16	1987 ± 5
15	3204 ± 14	2042 ± 6	3527 ± 16	2007 ± 5
17.5	3236 ± 14	2063 ± 6	3544 ± 16	2019 ± 5
20	3272 ± 14	2091 ± 6	3555 ± 16	2029 ± 6
22.5	3322 ± 15	2111 ± 6	3566 ± 16	2038 ± 6
25	3355 ± 15	2126 ± 6	3573 ± 16	2050 ± 6
22.5	3341 ± 15	2121 ± 6	3604 ± 16	2058 ± 6
20	3310 ± 15	2114 ± 6	3587 ± 16	2049 ± 6
17.5	3281 ± 14	2099 ± 6	3570 ± 16	2038 ± 6
15	3231 ± 14	2078 ± 6	3548 ± 16	2021 ± 5
12.5	3192 ± 14	2054 ± 6	3523 ± 16	2002 ± 5
10	3146 ± 14	2022 ± 5	3496 ± 16	1987 ± 5
7.5	3100 ± 13	1995 ± 5	3442 ± 15	1967 ± 5

Table C.69: Saturated velocities of sample 8-91 under constant differential pressure.

Confining pressure (MPa)	Pore pressure (MPa)	Vp (m/s)	Vs (m/s)
15	0	3536±16	2014±5
17.5	2.5	3534±16	2009±5
20	5	3539±16	2012±5
22.5	7.5	3545±16	2008±5
25	10	3548±16	2012±5

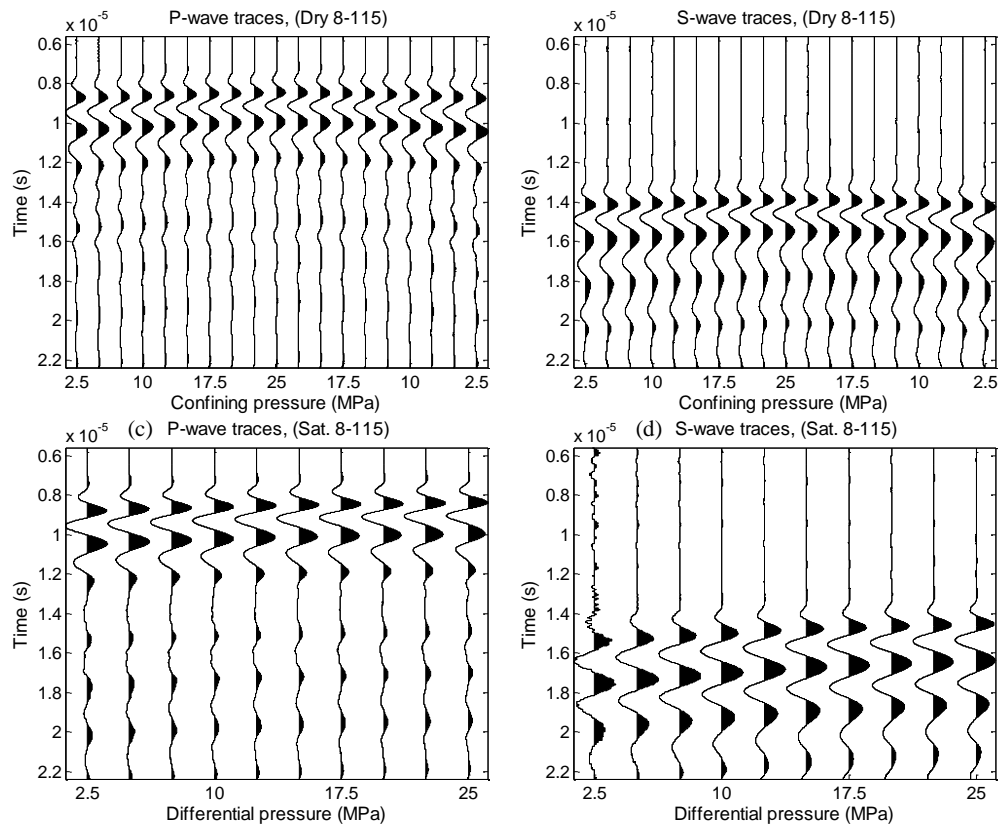


Figure C.37: Normalized waveforms of dry and saturated, P-wave (a and c respectively) and S-wave (b and d respectively) for sample 8-115 at different pressure.

Table C.70: Dry and saturated velocities of sample 8-115.

Pressure(MPa)	Dry		Saturated	
	Vp (m/s)	Vs (m/s)	Vp (m/s)	Vs (m/s)
2.5	4458 ± 16	2663 ± 6	4420 ± 16	2484 ± 5
5	4463 ± 16	2666 ± 6	4461 ± 16	2501 ± 5
7.5	4483 ± 16	2672 ± 6	4499 ± 16	2509 ± 5
10	4495 ± 16	2677 ± 6	4513 ± 16	2527 ± 5
12.5	4514 ± 16	2681 ± 6	4544 ± 17	2536 ± 5
15	4535 ± 17	2687 ± 6	4565 ± 17	2556 ± 5
17.5	4547 ± 17	2694 ± 6	4579 ± 17	2564 ± 5
20	4566 ± 17	2700 ± 6	4594 ± 17	2575 ± 5
22.5	4573 ± 17	2701 ± 6	4609 ± 17	2582 ± 5
25	4583 ± 17	2708 ± 6	4612 ± 17	2589 ± 5
22.5	4582 ± 17	2705 ± 6	-	-
20	4579 ± 17	2702 ± 6	-	-
17.5	4570 ± 17	2698 ± 6	-	-
15	4553 ± 17	2694 ± 6	-	-
12.5	4538 ± 17	2686 ± 6	-	-
10	4520 ± 16	2680 ± 6	-	-
7.5	4497 ± 16	2671 ± 6	-	-
5	4471 ± 16	2659 ± 6	-	-
2.5	4438 ± 16	2646 ± 6	-	-

Table C.71: Saturated velocities of sample 8-115 under constant differential pressure.

Confining pressure (MPa)	Pore pressure (MPa)	Vp (m/s)	Vs (m/s)
15	0	3596±14	2103±5
17.5	2.5	3593±14	2097±5
20	5	3592±14	2097±5
22.5	7.5	3595±14	2093±5
25	10	3599±14	2094±5

Table C.72: List of buffer pair sets and the samples measured using each pair.

Buffer set	Set 4	Set 5	Set 6	Set 8	Set 9	Set 10
Samples	3-104	2-131	2-10	1-11	1-288	3-331
		2-160	2-33	1-132	2-383	3-429
		7-16	2-59	1-304		4-09
		8-115	2-368	5-02		4-55
			2-432	5-289		4-97
			3-05	5-295		4-151
			3-90	7-20		4-180
			3-146	7-222		4-189
			3-471	7-240		4-326
			3-534			
			8-23			
			8-91			

Table C.73: P- and S-wave travel time of aluminum buffer set 4.

Pressure (MPa)	P-wave travel time (s)	S-wave travel time (s)
5	11.109	20.674
10	11.100	20.666
15	11.092	20.658
20	11.084	20.650
25	11.075	20.642
30	11.067	20.634
35	11.059	20.626
40	11.050	20.618
35	11.059	20.626
30	11.067	20.634
25	11.075	20.642
20	11.084	20.650
15	11.092	20.658
10	11.100	20.666
5	11.109	20.674

Table C.74: P- and S-wave travel time of aluminum buffer set 5.

Pressure (MPa)	P-wave travel time (μ s)	S-wave travel time (μ s)
2.5	11.529	20.719
5	11.526	20.717
7.5	11.523	20.714
10	11.520	20.712
12.5	11.517	20.710
15	11.514	20.708
17.5	11.511	20.706
20	11.507	20.704
22.5	11.504	20.701
25	11.501	20.699
22.5	11.504	20.701
20	11.507	20.704
17.5	11.511	20.706
15	11.514	20.708
12.5	11.517	20.710
10	11.520	20.712
7.5	11.523	20.714
5	11.526	20.717
2.5	11.529	20.719

Table C.75: P- and S-wave travel time of aluminum buffer set 6.

Pressure (MPa)	P-wave travel time (μ s)	S-wave travel time (μ s)
2.5	11.518	20.734
5	11.508	20.727
7.5	11.497	20.720
10	11.486	20.713
12.5	11.475	20.707
15	11.464	20.700
17.5	11.453	20.693
20	11.442	20.686
22.5	11.431	20.679
25	11.420	20.672
22.5	11.431	20.679
20	11.442	20.686
17.5	11.453	20.693
15	11.464	20.700
12.5	11.475	20.707
10	11.486	20.713
7.5	11.497	20.720
5	11.508	20.727
2.5	11.518	20.734

Table C.76: P- and S-wave travel time of aluminum buffer set 8.

Pressure (MPa)	P-wave travel time (μ s)	S-wave travel time (μ s)
5	11.635	20.820
7.5	11.613	20.804
10	11.598	20.789
12.5	11.587	20.775
15	11.577	20.762
17.5	11.569	20.750
20	11.562	20.740
22.5	11.556	20.730
25	11.551	20.722
22.5	11.556	20.730
20	11.562	20.740
17.5	11.569	20.750
15	11.577	20.762
12.5	11.587	20.775
10	11.598	20.789
7.5	11.613	20.804
5	11.635	20.820

Table C.77: P- and S-wave travel time of aluminum buffer set 9.

Pressure (MPa)	P-wave travel time (μ s)	S-wave travel time (μ s)
5	11.508	20.717
7.5	11.497	20.714
10	11.486	20.712
12.5	11.475	20.710
15	11.464	20.708
17.5	11.453	20.706
20	11.442	20.704
22.5	11.431	20.701
25	11.420	20.699
22.5	11.431	20.701
20	11.442	20.704
17.5	11.453	20.706
15	11.464	20.708
12.5	11.475	20.710
10	11.486	20.712
7.5	11.497	20.714
5	11.508	20.717

Table C.78: P- and S-wave travel time of aluminum buffer set 10.

Pressure (MPa)	P-wave travel time (μ s)	S-wave travel time (μ s)
5	9.265	16.860
7.5	9.249	16.838
10	9.232	16.817
12.5	9.215	16.796
15	9.198	16.775
17.5	9.181	16.754
20	9.164	16.733
22.5	9.147	16.712
25	9.131	16.690
22.5	9.147	16.712
20	9.164	16.733
17.5	9.181	16.754
15	9.198	16.775
12.5	9.215	16.796
10	9.232	16.817
7.5	9.249	16.838
5	9.265	16.860